Summer 2019

Polyurea aerogels: From nanoscopic to macroscopic properties

Tahereh Taghvaee

Department: Chemistry

POLYUREA AEROGELS: FROM NANOSCOPIC TO MACROSCOPIC PROPERTIES

by

TAHEREH TAGHVAEE

A DISSERTATION

Presented to the Faculty of the Graduate School of the

MISSOURI UNIVERSITY OF SCIENCE AND TECHNOLOGY

In Partial Fulfillment of the Requirements for the Degree

DOCTOR OF PHILOSOPHY

in

CHEMISTRY

2019

Approved by:

Dr. Nicholas Leventis, Advisor
Dr. Chariklia Sotiriou-Leventis
Dr. Amitava Choudhury
Dr. Manashi Nath
Dr. F. Scott Miller

PUBLICATION DISSERTATION OPTION

This dissertation consists of the following three articles, formatted in the style used by the Missouri University of Science and Technology:

Paper I: Pages 30-198 have been submitted to *ACS Nano* Journal.

Paper II: Pages 199-232 are intended for submission to *Soft Matter* Journal.

ABSTRACT

The morphology of a material is intrinsically a qualitative property and in order to relate nanomorphology to synthetic conditions, it is necessary to express nano/micro-structure quantitatively. In this context, polyurea aerogels were chosen as a model system with demonstrated potential for rich nanomorphology and being guided by a statistical Design-of-Experiments model, a large array of materials (208) with identical chemical composition, but quite different nanostructures were prepared. By reflecting upon the SEM images, it was realized that our first pre-verbal impression about a nanostructure is related to its openness and texture; the former is quantified by porosity (Π), and the latter is related to the contact angle (θ) of water droplets resting on the material. Herewith, the θ/Π ratio is referred to as the *K*-index, and it was noticed that all polyurea aerogel samples could be put in eight *K*-index groups with separate nanomorphologies. The *K*-index was validated as a morphology predictor by compressing samples to different strains: as porosity decreases, contact angle decreases proportionally, and the *K*-index remains constant. The predictive power of the *K*-index was demonstrated with new PUAs prepared in eight binary solvents. Finally, using response surface methodology, *K*-indexes and other material properties of interest were correlated to synthetic conditions, thus enabling synthesis of materials with prescribed properties at a time. The second part of this dissertation focuses on polyurea aerogels consisting of different arrangements of nanoparticles ($1.2 \leq$ *K*-index ≤ 1.5). SAXS, XRD and SEM have demonstrated that these nanostructures consist of similar-size primary particles. A model for the formation of these nanoparticles through Molecular Dynamic simulations is suggested.

ACKNOWLEDGMENTS

First and foremost, I would like to express my sincere gratitude to my advisor, Prof. Nicholas Leventis and co-advisor Prof. Chariklia Sotiriou-Leventis for their continuous guidance, encouragement, support and constructive criticism throughout my graduate study. Their input has been invaluable toward the completion of this dissertation. Prof. Nicholas Leventis' positive outlook and approach to research has been one of the highlights of my time in his group. I am truly grateful for the opportunity to be a part of his group and for all the things I have learned from him in my educational and professional development.

I would also like to thank Dr. M. Nath, Dr. A. Choudhury and Dr. F. Scott. Miller for serving on my PhD committee and providing me their valuable suggestions throughout the completion of this dissertation. I would like to extend my thanks to Dr. Chenglin Wu (Missouri S&T) and Dr. Hongbing Lu (UT-Dallas) for their valuable collaborations. I also thank the Chemistry Department of Missouri S&T for providing teaching assistantships and its resources. Special thanks are reserved for Dr. Vadym Mochalin, Mr. Jonathon Sidwell, Mr. Shannon Roark and Ms. Tina Blach for their help.

I would also like to thank all the past and current group members for their help and friendship: Adnan, Suraj, Hojat, Saidulu, Parwani, Chandana, Rushi, Shaheen and Vaibhav. I am also thankful to all my friends who have helped me throughout my time in Rolla: Saman, Armita, Ross, Casey, Hooman, Shadi, Baharan, Bahar, Mahboobeh and Clara.

I would also like to thank my brothers Abolfazl, Abolghasem, Omid and my lovely sisters Leila and Raheleh for their incomparable love, motivation and support. Most importantly, I would like to thank my parents who live in my heart forever. They supported me in every decision I have made in my life. Words alone cannot express the extent to which I owe them. This dissertation is dedicated to them.

TABLE OF CONTENTS

Page

LIST OF ILLUSTRATIONS

PAPER II

LIST OF SCHEMES

SECTION Page

LIST OF TABLES

1. INTRODUCTION

1.1. AEROGELS

Aerogels are highly porous ultralight materials consisting of three-dimensional assemblies of nanoparticles.[1] There are several definitions for the term "aerogel." But all definitions state that all aerogels are derived from wet-gels through a sol-gel process. The aerogel is defined by IUPAC as a "gel comprised of a microporous solid in which the dispersed phase is a gas."[2] Pierre by adopting the initial idea of Kistler defines aerogel as the "gels in which the liquid has been replaced by air, with very moderate shrinkage of the solid network."[1] This concept is simplified, appropriate, and widely acceptable. Hüsing in a similar but longer definition, describes aerogels as "materials in which the typical structure of the pores and the network is largely maintained, while the pore liquid of a gel is replaced by air."[3]

In all these definitions, the "aero" part is covered but not the "gel" part. In that regard, a more comprehensive definition of the term "aerogel" has been proposed by Leventis: "An open non-fluid colloidal network or polymer network that is expanded throughout its whole volume by a gas, and is formed by the removal of all swelling agents from a gel without substantial volume reduction or network compaction."[4] Furthermore, in this description, aerogels are differentiated from closed-cell foam xerogels.

Overall, aerogels are derived from wet-gels where the pore-filling solvent is replaced with liquid carbon dioxide which is gasified supercritically and vented off. This process retains the porous nanostructure of the original wet-gels into the dry solids with minimum shrinkage.

Aerogels can be classified through different ways. By considering their pore size, they can be divided into microporous, mesoporous, and macroporous aerogels, where the size of pores are less than 2 nm, between 2 and 50 nm, and greater than 50 nm, respectively. Based on their appearance, they can be classified as monolithic, powdery, and film.[5] In another classification, depending on the starting precursors, all aerogels fall into two major categories: organic and inorganic. Among inorganic aerogels, silica aerogel is by far the most studied system and is discussed in the following section.

1.2. SILICA AEROGELS

Silica aerogels were first produced by Samuel Stephens Kistler in the early 1930s.[6-7] They have a wide variety of exceptional properties, such as low density (~0.003 g/cm^3), high porosity (~99% *v/v*), high optical transmission (~99%) in the visible region, high specific surface area (~1000 m^2g^{-1}), high thermal insulation value (~0.01 W m^{-1} K^{-1}), low dielectric constant (~1.0 – 2.0), low index of refraction (~1.05), and low sound velocity (~100 m/s).[8-9] Due to these unusual characteristics, silica aerogels have been considered for many applications such as Cherenkov radiators,[10] thermal insulation materials in building industries,[11] and acoustic barrier materials in heat storage devices.[12] Silica aerogels were successfully used for many aerospace applications including insulation around the batteries for the rover in the NASA Mars mission to protect its electronic units.[13] Thermal insulation is not the only application of silica aerogels in space. Indeed, silica aerogels were also used to collect cosmic particles from the comet tail in the Stardust spacecraft,[14] to protect space mirrors and to design tank baffles.[15-16]

Nevertheless, the poor mechanical strength of these low-density materials limits their use in many practical applications.[17] In this context, many techniques have been adopted to reinforce silica aerogels by modifying their nanostructure, which requires a deep grasp on their formation through sol-gel process.

1.2.1. Sol-gel Chemistry. Basically, a three-dimensional nanostructured network of silica is the product of hydrolysis and condensation reactions of the silica precursor molecules, in which Si-O-R and Si-OH bonds are transformed to siloxane bridges (Si-O-Si).[1] Originally, Kistler using sodium silicate as the silica source made silica aerogels.[6-7] The reaction produced some by-products such as salts within the gel that were required to be removed during washing steps, which was tedious and time consuming.[18] Later on, Teichner et al. adopted Kistler's approach and made transparent silica aerogels derived from tetraalkoxysilanes ($Si(OR)_4$) and an alcohol such as methanol or ethanol. Hydrolysis reactions were initiated by the addition of water, during which Si-OH bonds were formed. The reaction is usually performed under acidic or basic conditions to accelerate hydrolysis of alkoxysilanes and in turn condensation reactions. The Teichner's technique had some advantages over Kistler's method; replacing water with alcohol bypasses the solvent exchange step and eliminates tedious washing steps required for removing formed salts, which decreases the processing time.

In addition, since many alkoxysilanes are not miscible with water, alcohols as bifunctional solvents are used to improve the miscibility of water with the organic phase. Alcohols act as ideal intermediate when the medium transforms from a protic to an aprotic. Interestingly, the structural and final material properties of the resulting aerogels are

significantly correlated to the choice of alcohol,[19-21] but mostly the same alcohol generated during the hydrolysis reactions is used to eliminate the alcohol exchange steps.

Mostly, silica aerogels are synthesized using silicon alkoxides such as tetramethyl orthosilicate (TMOS, Si $(OCH_3)_4$) and tetraethyl orthosilicate (TEOS, Si $(OCH_2CH_3)_4$).[22] With the development of the sol-gel technique, different organic functional groups can be attached to silicon to tailor target properties in the resulting gel. While the use of tetra-alkoxysilanes, $Si(OR)_4$, results in the formation of silica (SiO_2), organo-substituted derivatives with the chemical formula of $R'_XSi\ (OR)_{4-X}$ in which x varies from 1 to 3 resulting in mono, di and trifunctional organo silanes, forming the so-called "orgonosilsesquioxanes."[1] Other common organo silica precursors with general formula of $(OR)_3SiR'Si(OR)_3$ in which R′ is an alkyl, aryl, or alkenyl bridge group between two elements of silica result in the products referred to as "bridged organosilsesquioxane."[17, 23]

The use of silicon alkoxides avoids formation of salt byproducts and gives more possibilities to control the final product with respect to the texture and resulting properties. Scheme 1.1 indicates the formation of a three dimensionally continuous network of silica from TMOS in alcohol such as methanol or ethanol.

Scheme 1.1. Synthesis of silica structure through the hydrolysis and condensation of tetra methyl orthosilicate (TMOS).

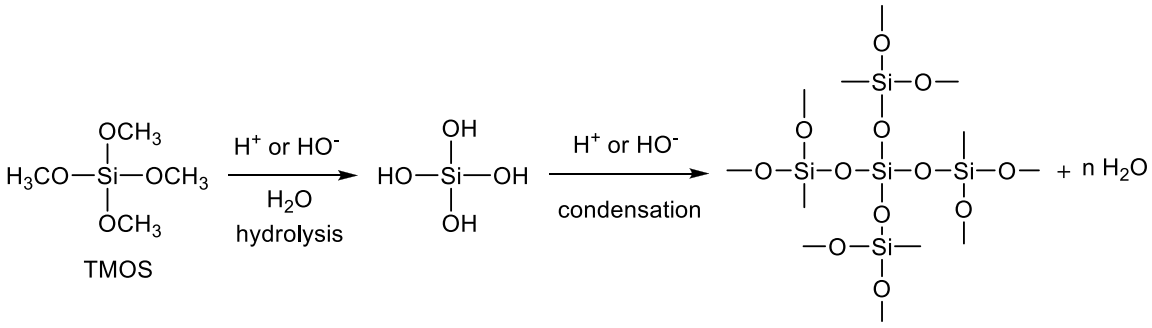

The sol–gel transition also known as gelation, as the name implies, is simply a transition from a liquid state to gel state. Before hydrolysis and condensation reactions, the soluble precursor molecules are free to move in the sol. But when the sol transforms into a gel, it is often said that the hydrolysis and condensation reactions are complete, and the soluble silica precursors phase separate into non-soluble small primary particles. Subsequently, the primary particles aggregate into secondary particles which finally agglomerate into fractal clusters until the percolation threshold is reached, and an extending network of particles is formed that is referred to as a wet-gel.[1]

To improve the mechanical strength of wet-gels an "aging" process is performed.[24] During this event, silica formed on the surface of the primary particles is dissolved and reprecipitated at the interparticle necks to enlarge the neck area. Figure 1.1 indicates the macroscopic appearance and the continuous 3D network of silica aerogel consisting of primary and secondary particles.

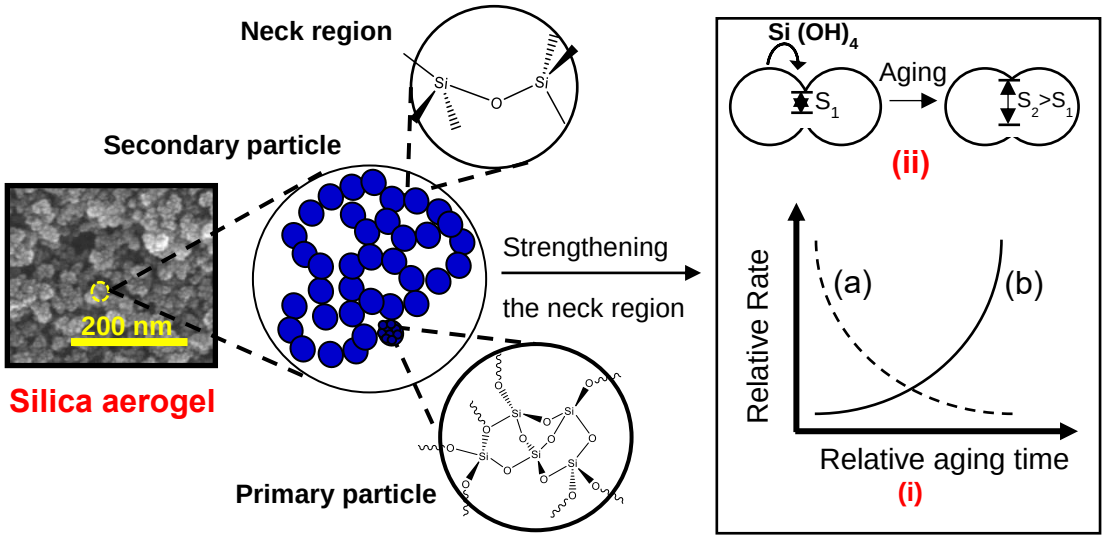

Figure 1.1. Typical macroscopic (left) and nanoscopic appearance of a silica aerogel (middle) along with neck growth mechanism of secondary silica particles (i) and relative aging rate as a function of aging time for two mechanisms (a, b) (ii) (right).[25]

1.2.2. Supercritical Fluid Drying Technique. By far one of the most challenging processes in aerogel preparation is drying wet-gels in which the solvent confined in the pores should be removed while preserving the nanoporous structure with the minimum shrinkage and without cracking. In general, there are three different drying methods:[25] (1) *Ambient air drying* without specific surface treatments usually results in dense and cracked materials, the so-called "xerogels". The densification during evaporation comes from condensation of the remaining reactive silica species. When the silica wet gel is subjected to the capillary pressure, the initially far distance surface hydroxyl/alkoxy groups come close enough to each other to react and generate new siloxane bonds, leading to the irreversible shrinkage due to the inherent flexibility of silica chains. The capillary tension in evaporative drying may reach 100–200 MPa. (2) *Freeze drying* in which the temperature of the wet-gel is lowered below the crystallization temperature of the solvent and then the frozen solvent is extracted by sublimation under vacuum resulting in cryogel.[22] During the crystallization, the volume of the solvent increases which applies stresses in the gel directed from the crust toward inside that cause shrinkage and breakage of the crust layers into small pieces. (3) *Supercritical drying*, also known as *critical-point drying*, is a method by which the pore-filling liquid in wet-gel is replaced by a supercritical fluid, usually carbon dioxide, which is subsequently removed above its critical pressure and temperature, i.e., in its supercritical state.[1] Due to the absence of surface tensions and capillary forces in the pores of wet-gel, this process avoids the gel nanostructure to be collapsed upon solvent removal resulting in dry solid objects referred to as aerogels. Figure 2.1 depicts the aerogel synthesis from the sol-gel process to the final step, which is supercritical drying.

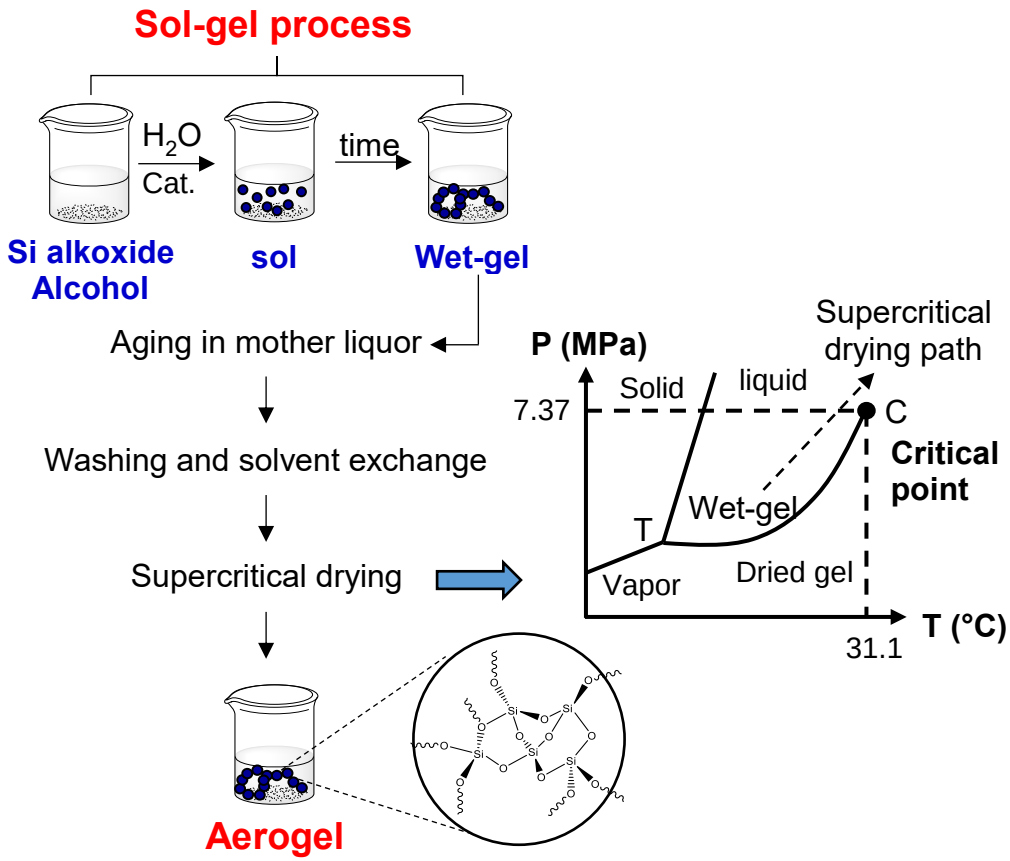

Figure 1.2. The sol-gel process for formation of silica aerogel.

1.2.3. Enhancing the Mechanical Strength of Silica Aerogels. Silica aerogels contain a very open structure in which only a few siloxane bonds link the secondary particles and lead to their intrinsic fragility. In fact, the brittle nature of silica aerogel imposes severe constrains on their different potential load bearing applications. In this context, many researchers have been mainly focused on finding methods for maximizing the mechanical stiffness of silica aerogels.[26-27] The "Aging" process is one of the techniques that is used to reinforce the framework of a silica wet-gel. A typical aging procedure involves soaking the gel in a mixture of water/alcohol with equal proportions to the original sol at pH 8–9.[28] Generally, there are two different mechanisms that occur

during the aging process that lead to reinforcing the structure of a resulting gel: (a) dissolution of silica formed on the surface of particles and reprecipitation onto necks between secondary particles, which leads to neck growth; and (b) dissolution of smaller particles and precipitation onto larger ones, which results in wider neck region (Figure. 1(i)).[29] These mechanisms occur simultaneously but with different rates (Figure. 1(ii)). Additionally, Brownian motion brings the silica particles in contact with each other, leading to more reactions between them, which in turn increases the number of siloxane linkages and reinforces the silica network in connection points.[30] Although the aging process can increase the Young's modulus of the silica by approximately a factor of two, the resulting aerogels remain fragile.

In another method, hybrid precursors such as poly(dimethylsiloxanes) are employed for hybridization of silica aerogels. During this event, the co-gelation of the silicon alkoxide with hybrid precursors results in gels are referred to as "ORMOSIL" hybrids which have more rubber-like flexibility.[31] Coupling the inorganic network of silica aerogels with various polymeric materials can significantly improve the tensile strength of the silica aerogel.[32] Furthermore, consolidation of silica aerogel with supporting materials, such as polymeric and carbon nanofibers[32-34] and fiberglass,[35] can fortify the structure of silica aerogels. The grid of fibers supports the aerogel skeleton and reduces the bulk size of aerogel within composite aerogel.[36]

1.3. ORGANIC AEROGELS

Organic aerogels, unlike inorganic aerogels, are polymers with an entirely organic framework. Their properties are generally different from inorganic aerogels such as silica

and metal oxide aerogels. For example, they are sturdier than inorganic aerogels. The first organic aerogel known as "resorcinol-formaldehyde (RF)" was introduced by Pekala et al. in 1987.[37] RF aerogel was prepared *via* condensation of resorcinol (R) with formaldehyde (F) under alkaline conditions. In the presence of a base, resorcinol as a nucleophile reacts with formaldehyde to form addition and condensation intermediates in the solution. At the beginning of polymerization, these intermediates form RF clusters, which consequently go through further reactions over the gelation leading to a highly crosslinked polymeric network.

The resulting RF polymeric clusters consist of particles very similar to those formed by silica aerogels. Leventis et al. indicated that the size of those particles is highly dependent on the [resorcinol]/[catalyst] ratio, the pH of the solution, and also on the temperature at which the reaction takes place.[38] The role of catalyst in the polymerization of RF and the extent of crosslinking is crucial because it facilities the formation of negatively charged resorcinol species that are highly reactive to formaldehyde. Therefore, the synthetic conditions, including the catalyst concentration, pH and temperature, control the structural and material properties of resulting aerogel.[38]

In 1993, Pakala and Schaefer used the small-angle X-ray scattering (SAXS) method to understand the structure of nanoporous RF aerogel.[39] The SAXS data showed a smooth surface with no fractal clusters or rough characteristics. It was then concluded that phase separation (restricted to nanometer size), due to insolubility of developing polymer in the sol during cross-linking, determines the morphology of these materials. Later, Nakanishi et al.[40] stated that the gels are formed *via* a phenomenon known as "chemical cooling," during which monomers react together resulting in phase-separation of small surface

primary particles. Those particles make covalent bonds between themselves to form a continuous three-dimensional structure.

For many years, the term “organic” was assigned to RF aerogel and research on organic aerogels were only dedicated to better understandimg the mechanism of formation of RF aerogels and improving their material properties such as bulk density, porosity, surface area and pore size.[41-42] However, other types of phenolic resin aerogels such as melamine formaldehyde, cresol formaldehyde and phenol-furfural were later synthesized based on formaldehyde-type resin chemistry.[43]

Today, the term “organic aerogels” is not limited to phenolic resins. Lately, the organic aerogels division has been expanded to other polymers such as polyurea (PUA),[44] polyimide (PI),[45] polyamide (PA),[46] copolymers of polyamide-polyimide-polyurea,[47] polyacrylonitrile (PAN),[4] polyurethane (PU),[48] polystyrene (PS),[49] polybenzoxazine (PBO),[50] and poly dicyclopentadiene (*p*-DCPD).[51]

As mentioned in previous sections, the low mechanical strength of silica aerogels hinders their use in many applications. In this context, organic aerogels due to high mechanical strength have shown great performance in many applications that are not attainable by inorganic aerogels. Furthermore, the organic aerogels with desirable material properties for target-specific applications can be tailored by controlling the synthetic conditions. For instance, Leventis et al. showed that there is a correlation between the molecular properties of the monomer and the flexibility of the resulting polymers. Using flexible aliphatic isocyanate, they were able to synthesize highly flexible and foldable polyurethane aerogels, while rigid aromatic isocyanates did not yield flexible polymers.[52]

In another study, Leventis and co-workers synthesized a series of shape memory polyurethane aerogels (SMPA) *via* the reaction of an aliphatic triisocyanate with ethylene glycol and its short derivatives ($H(OCH_2CH_2)_nOH$ ($1 \leq n \leq 4$)) in a mixture of acetone and acetonitrile as solvent.[48] Scanning electron microscopy analysis showed that the resulting aerogels consist of microspheres with densities in the range 0.2−0.4 g cm^{-3}. Glass transition temperatures (Tg) changed from 30 (n = 4) to 70 °C (n = 1). All shape memory aerogels showed super elasticity at Tg and above Tg. Furthermore, employing a design-of-experiment (DoE) technique, they optimized the synthetic conditions required for synthesis of a shape memory material. It was concluded that the longer diols and solvents with enhanced hydrogen bonding ability (more portion of acetone in the solvent blend) lead to more shrinkage resulting in denser polymer and therefore are not suitable for the synthesis of shape memory materials.[48]

Among organic aerogels, polyimides have received a lot of attention in thermal and acoustic applications in aerospace because of their high thermal resistance and great mechanical strength. Guo et al.[53] synthesized foldable polyimide aerogels cross-linked with octa(aminophenyl)silsesquioxane (OAPS). The obtained polyimides had low density (~0.1 g cm^{-3}), low shrinkage, high porosity (~92% *v/v*), high BET surface area (~260 m^2/g), and high decomposition temperature (~560 °C).

In the synthesis path of many organic aerogels such as polyurea and polyurethane, crosslinkers such as isocyanates play an important role. Therefore, we review the chemistry of isocyanates in the following section.

1.3.1. The Chemistry of Isocyanates. Isocyanates are essential components required for synthesis of many organic aerogels. They can be either aromatic or aliphatic,

containing two (di-isocyanates) or more (polyfunctional isocyanates) –NCO groups per molecule. The common aromatic isocyanates are toluene diisocyanates (TDI) and methylene diphenyl isocyanate (MDI). Every year, more than 5 million tons of MDI are produced in the world, which indicates that this isocyanate is the most used in the synthesis of organic polymers. Common aliphatic isocynates are hexane diisocyanate (HDI), isophorone diiscocyanate (IPDI), and methylene dicyclohexyl isocyanate (H_{12}MDI).[54] The structures of some common isocyanates are shown in Scheme 1.2.

Scheme 1.2. Common isocyanates.

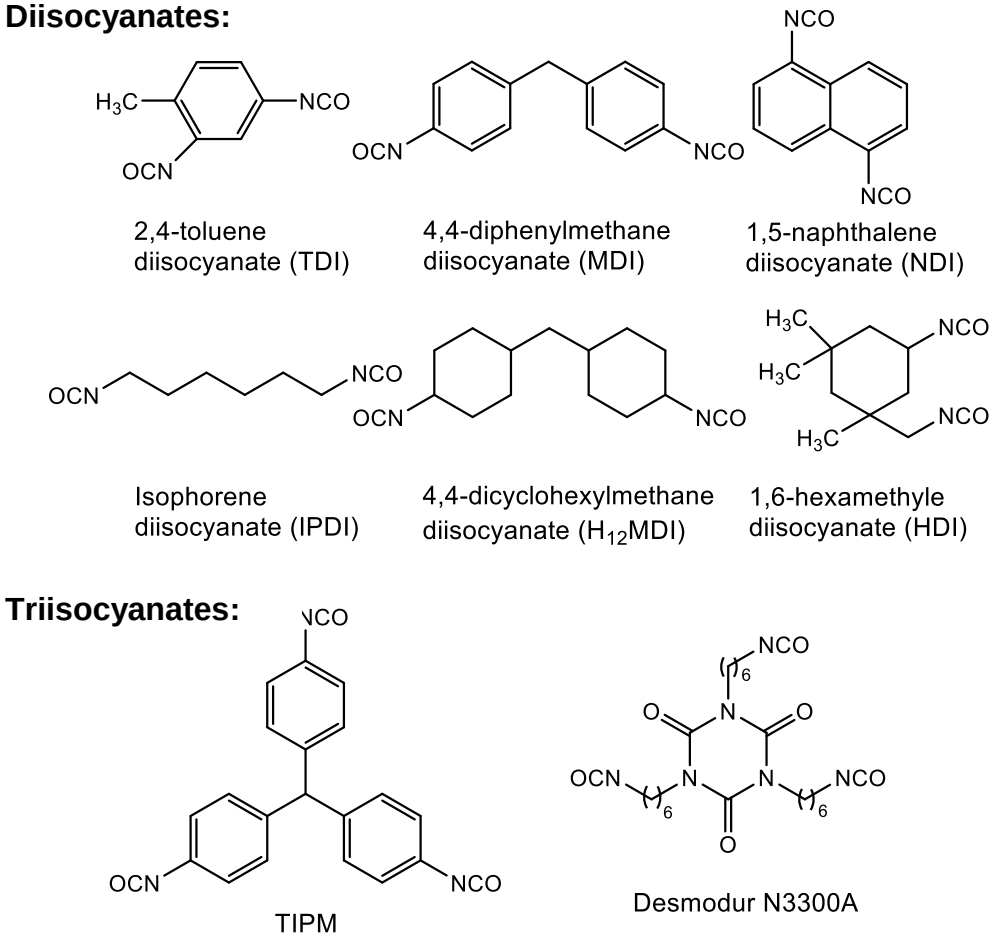

The -N=C=O group is highly reactive. Due to the presence of electron withdrawing atoms, including nitrogen and oxygen, a partial positive charge is induced on the carbon atom, which serves as an electrophile (Scheme 1.3).

Scheme 1.3. The -N=C=O group and possible resonance structures.

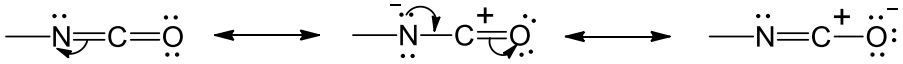

The nucleophilic attack on the isocyanate group is shown in Scheme 1.4. General nucleophiles and their relative reactivity are summarized in Table 1.1.

Scheme 1.4. The attack of a nucleophile on the carbon atom in the isocyanate group.

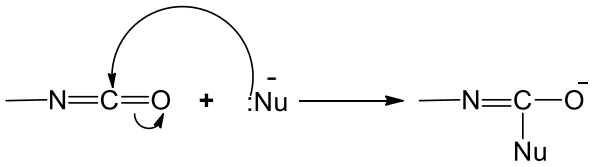

Table 1.1. Active hydrogen compounds ordered by decreasing nucleophilicity.[20]

Active hydrogen compound	**Typical structure**	**Relative reaction rate (uncatalyzed at 25 ºC)**
primary aliphatic amine	R-NH_2	100,000
secondary aliphatic amine	R_2-NH	20,000 - 50,000
primary aromatic amine	Ar-NH_2	200-300
primary hydroxyl	R-CH_2-OH	100
water	H-O-H	100
carboxylic acid	RCOOH	40
secondary hydroxyl	R_2CH-OH	30
urea	R-NH-CO-NH-R	15
urethane	R-HN-CO-OR	0.3
amide	RCO-NH_2	0.1

The reactivity of the isocyanate group can be altered by attaching electron donating and electron withdrawing groups to nitrogen atom. In that regard, the aromatic isocyanates are generally more reactive than their aliphatic counterparts.[54] Additionally, electron withdrawing groups induce a more positive charge on the carbon, which increase the reactivity of the isocyanate group towards nucleophilic attack.[22] Inversely, electron donating substitution decreases the reactivity of the isocyanate group. The reactions of alkyl and aryl isocyanates with various nucleophiles are summarized in Scheme 1.5.

Scheme 1.5. Reactions of isocyanate with some common nucleophiles.

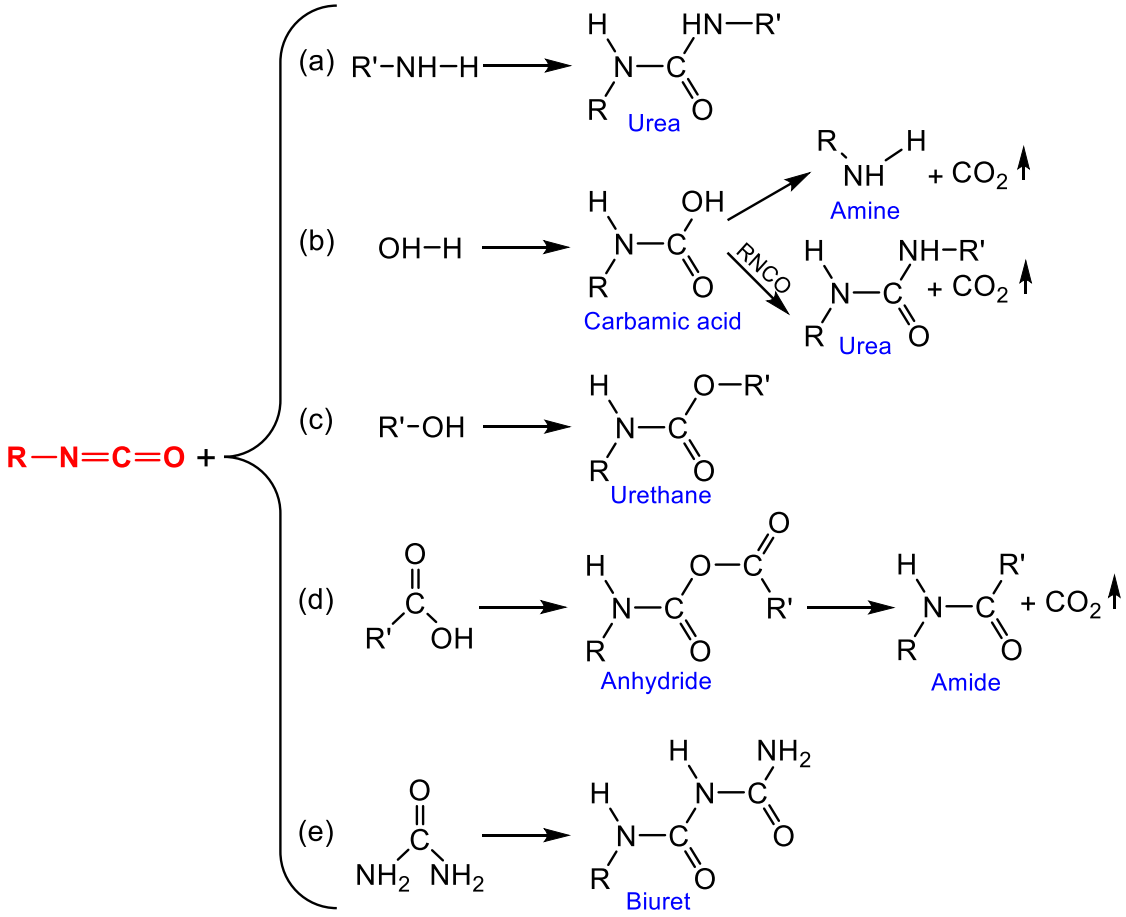

1.3.1.1. Reaction of isocyanates with amines. Urea is formed *Via* the nucleophilic attack of the amine group to the electrophilic carbonyl in the isocyanate (Scheme 1.6).

Scheme 1.6. Formation of urea from isocyanates and amines.

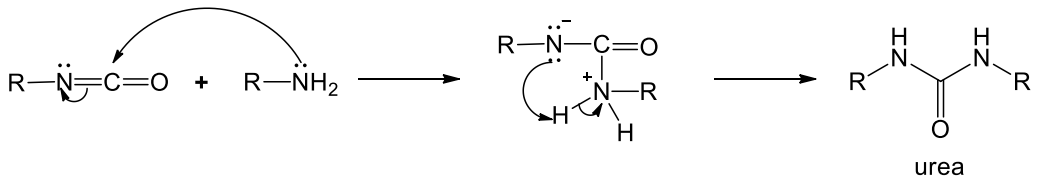

In general, this reaction is exothermic, very fast, and does not need any catalyst. Aromatic amines react more slowly than their aliphatic counterparts because of the delocalization of the amine electron pair in the aromatic ring through resonance.[55]

1.3.1.2. Reaction of isocyanates with water. During the nucleophilic attack of water to the carbonyl group, an unstable carbamic acid is formed which is decomposed into amine and carbon dioxide as a by-product. The *in-situ* generated amine reacts further with yet unreacted isocyanate to yield urea as illustrated in Scheme 1.7.[56]

Scheme 1.7. *In-situ* formation of amine from isocyanates and water.

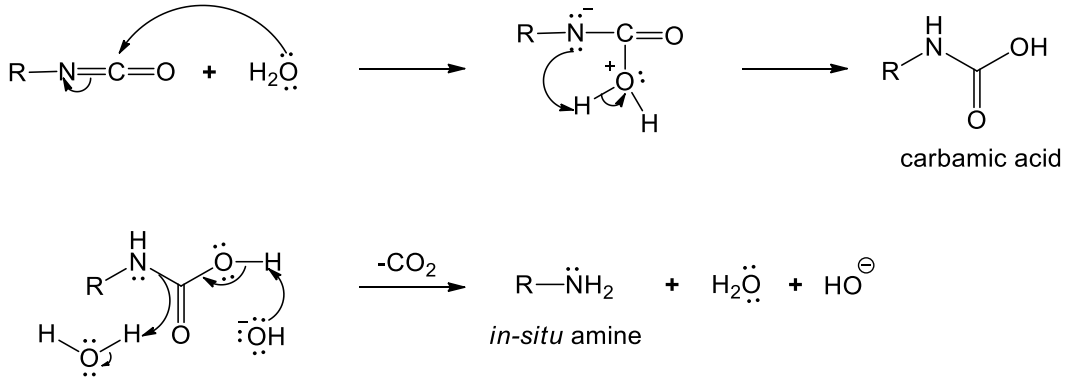

Gelation mechanism of urea formation *via* the reaction of isocyanate with water in the presence of triethylamine as a catalyst is shown in Scheme 1.8.

Scheme 1.8. Mechanism of urea formation through reaction of isocyanate with water in the presence of a catalyst.

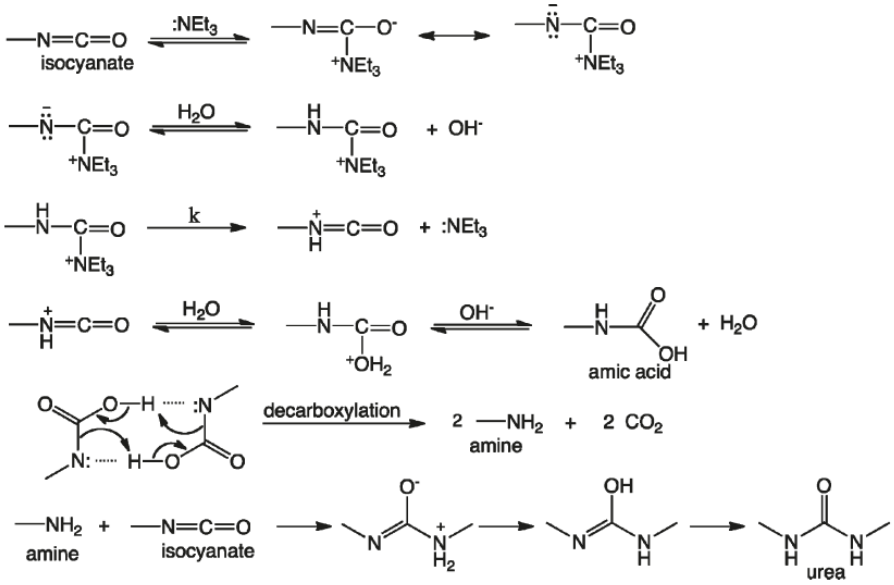

1.3.1.3. Further reactions of isocyanates with urea. During the nucleophile attack of water to the carbonyl group, urea, acting as a nucleophile itself, is capable of attacking excess isocyanate under more rigorous reaction conditions to yield biurets (Scheme 1.9).[54]

Scheme 1.9. Formation of biuret from isocyanate and urea.

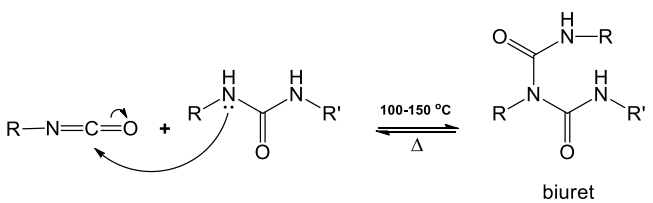

1.3.2. Polyurea Aerogels. The synthesis of polyurea (PUA) aerogels was first mentioned in 1994 in a U.S. patent [57] through nucleophilic addition of amines to isocyanates (Scheme 1.6). In 2009, Lee et al. synthesized polyurea aerogels using commercially available methylene diisocyanates (MDI, for polyurea 1) and polymeric MDI (for polyurea 2) with two different types of amine hardeners (Jeffamine-T3000 and T5000, Huntsman LLC).[58] In that study, the authors investigated the thermal insulation properties of obtained aerogels. They reported a particulate morphology for all the polyurea aerogels like what can be seen in silica aerogel. It was also shown that the small pore diameter and narrow size distributions were obtained with the aerogels synthesized from small molecule, in this case from MDI. The aerogels showed a wide range of final densities (0.098–0.116 g cm^{-3}), high porosity (90–91% *v/v*), low shrinkage (f = 1.14–2.95, f: the ratio of final density to target density), low thermal conductivities (18–19 mW m^{-1} K^{-1}), and good hydrophobicity.

There was no report on mechanical behavior of those aerogels until 2010. In 2010, Leventis et al. proposed an alternative method, both more cost-efficient and more environmentally friendly, which replaced the amine with water.[56] They synthesized mechanically strong polyurea aerogels in acetone from Desmodur N3300A triisocyanate, water, and triethylamine as catalyst (Scheme 1.8). Polyurea aerogels with a wide range of bulk densities (0.016–0.055 g cm^{-3}) were prepared and characterized. Interestingly, the nanomorphology of those aerogels varied from fibrous to particulate as the density increased. Two morphologies were formed because of distinct aggregation mechanisms where low concentration preferred a reaction limited aggregation to form the fibers, while high solution concentration led to cluster-cluster crowding. The Young's modulus of the polyurea aerogel with the highest bulk density was about 300 MPa, which is comparable

to the polymer reinforced silica aerogels. The PUA aerogels were proved to have high acoustic attenuation. It was also shown that polyurea aerogels derived from Desmodur RE exhibited high carbon yields due to their high aromatic ratio.[56] Simplified synthesis of PUA aerogels along with the exceptional mechanical properties and the expected low thermal conductivity led to the synthesis of density-gradient PUA aerogel monoliths by adopting the S. Jones method[59] as illustrated in Figure 1.3. The scanning electron micrographs showed that fibrous morphology was obtained with the low density end and particulate morphology was obtained with the high density end.

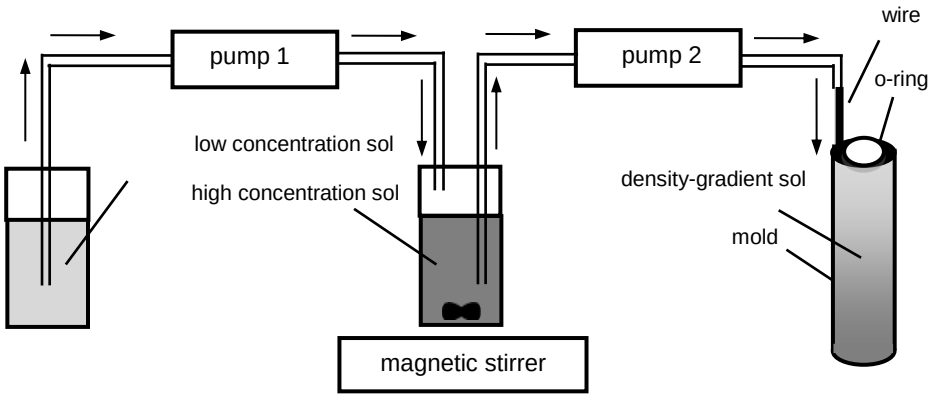

Figure 1.3. Synthesis of density-gradient PUA wet-gels.[59]

Reasoning that higher monomer concentrations (as high as 0.52 M) change the dielectric properties of the medium,[56] Leventis et al. studied that effect along with changing the polarity and hydrogen bonding ability of the solvent.[60] They synthesized PUA aerogels with nanostructures varying from like those obtained in acetone (e.g., in ethyl acetate) to cocoon-like structures embedded in a fiber web in acetonitrile. Some of those materials

synthesized in acetonitrile with high polarity and weak H-bonding ability were flexible and showed super-hydrophobicity.

Meador et al. prepared polyurea aerogels from (MDI) and aromatic diamines (4,4'-oxydianiline (ODA) or 2,2'-dimethylbenzidine (DMBZ)) *via* formation of a 3D crosslinked network using TAB.[61] They synthesized a series of polyurea aerogels in which the number of repeat units (*n*) in polyurea oligomers were varied (*n* = 3, 5 and 7). It was indicated that *n* had impact on the gelation time; the larger *n*, was the longer the gelation time. The resulting aerogels had densities in the range of 0.19–0.26 g cm^3, high porosity (79–86% *v/v*), BET surface area as high as 309 m^2 g^{-1}, and onset of thermal decomposition at 250 °C. The results indicated that the shrinkage in ODA-derived aerogels is higher than those prepared from DMBZ. One reason for this is that the flexibility of ODA along with electron donating ability of etheric oxygen in the linkage allows more H-bonding between the urea moieties which can explain the more shrinkage in the resulting aerogels. The larger *n* also caused more shrinkage due to the higher amounts of hydrogen bonding in the aerogels. The amount of hydrogen bonding in DMBZ-containing aerogels was lower, and consequently those materials did not show variation in density with an increase in crosslinking. Furthermore, the DMBZ-containing aerogels had smaller pores (~15 nm) compared to those obtained from ODA, and consequently these materials were stiffer. Moreover, there was a relationship between *n* and compressive modulus. It was found that smaller *n* corresponds to higher portions of crosslinker in the polyurea network, which in turn, results in stiffer aerogels with a higher Young's modulus. The highest E (69.4 MPa) was reported for MBZ-derived aerogels with *n*= 3 and the minimum strength (11.7 MPa) was measured for ODA-containing aerogels with *n*= 7.[61]

In the literature, mostly polyurea aerogels have been produced in the form of monoliths.[44, 56, 60, 62] However, there are some reports on the preparation of PUA aerogels in the form of powder and spherical beads.[63-65] Polyurea powders were synthesized *via* the reaction of tetrakis (4-aminophenyl) methane with various alkyl diisocyanates (with different length aliphatic chains) in DMF at room temperature, followed by adding acetone as a non-solvent.[63] The diisocyanate that were used include 1,4-diisocyanatobutane, hexamethylene diisocyanate, toluene 2,4-diisocyanate, 1,8-diisocyanatooctane, and 1,12-diisocyanatododecane. The resulting aerogel powders consisted of spherical particles in which the particle size was dependent on the aliphatic length chain of the diisocyanate; the longer the chain, the larger the particles obtained. The BET surface areas measured with N_2 sorption were in the range of 19–68 $m^2 g^{-1}$.

In another report, polyurea powders were prepared *via* the reaction of toluene 2,4-diisocyanate (2,4-TDI) with 4,4'-oxydianiline (4,4'-ODA) in acetone at 30 °C under mechanical agitation.[64] Under conditions of precipitation polymerization, polyurea precipitates were formed and then dried at 60 °C to powdery products. The study showed that when the total concentration of reactants (2,4-TDI and 4,4'-ODA) in the sol was kept constant at 1% *w*/*w*, the morphology of obtained powders was significantly related to the agitation rate. At a low stirring rate, a rope-form polymer was formed while an agglomerate of grainy polymers was observed with a stirring rate of 600 r per min or higher, and nanofibers were observed with idle shaking.[64] The effect of polymerization temperature on the morphology was also studied with a monomer concentration fixed at 1% *w*/*w* with no stirring. It was shown that grainy aggregates were formed at 0 °C, whereas fibrous polyurea was observed at 30 °C or higher. Furthermore, it was shown that the monomer

concentration affects the morphology: at 30 °C under shaking, nanofibers were obtained at 2% *w*/*w* of monomer concentration or lower, while spheres were formed at higher concentrations. The material characterization showed that the polyurea as prepared had high thermal stability and excellent solvent resistance.[64]

Polyurea aerogels were synthesized in the form of beads through the reaction of an aliphatic triisocyanate with ethylenediamine.[65] The triisocyanate was dissolved in propylene carbonate and added dropwise to a mixture of ethylene diamine and a heavy oil at room temperature, and as a result the polyurea beads were formed. The diameter of the resulting beads was approximately 2.7 mm (Figure 1.4) and their size distribution was narrow. The bulk densities of the spherical polyurea beads were low (0.166 g cm^{-3}), and they showed high porosity (87% *v*/*v*) and high surface area (197 m^2 g^{-1}). The material properties of the polyurea beads were similar to polyurea monoliths prepared with the same isocyanate with water in acetone. Also, SEM analysis indicates that morphologically they are similar, indicating the structure-property relationship in those aerogels. However, SEM analysis showed the presence of a porous thin skin on the surface of the beads with the same morphology but denser than their interior.[65]

Figure 1.4. Polyurea wet-gel beads soaked in acetone (before drying) (left) and polyurea aerogels beads after supercritical drying (middle and right).[65]

1.3.2.1. Polyurea based aerogel composites. Polyurea aerogel has been used as a soft matrix in the synthesis of many aerogel composites by different researchers. Wu et al. infiltrated the network of soft polyurea aerogel with magnesium phosphate cement (MPC) as a hard-inorganic filler resulting in a PUA/MPC composite aerogel.[66] The neat PUA aerogel had an entangled nanofibrous structure (Figure.1.5 (a)) where the fiber diameter was in the range of 17-24 nm from SANS data with an average cell size of ~200 nm based on SEM analysis. The open network of polyurea aerogels was loaded with MgO nanoparticles and formed MPC as soon as being wetted by the KDP-saturated solution (Figure.1.5 (b)). In Figure.1.5 (c), cluster-like ligaments were found in the PUA/MPC composite after the *in-situ* chemical reactions of MPC. It was also shown that micro pores of PUA were preserved. Figure.1.5 (d) shows that the MPC particles infiltrated the small pores at the nanometer level.[66]

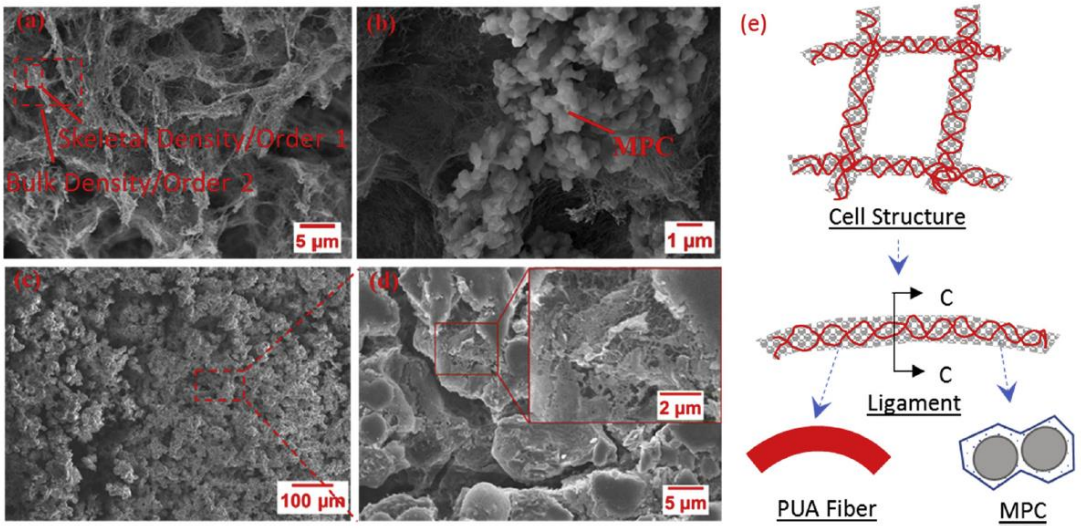

Figure 1.5. SEM of (a) Neat PUA ligament before infiltration, (b) The growth of MPC on MgO nanoparticles, (c) PUA/MPC structure at low magnification, (d) PUA/MPC structure at high magnification exhibiting PUA ligaments infiltrated and strengthened by MPC, (e) schematic illustration of MPC/PUA composite.

The physical characterization indicated that porous and lightweight features from PUA have been effectively retained in PUA/MPC composite aerogels. The bulk and skeletal densities of the PUA aerogels before infiltration were 0.123 and 1.197 g cm^{-3}, respectively, with an average porosity of 89.7% *v/v*. The bulk and skeletal densities after infiltration were measured to be 0.285 and 2.0979 g cm^{-3}, respectively, giving an average porosity of 86.4% *v/v*, which proves a moderate increase in the densities and an insignificant porosity reduction compared to PUA. The compression testing results indicate that the Young's modulus and yield strength of PUA/MPC composite aerogels are almost 10 times greater than those of neat PUA. Due to the nanoconfinement effect, the compressive strength of composites is highly dependent on the stiff matrix of MPC and can be predicted *via* an analytical model and enhanced by reducing the cell size of PUA.[66]

Organic polyurea aerogels reinforced with inorganic silica fillers were reported in a U.S patent in 2007.[69] The addition of reinforcing inorganic silica aerogel particles not only contributed to stronger materials with a low bulk density (0.08 to 0.293 g cm^{-3}), but also dramatically improved the thermal conductivity (15.2 to 20.3 mW m^{-1} K^{-1}). The improvement in thermal conductivity is very noteworthy since, and without being limited by theory, it is generally unexpected that an increase in the solid matter per unit volume of a material (along with accompanying microstructural changes) would necessarily result in reduced thermal conductivity. The addition of reinforcing inorganic aerogel particles significantly mitigates shrinkage of organic aerogels (shrinkage factor, f = 1.6 to 2.84) that inevitably occurs during sol-gel processing and supercritical drying. Furthermore, the resulting composites exhibited no dustiness, good flexibility, and hydrophobicity.

1.3.2.2. Biomedical application of polyurea aerogels. Recently, polyurea composite aerogels, due to their exceptional properties such as highly porous nature, low density, low thermal conductivity, and good mechanical properties have received a lot of interests in biomedical applications such as drug delivery, tissue engineering, cardiovascular implants, and imaging modalities.[70] However, the biocompatibility of these materials should be assessed for their biomaterial applications.

Sabri et al. evaluated the short- and long-term biocompatibility of polyurea crosslinked silica aerogel implants in a rat model.[71] Implants were inserted subcutaneously (SC) and intramuscularly (IM) in gluteal areas. The aerogels were well tolerated at both inserted locations over a period of twenty months. Histological evaluation showed no toxicity, inflammation, tissue injury, fibrosis and movement of implant in surrounding muscle or distant organs. This study proves that polyurea crosslinked silica aerogels could be useful as biomaterials.

The biocompatibility of polyurea cross-linked silica aerogels with platelets, blood plasma, and endothelial cells with respect to cell activation and inflammation was also investigated.[72] Platelets were incubated with the aerogels, and the results shows that the exposure of the aerogels with platelets did not cause platelet activation or interfere with their aggregation. The biocompatibility of the aerogels towards plasma was also determined by measuring the level of plasma anaphylatoxin C3a after incubation with aerogels. The C3a level did not change significantly, which indicates the biocompatibility of studied aerogels. Moreover, SEM analysis showed no protein precipitation on the samples after plasma incubation. The studied samples also caused no changes in endothelial cell culture factors after 5 days of incubation. The good biocompatibility of the

aerogels with plasma and studied cells along with their unique properties such as low density, high porosity, and good mechanical strength, make them able to be used in artificial heart valve leaflets.[72]

Sabri et al. investigated the ultrasonic behavior of polyurea crosslinked silica aerogels *in vivo* both in human cadaveric and a Sprague Dawley rat.[73] The aerogels were located at different depths; subcutaneously and sub-muscularly in the studied models. The aerogel implants showed a high contrast compared to surrounding tissues and were easily detected by ultrasonography when inserted in either of the areas in both rat and cadaveric models. Moreover, the implant size derived from the images matched the actual physical dimensions of the implants and did not cause any gross tissue damage.

1.4. HANSEN SOLUBILITY CONCEPT

The solubility parameter concept was first introduced as early as 1916, but was later formalized by Hildebrand and Scott in 1950.[74] Since then, the solubility parameter concept has been widely used as a powerful tool for quantifying intermolecular interactions between a solvent and another component for the selection of a solvent or solvents for a particular application.

The basic principle was “like dissolves like” since the theory was originally aimed for nonpolar and non-associating liquids. Today, the concept is extended to other systems and therefore “like dissolves like” can be modified to “like seeks like” since the concept is used in situations where the components do not actually dissolve but interact with each other. Therefore, solubility parameters give a systematic estimate for the compatibility

between the two components.[75] The Hildebrand solubility parameter of a substance, δ_i, is defined as the square root of the cohesive energy density:

$$\delta_i = \left(\frac{\Delta E_i}{V_i}\right)^{1/2} \quad \text{(Eq.1)}$$

where ΔE_i is the molar energy of vaporization (cohesive energy) and V_i is the molar volume of the pure solvent. The cohesive energy is associated with the net attractive interactions in a material.

The general concept of the Hildebrand solubility parameter is that two substances are miscible when their solubility parameters are close to each other or when the difference in solubility parameter is less than 2 $MPa^{1/2}$.[74] Materials with a high solubility parameter require more energy for dispersing than what is gained by mixing it with materials with a substantially lower solubility parameter, and thus these materials will be immiscible. On the other hand, two materials with similar solubility parameters will gain free energy when mixed together and they will, as an effect, be miscible.[76]

The equation for the solubility parameter is a simple definition, but it is not always easy to calculate. The solubility parameters do not take into account geometric aspects, such as size and structure of molecules, but, in general, compounds with smaller molar volume are better solvents than compounds with larger molar volumes.[74] For example, methanol and acetone can dissolve a polymer with larger solubility parameter differences than a solvent with larger molar volumes (e.g., n-hexadecane).[75]

Later, different models were developed from the Hildebrand solubility parameter concept taking into account that interactions between different compounds are of different kinds. The most widely known method is the Hansen solubility parameter.

1.4.1. Hansen Solubility Parameters. Hansen[75] assumed that the energy of evaporation, which is the total cohesive energy holding a liquid together, can be divided into contributions of dispersion, polar, and hydrogen bonding interactions:

$$E = E_P + E_H + E_D \quad \text{(Eq.2)}$$

where E is total cohesive energy and, E_P, E_H, and E_D are contributions of permanent dipole-permanent dipole forces, hydrogen bonding forces and dispersion (London) forces, respectively. Eq. 3 is Hansen's contribution to developing the solubility parameter as a more useful tool than it had been previously. Dividing the equation by the molar volume of a solvent, V, gives;

$$\frac{E}{V} = \frac{E_P}{V} + \frac{E_P}{V} + \frac{E_D}{V} \quad \text{(Eq.3)}$$

or

$$\delta_{tot}{}^2 = \delta_P{}^2 + \delta_H{}^2 + \delta_D{}^2$$

where δ_{tot} is the total solubility parameter and, δ_P, δ_H, and δ_D are components of the solubility parameter determined by the corresponding contributions to the cohesive energy. The solubility parameter of a given solvent can be considered a vector with components δ_P, δ_H and δ_D. This means that each solvent can be located in a 3D system as a fixed point with coordinates agreeing with equation above. The axes of the system are the polar axis, δ_P, the hydrogen bonding axis, δ_H, and the dispersion axis, δ_D.

Hansen's theory of solubility parameters is a valuable semi-quantitative method of solvent selection and reformulation in many fields such as polymer and materials science. Predictions of solubility from the theory cannot be regarded as unequivocal, but certainties

of greater than 80% can be achieved with careful solvent selection during the initial polymer solubility parameter determinations.

1.4.2. Hansen Solubility Sphere. The three Hansen parameters can be considered the coordinates of a point in the so-called Hansen space.[75] The closer two points are, the more likely the compounds are to dissolve into each other. In the case of a polymer, only solvents within a certain range will dissolve the polymer. This range is usually an ellipsoid and only solvents within this space are likely to dissolve the polymer in question.

Occasionally, the scale of the dispersion axis is doubled, providing approximately a spherical volume of solubility. Then, the HSP distance so-called R_a is defined as the distance of the solvent coordinates (δ_{P2}, δ_{H2}, δ_{D2}) from the center point (δ_{P1}, δ_{H1}, δ_{D1}) of the solute sphere[75] and is given by

$$Ra^2 = 4\,(\delta_{P1}-\delta_{P2})^2 + (\delta_{H1}-\delta_{H2})^2 + (\delta_{D1}-\delta_{D2})^2 \qquad \text{(Eq.4)}$$

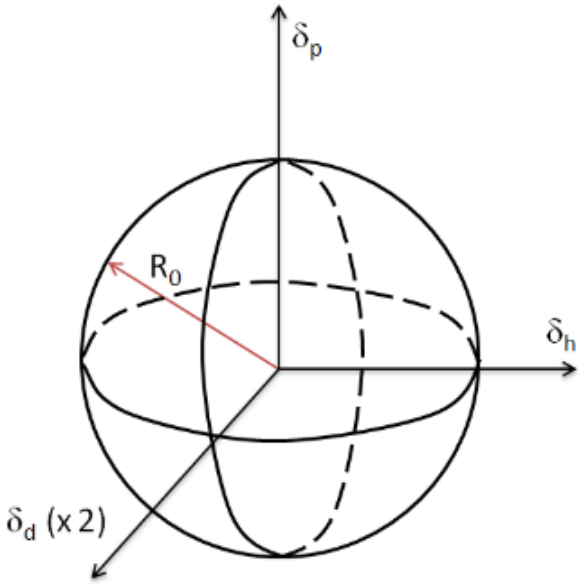

Figure 1.6. Hansen sphere.

The distance R_a in the equation above can be compared with the solubility radius of the polymer, R_0. If $R_a < R_0$ then there is a high likelihood of the solvent to dissolve the polymer. The radius of the solubility sphere is often called the "interaction radius," and the ratio R_a / R_0 is called the "Relative Energy Difference (RED)" of the system. If the RED < 1, then the compound is a solvent, but if RED > 1, then the compound is a non-solvent and the compound may cause swelling if RED = 0

Hansen Solubility Parameters have been used in many studies to optimize solvent properties for making a polymer with desirable performance. Zhu et al. systematically determined the effect of the gelation solvent with respect to Hansen's parameters on material properties and, in particular, on the thermal conductivity of polyurethane-polyisocyanurate aerogels (PUR−PIR).[77] First, in a pilot study, they synthesized PUR−PIR aerogels in different DMSO−acetone mixtures. When the volume fraction of DMSO in binary solvents was less than 7.5% the sol did not gel. More importantly, aerogels prepared in solvents with lower DMSO fractions had lower thermal conductivity values, and the aerogels prepared in a 15:85 DMSO: acetone blend exhibited the minimum thermal conductivity (20.1 mW $m^{-1} K^{-1}$). The Hansen solubility parameters, including δ_P, δ_H and δ_D for this solvent mixture, were measured to be, 11.30, 7.48, and 15.94 $MPa^{1/2}$, respectively. Based on the optimum solubility parameters for the DMSO acetone mixtures, they prepared the aerogels in 32 different binary solvents, divided into three series with δ_P, δ_H, and δ_D fixed at 11.30, 7.40, and 15.94 $MPa^{1/2}$, respectively. The data indicated that aerogels with minimum thermal conductivity can be synthesized in solvents with high hydrogen bonding ability (δ_H > 7.2 $MPa^{1/2}$) and a δ_D around 16.3 $MPa^{1/2}$. In contrast, the δ_P parameter is of lesser importance.

PAPER

I. *K*-INDEX: A DESCRIPTOR, PREDICTOR AND CORRELATOR OF COMPLEX NANOMORPHOLOGY TO OTHER MATERIAL PROPERTIES[1]

Tahereh Taghvaee, Suraj Donthula, Parwani M. Rewatkar, Hojat Majedi Far, Chariklia Sotiriou-Leventis, Nicholas Leventis*

Department of Chemistry, Missouri University of Science and Technology, Rolla, MO 65409, U.S.A.*Correspondence: leventis@mst.edu; Tel.: 573-341-4391

ABSTRACT

Morphology is a qualitative property of nanostructured matter and is articulated by visual inspection of micrographs. For deterministic procedures that relate nanomorphology to synthetic conditions, it is necessary to express nano/micro-structure numerically. Selecting polyurea aerogels as a model system with demonstrated potential for rich nanomorphology and guided by a statistical Design-of-Experiments model, we prepared a large array of materials (208) with identical chemical composition, but quite different nanostructures. By reflecting on SEM imaging it was realized that our first pre-verbal impression about a nanostructure is related to its openness and texture; the former is quantified by porosity (Π), and the latter is oftentimes related to hydrophobicity, which in turn is quantified by the contact angle (θ) of water droplets resting on the material.

---

[1] This paper was published in *ACS Nano 2019*, 13, 3, 3677-3690.

Herewith, the θ/Π ratio is referred to as *K*-index, and it was noticed that all polyurea samples of this study could be put in eight *K*-index groups with separate nanomorphologies ranging from caterpillar-like assemblies of nanoparticles, to thin nanofibers, to cocoon-like structures, to large bald microspheres. A first validation of the *K*-index as a morphology descriptor was based on compressing samples to different strains: it was observed that as the porosity decreases, the water contact angle decreases proportionally, and the *K*-index remains constant. The predictive power of the *K*-index was demonstrated with 20 polyurea aerogels prepared in eight binary solvent systems. Subsequently, several material properties were correlated to nanomorphology through the *K*-index and in turn, that provided insight about the root cause of the diversity of the nanostructure in polyurea aerogels. Finally, using response surface methodology, *K*-indexes and other material properties of practical interest were correlated to the monomer, water and catalyst concentrations as well as the three Hansen Solubility Parameters of the sol. That enabled synthesis of materials with up to six prescribed properties at a time, including nanomorphology, bulk density, BET surface area, elastic modulus, ultimate compressive strength, and thermal conductivity.

Keywords: *K*-index, descriptor, correlator, nanomorphology, polyurea, aerogels, properties.

1. INTRODUCTION

Properties of porous materials with technological interest such as mechanical strength,[1] thermal conductivity,[2] wettability,[3,4] surface area and gas sorption capacity,[5]

depend to a large extent on the morphology of their solid frameworks. Expanding porous materials to include certain precursors classified as soft matter,[6,7] *e.g.,* wet-gels,[8] control of nanomorphology may have a much broader impact than just in the field of material science. For example, formation of fibers leads to gelation in sickle-cell hemoglobin,[9] while supramolecular amyloid aggregates of certain proteins stick together into nanoscopic fibrils, which are linked to neurodegenerative diseases like Alzheimer's or bovine spongiform encephalopathy.[10,11] Thereby, targeted synthesis of complex nanostructures would not only comprise an efficient approach to functional materials,[12] but it also has the potential to revolutionize nanoscience across the board from nanotechnology to nanomedicine.

Observation of soft matter as close as possible to its original wet-gel state may involve conversion of the pore-filling solvent into a supercritical fluid that is vented off as a gas. That process eliminates surface tension forces on the delicate skeletal framework, and prevents macroscopic shrinkage and collapse upon drying.[13] The resulting porous, low-density solids are often classified as aerogels,[14] which in turn are materials pursued in their own right for applications in thermal insulation,[15] catalysis,[16,17] energy absorption,[18] and environmental remediation.[19,20] However, in spite of their practical applications, aerogels are in fact materials that were invented for conducting fundamental studies on the structure of their wet-gel precursors,[21] and in that sense redeployment of aerogels for the study of soft matter along their intended original use holds a special scientific significance. Indeed, as emerging from rapid developments in the field of polymeric aerogels in the last ten years, depending on synthetic conditions, oftentimes the nanostructure of wet-gels can be extremely broad and complex. Targeted synthesis of such nanostructures, that is relating

nanostructure to synthetic conditions, is highly desirable, however, predictive synthesis is elusive. The main reason is the difficulty to assign numerical values to nanomorphology, and as such it remains a qualitative property of matter.

No doubt, in the description of nanostructured matter, natural language is a powerful tool. Expressions such as random assemblies of nanoparticles, strings of nanoparticles, microspheres, microspheres embedded in nanofibers, fiber cocoons, or entangled nanofibers convey rather unambiguously what they refer to. Difficulty arises when one tries to correlate such linguistic descriptors to quantitative parameters. In that regard, if individual numerical identifiers could be assigned to different nanostructures, it is reasonable to expect that at the very least heuristic machine-learning techniques,[22] or perhaps response surface methodology[23,24] would link those identifiers to monomer and catalyst concentrations, solvent parameters, *etc.*, and thus will allow synthesis by design. This has been the goal of this effort.

Numerous attempts to infer nanomorphology from quantifiable material properties have focused on mechanical properties, which therefore have been assumed as the link between nanomorphology and synthetic conditions.[25,26] However, as demonstrated experimentally in this study, many material properties, including the elastic modulus, bulk density, thermal conductivity, *etc.*, are not single-valued functions of morphology. That is, two samples with completely different morphologies may have the same value of any of those properties. Thereby, there is a need for a different morphology descriptor. Along these lines, it was reasoned that our first, pre-verbal impression from visual inspection of electron micrographs (SEM) of a nanostructure is related to its openness and its texture. Openness is quantified by porosity, Π, and texture is oftentimes reflected on

hydrophobicity, which in turn is quantified by the contact angle, θ, of a water droplet on the surface of a material. Working with polyurea aerogels as our model system, we noticed that the θ/Π ratio, referred to herewith as the *K*-index ("*K*" phonetic for "correlator"), comprises a good descriptor of complex nanostructure that in turn can be used to correlate material properties with structure, and ultimately to predict and design nanostructure at will. Despite the complexity of the polyurea system, the *K*-index is well-behaved and resilient to all tests it has been subjected to. Preliminary screening has shown that it can be extended to related nanoporous polyurethanes. Strategies are being developed for its adaptability to other systems as well.

2. RESULTS AND DISCUSSION

2.1. MATERIALS SYNTHESIS

Quisque Polyurea (PUA) aerogels were chosen as the model system for this study because of their potential for quite diverge nanomorphology within the same chemical composition.[19,27-32] PUA wet-gels were prepared *via* the triethylamine (Et_3N) catalyzed reaction of 1,3,5-tris(6-isocyanatohexyl)-1,3,5-triazinane-2,4,6-trione (ISO) with water (Eq.1).[19,27,28,33] Wet-gels were dried into aerogels following standard procedures (refer to the Experimental Section).

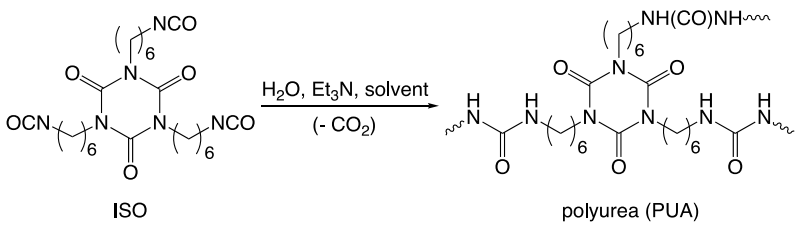

(Eq.1)

The nanomorphology of those PUA aerogels depends on the concentrations of ISO, H_2O and catalyst, as well as the solvent. The three concentrations were varied at five levels each. The two extreme concentrations of ISO are bracketing a broad area of interest in terms of density, and therefore of mechanical strength.[34] The five concentration levels of H_2O and Et_3N were pegged to each concentration level of ISO as shown in Figure 1a. The experimental H_2O:ISO mol/mol ratio was varied from 2.341 to 0.659, namely from an over- to a sub-stoichiometric amount of the water required by Eq 1 (= 1.5). Below the lowest end of that range, sols did not gel. Similarly, the range of the catalyst concentration was adjusted so that even the fastest gelation processes (*i.e.,* those at the high ends of ISO and H_2O concentrations) would still allow enough time to pour the sols into their molds. The concentration of ISO (expressed as its weight in a fixed volume of solvent), the H_2O:ISO mol/mol ratio, and the concentration of Et_3N (as its percent weight in the sol) are represented by [ISO], [H_2O] and [Et_3N], respectively, and were used as our three explanatory variables (n=3).

As detailed in Appendix I of the Supporting Information, the specific placement of the samples at the five levels of [ISO], [H_2O] and [Et_3N] was based on a Central Composite Rotatable Design (CCRD) model. In brief, that model uses coded values for the explanatory variables (Figure 1a), and places formulations (referred to as 'runs') at equal distances (*i.e.*, spherically) around a central point (coded as 0.000) at the common middle of the ranges of the three coded variables (Figure 1b). In addition to the central run, the five-level CCRD model borrowed 2^n runs from two levels of a "narrower" full factorial design at distances ±1.000 from the center, and superimposed them with two axial runs per explanatory variable, that is with $2n$ runs (referred to as "star" points) at distances $\pm\alpha$ relative to the

center of the design. On simple geometric grounds, it is calculated that $\alpha = (2^n)^{1/4}$, thus for n =3, α = 1.682. Thereby, in coded space the two runs at the extreme limits chosen for each of [ISO], [H_2O] and [Et_3N] were placed at ±1.682 from the center, and the remaining 3 runs for each variable were scaled accordingly to ±1.000 and 0.000 (Figure 1a). That placement of the runs within their domain is carried out in anticipation of a quadratic relationship between the explanatory variables and the properties of interest of the resulting materials.[35] Referring to Figure 1b, the total number of samples needed by the CCRD model was equal to $2^n + 2n + n_{center}$, whereas $n_{center} = 2$ (one central run plus one repeat). Thereby, the total design consisted of 16 runs. By comparison, a full factorial design of three variables (n = 3), at five levels each, requires (5^3 =) 125 samples.

Upon implementing that model, it was noted that a single (star) run at the highest [ISO] level (Level 5) could not capture all possible nanostructures at that level. As it turned out, micromorphology was very sensitive to both [H_2O] and [Et_3N] at Level 5, but not much so at Level 1. In order to handle that issue, the CCRD model of Figure 1b was enhanced with ten additional runs (pointed at with color-cored arrows to match the color code used for the levels of [ISO]), eight of which were placed at extreme [H_2O] and [Et_3N] positions within Levels 4 and 5, while the remaining two runs were placed at extreme positions within Level 1 of [ISO]. The final design consisted of 26 runs. For the exact position of Run 1 to Run 26 in the design space of Figure 1b, see Figure S.I.1 of Appendix I.

The 26-run experimental design was applied in eight different solvents selected based on their ability to develop polar, hydrogen bonding and dispersion interactions. Those properties are quantified by the Hansen Solubility Parameters (HSP: δP, δH, δD,

respectively) of each solvent.[36-38] Figure 1c shows the domain of δP and δH used for this study. (δD varied in a narrower range: $15.3 \leq \delta D \leq 20.0$; Refer to Table S.I.3.) Considering all solvents, the total number of possible formulations was 208. However, most of the gels that were prepared with higher [ISO] in high-δH DMF, as well as one high-[ISO] run in THF (Run 17) shrunk excessively during drying resulting in more-or-less dense pieces of plastic. Those samples were not considered for further study, and the entire design space ended up with 188 viable runs. All sol formulations used in this study, along with the phenomenological gelation times and the HSPs of all solvents, monomers and sols, are included in Appendix I of the Supporting Information.

2.2. INTRODUCING *K*-INDEX AS A NANOMORPHOLOGY DESCRIPTOR

A collection of quantifiable material properties of all PUA aerogels of this study, including the bulk density (ρ_b), the skeletal density (ρ_s), the BET surface area (σ), N_2-sorption data related to the pore structure, and the particle radii (r), is given in Appendix II. However, the main material property of interest here is nanomorphology. In SEM, samples were porous, as expected from typical aerogels, and displayed a rich variety of texture.

The percent porosity, Π, was calculated *via* $\Pi = 100 \times (\rho_s - \rho_b)/\rho_s$). Since all skeletal densities, ρ_s, were close to one another (1.17-1.28 g cm^{-3}), Π was essentially a function of ρ_b, which in turn was controlled by [ISO]. Except the small subset of samples that collapsed during drying, the porosity of all other samples that were included in this study ranged from 44% v/v (Run 22 in THF, $\rho_b = 0.662 \pm 0.007$ g cm^{-3}) to 97% v/v (Run 26 in CH_3CN, $\rho_b = 0.040 \pm 0.001$ g cm^{-3}). All porosity data are cited in Appendix II.

Texture, on the other hand, is linked to surface tension forces, which in turn are reflected on the hydrophilic/hydrophobic properties of materials.[39] The latter were evaluated from the contact angle (θ) of water droplets placed on internal flat surfaces of the samples, freshly cut with a knife from larger monoliths. Samples ranged from hydrophilic ($\theta < 90^o$) to superhydrophobic ($\theta > 150^o$) – see Figures 2 and S.III.1. At the hydrophilic end, the lowest contact angles were associated with higher-density materials and were in the neighborhood of 66.7^o – 69.6^o. The value of θ on completely dense, non-porous polymer derived from Eq 1 is 69.1 ± 0.2^o.[19] Contact angles lower than that value are due to surface roughness, according to the Wenzel model.[40] In the hydrophilic range, water droplets were eventually absorbed within the material, but in the beginning that process was relatively slow ($d\theta/dt \approx 2–4^o$ min^{-1} – see Movies "Hydrophilic 1-3" in Supporting Information), thus contact angle measurements, which are completed in a couple of seconds after adding the water droplet on the surface of the materials, were considered reliable. In the hydrophobic range ($\theta > 90^o$), under lower-magnification (*e.g.*, ×10k and below – Figures 2 and S.III.1) superhydrophobic samples had textural features in the micron range, like for example microspheres, or long-range entangled fibers. Other hydrophobic samples that under such low magnifications appeared smooth, they were never superhydrophobic (Figure 2). Most hydrophobic materials showed the Petal effect;[41] all superhydrophobic samples, together with several near-superhydrophobic ones ($\theta > 140^o$) showed the Lotus Leaf effect (see Movie "Superhydrophobic" in Supporting Information).[42] Since the polyurea of this study is an inherently hydrophilic polymer, any type of hydrophobicity is a Cassie-Baxter state, where water droplets touch only the apexes of the surface roughness.[43] Indeed, when submerged in water, hydrophobic PUA monoliths

appeared silvery, which suggests that they were shrouded by a layer of air that caused total reflection at the air-water boundary (see Movie "PUA monolith in water: Total reflection"). In spite of clear indications that the water contact angle is related to nanomorphology (Figures 2 and S.III.1),[44] correlation of the latter to contact angle data alone was difficult.

However, it was found out that if water contact angles are normalized by the sample porosity (θ/Π), the resulting ratios are associated in an one-to-one relationship with specific morphologies. Hereafter, the θ/Π ratio is abbreviated as the *K*-index, and the θ, Π and *K*-index data of the 188 samples considered in individual solvents, plus of another 20 samples prepared in mixed solvents for validation of the *K*-index (*vide infra*), are included in Appendix III. By the definition of the *K*-index, and the numerical precision of its components θ and Π, *K*-indexes have a three significant figure precision. In general, though, morphology and trends in material properties could be followed well with just two significant figures. Thus, guided only by the values of the *K*-index, and irrespective of sample history, namely of how each sample was prepared, in what solvent, or of the specific [ISO], [H_2O] and [Et_3N], all polyurea aerogels could be placed in eight morphology groups with separate *K*-indexes in the range of 1.2 to 1.9 (Figure 3). Those eight morphological groups included long caterpillar-like assemblies of nanoparticles (1.2), nanoworms with decreasing aspect ratios (1.3 to 1.4), assemblies of fused nanoparticles (1.5), entangled nanofibers (1.6), cocoon-like microspheres embedded in fibers (1.7), large microspheres trapped in a fiber web (1.8), and eventually large, almost bald microspheres (1.9). It is noted that most of the morphology groups of Figure 3 have been observed with other systems before. For example, "caterpillars," indistinguishable from those in Figure 3, is the typical morphology of vanadia aerogels.[45] Random assemblies of nanoparticles (*K*-index

= 1.4) is the usual structure of base-catalyzed silica,[46] and several other inorganic aerogels.[47] Assemblies of fused nanoparticles have been observed with numerous other higher-density polymeric aerogels,[48,49] while large micron-size bald microparticles have been typical of superelastic shape-memory polyurethane aerogels.[38] By the same token, we are not aware of any system where all those morphologies are displayed simultaneously, and in that regard, at this current moment, PUA aerogels appear to be conveniently special in that regard, and therefore quite suitable for the purpose of this study. After grouping all samples according to their morphologies, it was noted that nanostructures with *K*-indexes in the range 1.6 to 1.9 came exclusively from high-polarity solvents such as acetonitrile, nitromethane and propylene carbonate, while *K*-indexes in the range 1.2 to 1.5 were observed with all solvents.

2.3. INDEPENDENCE OF THE *K*-INDEX FROM THE CHEMICAL COMPOSITION

Within experimental error, the CHN composition of all runs in both individual and binary solvents did not vary with the *K*-index (Figure 4a and Table S.IV.1). The experimental data, C: 57.51 ± 0.27 %; H: 8.38 ± 0.12%; and, N: 17.15 ± 0.18%, were close to the values calculated assuming infinitely large star-like polymeric networks emanating from ISO cores and capped with shared –(C=O)– bridges: C: 58.06; H: 8.39; N: 18.06 (refer to Appendix IV). Similarly, over half of the samples were screened with solid-state CPMAS ^{13}C NMR and were identical to one another. Four specific hydrophobic samples covering the *K*-index range were also screened with solid-state CPMAS ^{15}N NMR spectroscopy (Figure 4b). The two main resonances were assigned to urea (82.1 ppm) and the isocyanurate (140.3 ppm) nitrogens. A small-intensity peak at 46 ppm from dangling

amine groups was discernible in the sample with *K*-index = 1.8. General absence of dangling amines, even from runs that employed a substoichiometric amount of H_2O (see legend of Figure 4), is attributed to hydrolysis of dangling unreacted NCO groups by residual water in wash acetone (see Experimental Section), followed by fast reaction of the newly formed dangling amines with nearby unreacted NCO groups.

Surface analysis with high-resolution O 1s and N 1s XPS (Figures 4c and 4d, respectively – see also Figures S.IV.1 and S.IV.2) showed only C=O oxygen (at 532.75 eV),[50] and no free $–NH_2$ nitrogen (expected at around 399 eV – the N 1s peak at 401.15 eV corresponds to urea and imide nitrogens[50,51]), supporting that the hydrophilic/ hydrophobic properties were not controlled by surface chemistry, thereby leaving that role to texture only.

Overall, and for all practical purposes, all PUA samples can be considered chemically identical, irrespective of nanostructure. Hydrophilicity/hydrophobicity could not be associated with variations either in their bulk chemical composition, or at their surfaces. The hydrophilic nature of polyurea from Eq 1 could only be associated with the slow uptake of water droplets in the bulk of hydrophilic samples (see Movies "Hydrophilic 1-3").

2.4. VALIDATION OF *K*-INDEX AS NANOMORPHOLOGY DESCRIPTOR VIA UNIAXIAL COMPRESSION

The rationale was that compression would reduce porosity, however, at least in the early stages of compression, nanomorphology should not be affected (that is, "caterpillars" will remain "caterpillars" and so on), and therefore the *K*-index should remain numerically constant. It follows that the contact angle should vary proportionally to Π. As strain

increases, porosity is reduced further, in principle, all the way to zero; θ, however, should converge to the value of the water contact angle on dense ISO-derived polyurea (about 69.1°, as cited above).[19] Thereby, beyond a certain point of compression the value of the *K*-index should start increasing. Eight different formulations corresponding to aerogels within the eight morphology groups of Figure 3 were selected randomly from the total set of samples prepared in individual solvents. Multiple aerogel monoliths were prepared from each formulation, they were subjected to compression at different strains, and *K*-indexes were determined (Figure 5 and Appendix V). Samples consisting of nanoparticles or fused nanoparticles ($1.2 \leq K\text{-index} \leq 1.5$) were relatively rigid and did not show large lateral expansion even up to compressive strains over 90%; in essence those samples were folded within their own empty spaces. At the end of the compression process porosities were reduced to less than 20% v/v, structural features were fused together, and samples became semi-transparent. In that type of materials, the *K*-index maintained its value up to strains of about 50% and porosities down to about 50% v/v. Beyond that point, *K*-index started increasing, as it was reasoned above. On the other hand, samples consisting of entangled fibers or spherical microparticles with or without "hair" ($1.6 \leq K\text{-index} \leq 1.9$), could be flexible (at *K*-index = 1.6), they showed large non-recoverable lateral expansion upon compression, and porosities were never reduced below 50% v/v, even at strains exceeding 90%. Those samples remained opaque white, and in general kept their *K*-indexes (and micromorphologies) throughout the compression process. Overall, at the early stages, compression does not alter microstructure, and as porosity is reduced, the water contact angle is reduced proportionally, and the value of the *K*-index is maintained (up to strains

of about 50% and porosities down to about 50% v/v) as expected from a quantity that describes morphology.

2.5. VALIDATION OF THE *K*-INDEX AS NANOMORPHOLOGY DESCRIPTOR BY PREDICTING THE MORPHOLOGY OF PUA AEROGELS PREPARED IN BINARY SOLVENT

The strategy here was to prepare samples randomly across the design space of Figure 1b using binary solvent systems (indicated with yellow circles in Figure 1c), measure their porosities and water contact angles, calculate their *K*-indexes, predict their micromorphologies, and confirm that they conform to those expected from the classification of Figure 3. Twenty (20) such samples were prepared, and all data relevant to their *K*-indexes, including SEM images, are shown in Appendix VI. Micrographs from four representative samples, prepared in the binary solvents indicated with arrows in Figure 1c, are shown in Figure 6. All 20 *K*-indexes were in the 1.2 – 1.9 range, and it was evident that all microstructures (Figures 6 and S.VI.2), did match those expected from the values of their *K*-indexes alone (Figure 3).

2.6. *K*-INDEX AS A CORRELATOR OF MATERIAL PROPERTIES TO NANOMORPHOLOGY

This section explores quantification of material properties as a function of nanomorphology through the *K*-index. Along the way, it sheds light to the question about the root cause of diverse nanomorphology in polyurea aerogels, and with an eye to other systems it addresses the wider applicability of the *K*-index as a morphology descriptor. Basic material properties considered for this discussion include bulk densities (ρ_b), water

contact angles (θ), BET surface areas (σ), and the average particle radii (r) (for the primary data see Appendices II and III). Properties related to applications of PUA aerogels in thermal insulation, or as structural materials include their total thermal conductivity (λ_{Total}), and their elastic modulus (E) (for the primary data see Appendices III and VII).

In that context, and for the purposes of the ensuing discussion, it is important to point out that although *K*-indexes are known with a three significant figure accuracy (Appendix III), in order to facilitate this discussion the *K*-index values have been binned to single decimal digits according to the rules of rounding. For example, a *K*-index = 1.54 has been rounded to 1.5, and a *K*-index = 1.55 has been rounded to 1.6. In that regard, the discontinuities encountered and discussed below are extremely sharp.

The variation of the bulk-density as a function of the *K*-index (Figure 7a) was discontinuous with two distinct "parallel" branches from 1.2 to 1.5 (1.54 actually), and from 1.6 (1.55 actually) to 1.9. In other words, most densities showed up at two different morphologies, yet, lowest-density samples were possible only with entangled fibers (*K*-index = 1.6), and the highest density ones consisted of assemblies of fused nanoparticles (*K*-index = 1.5). Other density-dependent properties, such as the total thermal conductivity (Figure 7b) and the elastic modulus (Figure 7c), followed similar trends with the *K*-index, however the correlations were different. Thereby, while low-λ samples were possible with both "caterpillars" (*K*-index = 1.2) and entangled fibers (*K*-index = 1.6), the former samples were on average significantly stiffer (E = 26 ± 20 MPa) than the latter (E = 7 ± 6 MPa), which, as mentioned above, could be flexible.

Two independent branches as a function of morphology were also followed by the contact angles of water droplets (Figure 7d). The discontinuity between the two branches

was again observed in the *K*-index range of 1.5-1.6. Consistent with texture-induced superhydrophobicity in fibrous materials deliberately seeded with particles,[52] PUA samples consisting of microspheres entangled with any amount of fiber (*i.e.*, $1.7 \leq K\text{-index} \leq 1.9$) were more hydrophobic than any type of assemblies of nanoparticles ($1.2 \leq K\text{-index} \leq 1.5$). Most importantly, however, samples consisting of thin entangled fibers (*K*-index = 1.6) were the most hydrophobic materials of all, with θ values reaching above 150°. Interestingly, the hydrophobicity of those samples correlated with materials having *K*-indexes in the 1.7-1.9 range, rather than with "caterpillars" (*K*-index = 1.2), which, it might be claimed, also possess a fibrous quality (*vide infra*). The superhydrophobicity at *K*-index = 1.6 is attributed to the larger-scale organization of fibers into node-like structures as seen in low-magnification SEM (Figure 2).

Using the two-branch dependence of ρ_b, λ, E and θ on *K*-index as a point of departure, it is noted that that behavior actually matches the morphological evolution of Figure 3, which is also discontinuous in the 1.5-1.6 region. For a better insight into that region, it was deemed necessary to compare 1.6-samples not only with 1.5-samples, but also with 1.2-samples at various magnifications. Thus, referring back to Figure 2, the 1.6 samples showed a self-similarity at length scales extending over three orders of magnitude, while no such similarity was obvious in any of the 1.2- and 1.5-samples. As it was pointed out above, at lower magnifications, the latter two types of samples appeared featureless. By the same token, at high magnification (×250k), the two extreme types of low-density samples (that is, those with *K*-indexes equal to 1.2 and 1.6) may look somewhat similar in terms of both having a fibrous quality and the type of interconnects between fibers, but they also had one most significant difference: "caterpillars" (*K*-index = 1.2) consisted of

discrete nanoparticles, while the surfaces of the long fibers (*K*-index = 1.6) were smooth, and in that regard they resembled the smooth surfaces of bald microspheres with *K*-index = 1.9 (Figure 3). The smoothness of the 1.6-fibers was reflected on their BET surface areas, σ, and the apparent particle radii, *r* [derived *via* $r = 1/(3\rho_s\sigma)$], both of which were continuous (albeit non-monotonic) across the *K*-index range (Figure 7e), underlining that irrespective of density, or any morphological similarities at short length scales, the 1.2 and 1.6 samples were in fact very different materials. The highest surface areas were measured, and correspondingly the smallest particle sizes, were calculated with high aspect ratio "caterpillars" at *K*-index = 1.2. The smallest surface areas were observed at the other end of the *K*-index range (1.9) with the largest bald microspheres. At both ends of the *K*-index range, calculated particle radii, *r*, matched, order-of-magnitude wise, the actual sizes noted in SEM ($13._6 \pm 3.8$ nm at K=1.2, and 356 ± 89 nm at K=1.9).

One possible way to justify the intermediate placement of entangled 1.6-fibers in terms of σ and *r* would be by assuming that they concealed small dense cores following either the trend of decreasing particle size as *K*-index decreased from 1.9 to 1.7, or the trend of fusing particles as *K*-index increased from 1.2 into the 1.5 range. Zooming in at all samples with *K*-indexes in the 1.45-1.64 range (55 out of 208 samples, see Figure S.IX.1) we saw no evidence for small concealed cores. Instead, along that search (Figure S.IX.1), we noted that the transition from fused particles (*K*-index = 1.5) to long entangled fiber (*K*-index = 1.6) was as sharp as the transition in bulk density and several other properties as discussed above. In other words there was no crossover among properties and the *K*-index values: *all* runs with a *K*-index $\leq$ 1.54 consisted of fused nanoparticles and were the highest-density, highest-modulus, and high-thermal conductivity samples; similarly, *all*

runs with a *K*-index ≥ 1.55 consisted of entangled fibers and were the lowest-density, lowest-modulus, and low thermal conductivity samples. Amongst those observations, it was thought in particular that the close association of the sharp transition in morphology with the sharp transition in density might be related to gelation kinetics. Furthermore, it was noted that fused nanoparticles within *K*-index = 1.5 were smooth, and in some cases fused nanoparticles formed 'knotty' strings (see Figure S.IX.1), and thus they may be considered as a preamble to the smooth fibers at *K*-index = 1.6. Based on those inferences, it was hypothesized that fused nanoparticles at *K*-index = 1.5 and entangled fibers at *K*-index = 1.6 might share a common formation mechanism.

For further insight into the last hypothesis, and thus into the root cause of the morphological diversity, it was decided to look into the gelation kinetics. Although the variation of the Log [phenomenological gelation time] *versus* the *K*-index is not monotonic in the transition range $1.5 \leq K\text{-index} < 1.6$ (Figure 7f), nevertheless it is continuous, despite the sharp drop in density (and thereby the monomer concentration) in that region. That observation, coupled with the fact that the 1.6-1.9 nanomorphologies were obtained exclusively in high-polarity acetonitrile, nitromethane and propylene carbonate, points to a solvent-related change in the gelation mechanism, for example from nucleation and growth of nanoparticles ($1.2 \leq K\text{-index} \leq 1.4$),[53,54] to chemical cooling-induced phase separation of liquid oligomers that undergo spheroidization while they still react and eventually solidify ($1.7 \leq K\text{-index} \leq 1.9$).[55-57] In that context, fused nanoparticles at *K*-index = 1.5 may be attributed to both nucleation and phase separation of liquid oligomers running in parallel, while entangled fibers described by *K*-index = 1.6 could be an early stage along

the latter process, before spheroidization sets in. The matter is considered open and is under further investigation.

Evidently, a large amount of information about a system can be extracted by correlating not only material properties, but also other parameters (*e.g.*, gelation times) with nanostructure through the *K*-index. The question then becomes whether *K*-index is an one-of-a-kind descriptor of nanomorphology, or whether it can be replaced by other material properties. As has been shown in this section, in the case of polyurea aerogels the bulk density, the BET surface area, the elastic modulus and the thermal conductivity are not single-valued functions of nanomorphology. Therefore, since at least in one case (polyurea) those properties cannot be used as unique descriptors of nanomorphology, they cannot be assumed a priori as such in any other case. The water contact angle, θ, is a more probable candidate, because, at least on average, it is a single value function of morphology (Figure 7d). However, direct adoption of θ as a proxy for morphology fails to capture the fact that early-stage compression does not alter morphology (Figure 5).

2.7. TOWARD MORPHOLOGY DESIGN: FITTING THE *K*-INDEX TO THE SYSTEM VARIABLES – THE EFFECT OF THE SOLVENT

K-indexes and contact angles directly, as well as other $\log_e$-transformed material properties measured or calculated in all individual solvents (up to 26 runs in each solvent – Tables S.II.1 and S.VII.1) were fitted to the three synthetic parameters ($n = 3$), x_1 = [ISO], x_2 = [H_2O] and x_3 = [Et_3N], using a fully quadratic model with 10 terms (Eq.2). Fitting in individual solvents is referred to herewith as "local fitting." Fitting procedures,

$$Property(m) = b_{m,0} + \sum_{i=1}^{n} b_{m,i}x_i + \sum_{i=1}^{n} b_{m,ii}x_i^2 + \sum_{i=1}^{n}\sum_{j<i}^{n} b_{m,ij}x_i x_j \qquad \text{(Eq.2)}$$

coefficients $b_{m,o}$, $b_{m,i}$, $b_{m,ii}$ and $b_{m,ij}$, and correlation coefficients (R^2) are cited in Tables S.X.3-S.X.10. Defining and focusing on *Property* (m = 1) ≡ *K*-index, fitting was carried out iteratively. In brief, working in each solvent separately, at first, terms of Eq 2 with a less than 90% confidence level, that is with null-hypothesis probability values $P > 0.1$, were deemed not statistically significant and were dropped from the model stepwise, one at a time. The resulting fitting equation was used to calculate the *K*-indexes for the experimental runs. The calculated values of the *K*-index were plotted against the experimental *K*-indexes and the expected linear correlation with slope = 1 and intercept = 0 was fitted with a linear weighted least square (WLS) method. The residuals from all runs were calculated and runs with residuals outside ±2 standard deviations from the average were rejected. The remaining runs were fitted again to the full Eq 2, the derived set of calculated *K*-indexes was plotted against the experimental values, the ±2 standard deviation criterion was applied again on the residuals, and the process was repeated until no more runs had residuals falling outside ±2 standard deviations from their average. Only one THF run was rejected; two CH_3CN runs were rejected after 2 iterations; 5 propylene carbonate runs were rejected after 4 iterations, and 6 CH_3NO_2 runs were rejected after 4 iterations. No acetone, 2-butanone and ethyl acetate runs were rejected. Correlation coefficients, R^2, ranged from 0.89 (THF) to 0.97 (acetone). The surviving terms of Eq 2 were different in different solvents (Table S.X.3). For example, in THF, only the linear [ISO] term survived. In high-polarity propylene carbonate only the $[Et_3N]^2$ term was rejected, while in high-polarity acetonitrile, in addition to the $[Et_3N]^2$ term, $[ISO]^2$ and $[ISO][H_2O]$ were also rejected. Although 8 terms survived in both acetone and CH_3NO_2, they were quite different: in acetone the two rejected terms were the $[Et_3N]$ and $[H_2O][Et_3N]$, while the coefficients

of the remaining terms were quite low, leaving the constant, $b_{1,0}$, as the dominant factor; in CH_3NO_2, the two rejected terms were the [ISO][H_2O] and [ISO][Et_3N], while the controlling terms by far were in order: [H_2O] > [Et_3N]^2 > [Et_3N]. That specific type of dependence of the *K*-index on the reagents in CH_3NO_2 becomes important in comparing and interpreting results from global vs. local fitting below.

Next, fitting of the same properties was carried out again by considering all runs in all individual and binary solvents simultaneously. That "global fitting" of the *K*-index considered all 188 runs in individual solvents, plus the 20 runs in mixed solvents, for a total of 208 runs. The effect of the solvent was modeled with three additional independent variables, the Hansen Solubility Parameters of each sol (calculated and listed in Parts B of Tables S.I.4-S.I.11 in Appendix I). Thereby, global fitting of Eq 2 used six independent variables (n = 6) and included 28 terms. All six independnent variables were orthogonalized in the [-1,1] interval. Referring back to the *K*-index, thirty one (31) runs were rejected after 6 iterations following the process described for single solvents above. At the beginning of the iterative process R^2 = 0.72; at the end R^2 = 0.95 with RMES = 0.04_7. The final global-fitting equation for the *K*-index included 19 terms (Table S.X.11). All linear terms ($b_{1,i}$) survived. Surviving square terms ($b_{1,ii}$) included [ISO]^2 and all three HSP^2, with coefficients in the order: $(\delta H_{sol})^2 > (\delta P_{sol})^2 > (\delta D_{sol})^2$. Most of the cross-terms ($b_{1,ij}$) that were rejected included [H_2O] and [Et_3N]. In particular, rejected cross-terms included [ISO]*[H_2O], but all other cross-terms of [ISO] survived. The only cross-term of [H_2O] that actually survived was the one with the H-bonding ability of the solvent, [H_2O]*δH_{sol}, yet with a small negative coefficient. Among cross terms of [Et_3N], only those with δH_{sol} and δP_{sol} survived, albeit with also very small coefficients.

The global-fitting equation for the *K*-index was used to back-calculate the *K*-indexes of the runs that survived the iterative process in all individual solvents (*vide ante*). Those *K*-indexes were treated as brand new sets of data for each individual solvent, and were fitted to [ISO], [H_2O] and [Et_3N], as it was described above for "local fitting" of the actual experimental *K*-index values. Fitting was carried out once: the values of R^2 were equal to 0.99 for all solvents, and no iterations were needed. Fitting surfaces from the calculated *versus* the experimental *K*-indexes in propylene carbonate and acetonitrile are compared in Figure 8. For the fitting surfaces of the remaining solvents refer to Appendix XI. Given the complexity of the problem, the agreement between the two sets of surfaces was deemed satisfactory: the main trends of the dependence of the *K*-index to [ISO], [H_2O], and [Et_3N] were retained for most solvents, supporting that handing the solvent effect on the *K*-index through the HSP of the sol was a valid approach, leaving no other significant system parameters, except the gelation temperature and pressure, unaccounted for. The main discrepancy was identified with CH_3NO_2, in which fitting of the calculated *K*-indexes failed to capture the curvature of the experimental surfaces (Figure S.XI.1). In that regard, it is noted that 14 out of the 30 runs that were rejected during global fitting of the *K*-index, were runs in CH_3NO_2. (Among the other rejected runs, 8 were in also high-polarity propylene carbonate, and 2 in acetonitrile.) It is noted also that in local fitting in CH_3NO_2, Eq 2 showed a strong dependence on [Et_3N] (Table S.X.3), while in global fitting most of the [Et_3N] terms were rejected (Table S.X.11). It is therefore speculated that the large discrepancy between the experimental and back-calculated surfaces of the *K*-index in CH_3NO_2 might be due to its acidity (*e.g.*, in DMSO $pK_{a,CH3NO2}$ = 17.2) that may interfere with the function of Et_3N as a catalyst. Notwithstanding the factors entering the adjustment

of the *K*-index in CH_3NO_2, within the quasi-heuristic approach of this study, employing CH_3NO_2 in mixed solvents should be approached with caution, and its use should be avoided in favor of its almost-equivalents, propylene carbonate and/or CH_3CN (Figure 1c).

2.8. *K*-INDEX AS A TOOL FOR SYNTHESIS OF MATERIALS WITH PRESCRIBED MORPHOLOGY

It is self-evident that for a given *K*-index, Eq 2 (m = 1) can be satisfied by infinite combinations of [ISO], [H_2O], [Et_3N], δP_{sol}, δH_{sol} and δD_{sol}. However, by setting values for six material properties simultaneously, the corresponding six fitting equations (Eq.2 with m = 1-6) comprise a system with an equal number of equations and unknowns. The selection of properties was guided by Figure 7, in the sense that certain combinations of properties are not possible. For example, while it is reasonable to request a low thermal conductivity (Figure 7b) and a high surface area (Figure 7e), by the same token that combination cannot be achieved with microspheres (*K*-index = 1.9 – see Figure 7a).

This procedure was tested with eight runs of polyurea aerogels with eight different combinations of density, *K*-index, BET surface area, Young's modulus, ultimate compressive strength and thermal conductivity (Appendix XII). Solving the resulting system of six equations gave the values of [ISO], [H_2O], [Et_3N]. The roots for the HSP of the sol, δP_{sol}, δH_{sol} and δD_{sol},, were used in order to calculate, based on the HSPs and concentrations of the ISO, H_2O and Et_3N, the HSP values of the "*Magic*" solvent that must be used for making the sol. The composition of the *Magic* solvent was calculated by selecting three neat solvents, whose HSP values bracketed the HSP of the *Magic* solvent.

That process yielded three equations with the volume fractions of the three components of the *Magic* solvent as unknowns (Appendix XII).

The experimental material properties of all eight test-samples are given in Tables S. XIII.1 and S. XIII.2. Figure 9 compares the experimental *versus* the expected values of the *K*-index, the bulk density, the BET surface area, the thermal conductivity and the elastic modulus. The lowest overall deviation from the set values was recorded for the *K*-index ($2._3 \pm 1.2\%$ - Figure 9a). Indeed, in reference to Figure 3, Figures 9b (see also Figure S.XIII.1) shows that the experimental micromorphologies matched closely to those expected from the values of the *K*-index. Similarly, experimental ρ_b, σ and λ_{Total} values matched closely the expected ones (Figures 9c-9e). The largest deviations from the set values were noted in the elastic modulus, *E*, yet the expected and experimental *E* values of seven out of the eight samples were no more than a factor of 1.8× from one another; that ratio for sample No. 5 was equal to 2.9 (see Figure 9f and Table S.XIII.2). The lower overall fidelity of the expected values of *E* suggests that the corresponding fitted relationship (Eq 2) is weaker than that of other properties, which in turn is attributed to the fact that the mechanical properties of samples with defects (mostly from lower concentration sols) were not tested. The properties of one sample in particular (Sample No. 2) were selected in order to probe the predictive power of the model at the low thermal conductivity limit in combination with other desirable properties for application in thermal insulation panels. Thus, by consulting Figure 7, the *K*-index was set at 1.16, ρ_b at 0.074 g cm^{-3}, λ_{Total} at 19.9 mW m^{-1} K^{-1}, and *E* at 8.4 MPa. The experimental values (average of three samples) were 1.21 ± 0.01, 0.091 ± 0.003 g cm^{-3}, 23.5 ± 0.9 mW m^{-1} K^{-1} and $12._6 \pm 2.2$ MPa, respectively, and were considered a good match.

3. CONCLUSIONS

The *K*-index has been a resilient descriptor and predictor of the diverse nanomorphology of polyurea aerogels, a correlator of nanostructure to material properties, and a quantitative tool for materials design. Identification of three-way quantitative relationships among nanostructure-property-synthetic conditions is expected to be an essential point of departure for fundamental bottom-up simulations of nanostructure formation. The question at this point becomes whether *K*-index is system-specific to polyurea aerogels. Certain nanostructured polyurethanes based on reaction of the same ISO of Eq 1 with oligomeric glycols consist of spinodal microstructures "frozen" at different stages of spheroidization, ranging from bicontinuous networks to large bald microspheres.[38] Those materials do follow the trend set by polyurea aerogels of this study (see Appendix XIV), with *K*-indexes in the range of 1.9 (for micron-size bald microspheres with $\theta = 135.2^{o}$ and $\Pi = 71.5\%$ v/v) to 2.1 (fused 10 μm spheroidal network with $\theta = 153.7^{o}$ and $\Pi = 72.2\%$ v/v). Difficulty is expected to arise with hydrophilic materials that may uptake water droplets into their bulk upon contact. In this category are oxide aerogels such as silica,[46] vanadia[45] *etc.*[47] That brings back the question about uniqueness of the *K*-index. In that regard, water contact angles as a proxy for texture may be substituted by roughness measurements, for example *via* profilometry on the same sample at different length scales. Other experimental strategies that could be developed to bypass that issue may include measuring contact angles of oil droplets, or perhaps still using water after surface hydrophobization with fluorine plasma (method particularly amenable to polymeric aerogels), or a combination of the above.

4. EXPERIMENTAL SECTION

4.1. MATERIALS

1,3,5-Tris(6-isocyanatohexyl)-1,3,5-triazinane-2,4,6-trione) (ISO, see Eq 1) is supplied commercially in pure form under the trade name Desmodur N3300A, and was donated generously by Covestro LLC, Pittsburgh, PA. Spectroscopic characterization data for ISO have been published previously.[27] Triethylamine (99% pure) was purchased from Acros-Organics Co., U.S.A., and was distilled before use. Anhydrous acetonitrile (ACN), nitromethane (NM), propylene carbonate (PC), acetone (ACE), tetrahydrofuran (THF), ethyl acetate (EA), 2-butanone (2-BU) and dimethylformamide (DMF) were purchased from Sigma-Aldrich Co., U.S.A. and were used as received.

4.2. PREPARATION OF PUA AEROGELS

Polyurea aerogel samples were prepared using response surface methodology (RSM), applied with a Central Composite Rotatable Design (CCRD) model as described briefly in the Results and Discussion section and in detail in Appendix I of the Supporting Information. The exact formulations of all samples, in all solvents, including the 20 mixed solvent systems used in this study, along with the phenomenological gelation times, namely the time intervals for sols to stop flowing, and the Hansen Solubility Parameters of each sol are given in Tables S.I.4 to S.I.12 of Appendix I in Supporting Information. As a typical example of the preparation procedure, Run 16 at Level 1 (refer to Figure 1, Figure S.1.1 and Table S.I.2) was prepared as follows: ISO (5.5 g, 0.0109 mol) was dissolved in 94 mL of anhydrous solvent (that volume remains constant for all runs in all solvents) followed

by the addition of 1.5 mol equivalents of water (0.0150 mol, 0.270 mL). The sol was obtained by adding 0.15 % w/w of triethylamine (catalyst) relative to the sol (namely to the total weight of N3300A, 94 mL of solvent, water and catalyst). Polypropylene syringes (Norm-ject^{TM} 10 mL, 14 mm diameter) were used as molds by cutting off the needle end. The sol was shaken vigorously and was poured into the molds. The open ends of the molds were wrapped with several layers of Parafilm^{TM}. Sols were allowed to gel and age in their molds. The gelation times of all samples of this study varied between 1 min and 5 days (refer to Tables S.I.4 to S.I.12). Aging times were either 24 h, or for wet-gels that took over one day to gel they were set equal to their gelation times. Wet gels were extracted from their molds into fresh technical grade acetone by inverting the syringes and depressing the plungers. The volume of acetone was approximately 4× the volume of each gel. The acetone bath was replaced four times every 8 h. Finally, wet-gels were dried with liquid CO_2 that was removed at the end as a supercritical fluid (SCF).

4.3. METHODS

4.3.1. Drying PUA Wet-gels into Aerogels. Drying of acetone-exchanged wet-gels with supercritical fluid (SCF) CO_2 was carried out in an autoclave (SPI-Dry Critical Point Dryer Jumbo size, SPI Supplies, Inc. West Chester, PA or a Spe-edSFE system, by Applied Separations, Allentown, PA). Wet-gels, submerged in acetone, were loaded into the autoclave. The high-pressure vessel was closed, and liquid CO_2 was allowed in at room temperature while the lower layer (acetone) was drained out. Liquid CO_2 was allowed in the vessel several more times until acetone was extracted out of the pores of the samples completely. The criterion for the latter was that CO_2 released from the vessel formed

powder of dry ice. At that point, the temperature of the autoclave was raised to 40 ^{o}C, and after a stay of 1 hour at that temperature, SCF CO_2 was vented off slowly (over a period of 12 h) as a gas.

4.3.2. Physical Characterization of PUA Aerogels. Bulk densities (ρ_b) were calculated from the sample weight and dimensions. Skeletal densities (ρ_s) were measured with helium pycnometry using a Micromeritics AccuPyc II 1340 instrument. Porosities (Π), as percent of empty space, were calculated from the ρ_b and ρ_s values *via* $\Pi = 100 *[(\rho_s - \rho_b)/ \rho_s]$. Samples were outgassed for 24 h, at 80 °C, under vacuum, before skeletal density determinations.

4.3.3. CHN Elemental Analysis. CHN elemental analysis was conducted with an Exeter Analytical Model CE440 elemental analyzer, calibrated with acetanilide, urea, and glycine. The combustion furnace was operated at 1,050 ^{o}C. All calibration standard (acetanilide obtained from NIST) was run three times. Aerogel samples were run once.

4.3.4. Neclear Magnetic Resonance. Solid-state CPMAS ^{13}C-NMR spectra were obtained with samples ground into fine powders on a Bruker Avance III 400 MHz spectrometer with a carbon frequency of 100 MHz, using a 7 mm Bruker MAS probe at a magic-angle spinning rate of 5 kHz, with broadband proton suppression, and CP TOSS pulse sequence. The Total Suppression of Spinning Sidebands (TOSS) pulse sequence was applied by using a series of four properly timed 180^{o} pulses on the carbon channel at different points of a cycle before the acquisition of the FID, after an initial excitation with a 90^{o} pulse on the proton channel. The 90^{o} excitation pulse on the proton and the 180^{o} excitation pulse on carbon were set to 4.2 μs and 10 μs, respectively. The cross-polarization contact time was set at 3000 μs. The ^{13}C-NMR spectra were referenced externally to

glycine (carbonyl carbon at 176.03 ppm). Chemical shifts are reported *versus* TMS (0 ppm). Solid-state CPMAS ^{15}N-NMR spectra were also obtained with samples ground into fine powders on the same Bruker spectrometer with a nitrogen frequency of 40.557 MHz, using a 7 mm Bruker MAS probe at a magic-angle spinning rate of 5 kHz. The number of scans was 8192. The 90º excitation pulse on the proton was set at 3.25 μs. The cross-polarization contact time and the relaxation delay were set at 2000 μs and 5 s, respectively. Chemical shifts were referenced externally to glycine (amine nitrogen at 33.40 ppm) and are reported *versus* liquid ammonia (0 ppm).

4.3.5. X-Ray Photoelectron Spectroscopy (XPS) was conducted with a Physical Electronics PHI 5000 VersaProbe II Scanning XPS Microprobe Instrument equipped with an Al x-ray source. The x-ray source was nearly normal to sample surface. The spectrometer (analyzer) was at an angle of 54.7º relative to the x-ray source. Typical settings for fine range scanning were 100 μm, 25 W / 15 kV for power, 23.5 eV for the pass energy, and 0.05 eV for step size. In order to reduce sample surface charge effects on the spectra, both ion neutralization and electron neutralization were turned on during the experiments. The vacuum was in the 10^{-7} Pa range. Samples for XPS were prepared by cutting monolithic cylinders with a knife. The exposed cross-sections were sputter-coated with a very small amount of Au-Pd that served as an internal energy standard. Samples without that coating gave the same results, confirming that the coating did not interfere with the chemical identity of the surface within the energy range of the functional groups involved in this study. Peaks, however, might be found shifted by up to 1 eV if no such calibration was applied.

4.3.6. Scanning Electron Microscopy (SEM) was performed with samples coated with Au-Pd using a Hitachi S-4700 field emission microscope.

4.3.7. Porosimetry. N_2-sorption porosimetry was carried out with a Micromeritics Tristar 3410 surface area and pore size distribution analyzer. Before analysis, samples were outgassed for 24 h, at 80 °C, under vacuum. Specific surface areas, σ, were determined using the Brunauer-Emmett-Teller (BET) equation. Average pore diameters were calculated using the $4\times V_{Total}/\sigma$ method, where V_{Total} is the total specific pore volume (*i.e.*, per gram of sample). V_{Total} was calculated either from the single highest volume of N_2 adsorbed along the adsorption isotherm (*i.e.*, at $P/P_0 \rightarrow 1$), or from the relationship $V_{Total} = (1/\rho_b) - (1/\rho_s)$. In mostly mesoporous materials, average pore diameters calculated using V_{Total} by the two methods converge. In mostly macroporous materials, average pore diameters calculated using $V_{Total} = (1/\rho_b) - (1/\rho_s)$ are significantly higher than those calculated using the highest volume of N_2 adsorbed method.

4.3.8. Water Contact Angles were measured with a Rame-Hart Model 250 standard goniometer equipped with a high-resolution camera, using the static sessile drop method, in which a 5 μL droplet of water is placed on the sample surface followed by imaging. Aerogel samples were prepared by cutting disks with a knife; surfaces were smoothened with sand paper (3 M Abrasives, 320 grit, part No. 32541) and were cleaned with a stream of dry N_2 at high pressure. Contact angle data were collected using three separate samples for each run (formulation), *immediately* upon placement of the water droplets on the samples. That was particularly important for hydrophilic samples, as the water droplets were uptaken slowly inside their bulk (see Movies provided as Supporting Information and labeled “Hydrophilic 1–3”). On the contrary, water droplets were stable

indefinitely on the hydrophobic samples. Contact angles were determined with the DROPimage Advanced v2.4 software. Ten measurement were taken by the computer in rapid succession. Results were reported as averages over the three samples (30 measurements) for each formulation.

4.3.9. Thermal Conductivity. The total thermal conductivities of all samples, λ_{Total}, were calculated at 23 °C *via* $\lambda_{Total} = R \times c_p \times \rho_b$. The thermal diffusivity, R, of each sample was determined at room temperature and atmospheric pressure with a Netzsch NanoFlash Model LFA 447 flash diffusivity instrument using disk samples ∼1 cm in diameter, 2−3 mm thick.[58] Specific heat capacities, c_p, at 23°C were measured with powders of the samples (5−10 mg) using a TA Instruments Differential Scanning Calorimeter Model Q2000 calibrated against a sapphire standard and run from 0 to 30 °C at 0.5 °C min^{-1} in the modulated T4P mode. The modulation amplitude was set at 0.133 ^{o}C, and the modulation period at 100 s. Polyurea aerogel samples and two standards (rutile and corundum) were outgassed for 24 h, at 80 °C, under vacuum, before heat capacity measurements. First, the heat capacities of rutile, and corundum were measured three times each just before running the polyurea samples. These experimental heat capacity values were compared with literature values and were used in order to calculate a calibration factor (= 1.033). Then, we measured the heat capacities of 16 PUA aerogels selected randomly in the design space from different solvents with variable bulk densities and morphologies. Each one of those polyurea aerogel samples was tested three times, and the c_p values were multiplied by the calibration factor. Thus, the average heat capacity of the polyurea aerogels was $c_p = 1.2_2 \pm 0.10$ J g^{-1} K^{-1}. The total thermal conductivities of the same 16 samples that were selected for measuring c_p were also measured using a custom-made heat

flow-meter that includes in sequence:[38] a hot plate (at 37.5 ^{o}C, bottom), the polyurea aerogel sample, a NIST-calibrated reference sample,[59] and a cold surface (an ice-water bucket). The polyurea aerogel samples used in that configuration were casted as large panels (10 cm × 5 cm × 1 cm). Two of those panels, placed tightly side-by-side, were used to cover the 10 cm × 10 cm stage of the hot-plate apparatus. It has been shown previously that the shim between the plates makes no difference (beyond experimental error) in the thermal conductivity values.[38] The thermal conductivity values obtained from the hot-plate method were compared with the values obtained with the laser flash method and both sets of data are provided in Table S.VII.3 of Appendix VII in Supporting Information. Although they were not used in this study, solid thermal conductivities, λ_s, were calculated *via* $\lambda_s = \lambda_{Total} - \lambda_g$, whereas gaseous thermal conductivities, λ_g, were calculated using the Knudsen equation.[60,61] All the λ_s and λ_g values of all samples are included in Appendix VII of the Supporting Information for future reference and further data analysis.

4.3.10. Quasistatic Mechanical Characterization. Compression testing was conducted according to the ASTM D1621-04a standard on cylindrical specimens, using an Instron 4469 Universal Testing Machine equipped with a 50 kN load cell. Three cylindrical samples from each run (formulation) were cut to give specimens with a height-to-diameter ratio of 1:1, according to that ASTM standard. Sample diameters were in the 1.2–1.4 cm range. Data acquisition carried out with the software of the Instron machine (Bluehill 3) and data analysis was done in the Excel file that is given as an output by Bluehill 3.

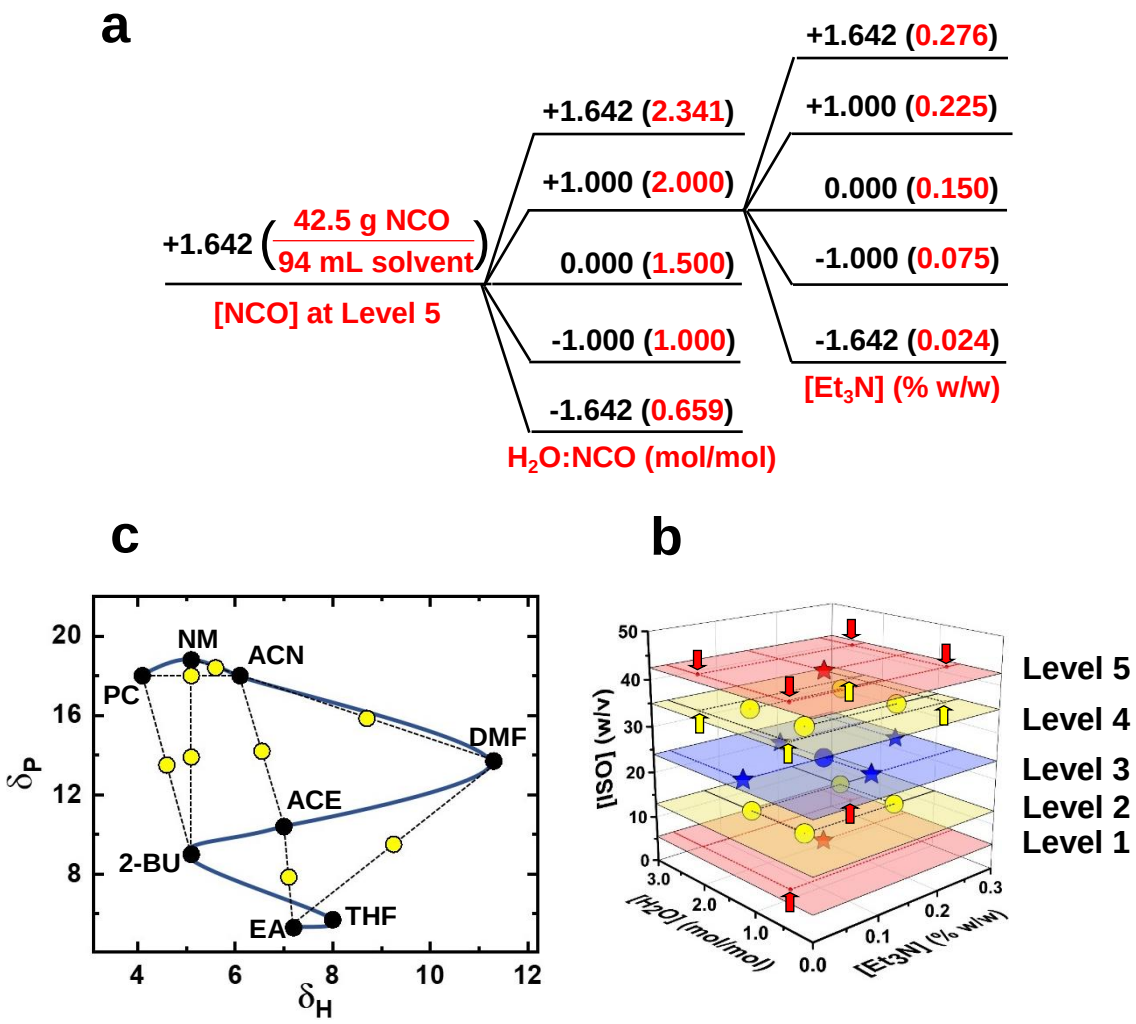

Figure 1. Formulations of polyurea aerogels based on an enhanced Central Composite Rotatable Design (CCRD) model. Independent variables: [ISO], [H_2O], [Et_3N] at 5 levels each. (a) One example showing how the 5 levels of [H_2O] and [Et_3N] were pegged to [ISO] at each of its levels. The particular example shows [ISO] at its highest concentration (at Level 5). Analogous branching is obtained *via* the CCRD at the other 4 levels of [ISO]. In black: coded values used by the CCRD model. In red: actual values of the variables in units shown within the frame. The two [Et_3N] levels marked with an asterisk (*) were not actually engaged by the CCRD with [ISO] being at Level 5 of this example. (b) The entire domain of the CCRD. Color-coding of the 5 levels of [ISO] is used for visualization purposes only. Circles: Factorial and central runs of the design. Stars: Star points of the design. Arrows: Extra runs added in order to capture the sensitivity of the nanostructure to [H_2O] and [Et_3N] at [ISO] at Levels 4 and 5. (c) Domain of solvents selected based on their δP and δH HSP values. Red arrows point at the binary solvents used for preparing the nanostructures of Figure 6.

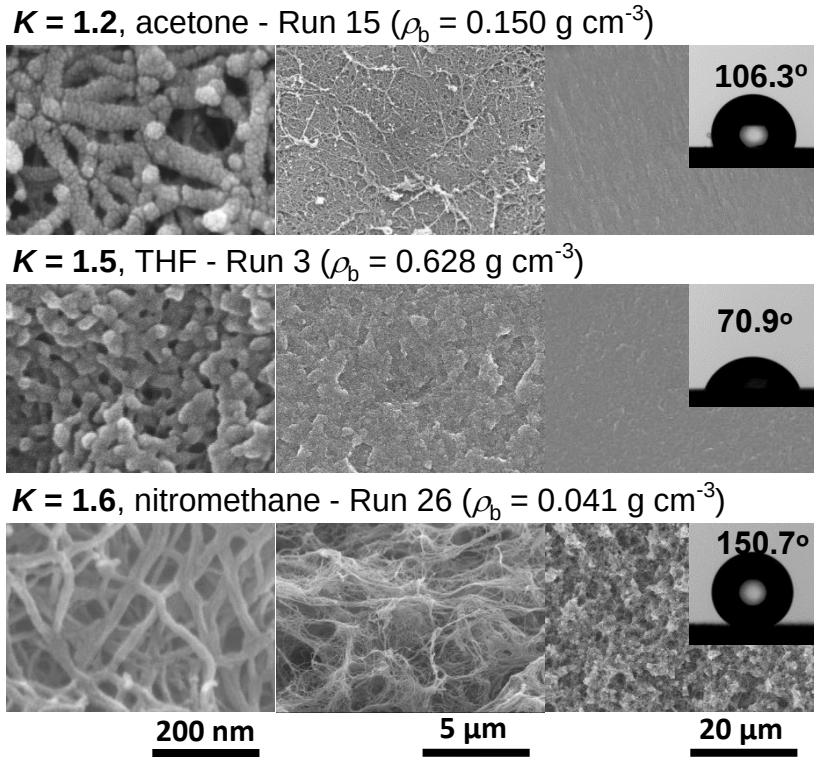

Figure 2. SEM of three random samples ranging from hydrophilic to superhydrophobic at three different magnifications: Left: 250 k; Middle: 10 k; and Right: 2.5 k. For the morphologies corresponding to the *K*-index values refer to Figure 3.

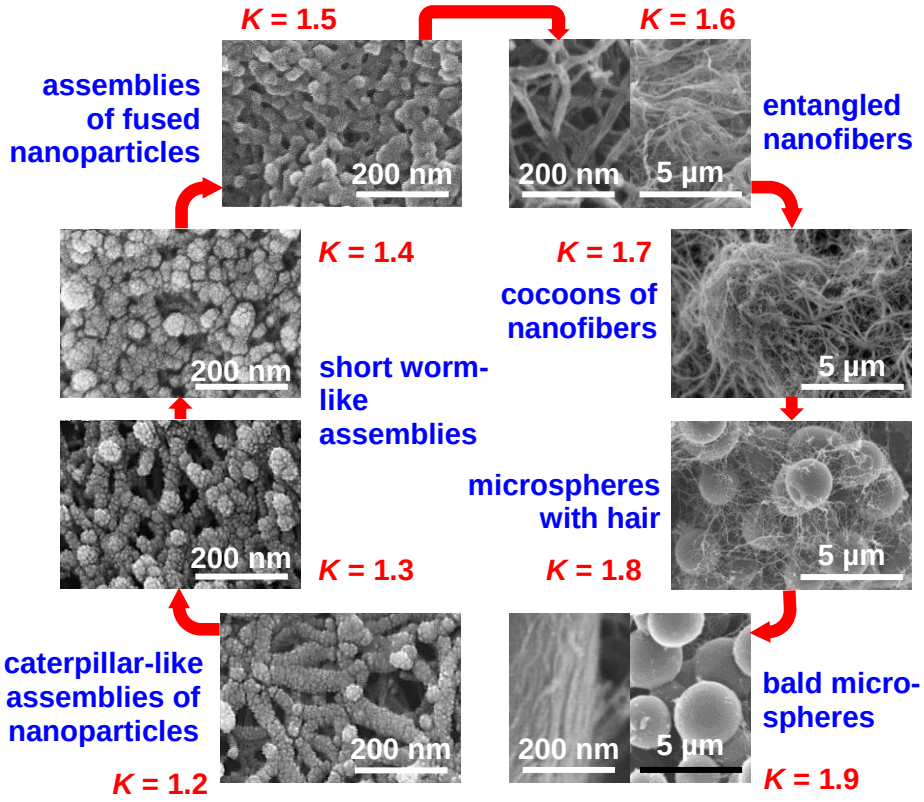

Figure 3. Eight nanomorphology groups identified from 188 formulations prepared in 8 solvents according to Figure 1. *K*-indexes were defined as the ratios of the water contact angles to the corresponding percent porosities (θ/Π).

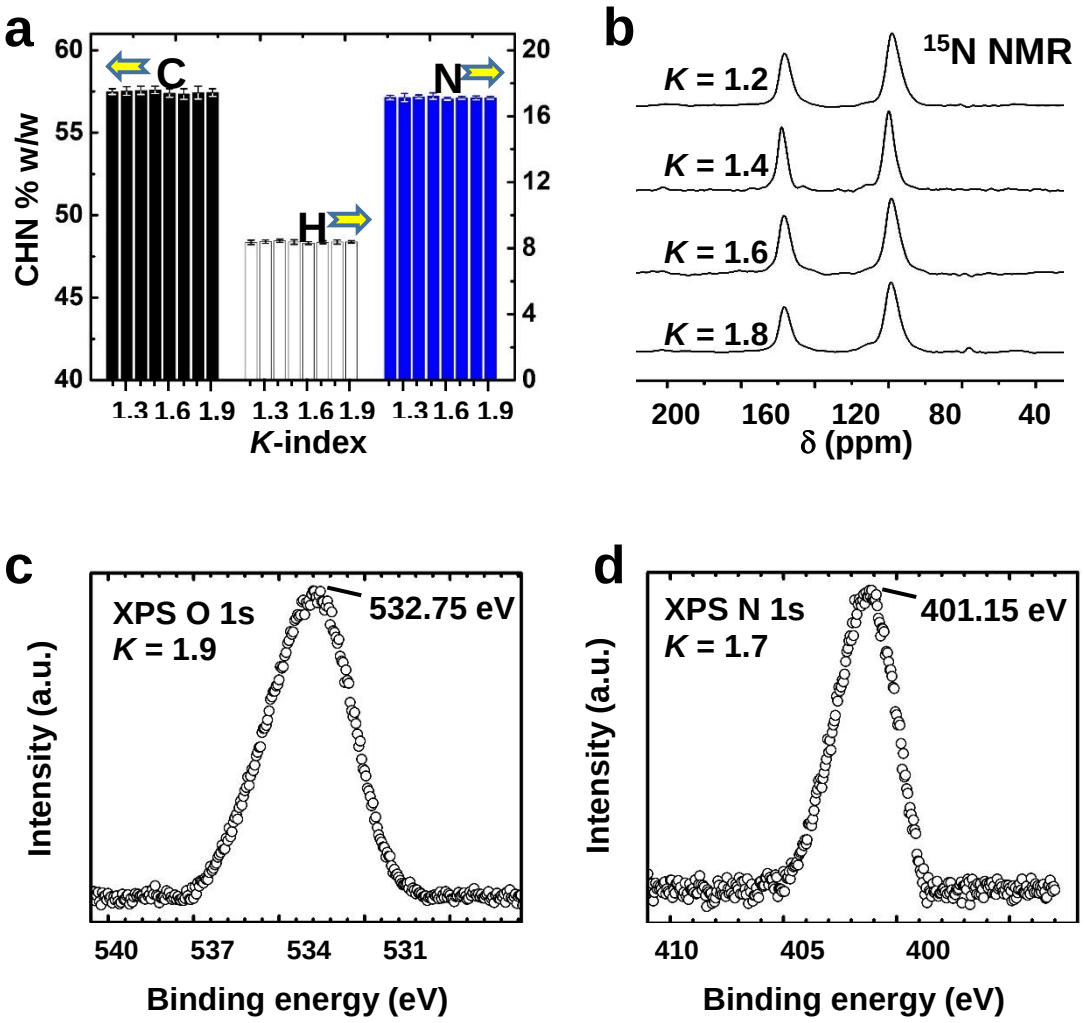

Figure 4. (a) CHN analysis data of all samples prepared in individual and binary solvents grouped together according to their *K*-indexes. (b) Solid-state ^{15}N NMR spectra of four hydrophobic samples with *K*-indexes. (c) O 1s XPS of CH_3CN – Run 21 ([ISO] at Level 4 with high [H_2O] and high [Et_3N]; $\theta = 128.7^{o}$). (d) N 1s XPS of CH_3CN – Run 10 ([ISO] at Level 3 with stoichiometric [H_2O] and low [Et_3N]; $\theta = 140.3^{o}$). For XPS of other samples over the entire *K*-index range refer to Appendix IV.

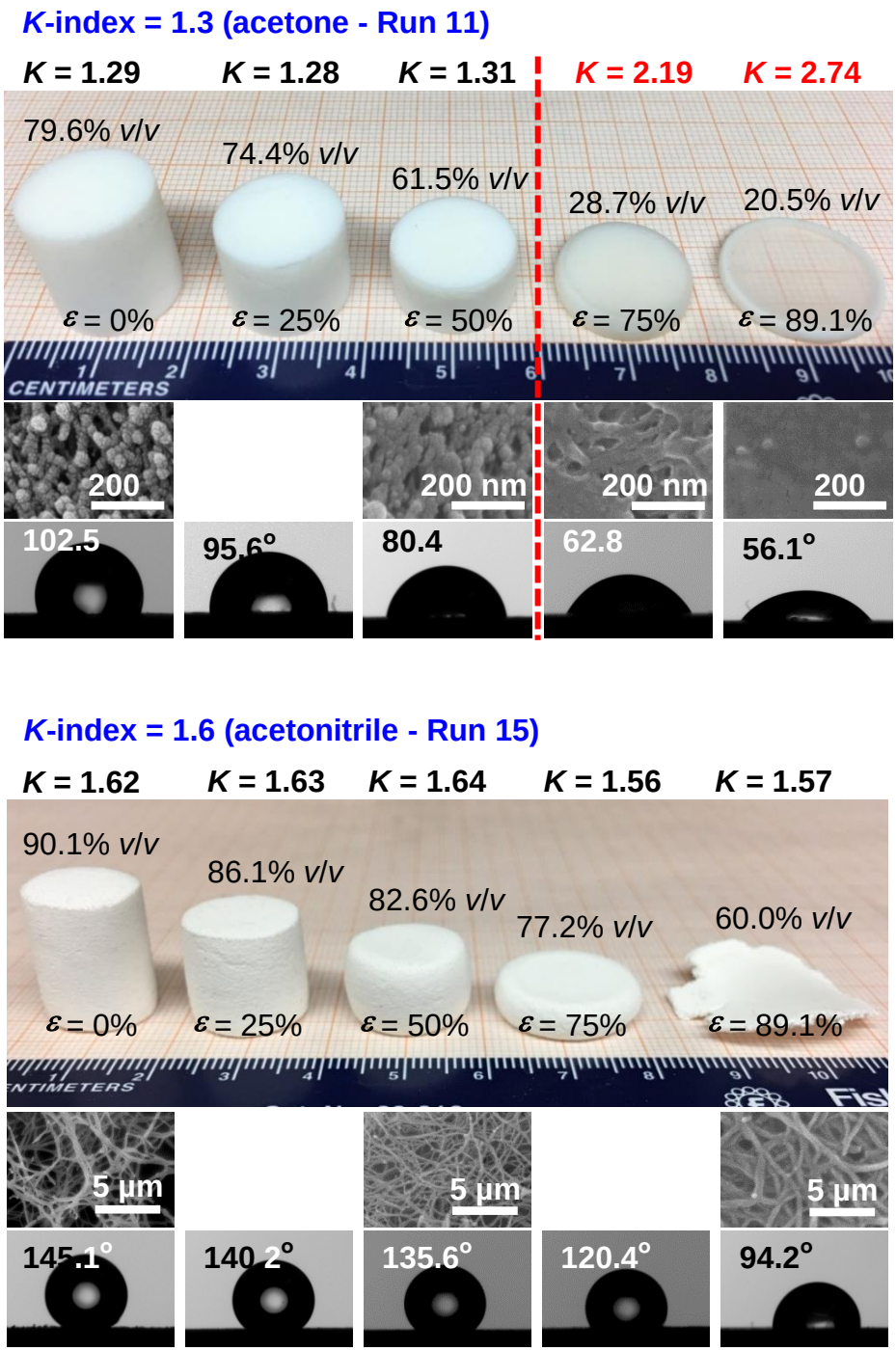

Figure 5. Evolution of the nanostructure and of the *K*-index of two representative samples along compression. (Other pertinent information contained in the frames includes percent porosities in v/v, percent compressive strains (ε), and water contact angles.) The red dashed vertical line in the upper frame shows the point beyond which θ no longer follows Π and the values of the *K*-index start increasing (see text). For additional examples spanning the entire rage of *K*-index refers to Appendix V.

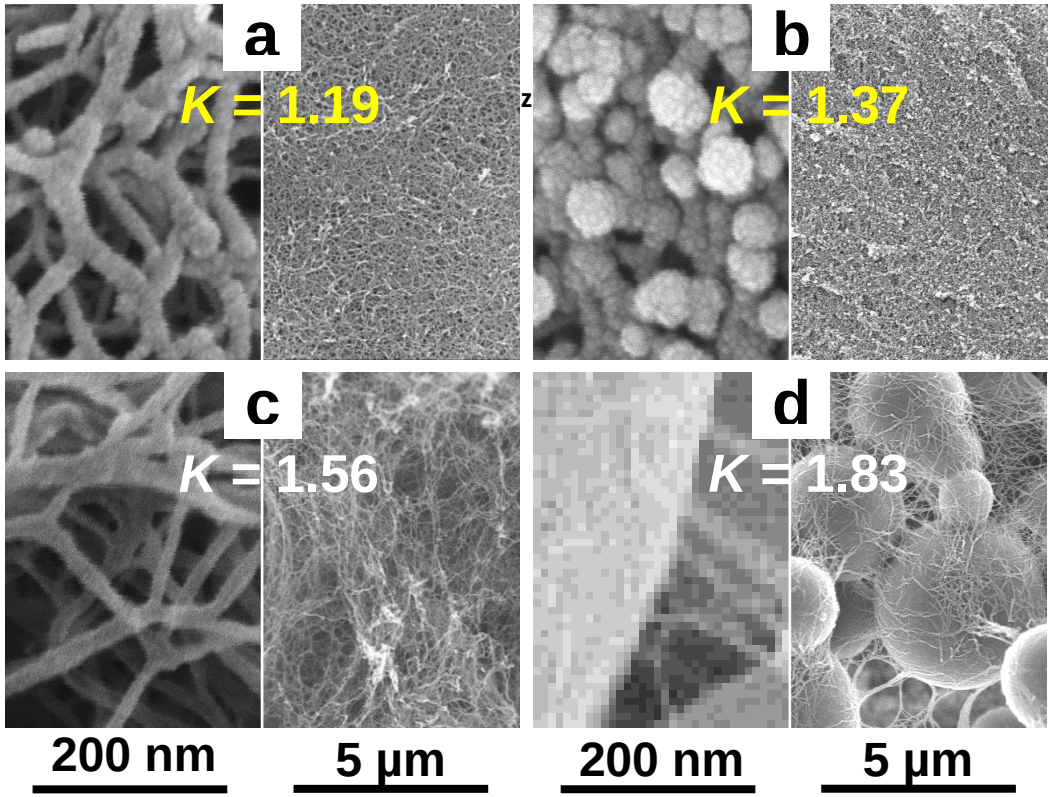

Figure 6. SEM of representative runs prepared in binary solvent systems (1:1 v/v, refer to red arrows in Figure 1c). (a) Acetonitrile-DMF, Run 16 ([ISO] at Level 1, Π = 93.4% v/v, θ = 110.8^{o}). (b) Acetonitrile-propylene carbonate, Run 8 ([ISO] at Level 3, Π = 79.7% v/v, θ = 109.2^{o}). (c) Acetonitrile-propylene carbonate, Run 26 ([ISO] at Level 1, Π = 96.1% v/v, θ = 149.8^{o}). (d) Acetonitrile-nitromethane, Run 2 ([ISO] at Level 4, Π = 69.9% v/v, θ = 128.1^{o}). (For SEM of the remaining 16 runs refer to Appendix VI.).

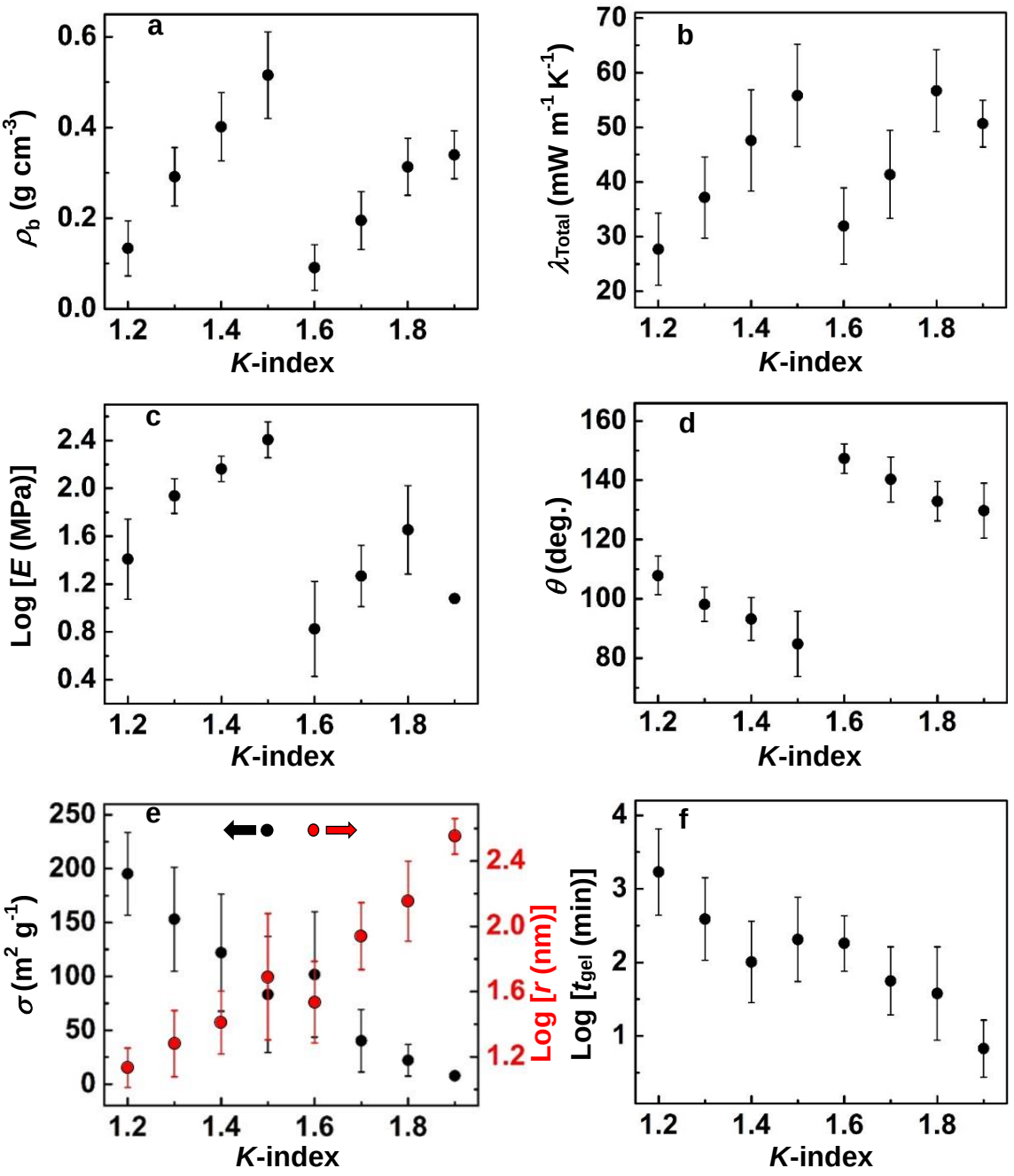

Figure 7. Selected material properties of all 208 samples prepared in individual and binary solvent systems as a function of their *K*-indexes. a) ρ_b: bulk density. b) λ_{Total}: total thermal conductivity. c) *E*: Young's modulus. d) θ: water contact angle. e) σ: BET surface area; and, *r*: particle radius. f) t_{gel}: phenomenological gelation time. (*K*-index values have been binned to single decimal digits to facilitate discussion

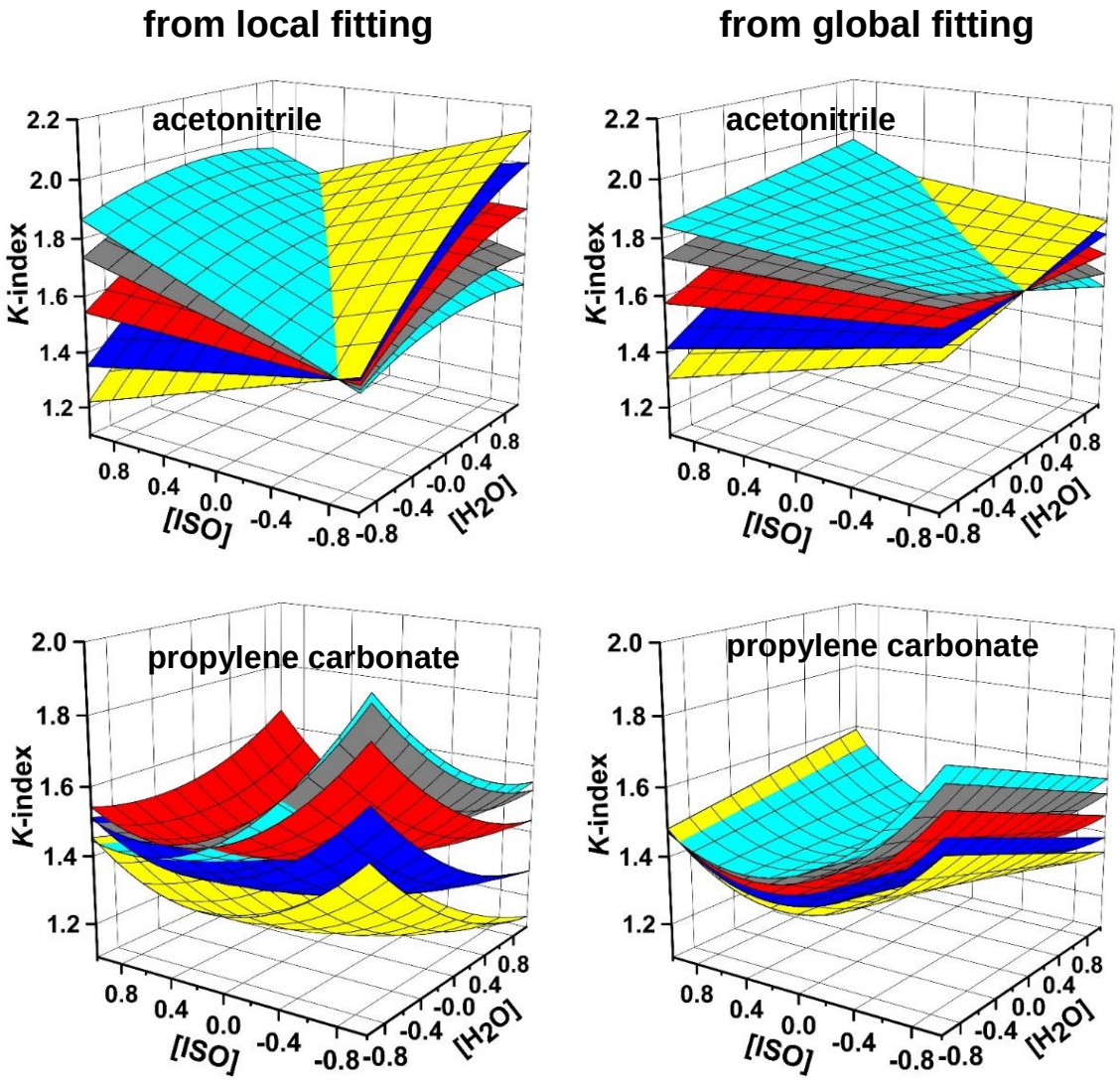

Figure 8. Local *versus* Global fitting of the *K*-index in two representative solvents as a function of orthogonalized [ISO], [H_2O] and [Et_3N] (color-coded). (For the index of color-coding, and the corresponding surfaces in all other solvents see Appendix XI.) [Local fitting: Surfaces from direct fitting of the experimental *K*-index data to the three independent variables in the solvent indicated. Global fitting: Surfaces from *K*-index values back-calculated *via* Equation 2 with the coefficients from a six-variable fitting routine using all data in all solvents (Table S.X.11), by setting δP_{sol}, δH_{sol}, and δD_{sol} at the appropriate values in each solvent at the points of [ISO], [H_2O] and [Et_3N] used in local fitting.

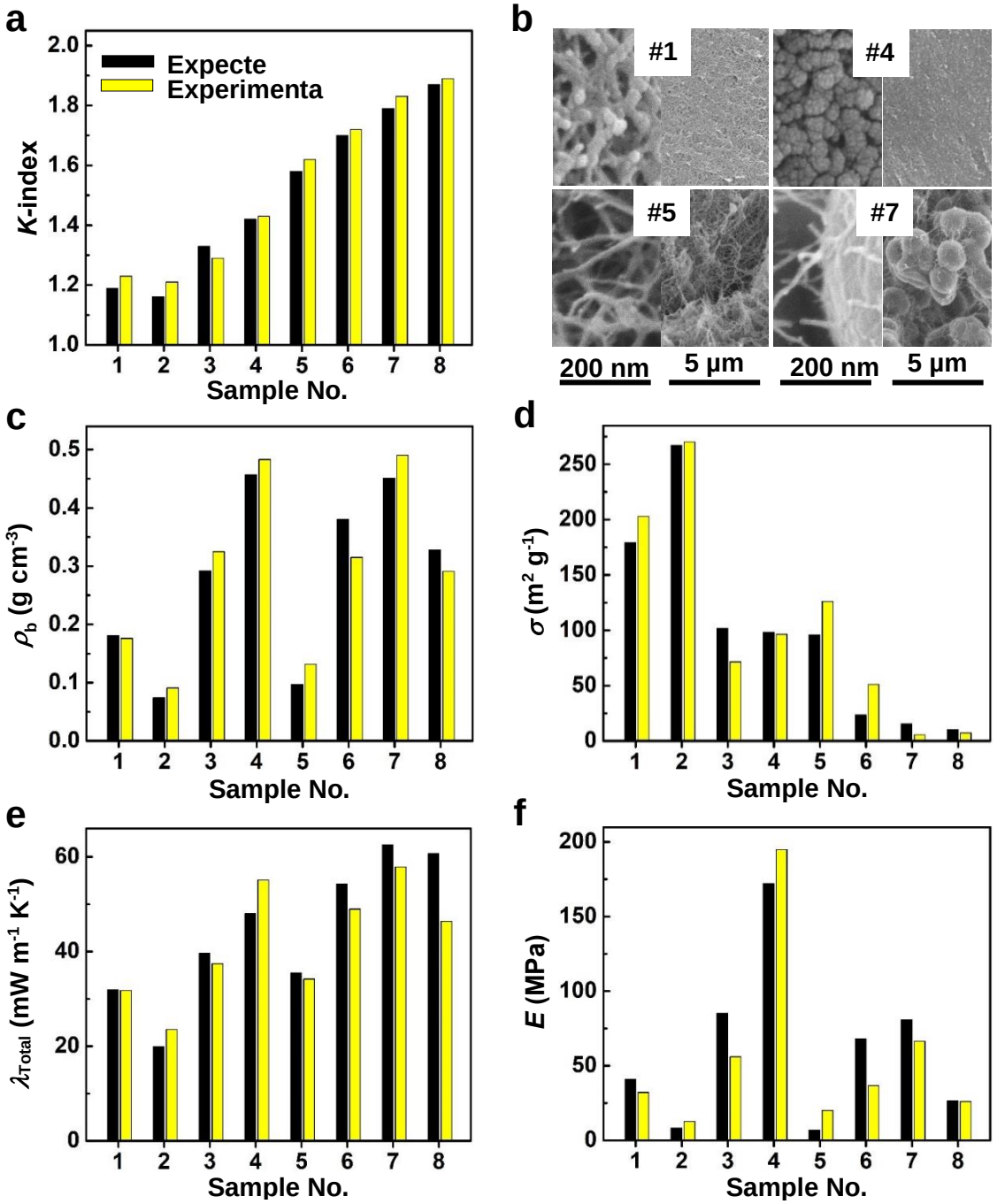

Figure 9. (a), (c)-(f): Selected experimental *versus* predicted properties of eight (8) samples prepared with six (6) predetermined material properties. Frame (b): SEMs of 4 of the eight samples, at two different magnifications (250 k and 10 k).

ACKNOWLEDGMENTS

This project was supported by the ARO under Award No. W911NF-14-1-0369. We also thank Covestro LLC for the generous supply of Desmodur N3300A.

REFERENCES

1. Kim, J.-H.; Hoh, J.; Choi, H.; Lee, J.-Y.; Kim, T.-S. Mechanical Properties of Polymer-Fullerene Bulk Heterojunction Films: Role of Nanomorphology of Composite Films. *Chem. Mater.* **2017**, *29*, 3954–3961.

2. Rizvi, A.; Chu, R. K. M.; Park, C. B. Scalable Fabrication of Thermally Insulating Mechanically Resilient Hierarchically Porous Polymer Foams. *ACS Appl. Mater. Interfaces* **2018**, *10*, 38410–38417.

3. Pakdel, A.; Bando, Y.; Golberg, D. Morphology-Driven Nonwettability of Nanostructured BN Surfaces. *Langmuir* **2013**, *29*, 7529–7533.

4. Yohe, S. Y.; Freedman, J. D.; Falde, E. J.; Colson, Y. L.; Grinstaff, M. W. A Mechanistic Study of Wetting Superhydrophobic Porous 3D Meshes. *Adv. Funct. Mater.* **2013**, *23*, 3628-3637.

5. Motahari, A.; Hu, N.; Vahid, A.; Omrani, A.; Rostami, A. A.; Schaefer, D. W. Multilevel Morphology of Complex Nanoporous Materials. *Langmuir* **2018**, *34*, 6719–6726.

6. De Sio, L.; D'Aquila, P.; Brunelli, E.; Strangi, G.; Bellizi, D.; Passarino, G.; Umeton, C.; Bartolino, R. Directed Organization of DNA Filaments in a Soft Matter Template. *Langmuir* **2013**, *29*, 3398–3403.

7. Nebot, V. J.; Escuder, B.; Miravet, J. F.; Smets, J.; Fernández-Prieto, S. Interplay of Molecular Hydrogelators and SDS Affords Responsive Soft Matter Systems with Tunable Properties. *Langmuir* **2013**, *29*, 9544–9550.

8. Creton, C. 50th Anniversary Perspective: Networks and Gels: Soft but Dynamic and Tough. *Macromolecules* **2017**, *50*, 8297–8316.

9. Samuel, R. E., Salmon, E. D. & Briehl, R. W. Nucleation and Growth of Fibers and Gel Formation in Sickel Cell Haemoglobin. *Nature* **1990**, *345*, 833–835.

10. Serpell, L. C. Alzheimer's Amyloid Fibrils: Structure and Assembly. *Biochim. et Biophys. Acta* **2000**, *1502*, 16–30.

11. Ross, C. A.; Poirier, M. A. Protein Aggregation and Neurodegenerative Disease. *Nat. Med.* **2004**, *10*, S10–S17.

12. Slater, A. G.; Cooper, A. I. Porous Materials. Function-led Design of New Porous Materials. *Science* **2015**, *348*, aaa8075.

13. Vareda, J. P.; Lamy-Mendes, A.; Durães, L. A Reconsideration on the Definition of the Term Aerogel Based on Current Drying Trends. *Microporous Mesoporous Mater.* **2018**, *258*, 211–216.

14. Pierre, A. C.; Pajonk, G. M. Chemistry of Aerogels and Their Applications. *Chem. Rev.* **2002**, *102*, 4243–4265.

15. Cuce, E.; Cuce, P. M.; Wood, C. J.; Riffat, S. B. Toward Aerogel Based Thermal Superinsulation in Buildings: A Comprehensive Review. *Renewable Sustainable Energy Rev.* **2014**, *34*, 273−299.

16. Liu, W.; Herrmann, A.-K.; Bigall, N. C.; Rodriguez, P.; Wen, D.; Oezasian, M.; Schmidt, T. J.; Eychmüller, A. Noble Metal Aerogels - Synthesis, Characterization, and Application as Electrocatalysts. *Acc. Chem. Res.* **2015**, *48*, 154−162.

17. Rolison, D. R. Catalytic Nanoarchitectures – The Importance of Nothing and the Unimportance of Periodicity. *Science* **2003**, *299*, 1698–1701.

18. Leventis, N.; Lu, H. Polymer Crosslinked Aerogels in *Aerogels Handbook - Advances in Sol-Gel Derived Materials and Technologies*, Aegerter, M.; Leventis, N.; Koebel, M. eds., Springer: New York, NY, pp 251-285 (2011).

19. Leventis, N.; Chidambareswarapattar, C.; Bang, A.; Sotiriou-Leventis, C. Cocoon-in-Web-Like Superhydrophobic Aerogels from Hydrophilic Polyurea and Use in Environmental Remediation. *ACS Appl. Mater. Interfaces* **2014**, *6*, 6872–6882.

20. Sun, H.; Xu, Z.; Gao, C. Multifunctional, Ultra-Flyweight, Synergistically Assembled Carbon Aerogels. *Adv. Mater.* **2013**, *25*, 2554−2560.

21. Kistler, S. S. Coherent Expanded Aerogels and Jellies. *Nature* **1931**, *127*, 741.

22. Cao, B.; Adutwum, L. A.; Oilnyk, A. O.; Luber, E. J.; Olsen, B. C.; Mar, A.; Buriak, J. M. How to Optimize Materials and Devices *via* Design of Experiments and Machine Learning. *ACS Nano* **2018**, *12*, 7434–7444.

23. Maleki, H.; Durães, L.; Portugal, A. Development of Mechanically Strong Ambient Pressure Dried Silica Aerogels with Optimized Properties. *J. Phys. Chem. C* **2015**, *119*, 7689−7703.

24. Meador, M. A. B.; Capadona, L. A.; MacCorkle, L.; Papadopoulos, D. S.; Leventis, N. Structure-Property Relationships in Porous 3D Nanostructures as a Function of Preparation Conditions: Isocyanate Cross-Linked Silica Aerogels. *Chem. Mater.* **2007**, *19*, 2247–2260.

25. Rege, A.; Preibisch, I.; Schestakow, M.; Ganesan, K.; Gurikov, P.; Milow, B.; Smirnova, I.; Itskov, M. Correlating Synthesis Parameters to Morphological Entities: Predictive Modeling of Biopolymer Aerogels. *Materials* **2018**, *11*, 1670.

26. Tripathi, A.; Parsons, G. N.; Khan, S. A.; Rojas, O. J. Synthesis of Organic Aerogels with Tailorable Morphology and Strength by Controlled Solvents Swelling Following Hansen Solubility. *Sci. Rep.* **2018**, *8*, 2106.

27. Leventis, N.; Sotiriou-Leventis, C.; Chandrasekaran, N.; Mulik, S.; Larimore, Z. J.; Lu, H.; Churu, G.; Mang, J. T. Multifunctional Polyurea Aerogels from Isocyanates and Water. A Structure-Property Case Study. *Chem. Mater.* **2010**, *22*, 6692–6710.

28. Weigold, L.; Mohite, D. P.; Mahadik-Khanolkar, S.; Leventis, N.; Reichenauer, G. Correlation of Microstructure and Thermal Conductivity in Nanoporous Solids: The Case of Polyurea Aerogels Synthesized from an Aliphatic Triisocyanate and Water. *J. Non-Cryst. Solids* **2013**, *368*, 105–111.

29. Yang, Y.; Jiang, X.; Zhu, X.; Kong, X. Z. A Facile Pathway to Polyurea Nanofiber Fabrication and Polymer Morphology Control in Copolymerization of Oxydianiline and Toluene Diisocyanate in Acetone. *RSC Adv.* **2015**, *5*, 7426–7432.

30. Leventis, N.; Sotiriou-Leventis, C.; Saeed, A. M.; Donthula, S.; Majedi Far, H.; Rewatkar, P. M.; Kaiser, H.; Robertson, J. D.; Lu, H.; Churu, G. Nanoporous Polyurea from a Triisocyanate and Boric Acid: A Paradigm of a General Reaction Pathway for Isocyanates and Mineral Acids. *Chem. Mater.* **2016**, *28*, 67–78.

31. Chriti, D.; Raptopoulos, G.; Papastergiou, M.; Paraskevopoulou, P. Millimeter-Size Spherical Polyurea Aerogels Beads with Narrow Size Distribution. *Gels* **2018**, *4*, 66.

32. Jiang, X.; Bashir, M. S.; Zhang, F.; Xiang Zheng Kong, X. Z. Formation and Shape Transition of Porous Polyurea of Exotic Forms Through Interfacial Polymerization of Toluene Diisocyanate in Aqueous Solution of Ethylenediamine and their Characterization. *Eur. Polym. J.* **2018**, *109*, 93–100.

33. Wu, C.; Taghvaee, T.; Wei, C.; Ghasemi, A.; Chen, G.; Leventis, N.; Gao, W. Multi-Scale Progressive Failure Mechanism and Mechanical Properties of Nanofibrous Polyurea Aerogels. *Soft Matter* **2018**, *14*, 7801–7808.

34. Ashby, M. F. The Properties of Foams and Lattices. *Phil. Trans. R. Soc. A* **2006**, *364*, 15–30.

35. Montgomery, D. C. *Design and Analysis of Experiments*. John Wiley & Sons: New York, 2006.

36. Hansen, C. M. *Hansen Solubility Parameters: A User's Handbook*. CRC Press, Boca Raton, Florida, 2007.

37. Zhu, Z.; Snellings, G. M. B. F.; Koebel, M. M.; Malfait, W. J. Superinsulating Polyisocyanate Based Aerogels: A Targeted Search for the Optimum Solvent System. *ACS Appl. Mater. Interfaces* **2017**, *9*, 18222–18230.

38. Donthula, S.; Mandal, C.; Schisler, J.; Leventis, T.; Meador, M. A. B.; Sotiriou-Leventis, C. Leventis, N. Nanostructured-Dependent Marcus-Type Correlation of the Shape Recovery Rate and the Young's Modulus in Shape Memory Polymer Aerogels. *ACS Appl. Mater. Interfaces* **2018**, *10*, 23321−23334.

39. Ma, M.; Hill, R. M.; Rutledge, G. C. A Review of Recent Results on Superhydrophobic Materials Based on Micro- and Nanofibers. *J. Adhes. Sci. Technol*. **2008**, *22*, 1799−1817.

40. Wenzel, R. N. Resistance of Solid Surfaces to Wetting by Water. *Ind. Eng. Chem.* **1935**, *40*, 546–551.

41. Feng, L.; Zhang, Y.; Xi, J.; Zhu, Y.; Wang, N.; Xia, F.; Jiang, L. Petal Effect: A Superhydrophobic State with High Adhesive Force. *Langmuir* **2008**, *24*, 4114–4119.

42. Barthlott, W.; Neinhuis, C. Purity of the Sacred Lotus or Escape from Contamination in Biological Surfaces. *Planta* **1997**, *202*, 1–8.

43. Cassie, A. B. D.; Baxter, S. Wettability of Porous Surfaces. *Trans. Faraday Soc.* **1944**, *40*, 546–551.

44. Sas, I.; Gorga, R. E.; Joins, J. A.; Thoney, K. A. Literature Review on Superhydrophobic Self-Cleaning Surfaces Produced by Electrospinning. *J. Polym. Sci., Part B: Polym. Phys.* **2012**, *50*, 824–845.

45. Leventis, N.; Sotiriou-Leventis, C.; Mulik, S.; Dass, A.; Schnobrich, J.; Hobbs, A.; Fabrizio, E. F.; Luo, H.; Churu, G.; Zhang, Y.; Lu, H. Polymer Nanoencapsulated Mesoporous Vanadia with Unusual Ductility at Cryogenic Temperatures. *J. Mater. Chem.* **2008,** *18*, 2475–2482.

46. Katti, A.; Shimpi, N.; Roy, S.; Lu, H.; Fabrizio, E. F.; Dass, A.; Capadona, L. A.; Leventis, N. Chemical, Physical and Mechanical Characterization of Isocyanate-Crosslinked Amine-Modified Silica Aerogels. *Chem. Mater.* **2006**, *18*, 285–296.

47. Leventis, N.; Vassilaras, P.; Fabrizio, E. F.; Dass, A. Polymer Nanoencapsulated Rare Earth Aerogels: Chemically Complex but Stoichiometrically Similar Core-Shell Superstructures with Skeletal Properties of Pure Compounds. *J. Mater. Chem.* **2007**, *17*, 1502–1508.

48. Chidambareswarapattar, C.; McCarver, P. M.; Luo, H.; Lu, H.; Sotiriou-Leventis, C.; Leventis, N. Fractal Multiscale Nanoporous Polyurethanes: Flexible to Extremely Rigid Aerogels from Multifunctional Small Molecules. *Chem. Mater.* **2013**, *25*, 3205–3224.

49. Bang, A.; Buback, C.; Sotiriou-Leventis, C.; Leventis, N. Flexible Aerogels from Hyperbranched Polyurethanes: Probing the Role of Molecular Rigidity with Poly(urethane acrylates) *versus* Poly(urethane norbornenes). *Chem. Mater.* **2014**, *26*, 6979–6993.

50. Thomas, R. R.; Buchwalter, S. L.; Buckwalter, L. P.; Chao, T. H. Organic Chemistry on a Polyimide Surface. *Macromolecules* **1992**, *25*, 4559-4568.

51. Yoon, S. C.; Ratner, B. D. Surface Structure of Segmented Poly(ether urethanes) and Poly(ether urethane ureas) with Various Perfluoro Chain Extenders. An X-ray Photoelectron Spectroscopic Investigation. *Macromolecules* **1986**, *19*, 1068–1079.

52. See for example: Ogawa, T.; Dibg, B.; Sone, Y.; Shiratori, S. Super-Hydrophobic Surfaces of Layer-by-Layer Structured Film Coated Electrospun Nanofibrous Membranes. *Nanotechnology* **2007**, *18*, 165607–165615.

53. Xiong, J.-Y.; Narayanan, J.; Liu, X.-Y.; Chong, T. K.; Chen, S. B.; Chung, T.-S. Topology Evolution and Gelation Mechanism of Agarose Gel. *J. Phys. Chem. B* **2005**, *109*, 5638–5643.

54. Gomez-Solano, J. R.; Blickle, V.; Bechinger, C. Nucleation and Growth of Thermoreversible Polymer Gels. *Phys. Rev. E* **2013**, *87*, 012308.

55. Nakanishi, K.; Tanaka, N. Sol-Gel with Phase Separation. Hierarchically Porous Materials Optimized for High-Performance Liquid Chromatography Separations. *Acc. Chem. Res.* **2007**, *40*, 863−873.

56. Nakanishi, K. Pore Structure Control of Silica Gels Based on Phase Separation. *J. Porous Mater.* **1997**, *4*, 67−112.

57. Kanamori, K.; Nakanishi, K.; Hanada, T. Rigid Macroporous Poly(divinylbenzene) Monoliths with a Well-Defined Bicontinuous Morphology Prepared by Living Radical Polymerization. *Adv. Mater.* **2006**, *18*, 2407−2411.

58. Parker, W. J.; Jenkins, R. J.; Butler, C. P.; Abbott, G. L. Flash Method of Determining Thermal Diffusivity, Heat Capacity, and Thermal Conductivity. *J. Appl. Phys.* **1961**, *32*, 1679–1684.

59. Zarr, R. R.; Pintar, A. L. Standard Reference Materials: SRM 1453, Expanded Polystyrene Board, for Thermal Conductivity from 281 K to 313K. NIST Special Publication **2012**, 260–175.

60. Lu, X.; Arduini-Schuster, M. C.; Kuhn, J.; Nilsson, O.; Fricke, J.; Pekala, R. W. Thermal Conductivity of Monolithic Organic Aerogels. *Science* **1992**, *255*, 971–972.

61. Reichenauer, G.; Heinemann, U.; Ebert, H.-P. Relationship between Pore Size and the Gas Pressure Dependence of the Gaseous Thermal Conductivity. *Colloids Surf., A* **2007**, *300*, 204–210.

SUPPORTING INFORMATION

APPENDIX I. MATERILAS DESIGN AND FORMULATIONS OF ALL SAMPLES

Formulation of polyurea aerogels: Polyurea aerogel samples were prepared using response surface methodology (RSM), that is, a statistical method for representing the domain of the controllable input parameters (*i.e.*, the independent or explanatory variables) with the minimum number of samples. RSM allows placing samples strategically within the domain of the explanatory variables in a way that minimizes the fitting error of properties of interest to the independent variables.[S.R.1] In this study, the explanatory variables within each gelation solvent were three: (a) the triisocyanate monomer concentration (represented by [ISO]); (b) the mol ratio of water to triisocyanate (represented by [H_2O]); and, (c) the weight percent of the catalyst in the sol (represented by [Et_3N]). Those variables were set at five levels each, between respective lowest and highest values that were determined in a preliminary pilot study. The specific placement of the samples at those five levels was determined with a Central Composite Rotatable Design (CCRD) model that uses spherical symmetry for the position of the samples around a central point (coded as 0), which is set at the common middle of the range of the three independent variables.[S.R.2] The CCRD model has been developed with an anticipated quadratic relationship between the properties of the samples and the exploratory variables. In addition to the central point, a five-level CCRD borrows two levels from a full factorial design, at distances ±1 from the central point, and superimposes them with two axial points per independent variable, which are placed at symmetric positions, ±α, relative to the common central point. The CCRD sphere inscribes a cube of a full factorial design and therefore it touches the cube at eight (= 2^n) points, where *n* is the number of independent variables; in our case n=3. In turn, in order to respect the rotatability of the design, therefore

based on simple geometry, α is calculated as equal to $(2^n)^{1/4}$; therefore, in our case $\alpha = 2^{3/4} = 1.682$. In summary, the total number of samples that need to be prepared according to CCRD is given as the sum of 2^n factorial runs, plus 2n axial runs, plus n_c center runs ($2^n + 2n + n_c$). In CCRD, $n_c = 2$: one central point plus one repeat run; therefore, the total number of samples was equal to 16. The five levels of each factor (that is, each independent variable in the coded CCRD space) are tabulated in Part A of Table S.I.1. In turn, Part B of Table S.I.1 matches the upper and lower limits of the coded variables with the experimental limits of the independent variables from the pilot study, and places proportionally the composition of the rest of the experimental samples to be prepared at the appropriate levels. However, the CCRD model of Table S.I.1 was not enough to capture the sensitivity of material properties, and specifically the variability of the sample morphology at the high-end of [ISO]. That is, the CCRD model places only a single star point at the highest [ISO]-level (Level 5), but empirically we found out that at Level 5 the sample micromorphology is very sensitive to [H_2O] and [Et_3N]. On the other hand, micromorphology is not very sensitive to those two variables at the lower [ISO] concentration (Level 1). Therefore, the CCRD model of Table S.I.1 was enhanced asymmetrically with ten additional formulations (also referred to as "runs") borrowed from a full factorial model.[S.R.3] Eight of those runs were placed at extreme positions within Levels 4 and 5, and two additional formulations were placed at extreme positions of Level 1. Figure S.I.1 shows the CCRD as derived from Table S.I.1, Part B, enhanced with the ten additional runs pointed at with arrows. The entire design, that is the CCRD with all extra points, is summarized in Table S.I.2.

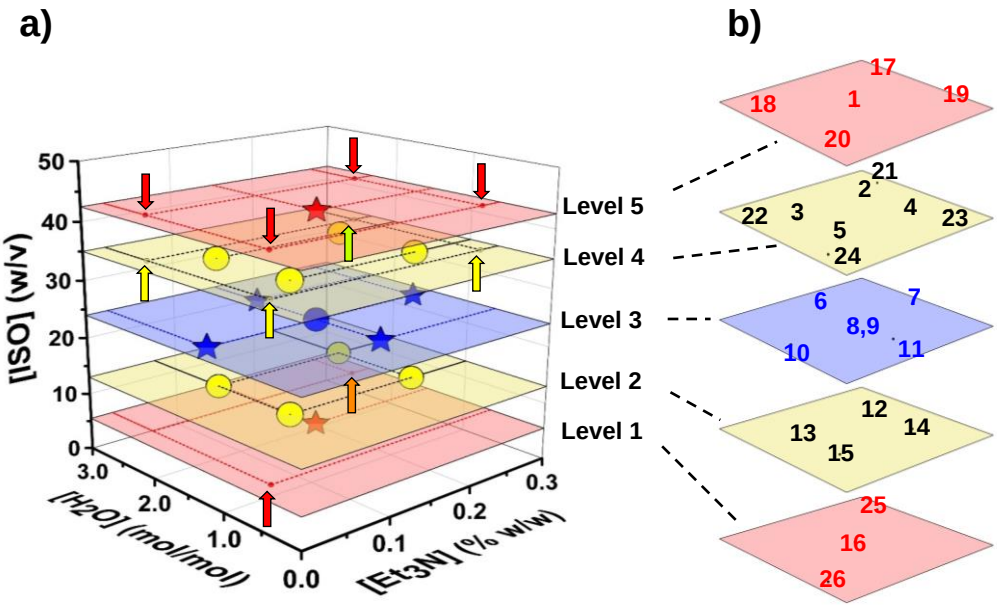

Figure S.I.1. a) Samples required by a CCRD with three variables at five levels each. Factorial and star points are shown explicitly. Arrows point at the 10 additional runs as described in the text. b) Run numbers (refer also to Table S.I.2).

Table S.I.1. Range and Levels of the Independent Variables in Coded and Actual (Experimental) Space.

Part A.	Levels of factors (independent variables) in CCRD					
Factors	**Symbol**	**Coded independent variables (factors) at 5 levels each**				
x_1	[ISO]	−1.682	−1.000	0.000	1.000	+1.682
x_2	[H_2O]	−1.682	−1.000	0.000	1.000	+1.682
x_3	[Et_3N]	−1.682	−1.000	0.000	1.000	+1.682
Part B.	Experimental Range and Levels of Samples to be Prepared					
Independent variables	**In unit of …**	**Level 1 (lowest)**	**Level 2**	**Level 3**	**Level 4**	**Level 5 (highest)**
[ISO]	grams	5.50	13.0	24.0	35.0	42.5
[H_2O]	mol:mol	0.659	1.000	1.500	2.000	2.341
[Et_3N]	% w/w in sol	0.024	0.075	0.15	0.225	0.276

The complete experimental design of Figure S.I.1 was applied eight times in eight different solvents: acetonitrile (ACN), nitromethane (NM), propylene carbonate (PC), acetone (ACE), tetrahydrofuran (THF), ethyl acetate (EA), 2-butanone (2-BU), and

dimethylformamide (DMF), for a total of 208 possible runs. Those gelation solvents were selected based on their Hansen Solubility Parameters (HSPs) (Table S.I.3).[S.R.4] Table S.I.3 includes also the HSPs of the mixed solvents used in this study (see Appendix VI). Subsequently, the exact formulations of all samples in all solvents, along with the gelation times, and the Hansen Solubility Parameters of all sols are given in Tables S.I.4 to S.I.12.

Table S.I.2. Design of Experiments (DoE): Central Composite Rotatable Design (CCRD) for the Synthesis of PUA Aerogels.[a]

DoE run No.	**ISO Level No.** [b]	**[ISO] (w/v)** [c]	**[H_2O] (mol/mol)** [d]	**[Et_3N] (% w/w)** [e]
1	5	42.500	1.500	0.150
2	4	35.000	2.000	0.225
3	4	35.000	2.000	0.075
4	4	35.000	1.000	0.225
5	4	35.000	1.000	0.075
6	3	24.000	2.341	0.150
7	3	24.000	1.500	0.276
8	3	24.000	1.500	0.150
9	3	24.000	1.500	0.150
10	3	24.000	1.500	0.024
11	3	24.000	0.659	0.150
12	2	13.000	2.000	0.225
13	2	13.000	2.000	0.075
14	2	13.000	1.000	0.225
15	2	13.000	1.000	0.075
16	1	5.500	1.500	0.150
Additional Runs [a]				
17	5	42.500	2.341	0.276
18	5	42.500	2.341	0.024
19	5	42.500	0.659	0.276
20	5	42.500	0.659	0.024
21	4	35.000	2.341	0.276
22	4	35.000	2.341	0.024
23	4	35.000	0.659	0.276
24	4	35.000	0.659	0.024
25	1	5.500	2.341	0.276
26	1	5.500	0.659	0.024

[a] Additional runs were added to the CCRD model of Table S.I.1 in order to capture the sensitivity of the nanostructure and of other material properties to [H_2O] and [Et_3N] at [ISO] Level 5 (see text).

Table S.I.3. Hansen Solubility Parameters of Gelation Solvents and Other Sol Precursors.[a]

	δP	δH	δD
Single Solvents			
Acetonitrile (ACN)	18.0	6.1	15.3
Nitromethane (NM)	18.8	5.1	15.8
Propylene carbonate (PC)	18.0	4.1	20.0
Acetone (ACE)	10.4	7.0	15.5
Tetrahydrofuran (THF)	5.7	8.0	16.8
Ethyl acetate (EA)	5.3	7.2	15.8
2-Butanone (2-BU)	9.0	5.1	16.0
Dimethylformamide (DMF)	13.7	11.3	17.4
Binary Solvent Systems [b]			
ACN-NM	18.4	5.6	15.6
ACN-PC	18.0	5.1	17.7
ACN-AN	14.2	6.6	15.4
ACE-EA	7.9	7.1	15.7
EA-DMF	9.5	9.3	16.6
ACN-DMF	15.9	8.7	16.4
NM-2-BU	13.9	5.1	15.9
PC-2-BU	13.5	4.6	18.0
Monomers and Catalyst			
ISO (Desmodur N3300A monomer) [c]	6.8	1.9	15.4
H_2O	16.0	42.3	15.6
NEt_3	3.7	1.9	14.6

[a] All Hansen Solubility Parameters (HSPs) in units of $MPa^{1/2}$.

[b] Binary solvent systems in 1:1 v/v. HSPs were calculated as averages of the corresponding values of each solvent.

[c] The Hansen Solubility Parameters of Desmodur N3300A triisocyanate were calculated using the HSPiP software package (purchased from https://www.hansen-solubility.com/buy-HSPiP-software.php) as follows: Using a ChemDraw file of Desmodur N3300A we created a SMILE file of Desmodur N3300A using the free online service Chem Spider (http://www.chemspider.com). The SMILE file was introduced to the HSPiP software and the HSPs were obtained. The reliability of those values was assessed as follows: Together with the HSP values, the HSPiP software also outputs the refractive index (1.524) and the density (1.176 g cm^{-3}) of Desmodur N3300A. Both of those two values agreed well with the corresponding experimental values: 1.478 and 1.170 g cm^{-3}, respectively.

Table S.I.4. Sol Formulations of PUA Aerogels Prepared in Acetonitrile According to the CCRD Model of Table S.I.2.

DoE run [Level] [b] No.	ISO (Desmodur N3300A)			H_2O				Et_3N			
	mass (g)	volume (mL)	[ISO] (M)	mass (mg)	volume (mL)	$[H_2O]$ (M)	$[H_2O]/[ISO]$ (mol/mol)	mass (mg)	volume (mL)	$[Et_3N]$ (M)	Et_3N (% w/w)
1 [5]	42.500	36.325	0.6346	2.276	2.276	0.9519	1.500	0.178	0.246	0.0133	0.150
2 [4]	35.000	29.915	0.5477	2.499	2.499	1.095	2.000	0.251	0.346	0.0196	0.225
3 [4]	35.000	29.915	0.5487	2.499	2.499	1.097	2.000	0.0836	0.115	0.00653	0.0750
4 [4]	35.000	29.915	0.5532	1.250	1.250	0.5532	1.000	0.248	0.343	0.0196	0.225
5 [4]	35.000	29.915	0.5542	1.250	1.250	0.5542	1.000	0.0827	0.114	0.00652	0.0750
6 [3]	24.000	20.513	0.4079	2.006	2.006	0.9548	2.341	0.150	0.207	0.0127	0.150
7 [3]	24.000	20.513	0.4098	1.285	1.285	0.6147	1.500	0.274	0.379	0.0233	0.276
8 [3]	24.000	20.513	0.4104	1.285	1.285	0.6156	1.500	0.149	0.205	0.0127	0.150
9 [3]	24.000	20.513	0.4104	1.285	1.285	0.6156	1.500	0.149	0.205	0.0127	0.150
10 [3]	24.000	20.513	0.4110	1.285	1.285	0.6165	1.500	0.0238	0.0328	0.00203	0.0240
11 [3]	24.000	20.513	0.4130	0.565	0.565	0.2721	0.659	0.148	0.204	0.0127	0.150
12 [2]	13.000	11.111	0.2426	0.928	0.928	0.4851	2.000	0.198	0.273	0.0184	0.225
13 [2]	13.000	11.111	0.2430	0.928	0.928	0.4859	2.000	0.0659	0.0909	0.00614	0.0750
14 [2]	13.000	11.111	0.2436	0.464	0.464	0.2436	1.000	0.197	0.272	0.0184	0.225
15 [2]	13.000	11.111	0.2440	0.464	0.464	0.2440	1.000	0.0656	0.0904	0.00613	0.0750
16 [1]	5.500	4.700	0.1100	0.295	0.295	0.1650	1.500	0.120	0.165	0.0119	0.150
Additional Runs [c]											
17 [5]	42.500	36.325	0.6276	3.552	3.552	1.469	2.341	0.332	0.458	0.0244	0.276
18 [5]	42.500	36.325	0.6295	3.552	3.552	1.474	2.341	0.0288	0.0397	0.00212	0.0240
19 [5]	42.500	36.325	0.6398	1.000	1.000	0.4216	0.659	0.325	0.448	0.0244	0.276
20 [5]	42.500	36.325	0.6418	1.000	1.000	0.4229	0.659	0.0282	0.0389	0.00212	0.0240
21 [4]	35.000	29.915	0.5455	2.925	2.925	1.277	2.341	0.309	0.427	0.0240	0.276
22 [4]	35.000	29.915	0.5472	2.925	2.925	1.281	2.341	0.0268	0.0370	0.00209	0.0240
23 [4]	35.000	29.915	0.5547	0.824	0.824	0.3656	0.659	0.304	0.419	0.0240	0.276
24 [4]	35.000	29.915	0.5564	0.824	0.824	0.3667	0.659	0.0263	0.0363	0.00209	0.0240
25 [1]	5.500	4.700	0.1097	0.460	0.460	0.2568	2.341	0.221	0.305	0.0220	0.276
26 [1]	5.500	4.700	0.1104	0.129	0.129	0.07273	0.659	0.0191	0.0263	0.00191	0.0240

[a] CCRD: Runs 1–16 (including one replicate: Run 9). All sols were made using 94 mL acetonitrile (73.884 g, based on $\rho_{acetonitrile}$ = 0.786 g cm^{-3}).

[b] "[Level]" refers to the 5 concentration levels of [ISO], (see Figure S.I.1).

[c] Extra samples (Runs 17–26) were added to the original CCRD to make the model stronger (see text).

Table S.I.5. Hansen Solubility Parameters (HSPs) and Gelation Times of Sols Prepared in Acetonitrile.

DoE run [Level] [a] No.	Sols Prepared in Acetonitrile					
	mass [b] (g)	volume [c] (mL)	gelation time	δP_{sol} [d] (MPa)	δH_{sol} [d] (MPa)	δD_{sol} [d] (MPa)
1 [5]	118.838	132.847	1 min	14.883 [0.480]	5.560 [− 0.508]	15.332 [− 0.981]
2 [4]	111.635	126.760	1 min	15.288 [0.543]	5.824 [− 0.435]	15.328 [− 0.983]
3 [4]	111.467	126.529	15 min	15.303 [0.545]	5.829 [− 0.434]	15.329 [− 0.983]
4 [4]	110.382	125.507	5 min	15.293 [0.544]	5.456 [− 0.537]	15.341 [− 0.977]
5 [4]	110.216	125.278	45 min	15.307 [0.546]	5.460 [− 0.536]	15.342 [− 0.977]
6 [3]	100.040	116.726	10 min	15.981 [0.651]	5.972 [− 0.394]	15.322 [− 0.986]
7 [3]	99.444	116.177	7 min	15.967 [0.649]	5.746 [− 0.457]	15.320 [− 0.987]
8 [3]	99.318	116.004	30 min	15.981 [0.651]	5.751 [− 0.455]	15.320 [− 0.987]
9 [3]	99.318	116.004	45 min	15.981 [0.651]	5.751 [− 0.455]	15.320 [− 0.987]
10 [3]	99.193	115.831	3 h	15.996 [0.653]	5.755 [− 0.454]	15.321 [− 0.986]
11 [3]	98.597	115.282	1 h	15.982 [0.651]	5.529 [− 0.517]	15.319 [− 0.987]
12 [2]	88.010	106.313	40 min	16.795 [0.778]	5.983 [− 0.391]	15.327 [− 0.984]
13 [2]	87.878	106.130	3 h	16.810 [0.780]	5.987 [− 0.390]	15.328 [− 0.983]
14 [2]	87.545	105.847	1 h, 30 min	16.787 [0.777]	5.795 [− 0.443]	15.310 [− 0.991]
15 [2]	87.414	105.666	3 h, 45 min	16.802 [0.779]	5.800 [− 0.442]	15.311 [− 0.991]
16 [1]	79.798	99.161	4 h	17.435 [0.878]	6.001 [− 0.386]	15.290 [− 1.000]
Additional Runs						
17 [5]	120.268	134.335	1 min	14.866 [0.477]	5.889 [− 0.417]	15.318 [− 0.988]
18 [5]	119.965	133.917	45 min	14.911 [0.484]	5.939 [− 0.403]	15.335 [− 0.980]
19 [5]	117.709	131.773	20 min	14.864 [0.477]	5.222 [− 0.602]	15.329 [− 0.983]
20 [5]	117.412	131.364	4 h	14.900 [0.483]	5.232 [− 0.600]	15.345 [− 0.975]
21 [4]	112.119	127.267	1 min	15.275 [0.541]	5.931 [− 0.405]	15.314 [− 0.989]
22 [4]	111.836	126.877	1 h	15.311 [0.547]	5.941 [− 0.402]	15.331 [− 0.982]
23 [4]	110.011	125.157	20 min	15.281 [0.542]	5.341 [− 0.569]	15.325 [− 0.984]
24 [4]	109.734	124.774	5 h	15.298 [0.545]	5.345 [− 0.568]	15.326 [− 0.984]
25 [1]	80.065	99.465	2 h, 50 min	17.435 [0.878]	6.075 [− 0.365]	15.305 [− 0.993]
26 [1]	79.533	98.857	7 h	17.460 [0.881]	5.935 [− 0.404]	15.305 [− 0.993]

[a] "[Level]" refers to the 5 levels of the [ISO] concentration.

[b] Total mass of N3300A monomer, water, catalyst and mass of 94 mL acetonitrile.

[c] Total volume of N3300A monomer, water, catalyst and 94 mL acetonitrile.

[d] First number: actual values; numbers in [brackets]: orthogonally-transformed global values (*i.e.*, considering all runs in all solvents simultaneously). The three Hansen Solubility Parameters (HSPs) of the sol, δP_{sol}, δH_{sol} and δD_{sol} (represented herewith collectively and individually by the symbol δ_{sol}) were calculated *via*:

$$\delta_{sol} = \delta_{acetonitrile} * X_{acetonitrile} + \delta_{N300A} * X_{N3300A} + \delta_{H2O} * X_{H2O} + \delta_{Et3N} * X_{Et3N}$$

where X_i is the volume fraction of component "i" in the sol and,

$\delta P_{acetonitrile} = 18.0$	$\delta H_{acetonitrile} = 6.1$	$\delta D_{acetonitrile} = 15.3$
$\delta P_{H2O} = 16.0$	$\delta H_{H2O} = 42.3$	$\delta D_{H2O} = 15.6$
$\delta P_{Et3N} = 3.7$	$\delta H_{Et3N} = 1.9$	$\delta D_{Et3N} = 14.6$
$\delta P_{N3300A} = 6.8$	$\delta H_{N3300A} = 1.9$	$\delta D_{N3300A} = 15.4$

Table S.I.6. Sol Formulations of PUA Aerogels Prepared in Nitromethane According to the CCRD Model of Table S.I.2.[a]

DoE run [Level] [b] No.	ISO (Desmodur N3300A)			H_2O				Et_3N			
	mass (g)	volume (mL)	[ISO] (M)	mass (mg)	volume (mL)	[H_2O] (M)	[H_2O]/[ISO] (mol/mol)	mass (mg)	volume (mL)	[Et_3N] (M)	Et_3N (% w/w)
1 [5]	42.500	36.325	0.6343	2.276	2.276	0.9514	1.500	0.228	0.315	0.0170	0.150
2 [4]	35.000	29.915	0.5473	2.499	2.499	1.095	2.000	0.326	0.450	0.0254	0.225
3 [4]	35.000	29.915	0.5486	2.499	2.499	1.097	2.000	0.109	0.150	0.00848	0.0750
4 [4]	35.000	29.915	0.5527	1.250	1.250	0.5527	1.000	0.323	0.446	0.0254	0.225
5 [4]	35.000	29.915	0.5540	1.250	1.250	0.5540	1.000	0.108	0.148	0.00849	0.0750
6 [3]	24.000	20.513	0.4076	2.006	2.006	0.9542	2.341	0.200	0.276	0.0169	0.150
7 [3]	24.000	20.513	0.4093	1.285	1.285	0.6140	1.500	0.367	0.506	0.0311	0.276
8 [3]	24.000	20.513	0.4101	1.285	1.285	0.6152	1.500	0.199	0.274	0.0169	0.150
9 [3]	24.000	20.513	0.4101	1.285	1.285	0.6152	1.500	0.199	0.274	0.0169	0.150
10 [3]	24.000	20.513	0.4110	1.285	1.285	0.6164	1.500	0.0318	0.0439	0.00271	0.0240
11 [3]	24.000	20.513	0.4127	0.565	0.565	0.2720	0.659	0.198	0.273	0.0170	0.150
12 [2]	13.000	11.111	0.2423	0.928	0.928	0.4846	2.000	0.273	0.377	0.0254	0.225
13 [2]	13.000	11.111	0.2429	0.928	0.928	0.4858	2.000	0.0909	0.125	0.00846	0.0750
14 [2]	13.000	11.111	0.2434	0.464	0.464	0.2434	1.000	0.272	0.375	0.0254	0.225
15 [2]	13.000	11.111	0.2440	0.464	0.464	0.2440	1.000	0.0905	0.125	0.00846	0.0750
16 [1]	5.500	4.700	0.1099	0.295	0.295	0.1649	1.500	0.170	0.234	0.0169	0.150
Additional Runs [c]											
17 [5]	42.500	36.325	0.6270	3.552	3.552	1.468	2.341	0.424	0.585	0.0312	0.276
18 [5]	42.500	36.325	0.6295	3.552	3.552	1.474	2.341	0.0368	0.0507	0.00271	0.0240
19 [5]	42.500	36.325	0.6391	1.000	1.000	0.4212	0.659	0.417	0.575	0.0312	0.276
20 [5]	42.500	36.325	0.6417	1.000	1.000	0.4229	0.659	0.0362	0.0499	0.00272	0.0240
21 [4]	35.000	29.915	0.5450	2.925	2.925	1.276	2.341	0.402	0.554	0.0311	0.276
22 [4]	35.000	29.915	0.5471	2.925	2.925	1.281	2.341	0.0348	0.0480	0.00271	0.0240
23 [4]	35.000	29.915	0.5542	0.824	0.824	0.3652	0.659	0.396	0.546	0.0312	0.276
24 [4]	35.000	29.915	0.5564	0.824	0.824	0.3666	0.6590	0.0343	0.0473	0.00272	0.0240
25 [1]	5.500	4.700	0.1095	0.460	0.460	0.2564	2.341	0.313	0.432	0.0311	0.276
26 [1]	5.500	4.700	0.1103	0.129	0.129	0.07272	0.659	0.0271	0.0373	0.00271	0.0240

[a] CCRD: Runs 1–16 including one replicate (Run 9). All sols were made using 94 mL nitromethane (107.16 g, based on $\rho_{\text{nitromethane}}$= 1.140 g cm^{-3}).
[b] "[Level]" refers to the 5 concentration levels of [ISO], (see Figure S.I.1).
[c] Extra samples (Runs 17–26) were added to the original CCRD to make the model stronger (see text).

Table S.I.7. Hansen Solubility Parameters (HSPs) and Gelation Times of Sols Prepared in Nitromethane.

DoE run [Level] [a] No.	Sols Prepared in Nitromethane					
	mass [b] (g)	volume [c] (mL)	gelation time	δP_{sol} [d] (MPa)	δH_{sol} [d] (MPa)	δD_{sol} [d] (MPa)
1 [5]	152.164	132.916	1 min	15.446 [0.568]	4.852 [− 0.705]	15.685 [− 0.824]
2 [4]	144.986	126.864	1 min	15.886 [0.636]	5.084 [− 0.641]	15.714 [− 0.811]
3 [4]	144.768	126.564	10 min	15.897 [0.638]	5.086 [− 0.640]	15.700 [− 0.817]
4 [4]	143.733	125.610	5 min	15.871 [0.634]	4.701 [− 0.747]	15.699 [− 0.818]
5 [4]	143.517	125.313	12 min	15.889 [0.637]	4.704 [− 0.746]	15.701 [− 0.817]
6 [3]	133.366	116.795	2 min	16.610 [0.749]	5.163 [− 0.619]	15.724 [− 0.806]
7 [3]	132.812	116.304	3 min	16.600 [0.747]	4.933 [− 0.683]	15.723 [− 0.807]
8 [3]	132.644	116.073	2 min	16.615 [0.750]	4.936 [− 0.682]	15.725 [− 0.806]
9 [3]	132.644	116.073	3 min	16.615 [0.750]	4.936 [− 0.682]	15.725 [− 0.806]
10 [3]	132.477	115.842	55 min	16.645 [0.754]	4.943 [− 0.680]	15.727 [− 0.805]
11 [3]	131.923	115.350	17 min	16.620 [0.751]	4.710 [− 0.745]	15.725 [− 0.806]
12 [2]	121.361	106.416	10 min	17.488 [0.886]	5.094 [− 0.638]	15.768 [− 0.787]
13 [2]	121.179	106.165	28 min	17.519 [0.891]	5.101 [− 0.636]	15.771 [− 0.786]
14 [2]	120.896	105.950	12 min	17.484 [0.885]	4.903 [− 0.691]	15.754 [− 0.793]
15 [2]	120.715	105.700	55 min	17.514 [0.890]	4.910 [− 0.689]	15.756 [− 0.792]
16 [1]	113.124	99.230	1 h, 45 min	18.197 [0.996]	5.055 [− 0.649]	15.778 [− 0.782]
Additional Runs						
17 [5]	153.636	134.462	1 min	15.423 [0.564]	5.189 [− 0.612]	15.667 [− 0.832]
18 [5]	153.249	133.928	1h	15.472 [0.572]	5.237 [− 0.598]	15.686 [− 0.823]
19 [5]	151.077	131.900	2 min	15.439 [0.567]	4.51 [− 0.800]	15.700 [− 0.817]
20 [5]	150.696	131.375	1 h, 30 min	15.472 [0.572]	4.516 [− 0.799]	15.703 [− 0.816]
21 [4]	145.487	127.394	3 min	15.870 [0.634]	5.194 [− 0.610]	15.698 [− 0.818]
22 [4]	145.120	126.888	40 min	15.904 [0.639]	5.200 [− 0.609]	15.701 [− 0.817]
23 [4]	143.379	125.284	5 min	15.867 [0.633]	4.586 [− 0.779]	15.699 [− 0.818]
24 [4]	143.018	124.785	1 h, 10 min	15.900 [0.638]	4.592 [− 0.778]	15.703 [− 0.816]
25 [1]	113.433	99.592	1 h, 15 min	18.177 [0.993]	5.126 [− 0.629]	15.777 [− 0.783]
26 [1]	112.816	98.867	1 h, 50 min	18.221 [1.000]	4.984 [− 0.669]	15.781 [− 0.781]

[a] "[Level]" refers to the 5 levels of the [ISO] concentration.

[b] Total mass of N3300A monomer, water, catalyst and mass of 94 mL nitromethane.

[c] Total volume of N3300A monomer, water, catalyst and 94 mL nitromethane.

[d] First number: actual values; numbers in [brackets]: orthogonally-transformed global values (*i.e.*, considering all runs in all solvents simultaneously). The three Hansen Solubility Parameters (HSPs) of the sol, δP_{sol}, δH_{sol} and δD_{sol} (represented herewith collectively and individually by the symbol δ_{sol}) were calculated *via*:

$$\delta_{sol} = \delta_{nitromethane} * X_{nitromethane} + \delta_{N3300A} * X_{N3300A} + \delta_{H2O} * X_{H2O} + \delta_{Et3N} * X_{Et3N}$$

where X_i is the volume fraction of component "i" in the sol and,

$\delta P_{nitromethane} = 18.8$ $\delta H_{nitromethane} = 5.1$ $\delta D_{nitromethane} = 15.8$

$\delta P_{H2O} = 16.0$ $\delta H_{H2O} = 42.3$ $\delta D_{H2O} = 15.6$

$\delta P_{Et3N} = 3.7$ $\delta H_{Et3N} = 1.9$ $\delta D_{Et3N} = 14.6$

$\delta P_{N3300A} = 6.8$ $\delta H_{N3300A} = 1.9$ $\delta D_{N3300A} = 15.4$

Table S.I.8. Sol Formulations of PUA Aerogels Prepared in Propylene Carbonate (PC) According to the CCRD Model of Table S.I.2.[a]

DoE run [Level] [b] No.	ISO (Desmodur N3300A)			H_2O				Et_3N			
	mass (g)	volume (mL)	[ISO] (M)	mass (mg)	volume (mL)	[H_2O] (M)	[H_2O]/[ISO] (mol/mol)	mass (mg)	volume (mL)	[Et_3N] (M)	Et_3N (% w/w)
1 [5]	42.500	36.325	0.6342	2.276	2.276	0.9513	1.500	0.237	0.327	0.0176	0.150
2 [4]	35.000	29.915	0.5472	2.499	2.499	1.094	2.000	0.339	0.467	0.0264	0.225
3 [4]	35.000	29.915	0.5485	2.499	2.499	1.097	2.000	0.113	0.156	0.00881	0.0750
4 [4]	35.000	29.915	0.5526	1.250	1.250	0.5526	1.000	0.336	0.464	0.0264	0.225
5 [4]	35.000	29.915	0.5540	1.250	1.250	0.5540	1.000	0.112	0.154	0.00882	0.0750
6 [3]	24.000	20.513	0.4076	2.006	2.006	0.9541	2.341	0.209	0.288	0.0176	0.150
7 [3]	24.000	20.513	0.4093	1.285	1.285	0.6139	1.500	0.382	0.527	0.0325	0.276
8 [3]	24.000	20.513	0.4101	1.285	1.285	0.6152	1.500	0.207	0.286	0.0177	0.150
9 [3]	24.000	20.513	0.4101	1.285	1.285	0.6152	1.500	0.207	0.286	0.0177	0.150
10 [3]	24.000	20.513	0.4110	1.285	1.285	0.6164	1.500	0.0331	0.0457	0.00283	0.0240
11 [3]	24.000	20.513	0.4127	0.565	0.565	0.2720	0.659	0.206	0.285	0.0177	0.150
12 [2]	13.000	11.111	0.2423	0.928	0.928	0.4846	2.000	0.286	0.394	0.0265	0.225
13 [2]	13.000	11.111	0.2429	0.928	0.928	0.4858	2.000	0.0951	0.131	0.00885	0.0750
14 [2]	13.000	11.111	0.2433	0.464	0.464	0.2433	1.000	0.285	0.393	0.0266	0.225
15 [2]	13.000	11.111	0.2440	0.464	0.464	0.2440	1.000	0.0948	0.131	0.00886	0.0750
16 [1]	5.500	4.700	0.1099	0.295	0.295	0.1649	1.500	0.178	0.246	0.0177	0.150
Additional Runs [c]											
17 [5]	42.500	36.325	0.6269	3.552	3.552	1.468	2.341	0.440	0.606	0.0323	0.276
18 [5]	42.500	36.325	0.6295	3.552	3.552	1.474	2.341	0.0381	0.0526	0.00281	0.0240
19 [5]	42.500	36.325	0.6390	1.000	1.000	0.4211	0.659	0.433	0.597	0.0324	0.276
20 [5]	42.500	36.325	0.6417	1.000	1.000	0.4229	0.659	0.0375	0.0518	0.00282	0.0240
21 [4]	35.000	29.915	0.5449	2.925	2.925	1.276	2.341	0.417	0.575	0.0324	0.276
22 [4]	35.000	29.915	0.5471	2.925	2.925	1.281	2.341	0.0362	0.0499	0.00282	0.0240
23 [4]	35.000	29.915	0.5541	0.824	0.824	0.3651	0.659	0.411	0.567	0.0324	0.276
24 [4]	35.000	29.915	0.5564	0.824	0.824	0.3666	0.659	0.0357	0.0492	0.00283	0.0240
25 [1]	5.500	4.700	0.1095	0.460	0.460	0.2564	2.341	0.329	0.453	0.0326	0.276
26 [1]	5.500	4.700	0.1103	0.129	0.129	0.07272	0.659	0.0284	0.0392	0.00284	0.0240

[a] CCRD: Runs 1–16 including one replicate (Run 9). All sols in 94 mL propylene carbonate (PC) (112.80 g, based on $\rho_{PC} = 1.200$ g cm^{-3}).
[b] "[Level]" refers to the 5 concentration levels of [ISO], (see Figure S.I.1).
[c] Extra samples (Runs 17–26) were added to the original CCRD to make the model stronger (see text).

Table S.I.9. Hansen Solubility Parameters (HSP) and Gelation Times of Sols Prepared in Propylene Carbonate.

DoE run [Level] [a] No.	Sols Prepared in Propylene Carbonate					
	mass [b] (g)	volume [c] (mL)	gelation time	δP_{sol} [d] (MPa)	δH_{sol} [d] (MPa)	δD_{sol} [d] (MPa)
1 [5]	157.813	132.927	1 min	14.880 [0.480]	4.144 [− 0.902]	18.659 [0.502]
2 [4]	150.638	126.881	1 min	15.292 [0.544]	4.342 [− 0.847]	18.830 [0.579]
3 [4]	150.412	126.569	5 min	15.303 [0.545]	4.343 [− 0.847]	18.821 [0.575]
4 [4]	149.386	125.628	1 min	15.272 [0.541]	3.952 [− 0.956]	18.845 [0.585]
5 [4]	149.162	125.319	1 min	15.289 [0.543]	3.954 [− 0.955]	18.851 [0.588]
6 [3]	139.015	116.806	1 min	15.966 [0.649]	4.358 [− 0.843]	19.105 [0.701]
7 [3]	138.468	116.325	2 min	15.953 [0.647]	4.124 [− 0.908]	19.121 [0.708]
8 [3]	138.293	116.084	3 min	15.967 [0.649]	4.126 [− 0.907]	19.127 [0.711]
9 [3]	138.293	116.084	4 min	15.967 [0.649]	4.126 [− 0.907]	19.127 [0.711]
10 [3]	138.119	115.844	1 h, 15 min	15.996 [0.653]	4.131 [− 0.906]	19.137 [0.715]
11 [3]	137.571	115.362	20 min	15.968 [0.649]	3.895 [− 0.971]	19.148 [0.720]
12 [2]	127.014	106.434	10 min	16.781 [0.776]	4.210 [− 0.884]	19.481 [0.869]
13 [2]	126.823	106.171	25 min	16.810 [0.780]	4.215 [− 0.882]	19.492 [0.874]
14 [2]	126.549	105.968	15 min	16.773 [0.774]	4.015 [− 0.938]	19.483 [0.870]
15 [2]	126.359	105.706	1 h	16.802 [0.779]	4.020 [− 0.937]	19.494 [0.875]
16 [1]	118.773	99.2412	3 h	17.439 [0.878]	4.107 [− 0.912]	19.760 [0.993]
Additional Runs						
17 [5]	159.292	134.484	1 min	14.863 [0.477]	4.489 [− 0.806]	18.607 [0.479]
18 [5]	158.891	133.930	15 min	14.911 [0.484]	4.535 [− 0.793]	18.635 [0.492]
19 [5]	156.733	131.921	5 min	14.850 [0.475]	3.792 [− 1.000]	18.679 [0.511]
20 [5]	156.338	131.377	50 min	14.900[0.483]	3.800 [− 0.998]	18.711 [0.526]
21 [4]	151.143	127.415	1 min	15.279 [0.542]	4.455 [− 0.816]	18.802 [0.566]
22 [4]	150.762	126.890	1 min	15.311 [0.547]	4.459 [− 0.815]	18.813 [0.571]
23 [4]	149.035	125.305	20 min	15.266 [0.540]	3.835 [− 0.988]	18.854 [0.589]
24 [4]	148.659	124.787	1 h	15.298 [0.545]	3.839 [− 0.987]	18.865 [0.594]
25 [1]	119.088	99.614	1 h	17.421 [0.875]	4.181 [− 0.892]	19.746 [0.987]
26 [1]	118.458	98.870	10 h	17.460 [0.881]	4.033 [− 0.933]	19.775 [1.000]

[a] "[Level]" refers to the 5 levels of the [ISO] concentration.

[b] Total mass of N3300A monomer, water, catalyst and mass of 94 mL propylene carbonate.

[c] Total volume of N3300A monomer, water, catalyst and 94 mL propylene carbonate.

[d] First number: actual values; numbers in [brackets]: orthogonally-transformed global values (*i.e.*, considering all runs in all solvents simultaneously). The three Hansen Solubility Parameters (HSPs) of the sol, δP_{sol}, δH_{sol} and δD_{sol} (represented herewith collectively and individually by the symbol δ_{sol}) were calculated *via*:

$$\delta_{sol} = \delta_{propylene\ carbonate} * X_{propylene\ carbonate} + \delta_{N3300A} * X_{N300A} + \delta_{H2O} * X_{H2O} + \delta_{Et3N} * X_{Et3N}$$

where X_i is the volume fraction of component "i" in the sol and,

$\delta P_{propylene\ carbonate} = 18.0$ $\delta H_{propylene\ carbonate} = 4.1$ $\delta D_{propylene\ carbonate} = 20.0$

$\delta P_{H2O} = 16.0$ $\delta H_{H2O} = 42.3$ $\delta D_{H2O} = 15.6$

$\delta P_{Et3N} = 3.7$ $\delta H_{Et3N} = 1.9$ $\delta D_{Et3N} = 14.6$

$\delta P_{N3300A} = 6.8$ $\delta H_{N3300A} = 1.9$ $\delta D_{N3300A} = 15.4$

Table S.I.10. Sol Formulations of PUA Aerogels Prepared in Acetone According to the CCRD Model of Table S.I.2.[a]

DoE run [Level] [b] No.	ISO (Desmodur N3300A)			H_2O				Et_3N			
	mass (g)	volume (mL)	[ISO] (M)	mass (mg)	volume (mL)	$[H_2O]$ (M)	$[H_2O]/[ISO]$ (mol/mol)	mass (mg)	volume (mL)	$[Et_3N]$ (M)	Et_3N (% w/w)
1 [5]	42.500	36.325	0.6346	2.276	2.276	0.9519	1.500	0.178	0.245	0.0132	0.150
2 [4]	35.000	29.915	0.5477	2.499	2.499	1.095	2.000	0.251	0.346	0.0195	0.225
3 [4]	35.000	29.915	0.5487	2.499	2.499	1.097	2.000	0.0835	0.115	0.00652	0.0750
4 [4]	35.000	29.915	0.5532	1.250	1.250	0.5532	1.000	0.248	0.342	0.0195	0.225
5 [4]	35.000	29.915	0.5542	1.250	1.250	0.5542	1.000	0.0825	0.114	0.00651	0.0750
6 [3]	24.000	20.513	0.4079	2.006	2.006	0.9548	2.341	0.150	0.207	0.0127	0.150
7 [3]	24.000	20.513	0.4098	1.285	1.285	0.6147	1.500	0.274	0.378	0.0233	0.276
8 [3]	24.000	20.513	0.4104	1.285	1.285	0.6156	1.500	0.149	0.205	0.0127	0.150
9 [3]	24.000	20.513	0.4104	1.285	1.285	0.6156	1.500	0.149	0.205	0.0127	0.150
10 [3]	24.000	20.513	0.4110	1.285	1.285	0.6165	1.500	0.0238	0.0328	0.00203	0.0240
11 [3]	24.000	20.513	0.4130	0.565	0.565	0.2721	0.659	0.148	0.204	0.0127	0.150
12 [2]	13.000	11.111	0.2426	0.928	0.928	0.4851	2.000	0.198	0.273	0.0184	0.225
13 [2]	13.000	11.111	0.2430	0.928	0.928	0.4860	2.000	0.0658	0.0907	0.00612	0.0750
14 [2]	13.000	11.111	0.2436	0.464	0.464	0.2436	1.000	0.197	0.271	0.0184	0.225
15 [2]	13.000	11.111	0.2440	0.464	0.464	0.2440	1.000	0.0654	0.0902	0.00612	0.0750
16 [1]	5.500	4.700	0.1100	0.295	0.295	0.1650	1.500	0.119	0.165	0.0119	0.150
Additional Runs [c]											
17 [5]	42.500	36.325	0.6276	3.552	3.552	1.469	2.341	0.331	0.457	0.0244	0.276
18 [5]	42.500	36.325	0.6295	3.552	3.552	1.474	2.341	0.0287	0.0397	0.00212	0.0240
19 [5]	42.500	36.325	0.6398	1.000	1.000	0.4216	0.659	0.324	0.447	0.0243	0.276
20 [5]	42.500	36.325	0.6418	1.000	1.000	0.4229	0.659	0.0281	0.0388	0.00212	0.0240
21 [4]	35.000	29.915	0.5455	2.925	2.925	1.277	2.341	0.309	0.426	0.0240	0.276
22 [4]	35.000	29.915	0.5472	2.925	2.925	1.281	2.341	0.0268	0.0370	0.00209	0.0240
23 [4]	35.000	29.915	0.5547	0.824	0.824	0.3656	0.659	0.303	0.418	0.0239	0.276
24 [4]	35.000	29.915	0.5564	0.824	0.824	0.3667	0.659	0.0263	0.0363	0.00208	0.0240
25 [1]	5.500	4.700	0.1097	0.460	0.460	0.2568	2.341	0.220	0.304	0.0219	0.276
26 [1]	5.500	4.700	0.1104	0.129	0.129	0.07273	0.659	0.0190	0.0263	0.00190	0.0240

[a] CCRD: Runs 1–16 including one replicate (Run 9). All sols were made using 94 mL acetone (73.696 g, based on $\rho_{acetone}$= 0.784 g cm^{-3}).
[b] "[Level]" refers to the 5 concentration levels of [ISO], (see Figure S.I.1).
[c] Extra samples (Runs 17–26) were added to the original CCRD to make the model stronger (see text).

Table S.I.11. Hansen Solubility Parameters (HSP) and Gelation Times of Sols Prepared in Acetone.

DoE run [Level] [a] No.	Sols Prepared in Acetone					
	mass [b] (g)	volume [c] (mL)	gelation time	δP_{sol} [d] (MPa)	δH_{sol} [d] (MPa)	δD_{sol} [d] (MPa)
1 [5]	118.650	132.846	20 min	9.502 [− 0.358]	6.198 [− 0.331]	15.473 [− 0.918]
2 [4]	111.446	126.760	35 min	9.649 [− 0.335]	6.492 [− 0.249]	15.477 [− 0.917]
3 [4]	111.279	126.529	40 min	9.656 [− 0.334]	6.497 [− 0.248]	15.478 [− 0.916]
4 [4]	110.194	125.506	1 h, 35 min	9.593 [− 0.344]	6.131 [− 0.350]	15.491 [− 0.910]
5 [4]	110.028	125.278	1h, 45 min	9.599 [− 0.343]	6.136 [− 0.348]	15.492 [− 0.910]
6 [3]	99.852	116.725	1 h, 50 min	9.855 [− 0.303]	6.697 [− 0.192]	15.483 [− 0.914]
7 [3]	99.255	116.176	2 h, 5 min	9.811 [− 0.310]	6.475 [− 0.254]	15.482 [− 0.914]
8 [3]	99.130	116.003	2 h, 15 min	9.818 [− 0.309]	6.481 [− 0.252]	15.483 [− 0.914]
9 [3]	99.130	116.003	2 h, 10 min	9.818 [− 0.309]	6.481 [− 0.252]	15.483 [− 0.914]
10 [3]	99.005	115.831	2 h, 20 min	9.824 [− 0.308]	6.486 [− 0.251]	15.483 [− 0.914]
11 [3]	98.408	115.281	4 h, 15 min	9.781 [− 0.315]	6.264 [− 0.313]	15.482 [− 0.914]
12 [2]	87.822	106.312	1 h, 45 min	10.069 [− 0.270]	6.779 [− 0.169]	15.504 [− 0.905]
13 [2]	87.690	106.130	3 h, 50 min	10.076 [− 0.269]	6.784 [− 0.168]	15.505 [− 0.904]
14 [2]	87.357	105.846	7 h, 30 min	10.031 [− 0.276]	6.596 [− 0.220]	15.488 [− 0.912]
15 [2]	87.226	105.666	8 h	10.038 [− 0.275]	6.601 [− 0.219]	15.489 [− 0.911]
16 [1]	79.610	99.1601	20 h, 30 min	10.231 [− 0.245]	6.854 [− 0.149]	15.479 [− 0.916]
Additional Runs						
17 [5]	120.080	134.334	12 min	9.546 [– 0.351]	6.519 [− 0.242]	15.458 [− 0.925]
18 [5]	119.777	133.917	2 h, 40 min	9.576 [− 0.347]	6.571 [− 0.227]	15.476 [− 0.917]
19 [5]	117.520	131.772	2 h, 50 min	9.438 [− 0.368]	5.865 [− 0.424]	15.471 [− 0.919]
20 [5]	117.224	131.364	4 h	9.458 [− 0.365]	5.877 [− 0.420]	15.489 [− 0.911]
21 [4]	111.930	127.266	20 min	9.659 [− 0.334]	6.596 [− 0.220]	15.462 [− 0.923]
22 [4]	111.648	126.877	4 h	9.679 [− 0.331]	6.608 [− 0.217]	15.479 [− 0.916]
23 [4]	109.823	125.156	2 h, 10 min	9.565 [− 0.348]	6.018 [− 0.381]	15.475 [− 0.918]
24 [4]	109.546	124.774	6 h	9.575 [− 0.347]	6.023 [− 0.380]	15.477 [− 0.917]
25 [1]	79.876	99.465	17 h	10.245 [− 0.243]	6.927 [− 0.128]	15.494 [− 0.909]
26 [1]	79.345	98.857	4 days	10.233 [− 0.244]	6.791 [− 0.166]	15.495 [− 0.909]

[a] "[Level]" refers to the 5 levels of the [ISO] concentration.
[b] Total mass of N3300A monomer, water, catalyst and mass of 94 mL acetone.
[c] Total volume of N3300A monomer, water, catalyst and 94 mL acetone.
[d] First number: actual values; numbers in [brackets]: orthogonally-transformed global values (*i.e.*, considering all runs in all solvents simultaneously). The three Hansen Solubility Parameters (HSPs) of the sol, δP_{sol}, δH_{sol} and δD_{sol} (represented herewith collectively and individually by the symbol δ_{sol}) were calculated *via*:

$$\delta_{sol} = \delta_{acetone} * X_{acetone} + \delta_{N3300A} * X_{N3300A} + \delta_{H2O} * X_{H2O} + \delta_{Et3N} * X_{Et3N}$$

where X_i is the volume fraction of component "i" in the sol and,

$\delta P_{acetone} = 10.4$ $\delta H_{acetone} = 7.0$ $\delta D_{acetone} = 15.0$

$\delta P_{H2O} = 16.0$ $\delta H_{H2O} = 42.3$ $\delta D_{H2O} = 15.6$

$\delta P_{Et3N} = 3.7$ $\delta H_{Et3N} = 1.9$ $\delta D_{Et3N} = 14.6$

$\delta P_{N3300A} = 6.8$ $\delta H_{N3300A} = 1.9$ $\delta D_{N3300A} = 15.4$

Table S.I.12. Sol Formulations of PUA Aerogels Prepared in THF According to the CCRD Model of Table S.I.2.[a]

DoE run [Level] [b] No.	ISO (Desmodur N3300A)			H_2O				Et_3N			
	mass (g)	volume (mL)	[ISO] (M)	mass (mg)	volume (mL)	$[H_2O]$ (M)	$[H_2O]/[ISO]$ (mol/mol)	mass (mg)	volume (mL)	$[Et_3N]$ (M)	Et_3N (% w/w)
1 [5]	42.500	36.325	0.6345	2.276	2.276	0.9517	1.500	0.193	0.266	0.0143	0.150
2 [4]	35.000	29.915	0.5476	2.499	2.499	1.095	2.000	0.273	0.377	0.0213	0.225
3 [4]	35.000	29.915	0.5487	2.499	2.499	1.097	2.000	0.0909	0.125	0.00710	0.0750
4 [4]	35.000	29.915	0.5530	1.250	1.250	0.5530	1.000	0.270	0.373	0.0213	0.225
5 [4]	35.000	29.915	0.5541	1.250	1.250	0.5541	1.000	0.0899	0.124	0.00709	0.0750
6 [3]	24.000	20.513	0.4078	2.006	2.006	0.9546	2.341	0.165	0.227	0.0139	0.150
7 [3]	24.000	20.513	0.4096	1.285	1.285	0.6145	1.500	0.301	0.416	0.0256	0.276
8 [3]	24.000	20.513	0.4103	1.285	1.285	0.6155	1.500	0.164	0.226	0.0139	0.150
9 [3]	24.000	20.513	0.4103	1.285	1.285	0.6155	1.500	0.164	0.226	0.0139	0.150
10 [3]	24.000	20.513	0.4110	1.285	1.285	0.6165	1.500	0.0261	0.0360	0.00223	0.0240
11 [3]	24.000	20.513	0.4129	0.565	0.565	0.2721	0.659	0.162	0.224	0.0139	0.150
12 [2]	13.000	11.111	0.2425	0.928	0.928	0.4850	2.000	0.220	0.303	0.0204	0.225
13 [2]	13.000	11.111	0.2430	0.928	0.928	0.4859	2.000	0.0732	0.101	0.00681	0.0750
14 [2]	13.000	11.111	0.2436	0.464	0.464	0.2436	1.000	0.219	0.302	0.0204	0.225
15 [2]	13.000	11.111	0.2440	0.464	0.464	0.2440	1.000	0.0728	0.100	0.00681	0.0750
16 [1]	5.500	4.700	0.1100	0.295	0.295	0.1650	1.500	0.134	0.185	0.0134	0.150
Additional Runs [c]											
17 [5]	42.500	36.325	0.6274	3.552	3.552	1.469	2.341	0.359	0.495	0.0264	0.276
18 [5]	42.500	36.325	0.6295	3.552	3.552	1.474	2.341	0.0311	0.0429	0.00230	0.0240
19 [5]	42.500	36.325	0.6396	1.000	1.000	0.4215	0.659	0.352	0.485	0.0264	0.276
20 [5]	42.500	36.325	0.6417	1.000	1.000	0.4229	0.659	0.0305	0.0421	0.00229	0.0240
21 [4]	35.000	29.915	0.5454	2.925	2.925	1.277	2.341	0.336	0.464	0.0261	0.276
22 [4]	35.000	29.915	0.5472	2.925	2.925	1.281	2.341	0.0292	0.0402	0.00227	0.0240
23 [4]	35.000	29.915	0.5546	0.824	0.824	0.3655	0.659	0.330	0.456	0.0261	0.276
24 [4]	35.000	29.915	0.5564	0.824	0.824	0.3667	0.659	0.0287	0.0395	0.00227	0.0240
25 [1]	5.500	4.700	0.1096	0.460	0.460	0.2567	2.341	0.248	0.342	0.0246	0.276
26 [1]	5.500	4.700	0.1104	0.129	0.129	0.07273	0.659	0.0214	0.0295	0.00214	0.0240

[a] CCRD: Runs 1–16 including one replicate (Run 9). All sols were made using 94 mL THF (83.566 g, based on ρ_{THF}= 0.889 g cm^{-3}).
[b] "[Level]" refers to the 5 concentration levels of [ISO], (see Figure S.I.1).
[c] Extra samples (Runs 17–26) were added to the original CCRD to make the model stronger (see text).

Table S.I.13. Hansen Solubility Parameters (HSP) and Gelation Times of Sols in THF.

DoE run [Level] [a] No.	Sols Prepared in THF					
	mass [b] (g)	volume [c] (mL)	gelation time	δP_{sol} [d] (MPa)	δH_{sol} [d] (MPa)	δD_{sol} [d] (MPa)
1 [5]	128.535	132.867	3 h	6.175 [− 0.877]	6.906 [− 0.134]	16.394 [− 0.508]
2 [4]	121.338	126.790	5 h	6.162 [− 0.879]	7.234 [− 0.043]	16.441 [− 0.487]
3 [4]	121.156	126.539	8 h, 15 min	6.164 [− 0.878]	7.240 [− 0.041]	16.443 [− 0.486]
4 [4]	120.086	125.537	7 h	6.055 [− 0.895]	6.871 [− 0.144]	16.434 [− 0.490]
5 [4]	119.906	125.288	9 h	6.064 [− 0.894]	6.879 [− 0.142]	16.451 [− 0.482]
6 [3]	109.737	116.746	15 h	6.067 [− 0.893]	7.503 [− 0.032]	16.531 [− 0.447]
7 [3]	109.153	116.214	4 h, 40 min	6.008 [− 0.903]	7.287 [− 0.028]	16.549 [− 0.439]
8 [3]	109.015	116.024	17 h	6.006 [− 0.903]	7.292 [− 0.027]	16.537 [− 0.444]
9 [3]	109.015	116.024	16 h	6.006 [− 0.903]	7.292 [− 0.027]	16.537 [− 0.444]
10 [3]	108.878	115.834	23 h	6.008 [− 0.903]	7.298 [− 0.025]	16.539 [− 0.443]
11 [3]	108.293	115.302	19 h	5.945 [− 0.912]	7.080 [− 0.086]	16.543 [− 0.441]
12 [2]	97.714	106.343	17 h	5.910 [− 0.918]	7.664 [0.077]	16.655 [− 0.391]
13 [2]	97.568	106.140	10 h	5.912 [− 0.918]	7.670 [0.078]	16.657 [− 0.390]
14 [2]	97.249	105.877	18 h	5.853 [− 0.927]	7.485 [0.027]	16.644 [− 0.396]
15 [2]	97.103	105.676	22 h	5.855 [− 0.926]	7.491 [0.028]	16.646 [− 0.395]
16 [1]	89.495	99.1806	2 days	5.775 [− 0.939]	7.802 [0.115]	16.712 [− 0.366]
Additional Runs						
17 [5]	129.977	134.372	1 h	6.260 [− 0.863]	7.220 [− 0.047]	16.383 [− 0.513]
18 [5]	129.650	133.920	9 h	6.276 [− 0.861]	7.273 [− 0.032]	16.388 [− 0.510]
19 [5]	127.418	131.810	6 h	6.086 [− 0.890]	6.581 [− 0.225]	16.414 [− 0.499]
20 [5]	127.097	131.367	14 h	6.093 [− 0.889]	6.593 [− 0.221]	16.419 [− 0.497]
21 [4]	121.828	127.304	2h	6.189 [− 0.874]	7.337 [− 0.014]	16.437 [− 0.489]
22 [4]	121.521	126.880	10 h, 30 min	6.197 [− 0.873]	7.349 [− 0.011]	16.442 [− 0.486]
23 [4]	119.720	125.194	7 h	6.035 [− 0.898]	6.772 [− 0.171]	16.467 [− 0.475]
24 [4]	119.418	124.778	18 h	6.036 [− 0.898]	6.776 [− 0.170]	16.456 [− 0.480]
25 [1]	89.774	99.502	24 h	5.799 [− 0.935]	7.873 [0.135]	16.724 [− 0.361]
26 [1]	89.217	98.856	4 days	5.763 [− 0.941]	7.742 [0.098]	16.732 [− 0.357]

[a] "Level" refers to the [ISO] concentration that was varied at 5 levels.
[b] Total mass of N3300A monomer, water, catalyst and mass of 94 mL THF.
[c] Total volume of N3300A monomer, water, catalyst and 94 mL THF.
[d] First number: actual values; numbers in [brackets]: orthogonally-transformed global values (*i.e.*, considering all runs in all solvents simultaneously). The three Hansen Solubility Parameters (HSPs) of the sol, δP_{sol}, δH_{sol} and δD_{sol} (represented herewith collectively and individually by the symbol δ_{sol}) were calculated *via*:

$$\delta_{sol} = \delta_{THF} * X_{THF} + \delta_{N3300A} * X_{N3300A} + \delta_{H2O} * X_{H2O} + \delta_{Et3N} * X_{Et3N}$$

where X_i is the volume fraction of component "i" in the sol and,

$\delta P_{THF} = 5.7$ $\delta H_{THF} = 8.0$ $\delta D_{THF} = 16.8$

$\delta P_{H2O} = 16.0$ $\delta H_{H2O} = 42.3$ $\delta D_{H2O} = 15.6$

$\delta P_{Et3N} = 3.7$ $\delta H_{Et3N} = 1.9$ $\delta D_{Et3N} = 14.6$

$\delta P_{N3300A} = 6.8$ $\delta H_{N3300A} = 1.9$ $\delta D_{N3300A} = 15.4$

Table S.I.14. Formulations of PUA Aerogels Prepared in Ethyl Acetate According to the CCRD Model of Table S.I.2.[a]

DoE run [Level] [b] No.	ISO (DesmodurN3300A)			H_2O				Et_3N			
	mass (g)	volume (mL)	[ISO] (M)	mass (mg)	volume (mL)	[H_2O] (M)	[H_2O]/[ISO] (mol/mol)	mass (mg)	volume (mL)	[Et_3N] (M)	Et_3N (% w/w)
1 [5]	42.500	36.325	0.6345	2.276	2.276	0.9517	1.500	0.195	0.268	0.0145	0.150
2 [4]	35.000	29.915	0.5476	2.499	2.499	1.095	2.000	0.276	0.380	0.0215	0.225
3 [4]	35.000	29.915	0.5487	2.499	2.499	1.097	2.000	0.0918	0.127	0.00717	0.0750
4 [4]	35.000	29.915	0.5530	1.250	1.250	0.5530	1.000	0.273	0.376	0.0215	0.225
5 [4]	35.000	29.915	0.5541	1.250	1.250	0.5541	1.000	0.0908	0.125	0.00717	0.0750
6 [3]	24.000	20.513	0.4078	2.006	2.006	0.9546	2.341	0.166	0.230	0.0141	0.150
7 [3]	24.000	20.513	0.4096	1.285	1.285	0.6144	1.500	0.305	0.420	0.0259	0.276
8 [3]	24.000	20.513	0.4103	1.285	1.285	0.6155	1.500	0.165	0.228	0.0141	0.150
9 [3]	24.000	20.513	0.4103	1.285	1.285	0.6155	1.500	0.165	0.228	0.0141	0.150
10 [3]	24.000	20.513	0.4110	1.285	1.285	0.6165	1.500	0.0264	0.0364	0.00225	0.0240
11 [3]	24.000	20.513	0.4129	0.565	0.565	0.2721	0.659	0.164	0.227	0.0141	0.150
12 [2]	13.000	11.111	0.2425	0.928	0.928	0.4850	2.000	0.223	0.307	0.0207	0.225
13 [2]	13.000	11.111	0.2429	0.928	0.928	0.4859	2.000	0.0741	0.102	0.00690	0.0750
14 [2]	13.000	11.111	0.2435	0.464	0.464	0.2435	1.000	0.222	0.306	0.0207	0.225
15 [2]	13.000	11.111	0.2440	0.464	0.464	0.2440	1.000	0.0737	0.102	0.00690	0.0750
16 [1]	5.500	4.700	0.1100	0.295	0.295	0.1650	1.500	0.136	0.188	0.0136	0.150
Additional Runs [c]											
17 [5]	42.500	36.325	0.6274	3.552	3.552	1.469	2.341	0.362	0.499	0.0266	0.276
18 [5]	42.500	36.325	0.6295	3.552	3.552	1.474	2.341	0.0314	0.0433	0.00232	0.0240
19 [5]	42.500	36.325	0.6396	1.000	1.000	0.4215	0.659	0.355	0.490	0.0266	0.276
20 [5]	42.500	36.325	0.6417	1.000	1.000	0.4229	0.659	0.0308	0.0425	0.00232	0.0240
21 [4]	35.000	29.915	0.5453	2.925	2.925	1.277	2.341	0.340	0.468	0.0264	0.276
22 [4]	35.000	29.915	0.5472	2.925	2.925	1.281	2.341	0.0295	0.0406	0.00229	0.0240
23 [4]	35.000	29.915	0.5545	0.824	0.824	0.3654	0.659	0.334	0.460	0.0263	0.276
24 [4]	35.000	29.915	0.5564	0.824	0.824	0.3667	0.659	0.0290	0.0399	0.00229	0.0240
25 [1]	5.500	4.700	0.1096	0.460	0.460	0.2567	2.341	0.251	0.346	0.0249	0.276
26 [1]	5.500	4.700	0.1104	0.129	0.129	0.07273	0.659	0.0217	0.0299	0.00217	0.0240

[a] CCRD: Runs 1–16 including one replicate (Run 9). All sols were made using 94 mL ethyl acetate (84.788 g, based on $\rho_{\text{ethyl acetate}} = 0.902$ g cm^{-3}).
[b] "[Level]" refers to the 5 concentration levels of [ISO], (see Figure S.I.1).
[c] Extra samples (Runs 17–26) were added to the original CCRD to make the model stronger (see text).

Table S.I.15. Hansen Solubility Parameters (HSP) and Gelation Times of Sols Prepared in Ethyl Acetate.

DoE run [Level] [a] No.	Sol Prepared in Ethyl Acetate					
	mass [b] (g)	volume [c] (mL)	gelation time	δP_{sol} [d] (MPa)	δH_{sol} [d] (MPa)	δD_{sol} [d] (MPa)
1 [5]	129.759	132.869	1 h	5.891 [− 0.921]	6.339 [− 0.292]	15.686 [− 0.823]
2 [4]	122.563	126.794	1 h, 35 min	5.865 [− 0.925]	6.641 [− 0.208]	15.699 [− 0.818]
3 [4]	122.379	126.540	3 h	5.866 [− 0.925]	6.646 [− 0.206]	15.700 [− 0.817]
4 [4]	121.311	125.541	2 h,30 min	5.756 [− 0.942]	6.272 [− 0.310]	15.685 [− 0.824]
5 [4]	121.129	125.290	4 h, 45 min	5.764 [− 0.941]	6.279 [− 0.308]	15.701 [− 0.817]
6 [3]	110.960	116.748	3 h, 15 min	5.744 [− 0.944]	6.859 [− 0.147]	15.725 [− 0.806]
7 [3]	110.378	116.218	2 h, 30 min	5.684 [− 0.953]	6.639 [− 0.208]	15.739 [− 0.800]
8 [3]	110.239	116.026	4 h	5.682 [− 0.953]	6.643 [− 0.207]	15.726 [− 0.806]
9 [3]	110.239	116.026	4 h, 10 min	5.682 [− 0.953]	6.643 [− 0.207]	15.726 [− 0.806]
10 [3]	110.100	115.835	6 h	5.683 [− 0.953]	6.648 [− 0.206]	15.727 [− 0.805]
11 [3]	109.517	115.304	5 h, 40 min	5.619 [− 0.963]	6.427 [− 0.267]	15.727 [− 0.805]
12 [2]	98.939	106.346	6 h	5.556 [− 0.973]	6.956 [− 0.120]	15.770 [− 0.786]
13 [2]	98.790	106.142	7 h, 30 min	5.558 [− 0.973]	6.961 [− 0.119]	15.771 [− 0.786]
14 [2]	98.474	105.881	7 h	5.497 [− 0.982]	6.773 [− 0.171]	15.755 [− 0.793]
15 [2]	98.326	105.677	11 h	5.499 [− 0.982]	6.779 [− 0.169]	15.756 [− 0.792]
16 [1]	90.719	99.183	4 days	5.396 [− 0.998]	7.044 [− 0.096]	15.764 [− 0.789]
Additional Runs						
17 [5]	131.203	134.377	50 min	5.980[− 0.907]	6.660 [− 0.203]	15.683 [− 0.825]
18 [5]	130.872	133.920	2 h	5.995 [− 0.905]	6.711 [− 0.188]	15.686 [− 0.823]
19 [5]	128.643	131.815	1 h, 45 min	5.800[− 0.935]	6.009 [− 0.384]	15.700 [− 0.817]
20 [5]	128.319	131.367	9 h	5.806 [− 0.934]	6.020 [− 0.381]	15.703 [− 0.816]
21 [4]	123.053	127.308	1 h, 20 min	5.894 [− 0.920]	6.746 [− 0.179]	15.698 [− 0.818]
22 [4]	122.743	126.881	4 h, 35 min	5.900 [− 0.919]	6.757 [− 0.176]	15.701 [− 0.817]
23 [4]	120.945	125.198	4 h, 10 min	5.734 [− 0.945]	6.170 [− 0.339]	15.715 [− 0.810]
24 [4]	120.640	124.778	6 h	5.735 [− 0.945]	6.174 [− 0.338]	15.703 [− 0.816]
25 [1]	90.999	99.507	17 h	5.425 [− 0.993]	7.118 [− 0.075]	15.792 [− 0.776]
26 [1]	90.439	98.860	5 days	5.383 [− 1.000]	6.981 [− 0.113]	15.781 [− 0.781]

[a] "[Level]" refers to the 5 levels of the [ISO] concentration.

[b] Total mass of N3300A monomer, water, catalyst and mass of 94 mL ethyl acetate.

[c] Total volume of N3300A monomer, water, catalyst and 94 mL ethyl acetate.

[d] First number: actual values; numbers in [brackets]: orthogonally-transformed global values (*i.e.,* considering all runs in all solvents simultaneously). The three Hansen Solubility Parameters (HSPs) of the sol, δP_{sol}, δH_{sol} and δD_{sol} (represented herewith collectively and individually by the symbol δ_{sol}) were calculated *via*:

$$\delta_{sol} = \delta_{ethyl\ acetate} * X_{ethyl\ acetate} + \delta_{N3300A} * X_{N3300A} + \delta_{H2O} * X_{H2O} + \delta_{Et3N} * X_{Et3N}$$

where X_i is the volume fraction of component "i" in the sol and,

$\delta P_{ethyl\ acetate} = 5.3$	$\delta H_{ethyl\ acetate} = 7.2$	$\delta D_{ethyl\ acetate} = 15.8$
$\delta P_{H2O} = 16.0$	$\delta H_{H2O} = 42.3$	$\delta D_{H2O} = 15.6$
$\delta P_{Et3N} = 3.7$	$\delta H_{Et3N} = 1.9$	$\delta D_{Et3N} = 14.6$
$\delta P_{N3300A} = 6.8$	$\delta H_{N3300A} = 1.9$	$\delta D_{N3300A} = 15.4$

Table S.I.16. Sol Formulations of PUA Aerogels Prepared in 2-butanone According to the CCRD Model of Table S.I.2.[a]

DoE run [Level] [b] No.	ISO (Desmodur N3300A)			H_2O				Et_3N			
	mass (g)	volume (mL)	[ISO] (M)	mass (mg)	volume (mL)	[H_2O] (M)	[H_2O]/[ISO] (mol/mol)	mass (mg)	volume (mL)	[Et_3N] (M)	Et_3N (% w/w)
1 [5]	42.500	36.325	0.6346	2.276	2.276	0.9519	1.500	0.181	0.250	0.0135	0.150
2 [4]	35.000	29.915	0.5477	2.499	2.499	1.095	2.000	0.255	0.352	0.0199	0.225
3 [4]	35.000	29.915	0.5487	2.499	2.499	1.097	2.000	0.0849	0.117	0.00663	0.0750
4 [4]	35.000	29.915	0.5531	1.250	1.250	0.5531	1.000	0.252	0.348	0.0199	0.225
5 [4]	35.000	29.915	0.5542	1.250	1.250	0.5542	1.000	0.0840	0.116	0.00663	0.0750
6 [3]	24.000	20.513	0.4078	2.006	2.006	0.9547	2.341	0.153	0.211	0.0129	0.150
7 [3]	24.000	20.513	0.4098	1.285	1.285	0.6146	1.500	0.279	0.385	0.0238	0.276
8 [3]	24.000	20.513	0.4104	1.285	1.285	0.6156	1.500	0.152	0.209	0.0129	0.150
9 [3]	24.000	20.513	0.4104	1.285	1.285	0.6156	1.500	0.152	0.209	0.0129	0.150
10 [3]	24.000	20.513	0.4110	1.285	1.285	0.6165	1.500	0.0242	0.0334	0.00207	0.0240
11 [3]	24.000	20.513	0.4129	0.565	0.565	0.2721	0.659	0.151	0.208	0.0129	0.150
12 [2]	13.000	11.111	0.2425	0.928	0.928	0.4851	2.000	0.202	0.279	0.0188	0.225
13 [2]	13.000	11.111	0.2430	0.928	0.928	0.4859	2.000	0.0672	0.0928	0.00626	0.0750
14 [2]	13.000	11.111	0.2436	0.464	0.464	0.2436	1.000	0.201	0.277	0.0188	0.225
15 [2]	13.000	11.111	0.2440	0.464	0.464	0.2440	1.000	0.0669	0.0923	0.00626	0.0750
16 [1]	5.500	4.700	0.1100	0.295	0.295	0.1650	1.500	0.122	0.169	0.0122	0.150
Additional Runs [c]											
17 [5]	42.500	36.325	0.6275	3.552	3.552	1.469	2.341	0.337	0.465	0.0248	0.276
18 [5]	42.500	36.325	0.6295	3.552	3.552	1.474	2.341	0.0292	0.0403	0.00216	0.0240
19 [5]	42.500	36.325	0.6397	1.000	1.000	0.4216	0.659	0.330	0.455	0.0247	0.276
20 [5]	42.500	36.325	0.6418	1.000	1.000	0.4229	0.659	0.0286	0.0395	0.00215	0.0240
21 [4]	35.000	29.915	0.5455	2.925	2.925	1.277	2.341	0.314	0.434	0.0244	0.276
22 [4]	35.000	29.915	0.5472	2.925	2.925	1.281	2.341	0.0273	0.0376	0.00212	0.0240
23 [4]	35.000	29.915	0.5547	0.824	0.824	0.3655	0.659	0.309	0.426	0.0244	0.276
24 [4]	35.000	29.915	0.5564	0.824	0.824	0.3667	0.659	0.0268	0.0369	0.00212	0.0240
25 [1]	5.500	4.700	0.1097	0.460	0.460	0.2568	2.341	0.226	0.312	0.0224	0.276
26 [1]	5.500	4.700	0.1104	0.129	0.129	0.07273	0.659	0.0195	0.0269	0.00195	0.0240

[a] CCRD: Runs 1–16 including one replicate (Run 9). All sols were made using 94 mL 2-butanone (75.670 g, based on $\rho_{2\text{-butanone}}$= 0.805 g cm^{-3}).
[b] "[Level]" refers to the 5 concentration levels of [ISO], (see Figure S.I.1).
[c] Extra samples (Runs 17–26) were added to the original CCRD to make the model stronger (see text).

Table S.I.17. Hansen Solubility Parameters (HSP) and Gelation Times of Sols Prepared in 2-butanone.

DoE run [Level] [a] No.	Sol Prepared in 2-butanone					
	mass [b] (g)	volume [c] (mL)	gelation time	δP_{sol} [d] (MPa)	δH_{sol} [d] (MPa)	δD_{sol} [d] (MPa)
1 [5]	120.627	132.851	20 min	8.511 [− 0.513]	4.852 [− 0.705]	15.827 [− 0.761]
2 [4]	113.425	126.766	1 h	8.610 [− 0.497]	5.082 [− 0.641]	15.848 [− 0.751]
3 [4]	113.254	126.531	2 h, 15 min	8.616 [− 0.496]	5.086 [− 0.640]	15.849 [− 0.751]
4 [4]	112.172	125.512	1 h, 30 min	8.534 [− 0.509]	4.701 [− 0.747]	15.850 [− 0.750]
5 [4]	112.004	125.280	3 h, 30 min	8.548 [− 0.507]	4.709 [− 0.745]	15.867 [− 0.743]
6 [3]	101.829	116.730	2 h	8.727 [− 0.479]	5.166 [− 0.618]	15.886 [− 0.734]
7 [3]	101.235	116.184	1 h, 20 min	8.677 [− 0.487]	4.936 [− 0.682]	15.887 [− 0.734]
8 [3]	101.107	116.007	3 h, 10 min	8.682 [− 0.486]	4.940 [− 0.681]	15.888 [− 0.733]
9 [3]	101.107	116.007	3 h, 30 min	8.682 [− 0.486]	4.940 [− 0.681]	15.888 [− 0.733]
10 [3]	100.980	115.832	14 h	8.688 [− 0.485]	4.943 [− 0.680]	15.889 [− 0.733]
11 [3]	100.385	115.285	15 h	8.638 [− 0.493]	4.713 [− 0.744]	15.890 [− 0.732]
12 [2]	89.800	106.318	4 h, 50 min	8.830 [− 0.463]	5.098 [− 0.637]	15.947 [− 0.707]
13 [2]	89.666	106.132	15 h	8.836 [− 0.462]	5.101 [− 0.636]	15.948 [− 0.707]
14 [2]	89.335	105.853	5 h	8.786 [− 0.470]	4.906 [− 0.690]	15.933 [− 0.713]
15 [2]	89.201	105.668	18 h	8.792 [− 0.469]	4.910 [− 0.689]	15.934 [− 0.713]
16 [1]	81.587	99.164	2 days	8.903 [− 0.452]	5.053 [− 0.649]	15.953 [− 0.704]
Additional Runs						
17 [5]	122.059	134.342	23 min	8.570 [− 0.504]	5.190 [− 0.611]	15.823 [− 0.762]
18 [5]	121.752	133.917	1 h, 45 min	8.593 [− 0.500]	5.237 [− 0.598]	15.827 [− 0.761]
19 [5]	119.500	131.780	55 min	8.442 [− 0.523]	4.510 [− 0.800]	15.843 [− 0.753]
20 [5]	119.199	131.364	8 h	8.456 [− 0.521]	4.516 [− 0.799]	15.847 [− 0.752]
21 [4]	113.910	127.274	20 min	8.624 [− 0.495]	5.192 [− 0.611]	15.831 [− 0.759]
22 [4]	113.623	126.878	8 h, 30 min	8.642 [− 0.492]	5.200 [− 0.609]	15.849 [− 0.751]
23 [4]	111.802	125.164	2 h, 5 min	8.513 [− 0.512]	4.589 [− 0.778]	15.851 [− 0.75]
24 [4]	111.520	124.775	11 h	8.521 [− 0.511]	4.592 [− 0.778]	15.853 [− 0.749]
25 [1]	81.856	99.472	13 h	8.921 [− 0.449]	5.129 [− 0.628]	15.967 [− 0.698]
26 [1]	81.319	98.857	5 days	8.901 [− 0.452]	4.984 [− 0.669]	15.971 [− 0.696]

[a] "[Level]" refers to the 5 levels of the [ISO] concentration.

[b] Total mass of N3300A monomer, water, catalyst and mass of 94 mL 2-butanone.

[c] Total volume of N3300A monomer, water, catalyst and 94 mL 2-butanone.

[d] First number: actual values; numbers in [brackets]: orthogonally-transformed global values (*i.e.*, considering all runs in all solvents simultaneously). The three Hansen Solubility Parameters (HSPs) of the sol, δP_{sol}, δH_{sol} and δD_{sol} (represented herewith collectively and individually by the symbol δ_{sol}) were calculated *via*:

$$\delta_{sol} = \delta_{2\text{-butanone}} * X_{2\text{-butanone}} + \delta_{N3300A} * X_{N3300A} + \delta_{H2O} * X_{H2O} + \delta_{Et3N} * X_{Et3N}$$

where X_i is the volume fraction of component "i" in the sol and,

$\delta P_{2\text{-butanone}} = 9.0$	$\delta H_{2\text{-butanone}} = 5.1$	$\delta D_{2\text{-butanone}} = 16.0$
$\delta P_{H2O} = 16.0$	$\delta H_{H2O} = 42.3$	$\delta D_{H2O} = 15.6$
$\delta P_{Et3N} = 3.7$	$\delta H_{Et3N} = 1.9$	$\delta D_{Et3N} = 14.6$
$\delta P_{N3300A} = 6.8$	$\delta H_{N3300A} = 1.9$	$\delta D_{N3300A} = 15.4$

Table S.I.18. Formulations of PUA Aerogels Prepared in DMF According to the CCRD Model of Table S.I.2.[a]

DoE run [Level] [b] No.	ISO (Desmodur N3300A)			H_2O				Et_3N			
	mass (g)	volume (mL)	[ISO] (M)	mass (mg)	volume (mL)	[H_2O] (M)	[H_2O]/[ISO] (mol/mol)	mass (mg)	volume (mL)	[Et_3N] (M)	Et_3N (% w/w)
12 [2]	13.000	11.111	0.2425	0.928	0.928	0.4849	2.000	0.232	0.319	0.0215	0.225
13 [2]	13.000	11.111	0.2429	0.928	0.928	0.4859	2.000	0.0771	0.106	0.00717	0.0750
14 [2]	13.000	11.111	0.2435	0.464	0.464	0.2435	1.000	0.230	0.318	0.0215	0.225
15 [2]	13.000	11.111	0.2440	0.464	0.464	0.2440	1.000	0.0767	0.106	0.00717	0.0750
16 [1]	5.500	4.700	0.1100	0.295	0.295	0.1650	1.500	0.142	0.196	0.0141	0.150
Additional Runs [c]											
25 [1]	5.500	4.700	0.1096	0.460	0.460	0.2566	2.341	0.262	0.361	0.0260	0.276
26 [1]	5.500	4.700	0.1104	0.129	0.129	0.07272	0.659	0.0227	0.0312	0.00226	0.0240

[a] CCRD: Runs 1–16 including one replicate (Run 9). All sols were made using 94 mL DMF (88.736 g, based on ρ_{DMF}= 0.944 g cm^{-3}).

[b] "[Level]" refers to the 5 concentration levels of [ISO], (see Figure S.I.1). All samples from Runs 1–11 and 17–24 collapsed, the bulk densities were >1.0 g cm^{-3} and the porosities were <30% v/v.

[c] Extra samples (Runs 17–26) were added to the original CCRD to make the model stronger (see text).

Table S.I.19. Hansen Solubility Parameters (HSP) and Gelation Times of Sols Prepared in DMF.

DoE run [Level] [a] No.	**Sol Prepared in DMF**					
	mass [b] (g)	**volume [c] (mL)**	**gelation time**	**δP_{sol} [d] (MPa)**	**δH_{sol} [d] (MPa)**	**δD_{sol} [d] (MPa)**
12 [2]	102.896	106.359	1 h, 20 min	12.990 [0.185]	10.585 [0.889]	17.186 [− 0.155]
13 [2]	102.741	106.146	4 h	13.000 [0.187]	10.594 [0.891]	17.188 [− 0.154]
14 [2]	102.431	105.893	2 h, 30 min	12.951 [0.179]	10.407 [0.839]	17.160 [− 0.166]
15 [2]	102.277	105.681	6 h	12.975 [0.183]	10.428 [0.845]	17.180 [− 0.157]
16 [1]	94.673	99.191	5 h	13.359 [0.243]	10.931 [0.985]	17.280 [− 0.113]
Extra Points						
25 [1]	94.958	99.522	2 h	13.357 [0.242]	10.985 [1.000]	17.289 [− 0.109]
26 [1]	94.388	98.862	2 days	13.371 [0.244]	10.880 [0.971]	17.302 [− 0.103]

[a] "[Level]" refers to the 5 levels of the [ISO] concentration.

[b] Total mass of N3300A monomer, water, catalyst and mass of 94 mL DMF.

[c] Total volume of N3300A monomer, water, catalyst and 94 mL DMF.

[d] First number: actual values; numbers in [brackets]: orthogonally-transformed global values (*i.e.*, considering all runs in all solvents simultaneously). The three Hansen Solubility Parameters (HSPs) of the sol, δP_{sol}, δH_{sol} and δD_{sol} (represented herewith collectively and individually by the symbol δ_{sol}) were calculated *via*:

$$\delta_{sol} = \delta_{DMF} * X_{DMF} + \delta_{N3300A} * X_{N3300A} + \delta_{H2O} * X_{H2O} + \delta_{Et3N} * X_{Et3N}$$

where X_i is the volume fraction of component "i" in the sol and,

$\delta P_{DMF} = 13.7$ $\delta H_{DMF} = 11.3$ $\delta D_{DMF} = 17.4$

$\delta P_{H2O} = 16.0$ $\delta H_{H2O} = 42.3$ $\delta D_{H2O} = 15.6$

$\delta P_{Et3N} = 3.7$ $\delta H_{Et3N} = 1.9$ $\delta D_{Et3N} = 14.6$

$\delta P_{N3300A} = 6.8$ $\delta H_{N3300A} = 1.9$ $\delta D_{N3300A} = 15.4$

Table S.I.20. Sol Formulations of PUA Aerogels Prepared in Binary Solvents According to the CCRD Model of Table S.I.2.[a]

DoE run [Level] [b] No.	ISO (Desmodur N3300A)			H_2O				Et_3N			
	mass (g)	volume (mL)	[ISO] (M)	mass (mg)	volume (mL)	[H_2O] (M)	[H_2O]/[ISO] (mol/mol)	mass (mg)	volume (mL)	[Et_3N] (M)	Et_3N (% w/w)
A: acetonitrile-nitromethane 1:1 v/v											
1 [5]	42.5	36.3	0.6344	2.28	2.28	0.9516	1.500	0.203	0.280	0.0151	0.150
24 [4]	35.0	29.9	0.5564	0.824	0.824	0.3667	0.6590	0.0303	0.0418	0.00240	0.0240
2 [4]	35.0	29.9	0.5475	2.50	2.50	1.095	2.000	0.289	0.398	0.0225	0.225
B: acetonitrile-propylene carbonate 1:1 v/v											
1 [5]	42.5	36.3	0.6344	2.28	2.28	0.9516	1.500	0.207	0.286	0.0154	0.150
8 [3]	24.0	20.5	0.4102	1.29	1.29	0.6154	1.500	0.178	0.246	0.0152	0.150
16 [1]	5.50	4.70	0.1100	0.295	0.295	0.1650	1.500	0.149	0.205	0.0148	0.150
26 [1]	5.50	4.70	0.1104	0.129	0.129	0.07272	0.6590	0.0238	0.0328	0.00237	0.0240
C: acetonitrile-acetone 1:1 v/v											
17 [5]	42.5	36.3	0.6276	3.55	3.55	1.469	2.341	0.332	0.457	0.0244	0.276
8 [3]	24.0	20.5	0.4104	1.29	1.29	0.6156	1.500	0.149	0.205	0.0127	0.150
16 [1]	5.50	4.70	0.1100	0.295	0.295	0.1650	1.500	0.120	0.165	0.0119	0.150
D: acetonitrile-DMF 1:1 v/v											
6 [3]	24.0	20.5	0.4078	2.01	2.01	0.9547	2.341	0.161	0.222	0.0136	0.150
13 [2]	13.0	11.1	0.2430	0.928	0.928	0.4859	2.000	0.0715	0.0986	0.00666	0.0750
16 [1]	5.50	4.70	0.1100	0.295	0.295	0.1650	1.500	0.131	0.180	0.0130	0.150
E: acetone-ethyl acetate 1:1 v/v											
17 [5]	42.5	36.3	0.6275	3.55	3.55	1.469	2.341	0.347	0.478	0.0255	0.276
8 [3]	24.0	20.5	0.4104	1.29	1.29	0.6155	1.500	0.157	0.217	0.0134	0.150
F: ethyl acetate-DMF 1:1 v/v											
15 [2]	13.0	11.1	0.2440	0.464	0.464	0.2440	1.000	0.0752	0.104	0.00703	0.0750
26 [1]	5.50	4.70	0.1104	0.129	0.129	0.07272	0.6590	0.0222	0.0306	0.00222	0.0240
G: nitromethane-2-butanone 1:1 v/v											
12 [2]	13.0	11.1	0.2424	0.928	0.928	0.4849	2.000	0.238	0.328	0.0221	0.225
22 [4]	35.0	29.9	0.5472	2.93	2.93	1.281	2.341	0.0310	0.0428	0.00242	0.0240
H: propylene carbonate-2-butanone 1:1 v/v											
25 [1]	5.50	4.70	0.1096	0.460	0.460	0.2566	2.341	0.277	0.382	0.0275	0.276

[a] Runs are referred to based on the nomenclature of the CCRD for single solvents system. All sols were made using 47 mL of Solvent 1 and 47 mL of Solvent 2. The mass of the mixture of the two solvents is equal to 2 × 47 mL× ($\rho_{\text{Solvent 1}} + \rho_{\text{Solvent 2}}$). Thereby, mass of binary solvent A: 90.522 g; mass of binary solvent B: 93.342 g; mass of binary solvent C: 73.790 g; mass of binary solvent D: 81.310 g; mass of binary solvent E: 79.242 g; mass of binary solvent F: 86.762 g; mass of binary solvent G: 91.415 g; mass of binary solvent H: 94.235 g. [b] "[Level]" refers to the [ISO] concentration that was varied at 5 levels.

Table S.I.21. Hansen Solubility Parameters (HSP) and Gelation Times of Sols Made in Binary Solvents.

DoE run [Level] [a] No.	Sol Prepared in Binary Solvents					
	mass [b] (g)	volume [c] (mL)	gelation time	δP_{sol} [d] (MPa)	δH_{sol} [d] (MPa)	δD_{sol} [d] (MPa)
A: acetonitrile- nitromethane 1:1 v/v						
1 [5]	135.501	132.881	5 min	15.170 [0.525]	5.208 [− 0.606]	15.559 [− 0.880]
24 [4]	126.376	124.780	2 h	15.599 [0.592]	4.969 [− 0.673]	15.552 [− 0.883]
2 [4]	128.310	126.812	3 h	15.585 [0.589]	5.453 [− 0.538]	15.551 [− 0.884]
B: acetonitrile-propylene carbonate 1:1 v/v						
1 [5]	138.326	132.887	2 min	14.887 [0.481]	4.854 [− 0.705]	17.046 [− 0.217]
8 [3]	118.806	116.044	10 min	15.985 [0.652]	4.942 [− 0.68]	17.281 [− 0.112]
16 [1]	99.285	99.201	1 h	17.439 [0.878]	5.055 [− 0.649]	17.579 [0.021]
26 [1]	98.995	98.863	4 h	17.460 [0.881]	4.984 [− 0.669]	17.588 [0.025]
C: acetonitrile-acetone 1:1 v/v						
17 [5]	120.174	134.335	2 min	12.206 [0.063]	6.239 [− 0.320]	15.388 [− 0.956]
8 [3]	99.224	116.003	3 h	13.046 [0.194]	6.214 [− 0.327]	15.401 [− 0.951]
16 [1]	79.704	99.160	7 h	13.898 [0.327]	6.482 [− 0.252]	15.384 [− 0.958]
D: acetonitrile-DMF 1:1 v/v						
6 [3]	107.477	116.741	35 min	14.288 [0.387]	8.068 [0.189]	16.209 [− 0.59]
13 [2]	95.310	106.138	10 min	14.949 [0.490]	8.290 [0.251]	16.302 [− 0.549]
16 [1]	87.235	99.176	2 h	15.445 [0.568]	8.466 [0.300]	16.332 [− 0.535]
E: acetone-ethyl acetate 1:1 v/v						
17 [5]	125.641	134.355	1 h	7.800 [− 0.623]	6.590 [− 0.222]	15.613 [− 0.856]
8 [3]	104.684	116.015	12 h	7.804 [− 0.623]	6.630 [− 0.211]	15.651 [− 0.839]
F: ethyl acetate-DMF 1:1 v/v						
15 [2]	100.301	105.679	10 h	9.292 [− 0.391]	8.783 [0.388]	16.505 [− 0.458]
26 [1]	92.414	98.861	5 days	9.394 [− 0.375]	9.043 [0.460]	16.537 [− 0.444]
G: nitromethane-2-butanone 1:1 v/v						
12 [2]	105.581	106.367	3 h	13.249 [0.225]	5.064 [− 0.646]	15.835 [− 0.757]
22 [4]	129.372	126.883	45 min	12.349 [0.085]	5.198 [− 0.609]	15.781 [− 0.781]
H: propylene carbonate-2-butanone 1:1 v/v						
25 [1]	100.472	99.543	5 h	13.229 [0.222]	4.640 [− 0.764]	17.882 [0.156]

[a] "[Level]" refers to the 5 levels of the [ISO] concentration. [b] Total mass of N3300A monomer, water, catalyst and mass of 94 mL mixed solvent. [c] Total volume of N3300A monomer, water, catalyst and 94 mL of mixed solvent. [d] Same footnote "d" as in Part B of Tables S.1.4 to S.I.11. The HSPs of the sol, δ_{sol}, were calculated *via*: $\delta_{sol} = \delta_{mixed\ solvent} * X_{mixed\ solvent} + \delta_{N3300A} * X_{N3300A} + \delta_{H2O} * X_{H2O} + \delta_{Et3N} * X_{Et3N}$

where $\delta_{mixed\ solvent}$: weighted average value, X_i: volume fraction of component "i" in the sol, and

$\delta P_{H2O} = 16.0$ $\delta H_{H2O} = 42.3$ $\delta D_{H2O} = 15.6$

$\delta P_{Et3N} = 3.7$ $\delta H_{Et3N} = 1.9$ $\delta D_{Et3N} = 14.6$

$\delta P_{N3300A} = 6.8$ $\delta H_{N3300A} = 1.9$ $\delta D_{N3300A} = 15.4$

$\delta P_{mixed\ solvent\ A} = 18.4$ $\delta H_{mixed\ solvent\ A} = 5.6$ $\delta D_{mixed\ solvent\ A} = 15.6$

$\delta P_{mixed\ solvent\ B} = 18.0$ $\delta H_{mixed\ solvent\ B} = 5.1$ $\delta D_{mixed\ solvent\ B} = 17.7$

$\delta P_{mixed\ solvent\ C} = 14.2$ $\delta H_{mixed\ solvent\ C} = 6.6$ $\delta D_{mixed\ solvent\ C} = 15.4$

$\delta P_{mixed\ solvent\ D} = 15.9$ $\delta H_{mixed\ solvent\ D} = 8.7$ $\delta D_{mixed\ solvent\ D} = 16.4$

$\delta P_{mixed\ solvent\ E} = 7.9$ $\delta H_{mixed\ solvent\ E} = 7.1$ $\delta D_{mixed\ solvent\ E} = 15.7$

$\delta P_{mixed\ solvent\ F} = 9.5$ $\delta H_{mixed\ solvent\ F} = 9.3$ $\delta D_{mixed\ solvent\ F} = 16.6$

$\delta P_{mixed\ solvent\ G} = 13.9$ $\delta H_{mixed\ solvent\ G} = 5.1$ $\delta D_{mixed\ solvent\ G} = 15.9$

$\delta P_{mixed\ solvent\ H} = 13.5$ $\delta H_{mixed\ solvent\ H} = 4.6$ $\delta D_{mixed\ solven}$

APPENDIX II. GENERAL MATERIAL PROPERTIES OF POLYUREA AEROGELS

Table S.II.1. General Material Properties of Polyurea Aerogels Prepared in Individual Solvents.

DoE run No.	linear shrinkage (%) [a,b]	bulk density (ρ_b, g cm^{-3}) [a]	skeletal density (ρ_s, g cm^{-3}) [c]	porosity (Π, % v/v) [d]	V_{Total} (cm^3 g^{-1}) [e]	single point volume ads. (V_{max}, cm^3 g^{-1}) [f]	Surface area (σ, m^2 g^{-1})	Ave. pore diameter (Φ, nm) [g]	particle radius (r, nm) [h]
acetonitrile									
1	14.88 ± 0.88	0.383 ± 0.001	1.226 ± 0.010	68.8 ± 1.0	1.80	0.067	20.4	360 (13)	123
2	10.88 ± 0.59	0.387 ± 0.003	1.186 ± 0.003	67.4 ± 0.4	1.74	0.013	4.37	1740 (13)	633
3	15.44 ± 0.13	0.328 ± 0.029	1.178 ± 0.003	72.2 ± 2.5	2.20	0.032	9.32	978 (14)	283
4	14.76 ± 0.42	0.327 ± 0.002	1.170 ± 0.001	69.4 ± 0.2	2.12	0.078	17.8	471 (17)	156
5	9.54 ± 0.28	0.330 ± 0.004	1.180 ± 0.001	72.0 ± 0.4	2.18	0.046	17.2	513 (11)	150
6	10.56 ± 0.94	0.259 ± 0.011	1.178 ± 0.001	78.0 ± 0.9	3.01	0.032	8.12	1505 (16)	319
7	10.6 ± 0.26	0.268 ± 0.002	1.178 ± 0.001	77.3 ± 0.2	2.88	0.026	8.53	1280 (12)	283
8	8.17 ± 0.37	0.265 ± 0.001	1.188 ± 0.004	77.7 ± 0.4	2.93	0.043	9.76	1172 (17)	253
9	8.63 ± 0.23	0.258 ± 0.001	1.187 ± 0.003	78.3 ± 0.3	3.03	0.075	23.1	527 (13)	110
10	8.88 ± 0.14	0.234 ± 0.001	1.230 ± 0.008	81.0 ± 0.8	3.46	0.086	24.2	577 (14)	102
11	8.17 ± 0.58	0.211 ± 0.003	1.173 ± 0.008	82.0 ± 0.9	3.89	1.329	113	138 (47)	23
12	11.08 ± 1.53	0.169 ± 0.006	1.187 ± 0.004	85.8 ± 0.7	5.07	0.050	16.9	1193 (12)	149
13	8.52 ± 1.20	0.151 ± 0.009	1.182 ± 0.003	87.2 ± 0.8	5.78	0.080	23.3	1005 (14)	111
14	9.58 ± 0.69	0.140 ± 0.002	1.221 ± 0.004	88.5 ± 0.5	6.32	0.140	32.8	766 (17)	75
15	3.85 ± 0.29	0.122 ± 0.001	1.236 ± 0.017	90.1 ± 1.9	7.39	1.543	97.7	302 (63)	25
16	5.52 ± 0.70	0.062 ± 0.001	1.199 ± 0.015	94.8 ± 1.7	15.30	0.245	60.2	1020 (16)	42
17	16.33 ± 0.56	0.396 ± 0.002	1.179 ± 0.002	66.4 ± 0.3	1.68	0.021	5.24	1344 (17)	509
18	14.13 ± 0.25	0.348 ± 0.002	1.200 ± 0.003	71.0 ± 0.3	2.04	0.019	4.85	1632 (15)	500
19	6.76 ± 0.65	0.381 ± 0.001	1.183 ± 0.002	67.8 ± 0.2	1.78	0.080	24.2	274 (12)	98
20	5.38 ± 0.37	0.263 ± 0.009	1.195 ± 0.002	78.0 ± 0.8	2.97	1.271	110	108 (46)	23
21	11.69 ± 0.57	0.376 ± 0.003	1.194 ± 0.004	68.5 ± 0.5	1.82	0.030	8.12	910 (15)	314
22	10.48 ± 0.56	0.372 ± 0.011	1.175 ± 0.002	68.3 ± 1.0	1.84	0.032	9.42	920 (16)	319
23	10.4 ± 0.86	0.295 ± 0.005	1.268 ± 0.017	76.7 ± 1.7	2.60	0.078	18.0	578 (17)	132
24	4.04 ± 0.72	0.216 ± 0.007	1.184 ± 0.002	81.8 ± 0.6	3.79	1.409	106	143 (53)	24
25	5.29 ± 0.43	0.071 ± 0.002	1.225 ± 0.018	94.2 ± 2.0	13.27	0.208	42.3	1264 (20)	59
26	5.92 ± 0.23	0.040 ± 0.001	1.261 ± 0.006	96.8 ± 0.7	24.21	2.509	202	479 (50)	12

[a] Average of 3 samples. [b] Linear shrinkage = 100 × (mold diameter – sample diameter)/ (mold diameter). [c] Single sample, average of 50 measurements. [d] Porosity (percent of empty space) $\Pi = 100 \times (\rho_s - \rho_b) / \rho_s$. [e] Calculated *via* $V_{Total} = (1/\rho_b) - (1/\rho_s)$. [f] The maximum volume of N_2 adsorbed along the isotherm as P/P_o approaches 1.0. [g] By the $4V/\sigma$ method; for the first number, V was taken equal to V_{Total} $(1/\rho_b) - (1/\rho_s)$; for the number in (parentheses), V was set equal to the maximum volume of N_2 adsorbed along the isotherm as P/P_o approaches 1.0. [h] Particle radius, $r = 3/(\rho_s \times \sigma)$.

Table S.II.1. General Material Properties of Polyurea Aerogels Prepared in Individual Solvents. (cont.)

DoE run No.	linear shrinkage (%) [a,b]	bulk density (ρ_b, g cm^{-3}) [a]	skeletal density (ρ_s, g cm^{-3}) [c]	porosity (Π, % v/v) [d]	V_{Total} (cm^3 g^{-1}) [e]	single point volume ads. (V_{max}, cm^3 g^{-1}) [f]	BET surface area (σ, m^2 g^{-1})	average pore diameter (Φ, nm) [g]	particle radius (r, nm) [h]
nitromethane									
1	20.96 ± 0.38	0.563 ± 0.035	1.177 ± 0.002	52.2 ± 0.3	0.93	0.033	29.1	128 (5)	88
2	21.42 ± 0.82	0.467 ± 0.015	1.189 ± 0.001	60.7 ± 1.3	1.30	0.045	22.2	236 (8)	115
3	18.42 ± 0.72	0.441 ± 0.012	1.179 ± 0.003	62.6 ± 1.1	1.42	0.057	22.1	258 (10)	116
4	17.75 ± 0.35	0.440 ± 0.014	1.190 ± 0.001	63.0 ± 1.2	1.43	0.062	42.2	136 (6)	60
5	18.50 ± 0.22	0.430 ± 0.005	1.194 ± 0.002	64.0 ± 0.5	1.49	0.151	38.8	153 (15)	65
6	16.25 ± 0.24	0.260 ± 0.012	1.179 ± 0.003	78.0 ± 1.1	3.00	0.045	15.2	800 (12)	170
7	14.62 ± 0.37	0.241 ± 0.015	1.196 ± 0.005	79.9 ± 1.4	3.31	0.048	23.2	576 (8)	109
8	13.85 ± 0.86	0.229 ± 0.011	1.173 ± 0.002	80.5 ± 1.0	3.51	0.122	39.3	334 (12)	61
9	14.13 ± 0.61	0.236 ± 0.009	1.182 ± 0.001	80.0 ± 0.8	3.39	0.119	44.5	323 (11)	61
10	14.23 ± 0.53	0.248 ± 0.002	1.180 ± 0.002	79.0 ± 0.3	3.18	0.208	42.3	303 (20)	61
11	14.69 ± 0.41	0.240 ± 0.035	1.209 ± 0.002	80.2 ± 2.9	3.34	0.025	95.2	141 (1)	26
12	14.27 ± 0.93	0.167 ± 0.016	1.193 ± 0.004	86.0 ± 1.4	5.15	0.032	26.1	792 (5)	97
13	9.35 ± 0.54	0.147 ± 0.002	1.180 ± 0.002	87.5 ± 0.3	5.96	0.049	17.4	1402 (12)	150
14	9.71 ± 0.76	0.146 ± 0.009	1.199 ± 0.005	87.8 ± 0.9	6.02	0.170	42.2	573 (16)	60
15	9.58 ± 0.51	0.132 ± 0.003	1.194 ± 0.007	88.9 ± 0.8	6.74	0.600	119	227 (20)	21
16	9.98 ± 0.14	0.068 ± 0.003	1.206 ± 0.020	94.4 ± 2.3	13.88	0.110	39.0	1424 (11)	64
17	23.90 ± 0.13	0.511 ± 0.023	1.183 ± 0.001	56.8 ± 1.9	1.11	0.025	9.36	493 (11)	282
18	21.46 ± 1.13	0.509 ± 0.008	1.180 ± 0.002	56.9 ± 0.7	1.12	0.037	12.2	373 (12)	212
19	22.63 ± 0.22	0.557 ± 0.016	1.185 ± 0.002	53.0 ± 1.4	0.95	0.193	45.1	84 (17)	57
20	10.06 ± 1.02	0.337 ± 0.003	1.178 ± 0.004	71.4 ± 0.5	2.12	0.282	74.1	115 (15)	35
21	20.25 ± 0.38	0.471 ± 0.005	1.188 ± 0.001	60.4 ± 0.4	1.28	0.046	15.1	341 (12)	169
22	19.21 ± 0.58	0.444 ± 0.008	1.185 ± 0.001	62.5 ± 0.7	1.41	0.048	16.2	353 (12)	158
23	18.34 ± 0.91	0.413 ± 0.007	1.189 ± 0.002	65.3 ± 0.6	1.58	0.175	45.3	140 (16)	56
24	9.83 ± 0.46	0.313 ± 0.007	1.190 ± 0.002	73.7 ± 0.6	2.35	0.394	95.2	99 (17)	27
25	9.38 ± 0.23	0.081 ± 0.001	1.164 ± 0.007	93.0 ± 0.8	11.49	0.077	32.9	1393 (9)	78
26	10.27 ± 0.73	0.041 ± 0.002	1.201 ± 0.023	96.6 ± 2.7	23.56	0.455	122	772 (15)	21

[a] Average of 3 samples. [b] Linear shrinkage = 100 × (mold diameter – sample diameter)/ (mold diameter). [c] Single sample, average of 50 measurements. [d] Porosity (percent of empty space) $\Pi = 100 \times (\rho_s - \rho_b) / \rho_s$. [e] Calculated *via* $V_{Total} = (1/\rho_b) - (1/\rho_s)$. [f] The maximum volume of N_2 adsorbed along the isotherm as P/P_o approaches 1.0. [g] By the $4V/\sigma$ method; for the first number, V was taken equal to $V_{Total} = (1/\rho_b) - (1/\rho_s)$; for the number in (parentheses), V was set equal to the maximum volume of N_2 adsorbed along the isotherm as P/P_o approaches 1.0. [h] Particle radius, $r = 3/(\rho_s \times \sigma)$.

Table S.II.1. General Material Properties of Polyurea Aerogels Prepared in Individual Solvents. (cont.)

DoE run No.	linear shrinkage (%) [a,b]	bulk density (ρ_b, g cm^{-3}) [a]	skeletal density (ρ_s, g cm^{-3}) [c]	porosity (Π, % v/v) [d]	V_{Total} (cm^3 g^{-1}) [e]	single point volume ads. (V_{max}, cm^3 g^{-1}) [f]	BET surface area (σ, m^2 g^{-1})	average pore diameter (Φ, nm) [h]	particle radius (r, nm) [i]
propylene carbonate									
1	25.83 ± 1.18	0.529 ± 0.018	1.195 ± 0.001	55.7 ± 1.5	1.05	0.287	75.0	56 (15)	34
2	25.87 ± 0.38	0.519 ± 0.020	1.181 ± 0.001	56.1 ± 1.7	1.08	0.190	81.5	53 (9)	31
3	26.56 ± 0.26	0.504 ± 0.022	1.214 ± 0.002	58.5 ± 1.8	1.16	0.220	54.8	86 (16)	46
4	24.79 ± 0.59	0.443 ± 0.019	1.197 ± 0.001	63.0 ± 1.6	1.42	0.259	73.5	77 (14)	34
5	24.31 ± 0.39	0.500 ± 0.017	1.185 ± 0.001	57.8 ± 1.4	1.16	0.190	86.4	54 (9)	30
6	22.50 ± 0.51	0.339 ± 0.015	1.180 ± 0.001	71.3 ± 1.3	2.10	0.137	82.4	102 (7)	31
7	22.81 ± 0.31	0.350 ± 0.013	1.201 ± 0.002	70.9 ± 1.1	2.02	0.154	87.7	92 (7)	29
8	19.72 ± 0.16	0.335 ± 0.012	1.188 ± 0.004	71.8 ± 1.1	2.14	0.405	78.3	110 (21)	33
9	19.42 ± 0.24	0.328 ± 0.010	1.188 ± 0.003	72.4 ± 0.9	2.21	0.417	75.3	118 (22)	34
10	18.06 ± 0.26	0.340 ± 0.017	1.192 ± 0.001	71.5 ± 1.4	2.10	0.276	69.1	122 (16)	37
11	18.97 ± 0.29	0.337 ± 0.009	1.204 ± 0.005	72.0 ± 0.9	2.14	0.533	123	70 (17)	21
12	14.19 ± 0.45	0.151 ± 0.006	1.198 ± 0.004	87.4 ± 0.7	5.79	0.088	67.6	341 (5)	37
13	11.66 ± 0.44	0.156 ± 0.003	1.176 ± 0.002	86.7 ± 0.3	5.56	0.170	49.4	445 (14)	51
14	15.38 ± 0.70	0.175 ± 0.005	1.218 ± 0.021	85.6 ± 2.3	4.89	0.058	46.3	425 (5)	54
15	12.94 ± 0.68	0.171 ± 0.001	1.210 ± 0.004	85.9 ± 0.4	5.02	0.185	78.5	254 (9)	32
16	12.75 ± 0.47	0.065 ± 0.001	1.225 ± 0.019	94.7 ± 2.1	14.57	0.073	60.9	955 (5)	40
17	28.77 ± 0.16	0.596 ± 0.031	1.200 ± 0.001	50.3 ± 2.6	0.84	0.302	69.9	48 (17)	36
18	27.71 ± 0.15	0.587 ± 0.034	1.203 ± 0.001	51.2 ± 2.8	0.87	0.208	47.3	74 (18)	53
19	23.54 ± 0.39	0.461 ± 0.014	1.195 ± 0.001	61.4 ± 1.2	1.33	0.721	137	40 (22)	19
20	19.48 ± 0.59	0.457 ± 0.041	1.198 ± 0.002	61.9 ± 3.4	1.35	0.706	237	23 (12)	11
21	28.75 ± 0.38	0.444 ± 0.020	1.189 ± 0.001	62.7 ± 1.7	1.41	0.567	86.8	65 (26)	29
22	26.88 ± 0.68	0.427 ± 0.018	1.219 ± 0.003	65.0 ± 1.5	1.52	0.518	73.4	83 (28)	34
23	25.21 ± 0.78	0.442 ± 0.004	1.194 ± 0.001	63.0 ± 0.3	1.42	0.188	77.3	74 (10)	33
24	7.50 ± 0.57	0.399 ± 0.054	1.188 ± 0.002	66.4 ± 4.5	1.66	1.872	227	29 (33)	11
25	10.94 ± 0.62	0.066 ± 0.001	1.202 ± 0.002	94.5 ± 0.2	14.32	0.060	50.6	1123 (5)	49
26	13.67 ± 0.26	0.080 ± 0.001	1.266 ± 0.008	93.7 ± 0.9	11.71	0.372	198	237 (8)	12

[a] Average of 3 samples. [b] Linear shrinkage = 100 × (mold diameter – sample diameter)/ (mold diameter). [c] Single sample, average of 50 measurements. [d] Porosity (percent of empty space) $\Pi = 100 \times (\rho_s - \rho_b) / \rho_s$. [e] Calculated *via* $V_{Total} = (1/\rho_b) - (1/\rho_s)$. [f] The maximum volume of N_2 adsorbed along the isotherm as P/P_o approaches 1.0. [h] By the $4V/\sigma$ method; for th first number, V was taken equal to $V_{Total} = (1/\rho_b) - (1/\rho_s)$; for the number in (parentheses), V was set equal to the maximum volume of N_2 adsorbed along the isotherm as P/P approaches 1.0. [i] Particle radius, $r = 3/(\rho_s \times \sigma)$.

Table S.II.1. General Material Properties of Polyurea Aerogels Prepared in Individual Solvents. (cont.)

DoE run No.	linear shrinkage (%) [a,b]	bulk density (ρ_b, g cm^{-3}) [a]	skeletal density (ρ_s, g cm^{-3}) [c]	porosity (Π, % v/v) [d]	V_{Total} (cm^3 g^{-1}) [e]	single point volume ads. (V_{max}, cm^3 g^{-1}) [f]	BET surface area (σ, m^2 g^{-1})	average pore diameter (Φ nm) [g]	particle radius (r, nm) [h]
acetone									
1	16.88 ± 1.02	0.584 ± 0.004	1.213 ± 0.002	51.9 ± 0.4	0.89	0.38	59.6	59 (25)	41
2	20.21 ± 0.29	0.488 ± 0.005	1.192 ± 0.004	59.1 ± 0.6	1.21	0.703	60.1	81 (47)	42
3	19.17 ± 0.29	0.531 ± 0.005	1.202 ± 0.002	55.8 ± 0.5	1.05	0.429	60.7	69 (28)	41
4	7.71 ± 0.59	0.358 ± 0.001	1.206 ± 0.001	70.3 ± 0.1	1.96	0.914	105	75 (35)	24
5	6.67 ± 0.59	0.349 ± 0.004	1.206 ± 0.006	71.1 ± 0.7	2.04	1.228	162	50 (30)	16
6	9.48 ± 0.39	0.274 ± 0.001	1.194 ± 0.001	77.1 ± 0.1	2.81	0.691	133	85 (21)	19
7	7.92 ± 0.15	0.270 ± 0.001	1.201 ± 0.006	77.5 ± 0.6	2.87	1.066	121	95 (35)	21
8	8.44 ± 0.26	0.277 ± 0.002	1.201 ± 0.001	76.9 ± 0.2	2.78	0.956	151	74 (25)	17
9	8.25 ± 0.19	0.266 ± 0.004	1.203 ± 0.003	77.9 ± 0.5	2.93	0.999	145	81 (28)	17
10	7.60 ± 0.53	0.266 ± 0.003	1.208 ± 0.001	78.0 ± 0.3	2.93	1.293	178	66 (29)	14
11	6.46 ± 0.59	0.244 ± 0.002	1.195 ± 0.004	79.6 ± 0.5	3.26	1.795	199	66 (36)	13
12	7.40 ± 0.82	0.166 ± 0.002	1.239 ± 0.007	86.6 ± 0.8	5.22	0.892	178	117 (20)	14
13	8.65 ± 0.29	0.162 ± 0.001	1.215 ± 0.004	86.7 ± 0.4	5.35	0.503	192	111 (10)	13
14	6.88 ± 0.88	0.159 ± 0.001	1.195 ± 0.002	86.7 ± 0.2	5.45	1.371	175	125 (31)	15
15	7.08 ± 0.29	0.150 ± 0.002	1.196 ± 0.004	87.5 ± 0.5	5.83	0.586	185	126 (13)	14
16	6.65 ± 0.29	0.082 ± 0.001	1.230 ± 0.023	93.3 ± 2.6	11.38	1.298	220	207 (24)	11
17	23.77 ± 1.07	0.625 ± 0.006	1.185 ± 0.003	47.3 ± 0.6	0.76	0.687	71.0	43 (39)	36
18	21.88 ± 1.02	0.605 ± 0.006	1.162 ± 0.011	47.9 ± 1.2	0.79	0.466	65.4	49 (29)	40
19	9.58 ± 0.29	0.416 ± 0.007	1.199 ± 0.005	65.3 ± 0.8	1.57	0.957	139	45 (28)	18
20	8.57 ± 0.35	0.321 ± 0.003	1.192 ± 0.003	73.1 ± 0.4	2.28	0.502	175	52 (11)	15
21	19.69 ± 1.33	0.492 ± 0.001	1.193 ± 0.001	58.8 ± 0.1	1.19	0.234	50.2	97 (19)	52
22	18.44 ± 0.68	0.480 ± 0.001	1.202 ± 0.001	60.1 ± 0.1	1.25	0.405	53.5	98 (32)	49
23	6.25 ± 0.65	0.321 ± 0.001	1.194 ± 0.002	73.1 ± 0.2	2.28	1.291	193	47 (27)	13
24	7.29 ± 0.15	0.323 ± 0.002	1.199 ± 0.003	73.1 ± 0.4	2.26	1.781	205	44 (35)	13
25	6.67 ± 0.59	0.064 ± 0.001	1.277 ± 0.025	95.0 ± 2.7	14.84	0.621	186	319 (13)	13
26	6.13 ± 0.35	0.079 ± 0.001	1.271 ± 0.022	93.8 ± 2.4	11.87	1.797	242	207 (31)	11

[a] Average of 3 samples. [b] Linear shrinkage = 100 × (mold diameter – sample diameter)/ (mold diameter). [c] Single sample, average of 50 measurements. [d] Porosity (percent of empty space) $\Pi = 100 \times (\rho_s - \rho_b) / \rho_s$. [e] Calculated *via* $V_{Total} = (1/\rho_b) - (1/\rho_s)$. [f] The maximum volume of N_2 adsorbed along the isotherm as P/P_o approache 1.0. [g] By the $4V/\sigma$ method; for the first number, V was taken equal to $V_{Total} = (1/\rho_b) - (1/\rho_s)$; for the number in (parentheses), V was set equal to the maximun volume of N_2 adsorbed along the isotherm as P/P_o approaches 1.0. [h] Particle radius, $r = 3/(\rho_s \times \sigma)$.

Table S.II.1. General Material Properties of Polyurea Aerogels Prepared in Individual Solvents. (cont.)

DoE run No.	linear shrinkage (%) [a,b]	bulk density (ρ_b, g cm^{-3}) [a]	skeletal density (ρ_s, g cm^{-3}) [c]	porosity (Π, % v/v) [d]	V_{Total} (cm^3 g^{-1}) [e]	single point volume ads. (V_{max}, cm^3 g^{-1}) [f]	surface area (σ, m^2 g^{-1})	average pore diameter (Φ, nm) [g]	particle radius (r, nm) [h]
THF									
1	20.23 ± 1.21	0.672 ± 0.037	1.210 ± 0.002	44.5 ± 3.1	0.66	0.276	73.1	36 (15)	34
2	27.13 ± 0.62	0.604 ± 0.098	1.175 ± 0.003	48.6 ± 8.3	0.80	0.299	69.1	45 (17)	36
3	21.10 ± 0.66	0.628 ± 0.018	1.183 ± 0.002	46.9 ± 1.5	0.75	0.363	109	28 (13)	24
4	18.75 ± 0.81	0.507 ± 0.051	1.197 ± 0.001	57.6 ± 4.3	1.14	0.394	114	40 (14)	22
5	17.13 ± 0.52	0.489 ± 0.009	1.207 ± 0.002	59.5 ± 0.8	1.22	0.679	157	31 (18)	16
6	23.29 ± 0.98	0.437 ± 0.011	1.179 ± 0.005	62.9 ± 1.1	1.44	1.068	130	44 (33)	20
7	20.23 ± 0.31	0.412 ± 0.008	1.167 ± 0.005	64.7 ± 0.9	1.57	1.100	152	41 (29)	17
8	19.54 ± 0.46	0.384 ± 0.008	1.183 ± 0.004	67.5 ± 0.8	1.76	1.312	184	38 (29)	14
9	17.52 ± 0.26	0.381 ± 0.009	1.187 ± 0.003	67.9 ± 0.8	1.78	1.354	181	39 (30)	14
10	15.15 ± 0.66	0.341 ± 0.019	1.192 ± 0.002	71.4 ± 1.6	2.09	1.383	182	46 (31)	14
11	14.85 ± 0.60	0.358 ± 0.007	1.187 ± 0.001	69.8 ± 0.6	1.95	1.731	208	38 (33)	12
12	13.23 ± 0.61	0.201 ± 0.012	1.222 ± 0.007	83.6 ± 1.2	4.16	0.889	165	101 (22)	15
13	14.73 ± 0.87	0.247 ± 0.001	1.215 ± 0.004	79.7 ± 0.4	3.23	1.776	199	65 (36)	13
14	14.71 ± 0.33	0.211 ± 0.007	1.198 ± 0.002	82.4 ± 0.6	3.90	2.077	188	83 (44)	14
15	12.06 ± 0.81	0.210 ± 0.005	1.223 ± 0.007	82.8 ± 0.8	3.94	1.531	231	68 (27)	11
16	9.57 ± 0.60	0.079 ± 0.002	1.211 ± 0.006	93.5 ± 0.7	11.83	1.779	242	196 (29)	10
17	[j]	[j]	[j]	[j]	[j]	[j]	[j]	[j]	[j]
18	21.44 ± 0.49	0.648 ± 0.010	1.209 ± 0.008	46.4 ± 1.1	0.72	0.313	81.9	35 (15)	31
19	14.71 ± 0.21	0.560 ± 0.010	1.191 ± 0.015	53.0 ± 1.7	0.95	0.762	178	21 (17)	14
20	14.81 ± 1.61	0.410 ± 0.014	1.222 ± 0.006	66.5 ± 1.3	1.62	1.379	219	30 (25)	11
21	22.15 ± 0.56	0.608 ± 0.016	1.205 ± 0.004	49.5 ± 1.4	0.81	0.491	95.1	34 (21)	26
22	27.65 ± 0.18	0.662 ± 0.007	1.186 ± 0.009	44.2 ± 1.0	0.67	0.251	71.2	38 (14)	36
23	15.44 ± 0.20	0.431 ± 0.008	1.210 ± 0.005	64.4 ± 0.8	1.49	0.854	167	36 (20)	15
24	8.75 ± 0.31	0.308 ± 0.036	1.263 ± 0.029	75.6 ± 4.1	2.45	1.921	242	40 (32)	10
25	10.18 ± 0.35	0.082 ± 0.003	1.210 ± 0.003	93.2 ± 0.4	11.37	1.744	232	201 (31)	11
26	9.36 ± 0.28	0.078 ± 0.002	1.221 ± 0.004	93.6 ± 0.5	12.00	1.838	242	198 (30)	10

[a] Average of 3 samples. [b] Linear shrinkage = 100 × (mold diameter – sample diameter)/ (mold diameter). [c] Single sample, average of 50 measurements. [d] Porosity (percent of empty space) $\Pi = 100 \times (\rho_s - \rho_b)/\rho_s$. [e] Calculated *via* $V_{Total} = (1/\rho_b) - (1/\rho_s)$. [f] The maximum volume of N_2 adsorbed along the isotherm as P/P_o approache 1.0. [h] By the $4V/\sigma$ method; for the first number, V was taken equal to $V_{Total} = (1/\rho_b) - (1/\rho_s)$; for the number in (parentheses), V was set equal to the maximun volume of N_2 adsorbed along the isotherm as P/P_o approaches 1.0. [i] Particle radius, $r = 3/(\rho_s \times \sigma)$. [j] That sample collapsed, the bulk density was >1.0 g cm^{-3} and th porosity was <30% v/v.

Table S.II.1. General Material Properties of Polyurea Aerogels Prepared in Individual Solvents. (cont.)

DoE run No.	linear shrinkage (%) [a,b]	bulk density (ρ_b, g cm^{-3}) [a]	skeletal density (ρ_s, g cm^{-3}) [c]	porosity (Π, % v/v) [d]	V_{Total} (cm^3 g^{-1}) [e]	single point volume ads. (V_{max}, cm^3 g^{-1}) [f]	BET surface area (σ, m^2 g^{-1})	average pore diameter (Φ, nm) [h]	particle radius (r, nm) [i]
ethyl acetate									
1	12.19 ± 0.72	0.347 ± 0.006	1.186 ± 0.006	70.7 ± 0.8	2.04	0.973	109	75 (36)	23
2	11.25 ± 0.83	0.375 ± 0.003	1.188 ± 0.001	68.4 ± 0.3	1.82	0.228	63.7	114 (14)	40
3	8.33 ± 0.81	0.358 ± 0.003	1.195 ± 0.001	70.0 ± 0.3	1.96	1.370	143	55 (38)	18
4	7.69 ± 0.66	0.334 ± 0.001	1.195 ± 0.005	72.1 ± 0.5	2.16	0.780	136	64 (23)	19
5	7.60 ± 0.64	0.323 ± 0.003	1.207 ± 0.001	73.2 ± 0.3	2.27	0.464	146	62 (13)	17
6	11.35 ± 0.15	0.279 ± 0.001	1.192 ± 0.001	76.6 ± 0.1	2.75	0.436	106	104 (16)	24
7	10.42 ± 0.69	0.279 ± 0.001	1.244 ± 0.005	77.6 ± 0.5	2.78	0.521	107	104 (19)	23
8	10.73 ± 0.41	0.270 ± 0.003	1.193 ± 0.001	77.4 ± 0.3	2.87	1.269	156	74 (33)	16
9	10.65 ± 0.39	0.270 ± 0.001	1.196 ± 0.003	77.4 ± 0.3	2.87	1.176	150	77 (31)	17
10	9.69 ± 0.42	0.270 ± 0.004	1.219 ± 0.003	77.9 ± 0.5	2.88	1.145	148	78 (31)	17
11	9.27 ± 0.68	0.254 ± 0.013	1.218 ± 0.002	79.2 ± 1.1	3.12	1.306	177	71 (30)	14
12	10.94 ± 0.42	0.170 ± 0.001	1.196 ± 0.002	85.8 ± 0.2	5.05	0.367	145	139 (10)	18
13	8.54 ± 0.54	0.177 ± 0.002	1.197 ± 0.003	85.2 ± 0.4	4.81	0.753	173	111 (17)	15
14	10.10 ± 0.64	0.168 ± 0.004	1.220 ± 0.004	86.2 ± 0.5	5.13	1.055	200	103 (21)	13
15	10.00 ± 0.51	0.167 ± 0.002	1.200 ± 0.003	86.1 ± 0.4	5.15	1.104	193	107 (23)	13
16	7.29 ± 0.34	0.080 ± 0.003	1.213 ± 0.010	93.4 ± 1.2	11.68	0.969	206	227 (19)	12
17	12.69 ± 0.3	0.405 ± 0.002	1.176 ± 0.004	65.6 ± 0.4	1.62	0.702	98.5	66 (29)	26
18	11.92 ± 0.46	0.410 ± 0.004	1.192 ± 0.004	65.6 ± 0.5	1.60	0.946	124	52 (31)	21
19	6.17 ± 0.26	0.327 ± 0.004	1.180 ± 0.004	72.3 ± 0.5	2.21	1.386	191	46 (29)	14
20	7.60 ± 0.55	0.316 ± 0.008	1.183 ± 0.003	73.3 ± 0.7	2.32	1.421	188	49 (30)	14
21	10.19 ± 0.37	0.346 ± 0.001	1.193 ± 0.005	71.0 ± 0.5	2.05	0.327	69.3	119 (19)	37
22	17.94 ± 0.29	0.352 ± 0.002	1.191 ± 0.004	70.5 ± 0.4	2.00	1.588	139	58 (46)	18
23	9.90 ± 0.49	0.285 ± 0.001	1.199 ± 0.001	76.2 ± 0.1	2.67	1.705	205	52 (33)	12
24	8.02 ± 0.64	0.278 ± 0.001	1.201 ± 0.001	76.9 ± 0.1	2.76	1.722	210	53 (33)	12
25	9.38 ± 0.40	0.071 ± 0.001	1.195 ± 0.001	94.1 ± 0.1	13.25	0.489	195	272 (10)	13
26	7.56 ± 0.44	0.071 ± 0.003	1.231 ± 0.002	94.2 ± 0.3	13.27	1.028	214	248 (19)	12

[a] Average of 3 samples. [b] Linear shrinkage = 100 × (mold diameter – sample diameter)/ (mold diameter). [c] Single sample, average of 50 measurements. [d] Porosity (percent of empty space) $\Pi = 100 \times (\rho_s - \rho_b) / \rho_s$. [e] Calculated *via* $V_{Total} = (1/\rho_b) - (1/\rho_s)$. [f] The maximum volume of N_2 adsorbed along the isotherm as P/P_o approaches 1.0. [h] By the $4V/\sigma$ method; for the first number, V was taken equal to $V_{Total} = (1/\rho_b) - (1/\rho_s)$; for the number in (parentheses), V was set equal to the maximum volume of N_2 adsorbed along the isotherm as P/P_o approaches 1.0. [i] Particle radius, $r = 3/(\rho_s \times \sigma)$.

Table S.II.1. General Material Properties of Polyurea Aerogels Prepared in Individual Solvents. (cont.)

DoE run No.	linear shrinkage (%) [a,b]	bulk density (ρ_b, g cm^{-3}) [a]	skeletal density (ρ_s, g cm^{-3}) [c]	porosity (Π, % v/v) [d]	V_{Total} (cm^3 g^{-1}) [e]	single point volume ads. (V_{max}, cm^3 g^{-1}) [f]	BET surface area (σ, m^2 g^{-1})	average pore diameter (Φ, nm) [h]	particle radius (r, nm) [i]
2-butanone									
1	22.90 ± 0.19	0.624 ± 0.002	1.182 ± 0.002	47.2 ± 0.3	0.76	0.679	89.2	34 (31)	29
2	22.21 ± 0.59	0.532 ± 0.011	1.186 ± 0.002	55.1 ± 0.9	1.04	0.698	78.5	53 (36)	33
3	20.54 ± 0.88	0.496 ± 0.013	1.184 ± 0.004	58.1 ± 1.2	1.17	0.946	93.4	50 (41)	27
4	9.71 ± 0.67	0.338 ± 0.009	1.189 ± 0.002	71.6 ± 0.8	2.12	1.496	174	49 (34)	15
5	8.38 ± 0.05	0.318 ± 0.001	1.197 ± 0.005	73.4 ± 0.5	2.31	1.779	232	40 (31)	11
6	15.44 ± 0.33	0.309 ± 0.002	1.192 ± 0.003	74.1 ± 0.4	2.40	0.558	107	90 (21)	24
7	12.67 ± 0.25	0.310 ± 0.004	1.197 ± 0.004	74.1 ± 0.5	2.39	1.614	167	57 (39)	15
8	9.75 ± 0.28	0.265 ± 0.004	1.202 ± 0.007	78.0 ± 0.8	2.94	1.288	170	69 (30)	15
9	9.62 ± 0.20	0.266 ± 0.003	1.198 ± 0.005	77.8 ± 0.6	2.92	1.221	170	69 (29)	15
10	8.35 ± 0.16	0.261 ± 0.001	1.224 ± 0.011	78.7 ± 1.1	3.01	1.469	172	70 (34)	14
11	7.92 ± 0.26	0.230 ± 0.001	1.184 ± 0.002	80.6 ± 0.2	3.50	1.690	194	72 (35)	13
12	9.06 ± 0.10	0.150 ± 0.001	1.210 ± 0.015	87.6 ± 1.7	5.84	1.113	191	122 (23)	13
13	7.90 ± 0.11	0.147 ± 0.001	1.205 ± 0.009	87.8 ± 1.0	5.97	0.918	177	135 (21)	14
14	8.69 ± 0.27	0.160 ± 0.002	1.252 ± 0.011	87.2 ± 1.2	5.45	1.852	197	111 (38)	12
15	8.56 ± 0.31	0.149 ± 0.001	1.226 ± 0.015	87.9 ± 1.6	5.90	1.500	211	112 (28)	12
16	8.92 ± 0.21	0.066 ± 0.002	1.238 ± 0.028	94.7 ± 3.1	14.34	0.741	216	266 (14)	11
17	22.42 ± 0.64	0.610 ± 0.014	1.207 ± 0.005	49.5 ± 1.2	0.81	0.607	81.8	40 (30)	31
18	23.13 ± 0.32	0.639 ± 0.004	1.237 ± 0.002	48.3 ± 0.4	0.76	0.591	85.9	35 (27)	28
19	10.21 ± 0.28	0.365 ± 0.007	1.190 ± 0.002	69.3 ± 0.6	1.90	1.028	178	43 (23)	14
20	8.46 ± 0.34	0.340 ± 0.002	1.194 ± 0.001	71.5 ± 0.2	2.10	1.350	199	42 (27)	13
21	21.98 ± 0.59	0.519 ± 0.011	1.184 ± 0.001	56.2 ± 0.9	1.08	1.053	153	28 (28)	17
22	18.25 ± 0.64	0.444 ± 0.006	1.186 ± 0.001	62.6 ± 0.5	1.41	1.272	164	34 (31)	16
23	9.50 ± 0.18	0.319 ± 0.006	1.186 ± 0.003	73.1 ± 0.6	2.29	1.530	207	44 (30)	12
24	10.58 ± 0.59	0.291 ± 0.008	1.185 ± 0.003	75.4 ± 0.7	2.59	1.789	227	46 (32)	11
25	9.17 ± 0.30	0.069 ± 0.001	1.209 ± 0.018	94.3 ± 2.0	13.67	1.172	223	245 (21)	11
26	11.13 ± 1.52	0.051 ± 0.001	1.215 ± 0.019	95.8 ± 2.2	18.78	1.564	242	310 (26)	10

[a] Average of 3 samples. [b] Linear shrinkage = 100 × (mold diameter – sample diameter)/ (mold diameter). [c] Single sample, average of 50 measurements. [d] Porosity (percent of empty space) $\Pi = 100 \times (\rho_s - \rho_b) / \rho_s$. [e] Calculated *via* $V_{Total} = (1/\rho_b) - (1/\rho_s)$. [f] The maximum volume of N_2 adsorbed along the isotherm as P/P_o approaches1.0. [h] By the $4V/\sigma$ method; for the first number, V was taken equal to $V_{Total} = (1/\rho_b) - (1/\rho_s)$; for the number in (parentheses), V was set equal to the maximum volume of N_2 adsorbed along the isotherm as P/P_o approaches 1.0. [i] Particle radius, $r = 3/(\rho_s \times \sigma)$.

Table S.II.1. General Material Properties of Polyurea Aerogels Prepared in Individual Solvents. (cont.)

DoE run No.	linear shrinkage (%) [a,b]	bulk density (ρ_b, g cm^{-3}) [a]	skeletal density (ρ_s, g cm^{-3}) [c]	porosity (Π, % v/v) [d]	V_{Total} (cm^3 g^{-1}) [e]	single point volume ads. (V_{max}, cm^3 g^{-1}) [f]	BET surface area (σ, m^2 g^{-1})	average pore diameter (Φ, nm) [h]	particle radius (r, nm) [i]
DMF [j]									
12	34.69 ± 0.26	0.326 ± 0.002	1.215 ± 0.002	73.2 ± 0.3	2.24	0.526	133	67 (16)	19
13	31.46 ± 1.26	0.350 ± 0.022	1.228 ± 0.005	71.5 ± 1.9	2.04	0.611	144	57 (17)	17
14	34.48 ± 0.29	0.310 ± 0.004	1.214 ± 0.005	74.5 ± 0.6	2.40	0.443	128	75 (14)	19
15	33.23 ± 0.39	0.298 ± 0.009	1.226 ± 0.005	75.7 ± 0.9	2.54	0.461	104	98 (18)	24
16	19.06 ± 0.79	0.101 ± 0.003	1.229 ± 0.006	91.8 ± 0.7	9.09	0.282	228	159 (5)	11
25	22.44 ± 0.39	0.121 ± 0.004	1.234 ± 0.004	90.2 ± 0.5	7.45	1.452	199	150 (29)	12
26	21.54 ± 0.62	0.085 ± 0.003	1.222 ± 0.005	93.0 ± 0.6	10.95	1.571	230	190 (27)	11

[a] Average of 3 samples. [b] Linear shrinkage = 100 × (mold diameter – sample diameter)/ (mold diameter). [c] Single sample, average of 50 measurements. [d] Porosity (percent of empty space) $\Pi = 100 \times (\rho_s - \rho_b) / \rho_s$. [e] Calculated *via* $V_{Total} = (1/\rho_b) - (1/\rho_s)$. [f] The maximum volume of N_2 adsorbed along the isotherm as P/P_o approaches 1.0. [g] Cumulative volume of pores between 1.7 nm and 300 nm from N_2-sorption data and the BJH desorption method. [h] By the $4V/\sigma$ method; for the first number, V was taken equal to $V_{Total} = (1/\rho_b) - (1/\rho_s)$; for the number in (parentheses), V was set equal to the maximum volume of N_2 adsorbed along the isotherm as P/P_o approaches 1.0. [i] Particle radius, $r = 3/(\rho_s \times \sigma)$. [j] All samples from Runs 1–11 and 17–24 collapsed, the bulk densities were >1.0 g cm^{-3} and the porosities were <30% v/v. Those samples were not considered further.

Table S.II.2. General Material Properties of Polyurea Aerogels Prepared in Binary Solvent Systems.

DoE run No. [a]	linear shrinkage (%) [b,c]	bulk density (ρ_b, g cm^{-3}) [b]	skeletal density (ρ_s, g cm^{-3}) [d]	porosity (Π, % v/v) [e]	V_{Total} (cm^3 g^{-1}) [f]	single point volume ads. (V_{max}, cm^3 g^{-1}) [g]	surface area (σ, m^2 g^{-1})	average pore diameter (Φ, nm) [i]	particle radius (r, nm) [j]
BINARY SOLVENT SYSTEMS									
A: acetonitrile-nitromethane 1:1 v/v									
1	23.47 ± 0.94	0.537 ± 0.020	1.180 ± 0.001	54.5 ± 1.7	1.01	0.075	23.2	144 (11)	91
24	8.03 ± 0.74	0.257 ± 0.003	1.197 ± 0.004	78.5 ± 0.5	3.06	1.010	107	114 (38)	23
2	18.25 ± 0.54	0.355 ± 0.005	1.178 ± 0.005	69.9 ± 0.7	1.97	0.398	17.5	450 (91)	146
B: acetonitrile-propylene carbonate 1:1 v/v									
1	22.79 ± 0.98	0.508 ± 0.012	1.188 ± 0.001	57.2 ± 1.0	1.13	0.129	37.9	119 (14)	67
8	16.53 ± 0.31	0.241 ± 0.008	1.184 ± 0.009	79.7 ± 1.2	3.30	0.216	63.7	208 (14)	40
16	4.78 ± 0.24	0.059 ± 0.002	1.257 ± 0.052	95.3 ± 5.7	16.15	0.309	131	493 (9)	18
26	4.97 ± 0.41	0.050 ± 0.004	1.272 ± 0.106	96.1 ± 1.6	19.21	0.933	222	346 (17)	11
C: acetonitrile-acetone 1:1 v/v									
17	19.44 ± 0.19	0.511 ± 0.010	1.174 ± 0.002	56.5 ± 0.9	1.11	0.134	46.3	95 (12)	55
8	9.02 ± 0.46	0.258 ± 0.004	1.171 ± 0.001	78.0 ± 0.4	3.02	0.348	58.9	205 (24)	43
16	4.94 ± 0.31	0.054 ± 0.001	1.190 ± 0.029	95.5 ± 3.4	17.68	0.439	115	615 (15)	22
D: acetonitrile-DMF 1:1 v/v									
6	26.54 ± 0.43	0.411 ± 0.007	1.195 ± 0.003	65.6 ± 0.7	1.60	0.158	67.7	94 (9)	37
13	21 ± 0.21	0.175 ± 0.003	1.199 ± 0.002	85.4 ± 0.3	4.88	1.520	158	124 (38)	16
16	11.31 ± 0.54	0.079 ± 0.002	1.204 ± 0.005	93.4 ± 0.6	11.83	1.351	204	232 (26)	12
E: acetone-ethyl acetate 1:1 v/v									
17	20.9 ± 0.24	0.587 ± 0.004	1.178 ± 0.002	50.2 ± 0.4	0.85	0.466	57.9	59 (32)	44
8	11.29 ± 0.06	0.274 ± 0.002	1.161 ± 0.001	76.4 ± 0.2	2.79	1.654	176	63 (38)	15
F: ethyl acetate-DMF 1:1 v/v									
15	20.00 ± 0.19	0.191 ± 0.003	1.199 ± 0.003	84.1 ± 0.4	4.40	1.562	189	93 (33)	13
26	27.00 ± 0.75	0.075 ± 0.003	1.175 ± 0.017	93.6 ± 2.0	12.48	1.132	263	190 (17)	10
G: nitromethane-2-butanone 1:1 v/v									
12	9.31 ± 0.11	0.159 ± 0.002	1.197 ± 0.003	86.7 ± 0.4	5.45	0.558	105	208 (21)	24
22	19.63 ± 0.49	0.405 ± 0.005	1.196 ± 0.002	66.1 ± 0.5	1.63	0.091	87.3	75 (4)	29
H: propylene carbonate-2-butanone v/v									
25	4.65 ± 0.31	0.065 ± 0.001	1.231 ± 0.013	94.7 ± 1.5	14.57	1.527	209	279 (29)	12

[a] Run numbers were selected randomly from Table S.I.2 of Appendix I. [b] Average of 3 samples. [c] Linear shrinkage = 100 × (mold diameter – sample diameter)/ (mold diameter). [d] Single sample, average of 50 measurements. [e] Porosity (percent of empty space) $\Pi = 100 \times (\rho_s - \rho_b) / \rho_s$. [f] Calculated *via* $V_{Total} = (1/\rho_b) - (1/\rho_s)$. [g] The maximum volume of N_2 adsorbed along the isotherm as P/P_o approaches 1.0. [i] By the $4V/\sigma$ method; for the first number, V was taken equal to $V_{Total} = (1/\rho_b - (1/\rho_s)$; for the number in (parentheses), V was set equal to the maximum volume of N_2 absorbed along the isotherm as P/P_o approaches 1.0. [j] Particle radius, $= 3/(\rho_s \times \sigma)$

APPENDIX III. POROSITIES, CONTACT ANGLES AND *K*-INDEXES OF ALL POLYUREA AEROGELS PREPARED IN INDIVIDULA AND BINARY SOLVENT SYSTEMS

Table S.III.1. *K*-indexes of Polyurea Aerogels Prepared in Individual and Binary Solvent Systems, and Data Used for their Calculation.

DoE run No.	porosity (*Π*, % v/v) [a]	contact angle (*θ*, deg.)	*K*-index
acetonitrile			
1	68.8 ± 1.0	125.2 ± 0.5	1.82 ± 0.03
2	67.4 ± 0.4	121.4 ± 0.6	1.80 ± 0.01
3	72.2 ± 2.5	133.6 ± 0.1	1.85 ± 0.06
4	69.4 ± 0.2	126.7 ± 0.9	1.83 ± 0.01
5	72.0 ± 0.4	132.4 ± 1.1	1.84 ± 0.02
6	78.0 ± 0.9	144.1 ± 0.1	1.85 ± 0.02
7	77.3 ± 0.2	137.8 ± 0.4	1.78 ± 0.01
8	77.7 ± 0.4	139.3 ± 1.4	1.79 ± 0.02
9	78.3 ± 0.3	137.1 ± 0.1	1.75 ± 0.01
10	81.0 ± 0.8	140.3 ± 1.1	1.73 ± 0.02
11	82.0 ± 0.9	134.6 ± 0.5	1.64 ± 0.02
12	85.8 ± 0.7	142.5 ± 0.9	1.66 ± 0.02
13	87.2 ± 0.8	144.5 ± 0.4	1.66 ± 0.02
14	88.5 ± 0.5	146.8 ± 0.3	1.66 ± 0.01
15	90.1 ± 1.9	146.4 ± 1.6	1.62 ± 0.04
16	94.8 ± 1.7	152.3 ± 2.1	1.61 ± 0.04
17	66.4 ± 0.3	127.8 ± 1.1	1.92 ± 0.02
18	71.0 ± 0.3	128.5 ± 2.1	1.81 ± 0.03
19	67.8 ± 0.2	123.8 ± 1.4	1.83 ± 0.02
20	78.0 ± 0.8	90.00 ± 0.3	1.15 ± 0.01
21	68.5 ± 0.5	128.7 ± 0.5	1.88 ± 0.01
22	68.3 ± 1.0	126.0 ± 1.2	1.84 ± 0.03
23	76.7 ± 1.7	132.8 ± 0.9	1.73 ± 0.04
24	81.8 ± 0.6	102.1 ± 1.6	1.25 ± 0.02
25	94.2 ± 2.0	151.2 ± 1.8	1.61 ± 0.04
26	96.8 ± 0.7	152.3 ± 1.3	1.57 ± 0.02

DoE run No.	porosity (*Π*, % v/v) [a]	contact angle (*θ*, deg.)	*K*-index
nitromethane			
1	52.2 ± 3.0	79.90 ± 0.2	1.53 ± 0.09
2	60.7 ± 1.3	88.30 ± 0.1	1.45 ± 0.03
3	62.6 ± 1.1	92.00 ± 0.6	1.47 ± 0.03
4	63.0 ± 1.2	91.50 ± 0.1	1.45 ± 0.03
5	64.0 ± 0.5	117.8 ± 0.3	1.84 ± 0.01
6	78.0 ± 1.1	138.0 ± 1.6	1.77 ± 0.03
7	79.9 ± 1.4	140.3 ± 0.5	1.76 ± 0.03
8	80.5 ± 1.0	141.3 ± 0.1	1.76 ± 0.02
9	80.0 ± 0.8	141.4 ± 0.1	1.77 ± 0.02
10	79.0 ± 0.3	135.7 ± 2.1	1.72 ± 0.03
11	80.2 ± 2.9	94.40 ± 1.2	1.18 ± 0.05
12	86.0 ± 1.4	143.7 ± 0.8	1.67 ± 0.03
13	87.5 ± 0.3	146.1 ± 1.2	1.67 ± 0.01
14	87.8 ± 0.9	145.1 ± 0.2	1.65 ± 0.02
15	88.9 ± 0.8	145.5 ± 1.1	1.64 ± 0.02
16	94.4 ± 2.3	151.4 ± 1.4	1.60 ± 0.04
17	56.8 ± 1.9	86.50 ± 0.4	1.52 ± 0.05
18	56.9 ± 0.7	85.50 ± 0.9	1.50 ± 0.02
19	53.0 ± 1.4	81.10 ± 0.1	1.53 ± 0.04
20	71.4 ± 0.5	95.30 ± 0.6	1.33 ± 0.01
21	60.4 ± 0.4	89.20 ± 0.5	1.48 ± 0.01
22	62.5 ± 0.7	93.00 ± 1.0	1.49 ± 0.02
23	65.3 ± 0.6	87.20 ± 0.5	1.34 ± 0.01
24	73.7 ± 0.6	98.10 ± 0.3	1.33 ± 0.01
25	93.0 ± 0.8	152.0 ± 1.2	1.63 ± 0.02
26	96.6 ± 2.7	150.7 ± 0.9	1.56 ± 0.04

Table S.III.1. *K*-indexes of Polyurea Aerogels Prepared in Individual and Binary Solvent Systems, and Data Used for their Calculation. (cont.)

DoE run No.	porosity (*Π*, % v/v) [a]	contact angle (*θ*, deg.)	*K*-index
propylene carbonate			
1	55.7 ± 1.5	85.00 ± 0.8	1.53 ± 0.04
2	56.1 ± 1.7	80.40 ± 1.3	1.43 ± 0.05
3	58.5 ± 1.8	83.90 ± 1.1	1.43 ± 0.05
4	63.0 ± 1.6	91.20 ± 0.1	1.45 ± 0.04
5	57.8 ± 1.4	82.50 ± 0.8	1.43 ± 0.04
6	71.3 ± 1.3	95.00 ± 0.9	1.33 ± 0.03
7	70.9 ± 1.1	95.10 ± 0.5	1.34 ± 0.02
8	71.8 ± 1.1	95.30 ± 1.3	1.33 ± 0.03
9	72.4 ± 0.9	95.70 ± 0.9	1.32 ± 0.02
10	71.5 ± 1.4	96.20 ± 0.1	1.35 ± 0.03
11	72.0 ± 0.9	118.8 ± 1.2	1.65 ± 0.03
12	87.4 ± 0.7	145.0 ± 0.5	1.66 ± 0.01
13	86.7 ± 0.3	143.5 ± 1.3	1.65 ± 0.02
14	85.6 ± 2.3	140.4 ± 1.1	1.64 ± 0.05
15	85.9 ± 0.4	140.2 ± 0.9	1.63 ± 0.01
16	94.7 ± 2.1	147.4 ± 1.2	1.56 ± 0.04
17	50.3 ± 2.6	77.20 ± 0.5	1.53 ± 0.08
18	51.2 ± 2.8	78.50 ± 0.2	1.53 ± 0.08
19	61.4 ± 1.2	88.60 ± 0.4	1.44 ± 0.03
20	61.9 ± 3.4	88.40 ± 1.2	1.43 ± 0.08
21	62.7 ± 1.7	90.50 ± 0.1	1.44 ± 0.04
22	65.0 ± 1.5	90.50 ± 0.5	1.39 ± 0.03
23	63.0 ± 0.3	91.00 ± 0.1	1.44 ± 0.01
24	66.4 ± 4.5	88.40 ± 0.7	1.33 ± 0.09
25	94.5 ± 0.2	148.1 ± 1.4	1.57 ± 0.02
26	93.7 ± 0.9	146.0 ± 0.6	1.56 ± 0.02

DoE run No.	porosity (*Π*, % v/v) [a]	contact angle (*θ*, deg.)	*K*-index
acetone			
1	51.9 ± 0.4	77.80 ± 0.9	1.50 ± 0.02
2	59.1 ± 0.6	81.90 ± 1.2	1.39 ± 0.02
3	55.8 ± 0.5	80.20 ± 0.4	1.44 ± 0.01
4	70.3 ± 0.1	95.40 ± 1.0	1.36 ± 0.01
5	71.1 ± 0.7	96.40 ± 0.4	1.36 ± 0.01
6	77.1 ± 0.1	97.10 ± 0.3	1.26 ± 0.00
7	77.5 ± 0.6	98.50 ± 1.4	1.27 ± 0.02
8	76.9 ± 0.2	98.50 ± 0.1	1.28 ± 0.00
9	77.9 ± 0.5	100.0 ± 0.3	1.28 ± 0.01
10	78.0 ± 0.3	99.50 ± 1.1	1.28 ± 0.01
11	79.6 ± 0.5	102.5 ± 2.0	1.29 ± 0.03
12	86.6 ± 0.8	104.3 ± 0.6	1.20 ± 0.01
13	86.7 ± 0.4	105.9 ± 1.8	1.22 ± 0.02
14	86.7 ± 0.2	107.1 ± 1.0	1.24 ± 0.01
15	87.5 ± 0.5	106.3 ± 0.7	1.21 ± 0.01
16	93.3 ± 2.6	115.3 ± 0.6	1.24 ± 0.03
17	47.3 ± 0.6	70.90 ± 0.3	1.50 ± 0.02
18	47.9 ± 1.2	71.90 ± 0.1	1.50 ± 0.04
19	65.3 ± 0.8	93.60 ± 0.5	1.43 ± 0.02
20	73.1 ± 0.4	102.3 ± 0.7	1.40 ± 0.01
21	58.8 ± 0.1	84.00 ± 1.1	1.43 ± 0.02
22	60.1 ± 0.1	86.90 ± 0.1	1.45 ± 0.00
23	73.1 ± 0.2	96.80 ± 0.1	1.32 ± 0.00
24	73.1 ± 0.4	97.30 ± 0.6	1.33 ± 0.01
25	95.0 ± 2.7	113.8 ± 0.2	1.20 ± 0.03
26	93.8 ± 2.4	112.6 ± 1.1	1.20 ± 0.03

Table S.III.1. *K*-indexes of Polyurea Aerogels Prepared in Individual and Binary Solvent Systems, and Data Used for their Calculation. (cont.)

DoE run No.	porosity (*Π*, % v/v) [a]	contact angle (*θ*, deg.)	*K*-index
THF			
1	44.5 ± 3.1	66.70 ± 0.1	1.50 ± 0.10
2	48.6 ± 8.3	74.50 ± 0.6	1.53 ± 0.26
3	46.9 ± 1.5	70.90 ± 0.1	1.51 ± 0.05
4	57.6 ± 4.3	88.30 ± 0.7	1.53 ± 0.11
5	59.5 ± 0.8	89.10 ± 0.9	1.50 ± 0.02
6	62.9 ± 1.1	91.20 ± 0.1	1.45 ± 0.02
7	64.7 ± 0.9	91.50 ± 1.6	1.41 ± 0.03
8	67.5 ± 0.8	87.80 ± 0.1	1.30 ± 0.02
9	67.9 ± 0.8	90.20 ± 0.1	1.33 ± 0.02
10	71.4 ± 1.6	95.20 ± 1.3	1.33 ± 0.04
11	69.8 ± 0.6	92.80 ± 0.6	1.33 ± 0.01
12	83.6 ± 1.2	100.1 ± 0.5	1.20 ± 0.02
13	79.7 ± 0.4	97.80 ± 1.7	1.23 ± 0.02
14	82.4 ± 0.6	100.4 ± 0.4	1.22 ± 0.01
15	82.8 ± 0.8	101.4 ± 1.4	1.22 ± 0.02
16	93.5 ± 0.7	112.0 ± 1.4	1.20 ± 0.02
17	[b]	[b]	[b]
18	46.4 ± 1.1	69.60 ± 0.1	1.50 ± 0.04
19	53.0 ± 1.7	80.70 ± 1.1	1.52 ± 0.05
20	66.5 ± 1.3	100.8 ± 0.6	1.52 ± 0.03
21	49.5 ± 1.4	76.40 ± 0.1	1.54 ± 0.04
22	44.2 ± 1.0	67.20 ± 0.2	1.52 ± 0.04
23	64.4 ± 0.8	95.60 ± 0.1	1.48 ± 0.02
24	75.6 ± 4.1	115.1 ± 1.5	1.52 ± 0.08
25	93.2 ± 0.4	113.4 ± 0.1	1.22 ± 0.01
26	93.6 ± 0.5	113.8 ± 0.5	1.22 ± 0.01

DoE run No.	porosity (*Π*, % v/v) [a]	contact angle (*θ*, deg.)	*K*-index
ethyl acetate			
1	70.7 ± 0.8	97.90 ± 0.1	1.38 ± 0.02
2	68.4 ± 0.3	91.40 ± 0.3	1.34 ± 0.01
3	70.0 ± 0.3	93.10 ± 1.4	1.33 ± 0.02
4	72.1 ± 0.5	96.50 ± 1.3	1.34 ± 0.02
5	73.2 ± 0.3	96.60 ± 1.5	1.32 ± 0.02
6	76.6 ± 0.1	98.50 ± 1.6	1.29 ± 0.02
7	77.6 ± 0.5	98.50 ± 0.1	1.27 ± 0.01
8	77.4 ± 0.3	98.70 ± 0.1	1.28 ± 0.00
9	77.4 ± 0.3	98.40 ± 1.6	1.27 ± 0.02
10	77.9 ± 0.5	98.60 ± 0.1	1.27 ± 0.01
11	79.2 ± 1.1	99.60 ± 0.2	1.26 ± 0.02
12	85.8 ± 0.2	102.5 ± 1.5	1.19 ± 0.02
13	85.2 ± 0.4	105.5 ± 0.1	1.24 ± 0.01
14	86.2 ± 0.5	106.2 ± 0.1	1.23 ± 0.01
15	86.1 ± 0.4	105.3 ± 1.4	1.22 ± 0.02
16	93.4 ± 1.2	114.2 ± 0.1	1.22 ± 0.02
17	65.6 ± 0.4	93.50 ± 0.1	1.43 ± 0.01
18	65.6 ± 0.5	90.10 ± 0.4	1.37 ± 0.01
19	72.3 ± 0.5	98.40 ± 0.9	1.36 ± 0.02
20	73.3 ± 0.7	101.8 ± 0.8	1.39 ± 0.02
21	71.0 ± 0.5	95.50 ± 0.6	1.35 ± 0.01
22	70.5 ± 0.4	93.20 ± 0.5	1.32 ± 0.01
23	76.2 ± 0.1	99.10 ± 0.1	1.30 ± 0.00
24	76.9 ± 0.1	99.40 ± 1.1	1.29 ± 0.01
25	94.1 ± 0.1	116.1 ± 0.1	1.23 ± 0.00
26	94.2 ± 0.3	114.1 ± 0.4	1.21 ± 0.01

Table S.III.1. *K*-indexes of Polyurea Aerogels Prepared in Individual and Binary Solvent Systems, and Data Used for their Calculation. (cont.)

DoE run No.	porosity (*Π*, % v/v) [a]	contact angle (*θ*, deg.)	*K*-index
2-butanone			
1	47.2 ± 0.3	70.80 ± 0.6	1.50 ± 0.02
2	55.1 ± 0.9	79.70 ± 1.2	1.45 ± 0.03
3	58.1 ± 1.2	84.10 ± 0.1	1.45 ± 0.03
4	71.6 ± 0.8	96.70 ± 1.1	1.35 ± 0.02
5	73.4 ± 0.5	99.20 ± 0.1	1.35 ± 0.01
6	74.1 ± 0.4	96.80 ± 1.5	1.31 ± 0.02
7	74.1 ± 0.5	96.70 ± 1.1	1.30 ± 0.02
8	78.0 ± 0.8	99.30 ± 1.6	1.27 ± 0.02
9	77.8 ± 0.6	98.20 ± 1.4	1.26 ± 0.02
10	78.7 ± 1.1	98.60 ± 0.2	1.25 ± 0.02
11	80.6 ± 0.2	101.6 ± 0.7	1.26 ± 0.01
12	87.6 ± 1.7	106.5 ± 1.2	1.22 ± 0.03
13	87.8 ± 1.0	109.5 ± 0.1	1.25 ± 0.01
14	87.2 ± 1.2	113.9 ± 1.5	1.31 ± 0.02
15	87.9 ± 1.6	113.5 ± 0.1	1.29 ± 0.02
16	94.7 ± 3.1	114.7 ± 1.2	1.21 ± 0.04
17	49.5 ± 1.2	74.20 ± 1.4	1.50 ± 0.05
18	48.3 ± 0.4	72.50 ± 0.1	1.50 ± 0.01
19	69.3 ± 0.6	94.20 ± 0.1	1.36 ± 0.01
20	71.5 ± 0.2	96.80 ± 0.1	1.35 ± 0.00
21	56.2 ± 0.9	80.90 ± 0.9	1.44 ± 0.03
22	62.6 ± 0.5	90.70 ± 0.1	1.45 ± 0.01
23	73.1 ± 0.6	95.50 ± 0.6	1.31 ± 0.01
24	75.4 ± 0.7	98.10 ± 0.8	1.30 ± 0.02
25	94.3 ± 2.0	110.5 ± 0.6	1.17 ± 0.03
26	95.8 ± 2.2	117.6 ± 1.3	1.23 ± 0.03

DoE run No.	porosity (*Π*, % v/v) [a]	contact angle (*θ*, deg.)	*K*-index
DMF [c]			
12	73.2 ± 0.3	111.4 ± 0.1	1.52 ± 0.01
13	71.5 ± 1.9	103.4 ± 0.1	1.45 ± 0.04
14	74.5 ± 0.6	106.3 ± 1.0	1.43 ± 0.02
15	75.7 ± 0.9	109.6 ± 0.1	1.45 ± 0.02
16	91.8 ± 0.7	113.3 ± 0.3	1.23 ± 0.01
25	90.2 ± 0.5	109.8 ± 0.8	1.22 ± 0.01
26	93.0 ± 0.6	116.0 ± 0.1	1.25 ± 0.01

Table S.III.1. *K*-indexes of Polyurea Aerogels Prepared in Individual and Binary Solvent Systems, and Data Used for their Calculation. (cont.)

DoE run No. [d]	porosity (*Π*, % v/v) [a]	contact angle (*θ*, deg.)	*K*-index
BINARY SOLVENT SYSTEMS			
A: acetonitrile-nitromethane 1:1 v/v			
1	54.5 ± 1.7	83.80 ± 0.5	1.54 ± 0.05
24	78.5 ± 0.5	100.6 ± 1.0	1.28 ± 0.02
2	69.9 ± 0.7	128.1 ± 1.1	1.83 ± 0.02
B: acetonitrile-propylene carbonate 1:1 v/v			
1	57.2 ± 1.0	88.30 ± 0.1	1.54 ± 0.03
8	79.7 ± 1.2	109.2 ± 0.5	1.37 ± 0.02
16	95.3 ± 5.7	149.2 ± 1.5	1.57 ± 0.10
26	96.1 ± 11.6	149.8 ± 1.6	1.56 ± 0.19
C: acetonitrile-acetone 1:1 v/v			
17	56.5 ± 0.9	85.80 ± 0.3	1.52 ± 0.02
8	78.0 ± 0.4	138.6 ± 2.1	1.78 ± 0.03
16	95.5 ± 3.4	149.7 ± 2.3	1.57 ± 0.06
D: acetonitrile-DMF 1:1 v/v			
6	65.6 ± 0.7	93.60 ± 0.3	1.43 ± 0.02
13	85.4 ± 0.3	100.7 ± 0.1	1.18 ± 0.00
16	93.4 ± 0.6	110.8 ± 1.6	1.19 ± 0.02
E: acetone-ethyl acetate 1:1 v/v			
17	50.2 ± 0.4	76.80 ± 0.1	1.53 ± 0.01
8	76.4 ± 0.2	99.10 ± 1.2	1.30 ± 0.02
F: ethyl acetate-DMF 1:1 v/v			
15	84.1 ± 0.4	103.9 ± 1.0	1.24 ± 0.01
26	93.6 ± 2.0	110.3 ± 0.4	1.18 ± 0.03
G: nitromethnae-2-butanone 1:1 v/v			
12	86.7 ± 0.4	107.8 ± 0.4	1.24 ± 0.01
22	66.1 ± 0.5	100.6 ± 1.6	1.52 ± 0.03
H: propylene carbonate-2-butanone 1:1 v/v			
25	94.7 ± 1.5	116.2± 1.5	1.23 ± 0.02

[a] Data from the Tables S.II.1 and S.II.2 of Appendix II.

[b] Sample collapsed during drying and was not considered further.

[c] All samples from Runs 1–11 and 17–24 collapsed, the bulk densities were >1.0 g cm^{-3} and the porosities were <30% v/v. Those samples were not considered further.

[d] Runs were selected randomly from Table S.I.2 of Appendix .

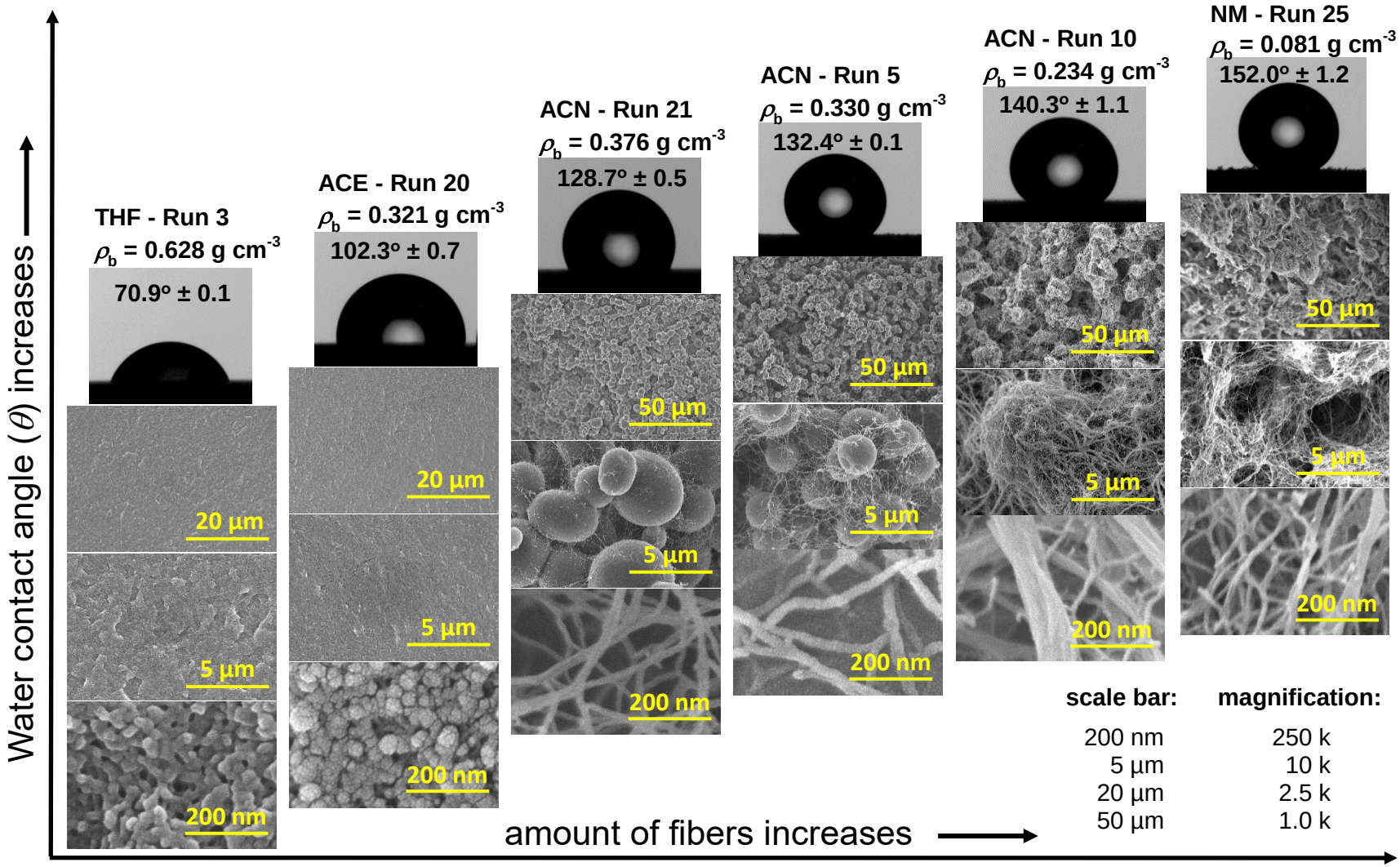

Figure S.III.1. Water contact angles (θ) on PUA aerogels as a function of surface texture.

APPENDIX IV. CHN ELEMENTAL ANALYSIS AND XPS DATA

Polyurea grows radially out in a dendritic fashion from ISO cores *via* Eq 1 of the main article. If every additional ISO branch is considered a "generation," *G*, then the formula of the n^{th} generation dendrimer was calculated in the Supporting Information of Reference S.R.5 and is given by:

$$G_n = T - 3(C+T)(1-2^n) + 3' 2^n' cap$$

Assuming that every two branch tips share a common cap (C=O), that is a carbonyl group coming from reaction of terminal $–NH_2$ on one branch and a terminal –N=C=O group on another branch nearby, the fragments T, C and *cap* and their weights are summarized in Scheme S.IV.1 below.

Scheme S.IV.1 Molecular fragments of polyurea aerogels, and their formula weights.

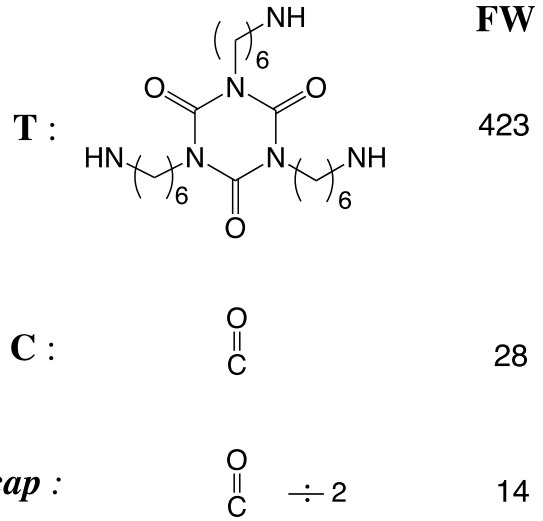

Plugging in the formula weights of the fragments into the equation above, for *n* ----> infinity, it is calculated that: C: 58.06%, H: 8.39% and N: 18.06%.

Experimental CHN analysis results for all samples are given in Table S.IV.1 below.

Table S.IV.1. CHN Elemental Analysis of all Polyurea Aerogels Prepared in Different Solvents.

DoE run No.	% C	% H	% N
acetonitrile			
1	56.85	8.24	16.91
2	57.87	8.51	17.20
3	57.60	8.43	17.20
4	57.50	8.39	17.18
5	57.60	8.44	17.15
6	57.65	8.49	17.18
7	57.91	8.49	17.20
8	57.56	8.37	17.06
9	57.44	8.44	17.23
10	57.37	8.32	17.06
11	57.56	8.36	17.11
12	57.53	8.42	17.07
13	57.70	8.51	17.18
14	57.70	8.41	17.24
15	57.59	8.44	17.04
16	57.53	8.36	17.08
17	57.05	8.31	17.00
18	56.97	8.27	16.95
19	57.41	8.36	17.12
20	57.59	8.37	17.11
21	57.45	8.32	17.08
22	57.67	8.51	17.16
23	57.56	8.48	17.11
24	57.41	8.33	17.01
25	57.61	8.33	17.12
26	57.20	8.18	16.90

DoE run No.	% C	% H	% N
nitromethane			
1	57.62	8.26	17.24
2	57.51	8.20	17.48
3	57.91	8.31	17.34
4	57.52	8.18	17.29
5	56.56	8.10	16.91
6	57.83	8.33	17.24
7	57.69	8.31	17.19
8	57.75	8.27	17.27
9	56.85	8.23	17.01
10	56.83	8.23	17.03
11	57.20	8.09	17.30
12	57.01	8.26	17.00
13	57.58	8.38	17.16
14	56.71	8.22	16.99
15	56.71	8.14	16.97
16	57.49	8.34	17.21
17	57.78	8.13	17.96
18	57.91	8.31	17.37
19	57.45	8.19	17.20
20	57.85	8.36	17.30
21	57.49	8.32	17.18
22	56.76	8.20	16.99
23	56.62	8.19	17.03
24	57.08	8.64	15.97
25	57.52	8.39	17.11
26	57.26	8.18	17.03

Table S.IV.1. CHN Elemental Analysis of all Polyurea Aerogels Prepared in Different Solvents. (cont.)

DoE run No.	% C	% H	% N
propylene carbonate			
1	56.94	8.11	17.87
2	57.58	8.49	17.09
3	57.58	8.54	17.34
4	57.62	8.42	17.23
5	57.40	8.53	17.12
6	57.45	8.53	17.29
7	57.53	8.54	17.29
8	57.49	8.40	17.20
9	57.36	8.33	16.99
10	57.67	8.36	17.19
11	57.44	8.42	17.20
12	57.19	8.35	17.16
13	57.54	8.33	17.12
14	57.06	8.18	17.02
15	57.57	8.35	17.14
16	57.53	8.38	17.13
17	57.49	8.57	17.11
18	57.73	8.50	17.21
19	57.27	8.44	17.07
20	57.26	8.41	17.02
21	57.51	8.61	17.25
22	57.29	8.37	16.98
23	56.71	8.16	16.90
24	57.32	8.55	17.15
25	57.88	8.32	17.00
26	57.28	8.40	17.12

DoE run No.	% C	% H	% N
acetone			
1	57.68	8.49	17.11
2	57.37	8.50	17.21
3	57.56	8.45	17.15
4	57.57	8.40	17.12
5	57.80	8.48	17.28
6	57.59	8.33	17.08
7	57.55	8.39	17.12
8	57.48	8.52	17.08
9	56.77	8.39	17.06
10	57.72	8.69	16.13
11	57.57	8.36	17.08
12	57.51	8.52	17.25
13	57.69	8.46	17.10
14	57.67	8.61	17.17
15	57.60	8.43	17.19
16	57.55	8.34	17.11
17	57.63	8.36	17.12
18	57.64	8.36	17.10
19	57.28	8.41	17.00
20	57.55	8.59	17.16
21	57.62	8.53	17.28
22	57.88	8.49	17.21
23	57.61	8.33	17.15
24	57.66	8.43	17.21
25	57.58	8.39	17.08
26	57.58	8.44	17.09

Table S.IV.1. CHN Elemental Analysis of all Polyurea Aerogels Prepared in Different Solvents. (cont.)

DoE run No.	% C	% H	% N
THF			
1	57.83	8.36	17.17
2	57.50	8.37	17.11
3	57.44	8.31	17.09
4	57.71	8.43	17.18
5	57.35	8.27	17.16
6	57.73	8.38	17.24
7	57.81	8.38	17.25
8	57.64	8.39	17.21
9	57.53	8.33	17.16
10	58.15	8.41	17.26
11	57.81	8.36	17.13
12	57.24	8.27	17.07
13	57.41	8.29	17.12
14	57.78	8.49	17.24
15	57.50	8.31	17.02
16	57.19	8.24	16.96
17	[a]	[a]	[a]
18	57.77	8.45	17.08
19	57.55	8.30	17.07
20	57.85	8.31	17.18
21	57.38	8.30	17.08
22	57.95	8.45	17.35
23	57.72	8.46	17.28
24	57.50	8.34	17.05
25	57.29	8.27	16.93
26	57.50	8.44	16.88

DoE run No.	% C	% H	% N
ethyl acetate			
1	57.53	8.33	17.18
2	57.45	8.46	17.19
3	57.45	8.40	17.28
4	57.56	8.20	17.19
5	57.75	8.29	17.25
6	57.45	8.46	17.31
7	57.45	8.46	17.31
8	57.41	8.40	17.26
9	57.90	8.52	17.37
10	57.39	8.37	17.24
11	57.49	8.32	17.27
12	57.32	8.28	17.15
13	57.54	8.28	17.16
14	57.64	8.33	17.30
15	57.37	8.11	17.10
16	57.64	8.37	17.13
17	57.45	8.37	17.03
18	57.71	8.42	17.15
19	57.67	8.41	17.22
20	57.54	8.45	17.24
21	57.62	8.40	17.17
22	57.94	8.36	17.27
23	57.65	8.43	17.26
24	57.52	8.42	17.31
25	57.30	8.25	17.11
26	57.12	8.28	16.92

Table S.IV.1. CHN Elemental Analysis of all Polyurea Aerogels Prepared in Different Solvents. (cont.)

DoE run No.	% C	% H	% N
2-butanone			
1	58.09	8.48	17.35
2	57.60	8.43	17.25
3	57.43	8.34	17.05
4	57.81	8.44	17.25
5	57.83	8.45	17.27
6	57.70	8.37	17.12
7	57.79	8.36	17.10
8	57.45	8.28	17.05
9	57.63	8.34	17.12
10	57.69	8.51	17.24
11	57.22	8.45	17.01
12	57.54	8.33	17.09
13	57.70	8.39	17.23
14	57.63	8.42	17.15
15	57.32	8.28	17.02
16	57.53	8.23	17.61
17	57.52	8.37	17.18
18	57.50	8.29	17.09
19	57.67	8.45	17.18
20	57.68	8.38	17.13
21	57.77	8.44	17.22
22	57.43	8.30	16.97
23	57.33	8.24	16.98
24	57.77	8.48	17.23
25	57.63	8.35	17.09
26	57.83	8.47	17.17

DoE run No.	% C	% H	% N
DMF [b]			
12	57.61	8.53	17.22
13	57.58	8.40	17.18
14	57.79	8.70	17.34
15	57.56	8.57	17.30
16	57.54	8.44	17.24
25	57.37	8.33	17.09
26	57.50	8.47	17.11

Table S.IV.1. CHN Elemental Analysis of all Polyurea Aerogels Prepared in Different Solvents. (cont.)

DoE run No. [c]	% C	% H	% N
BINARY SOLVENT SYSTEMS			
A: acetonitrile-nitromethane			
1	57.66	8.68	17.24
24	57.46	8.55	17.16
2	57.25	8.45	16.94
B: acetonitrile-propylene carbonate			
1	57.5	8.54	17.16
8	57.68	8.62	17.22
16	57.55	8.38	17.09
26	57.35	8.21	16.99
C: acetonitrile-acetone			
17	57.58	8.56	17.08
8	57.66	8.61	17.15
16	57.28	8.20	16.94
D: acetonitrile-DMF			
6	58.12	8.52	17.33
13	57.31	8.17	17.21
16	57.61	8.18	17.25
E: acetone-ethyl acetate			
17	57.69	8.69	17.28
8	57.62	8.35	17.36
F: ethyl acetate-DMF			
15	57.61	8.71	17.18
26	57.69	8.69	17.28
G: nitromethnae-2-butanone			
12	57.41	8.25	17.15
22	57.66	8.11	17.44
H: propylene carbonate-2-butanone			
25	57.36	8.31	16.92

[a] Samples collapsed during drying and were not considered further.

[b] All samples from Runs 1–11 and 17–24 collapsed, the bulk densities were >1.0 g cm^{-3} and the porosities were <30% v/v. Those samples were not considered further.

[c] Runs were selected randomly from Table S.I.2 of Appendix I.

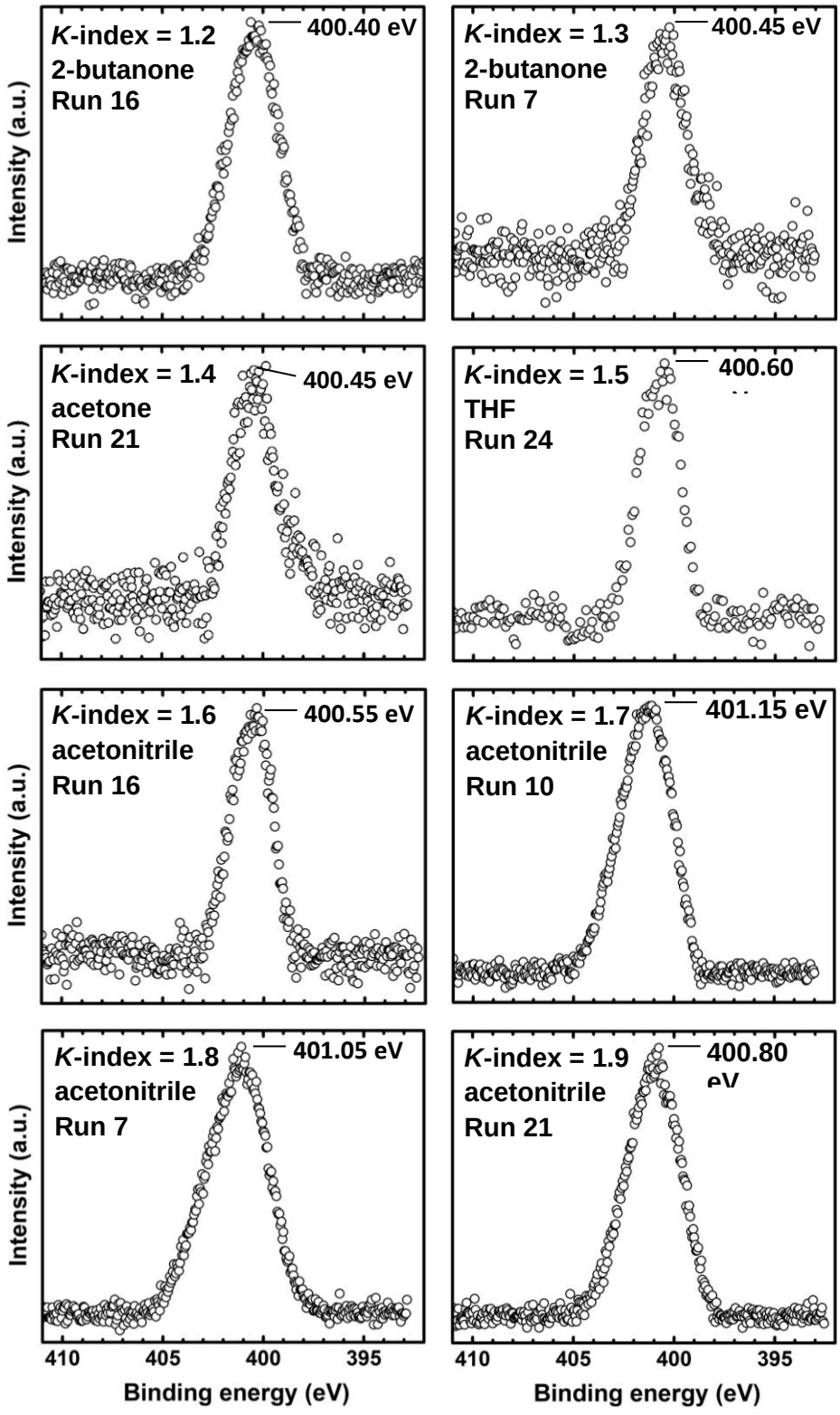

Figure S.IV.1. High resolution N 1s XPS data of random samples with different *K*-indexes.

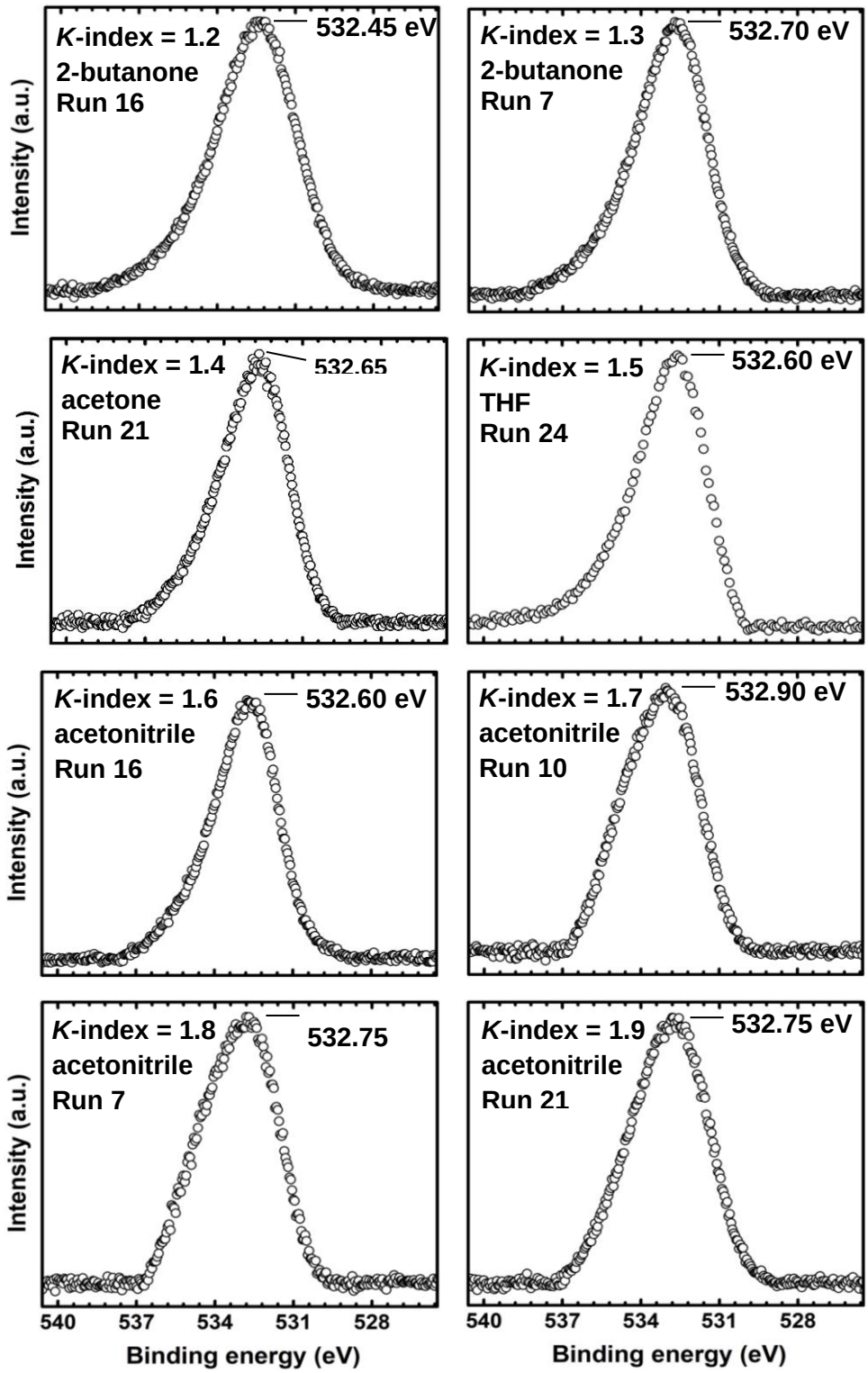

Figure S.IV.2. High resolution O 1s XPS data of random samples with different *K*-indexes.

APPENDIX V. VALIDATION OF *K*-INDEX VIA UNIAXIAL COMPRESSION

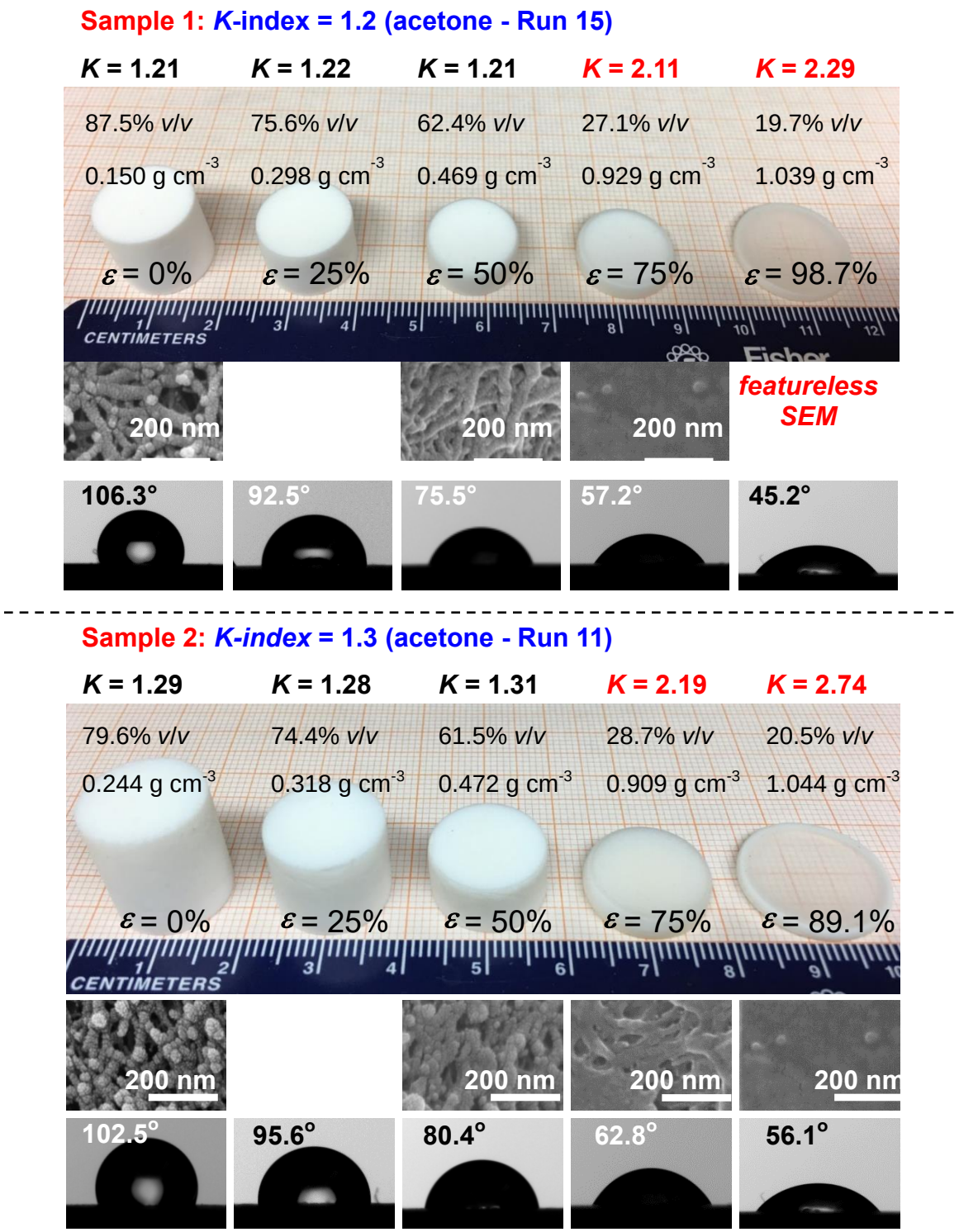

Figure S.V.1. Evolution of relevant properties, including the *K*-index, of eight (8) PUA aerogel samples compressed at different strains.

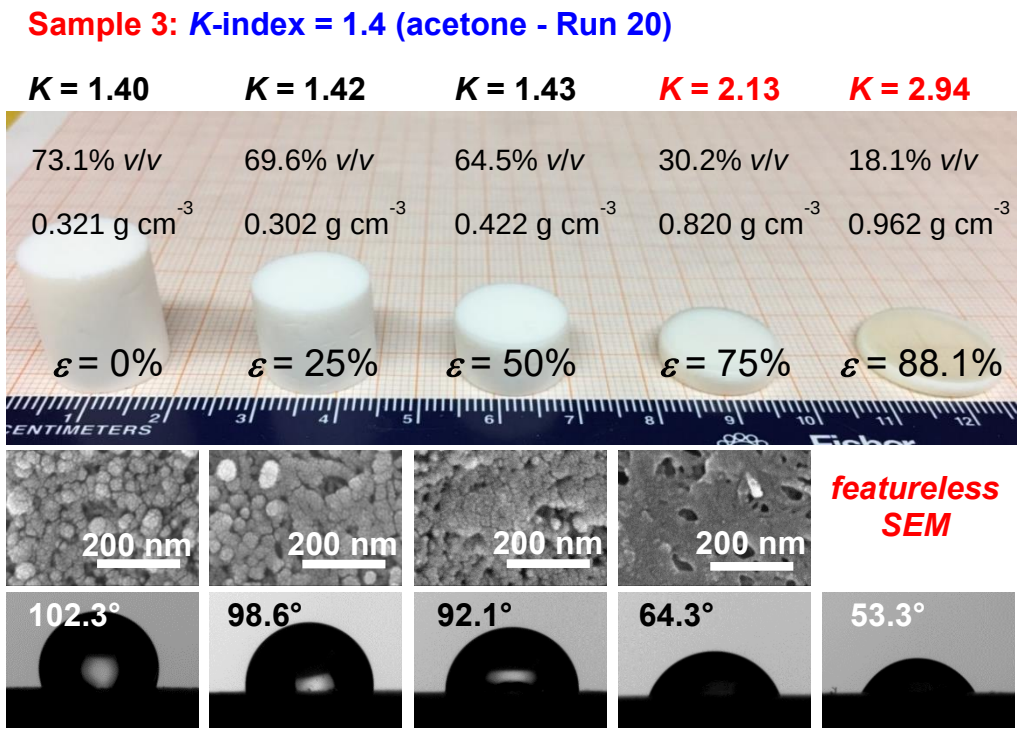

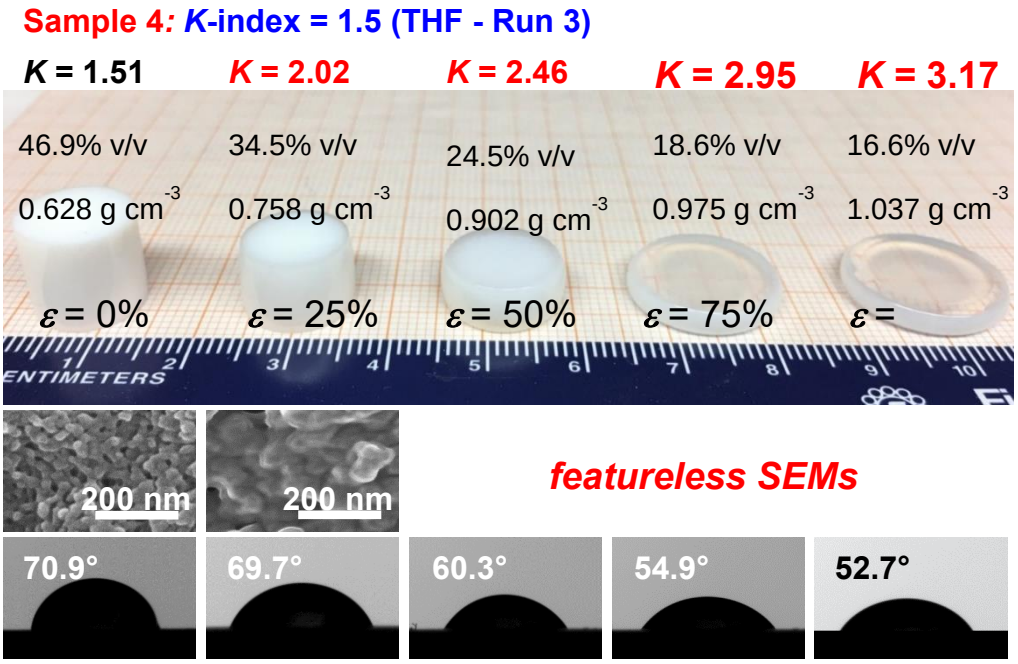

Figure S.V.1. Evolution of relevant properties, including the *K*-index, of eight (8) PUA aerogel samples compressed at different strains. (cont.)

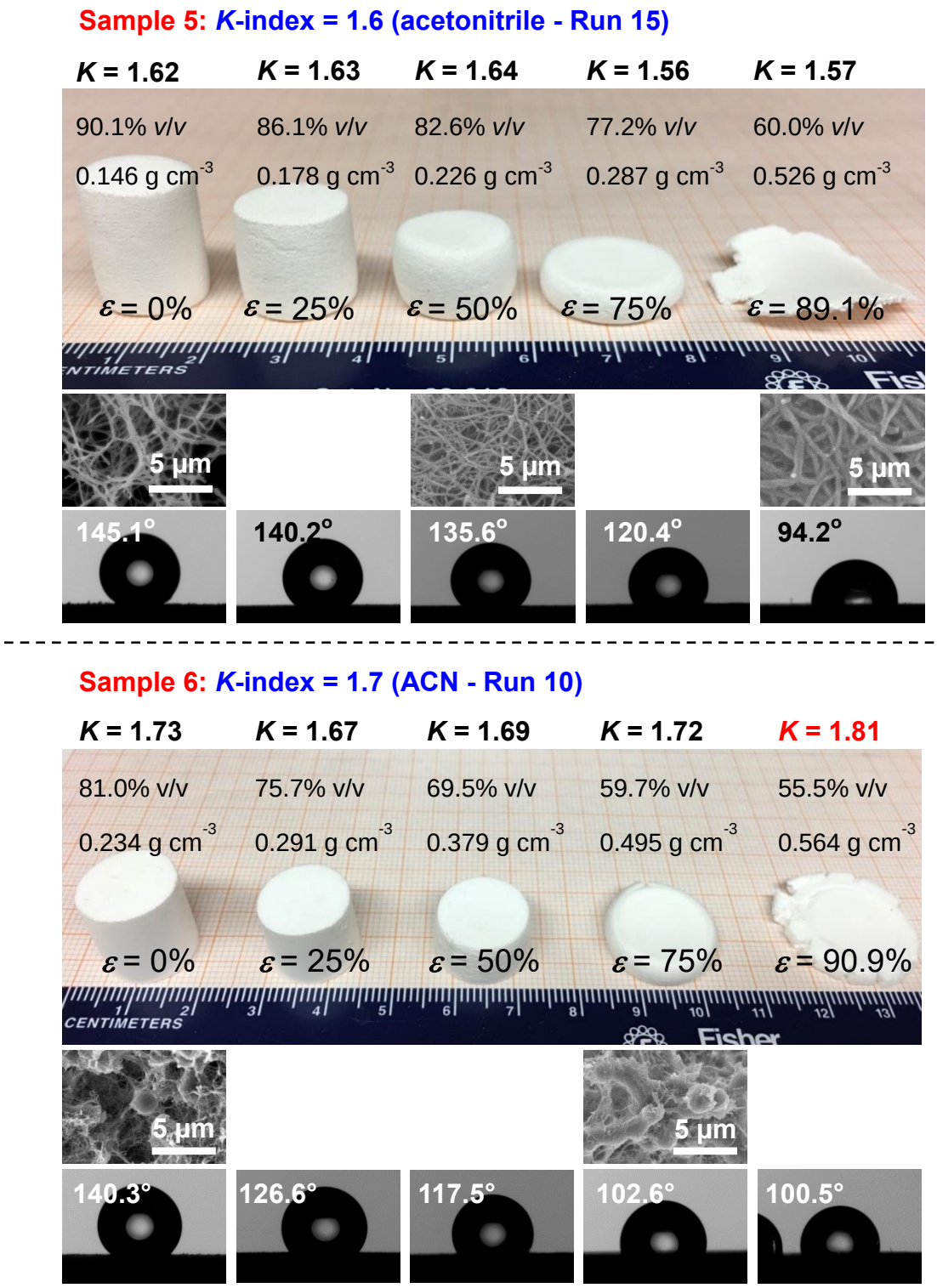

Figure S.V.1. Evolution of relevant properties, including the *K*-index, of eight (8) PUA aerogel samples compressed at different strains. (cont.)

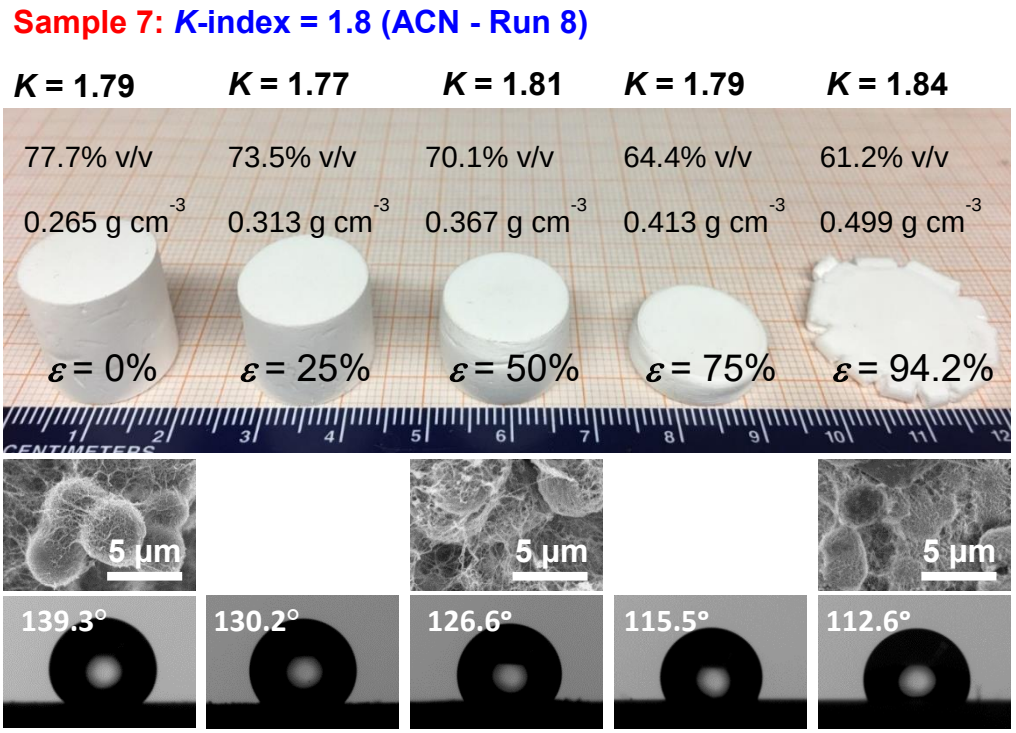

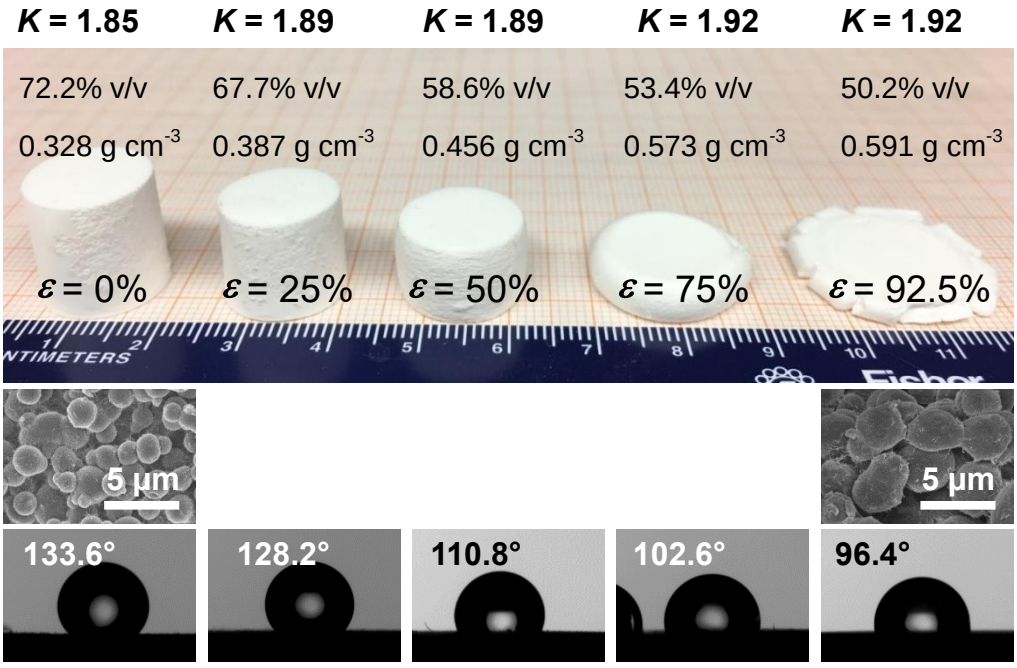

Figure S.V.1. Evolution of relevant properties, including the *K*-index, of eight (8) PUA aerogel samples compressed at different strains. (cont.)

Table S.V.1. Summary of *K*-index Data through Uniaxial Compression of 8 Samples at Different Strains (see Figure S.V.1 above).[a]

Sample 1: *K*-index = 1.2 "**caterpillar-like assemblies of nanoparticles**" (acetone - Run 15)

Sample property	**Before compression**	**After compression at different strains (ε)**			
	ε = 0 %	ε = 25 %	ε = 50 %	ε = 75 %	ε_{max} = 98.7 % [b]
bulk density, ρ_b (g cm^{-3})	0.150 ± 0.002	0.298	0.469	0.929	1.039
porosity, Π (% v/v)	87.5 ± 0.5	75.6	62.4	27.1	19.7
contact angle, θ (deg.)	106.3 ± 0.7	92.5	75.5	57.2	45.2
***K*-index**	1.21 ± 0.01	1.22	1.21	2.11	2.29

Sample 2: *K*-index = 1.3 "**worm-like assemblies of nanoparticles**" (acetone - Run 11)

Sample property	**Before compression**	**After compression at different strains (ε)**			
	ε = 0 %	ε = 25 %	ε = 50 %	ε = 75 %	ε_{max} = 89.1 % [b]
bulk density, ρ_b (g cm^{-3})	0.244 ± 0.002	0.318	0.472	0.909	1.044
porosity, Π (% v/v)	79.6 ± 0.5	74.4	61.5	28.7	20.5
contact angle, θ (deg.)	102.5 ± 2.0	95.6	80.4	62.8	56.1
***K*-index**	1.29 ± 0.03	1.28	1.31	2.19	2.74

Sample 3: *K*-index = 1.4 "**nanoparticle aggregates**" (acetone - Run 20)

Sample property	**Before compression**	**After compression at different strains (ε)**			
	ε = 0 %	ε = 25 %	ε = 50 %	ε = 75 %	ε_{max} = 88.1 % [b]
bulk density, ρ_b (g cm^{-3})	0.321 ± 0.003	0.302	0.422	0.820	0.962
porosity, Π (% v/v)	73.1 ± 0.4	69.6	64.5	30.2	18.1
contact angle, θ (deg.)	102.3 ± 0.7	98.6	92.1	64.3	53.3
***K*-index**	1.40 ± 0.01	1.42	1.43	2.13	2.94

Sample 4: *K*-index = 1.5 "**assemblies of fused nanoparticles**" (THF - Run 3)

Sample property	**Before compression**	**After compression at different strains (ε)**			
	ε = 0 %	ε = 25 %	ε = 50 %	ε = 75 %	ε_{max} = 84.5 % [b]
bulk density, ρ_b (g cm^{-3})	0.628 ± 0.018	0.758	0.902	0.975	1.037
porosity, Π (% v/v)	46.9 ± 1.5	34.5	24.5	18.6	16.6
contact angle, θ (deg.)	70.9 ± 0.1	69.7	60.3	54.9	52.7
***K*-index**	1.51 ± 0.05	2.02	2.46	2.95	3.17

Table S.V.1. Summary of *K*-index Data through Uniaxial Compression of 8 Samples at Different Strains (see Figure S.V.1 above).[a] (cont.)

Sample 5: *K*-index = 1.6 "**thin hair-like entangled nanofibers**" (acetonitrile - Run 15)

Sample property	**Before compression**	**After compression at different strains (ε)**			
	ε = 0 %	ε = 25 %	ε = 50 %	ε = 75 %	ε_{max} = 98.7 % [b]
bulk density, ρ_b (g cm^{-3})	0.140 ± 0.002	0.178	0.226	0.287	0.526
porosity, Π (% v/v)	90.1 ± 0.1	86.1	82.6	77.2	60.0
contact angle, θ (deg.)	146.4 ± 0.3	140.2	135.6	120.4	94.2
***K*-index**	1.62 ± 0.04	1.63	1.64	1.56	1.57

Sample 6: *K*-index = 1.7 "**cocoons of nanofibers**" (acetonitrile - Run 10)

Sample property	**Before compression**	**After compression at different strains (ε)**			
	ε = 0 %	ε = 25 %	ε = 50 %	ε = 75 %	ε_{max} = 90.9 % [b]
bulk density, ρ_b (g cm^{-3})	0.234 ± 0.001	0.291	0.379	0.495	0.564
porosity, Π (% v/v)	81.0 ± 0.2	75.7	69.5	59.7	55.5
contact angle, θ (deg.)	140.3 ± 1.1	126.6	117.5	102.6	100.5
***K*-index**	1.73 ± 0.02	1.67	1.69	1.72	1.81

Sample 7: *K*-index = 1.8 "**microspheres with hair**" (acetonitrile - Run 8)

Sample property	**Before compression**	**After compression at different strains (ε)**			
	ε = 0 %	ε = 25 %	ε = 50 %	ε = 75 %	ε_{max} = 94.2 % [b]
bulk density, ρ_b (g cm^{-3})	0.265 ± 0.001	0.313	0.367	0.413	0.499
porosity, Π (% v/v)	77.7 ± 0.4	73.5	70.1	64.4	61.2
contact angle, θ (deg.)	139.3 ± 1.4	130.2	126.6	115.5	112.6
***K*-index**	1.79 ± 0.02	1.77	1.81	1.79	1.84

Sample 8: *K*-index = 1.9 "**bald microspheres**" (acetonitrile - Run 3)

Sample property	**Before compression**	**After compression at different strains (ε)**			
	ε = 0 %	ε = 25 %	ε = 50 %	ε = 75 %	ε_{max} = 92.5 % [b]
bulk density, ρ_b (g cm^{-3})	0.328 ± 0.029	0.387	0.456	0.573	0.591
porosity, Π (% v/v)	72.2 ± 2.5	67.7	58.6	53.4	50.2
contact angle, θ (deg.)	133.6 ± 0.1	128.2	110.8	102.6	96.4
***K*-index**	1.85 ± 0.06	1.89	1.89	1.92	1.92

[a] Experiments were conducted with five monoliths at each formulation. One was characterized in its initial state (uncompressed); another one was compressed at 25 % strain; another one at 50 % strain; and, another one at 75 % strain. The last sample was compressed at the maximum load that could be applied by the instrument. [b] Maximum strain at which the load cell reaches its compliance (50 kN).

APPENDIX VI. VALIDATION OF THE *K*-INDEX BY THE MORPHOLOGY OF POLYUREA AEROGELS PREPARED IN BINARY SOLVENT SYSTEMS

Scheme S.VI.1. Algorithm for Cross-checking the Predicted Morphology of Samples Prepared in Binary Solvents (see Figure S.VI.1).

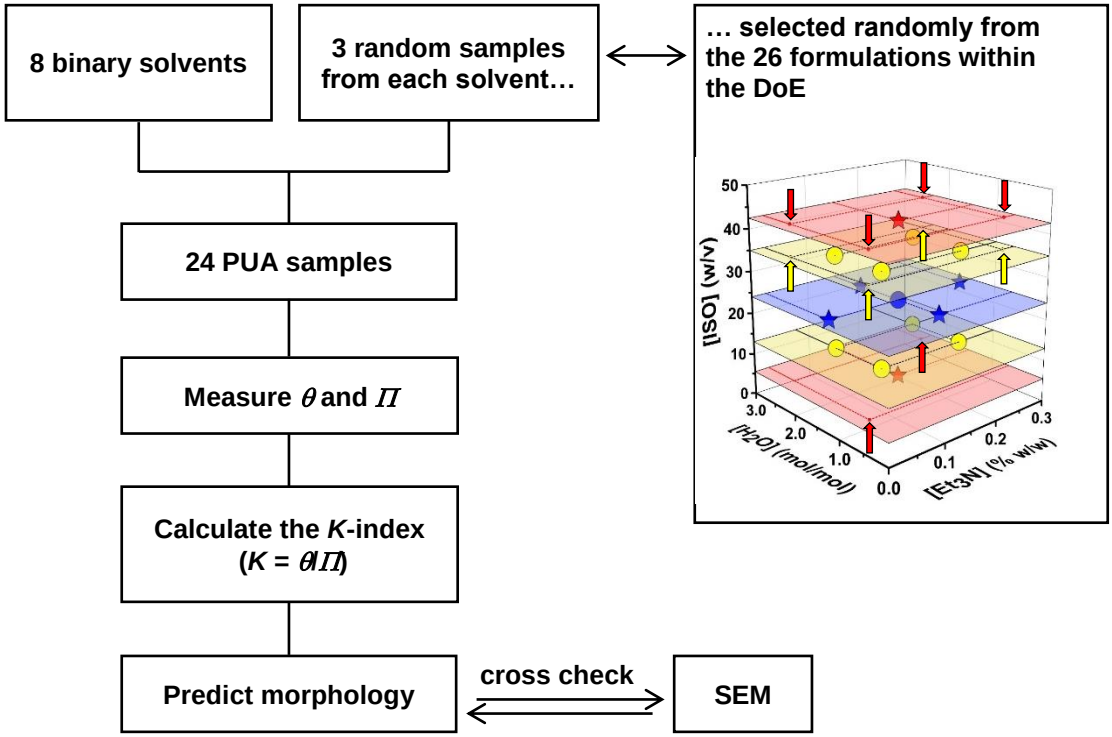

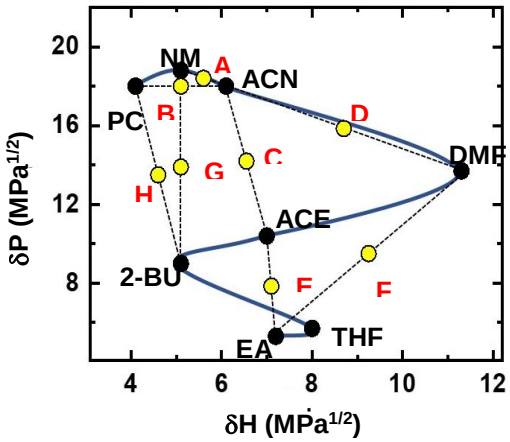

Figure S.VI.1. Placement of the binary solvents (yellow circles) in the domain of the δP and δH values of the individual solvents used in the study.

Table S.VI.1. *K*-indexes of the Polyurea Aerogels Prepared in Binary Solvents (Porosity and Contact Angle Data are Reproduced from Table S.III.1 of Appendix III).

DoE run No. [a]	Porosity (Π, % v/v)	contact angle (θ, deg.)	*K*-index	Expected Morphology
BINARY SOLVENT SYSTEMS				
A: acetonitrile-nitromethane 1:1 v/v				
1	54.5 ± 1.7	83.80 ± 0.5	1.54 ± 0.05	assembly of fused nanoparticles
24	78.5 ± 0.5	100.6 ± 1.0	1.28 ± 0.02	worm-like assembly of nanoparticles
2	69.9 ± 0.7	128.1 ± 1.1	1.83 ± 0.02	microspheres with hair
B: acetonitrile-propylene carbonate 1:1 v/v				
1	57.2 ± 1.0	88.30 ± 0.1	1.54 ± 0.03	assembly of fused nanoparticles
8	79.7 ± 1.2	109.2 ± 0.5	1.37 ± 0.02	nanoparticle aggregates
16	95.3 ± 5.7	149.2 ± 1.5	1.57 ± 0.10	thin hair-like entangled nanofibers
26	96.1 ± 11.6	149.8 ± 1.6	1.56 ± 0.19	thin hair-like entangled nanofibers
C: acetonitrile-acetone 1:1 v/v				
17	56.5 ± 0.9	85.80 ± 0.3	1.52 ± 0.02	assembly of fused nanoparticles
8	78.0 ± 0.4	138.6 ± 2.1	1.78 ± 0.03	microspheres with hair
16	95.5 ± 3.4	149.7 ± 2.3	1.57 ± 0.06	thin hair-like entangled nanofibers
D: acetonitrile-DMF 1:1 v/v				
6	65.6 ± 0.7	93.60 ± 0.3	1.43 ± 0.02	nanoparticle aggregates
13	85.4 ± 0.3	100.7 ± 0.1	1.18 ± 0.00	caterpillar-like assembly of nanoparticles
16	93.4 ± 0.6	110.8 ± 1.6	1.19 ± 0.02	caterpillar-like assembly of nanoparticles
E: acetone-ethyl acetate 1:1 v/v				
17	50.2 ± 0.4	76.80 ± 0.1	1.53 ± 0.01	assembly of fused nanoparticles
8	76.4 ± 0.2	99.10 ± 1.2	1.30 ± 0.02	worm-like assembly of nanoparticles
F: ethyl acetate-DMF (F) 1:1 v/v				
15	84.1 ± 0.4	103.9 ± 1.0	1.24 ± 0.01	caterpillar-like assembly of nanoparticles
26	93.6 ± 2.0	110.3 ± 0.4	1.18 ± 0.03	caterpillar-like assembly of nanoparticles
G: nitromethnae-2-butanone 1:1 v/v				
12	86.7 ± 0.4	107.8 ± 0.4	1.24 ± 0.01	caterpillar-like assembly of nanoparticles
22	66.1 ± 0.5	100.6 ± 1.6	1.52 ± 0.03	assembly of fused nanoparticles
H: propylene carbonate-2-butanone 1:1 v/v				
25	94.7 ± 1.5	116.3± 1.5	1.23 ± 0.02	caterpillar-like assembly of nanoparticles

[a] Runs were selected randomly from the design space of Figure S.I.1 and Table S.I.2 of Appendix I. Synthetic conditions are cited in Table S.I.12 of Appendix I. General material properties are shown in Table S.II.2 of Appendix II.

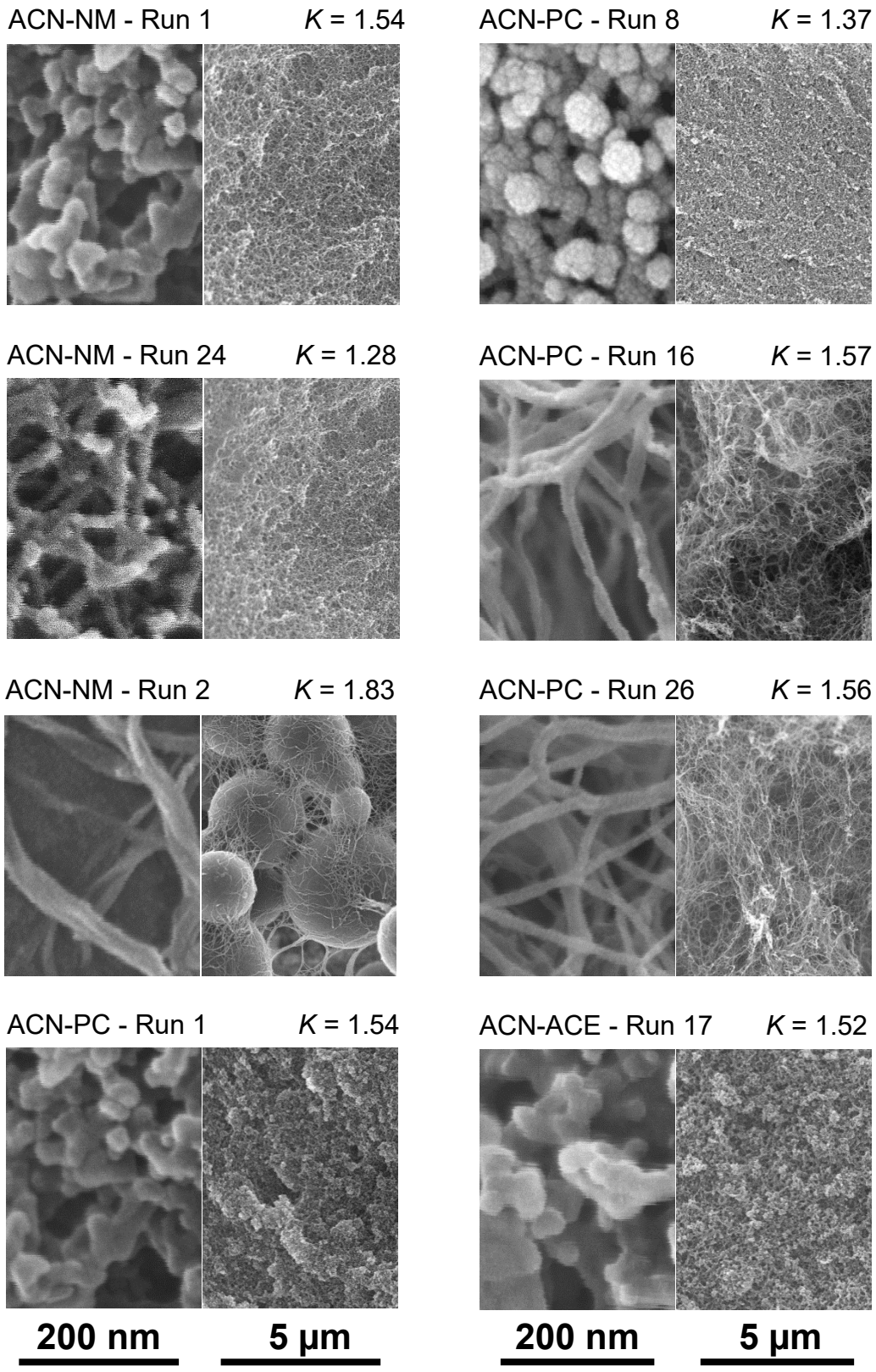

Figure S.VI.2. SEM Images of the 20 PUA Aerogels Prepared in Binary Solvents.

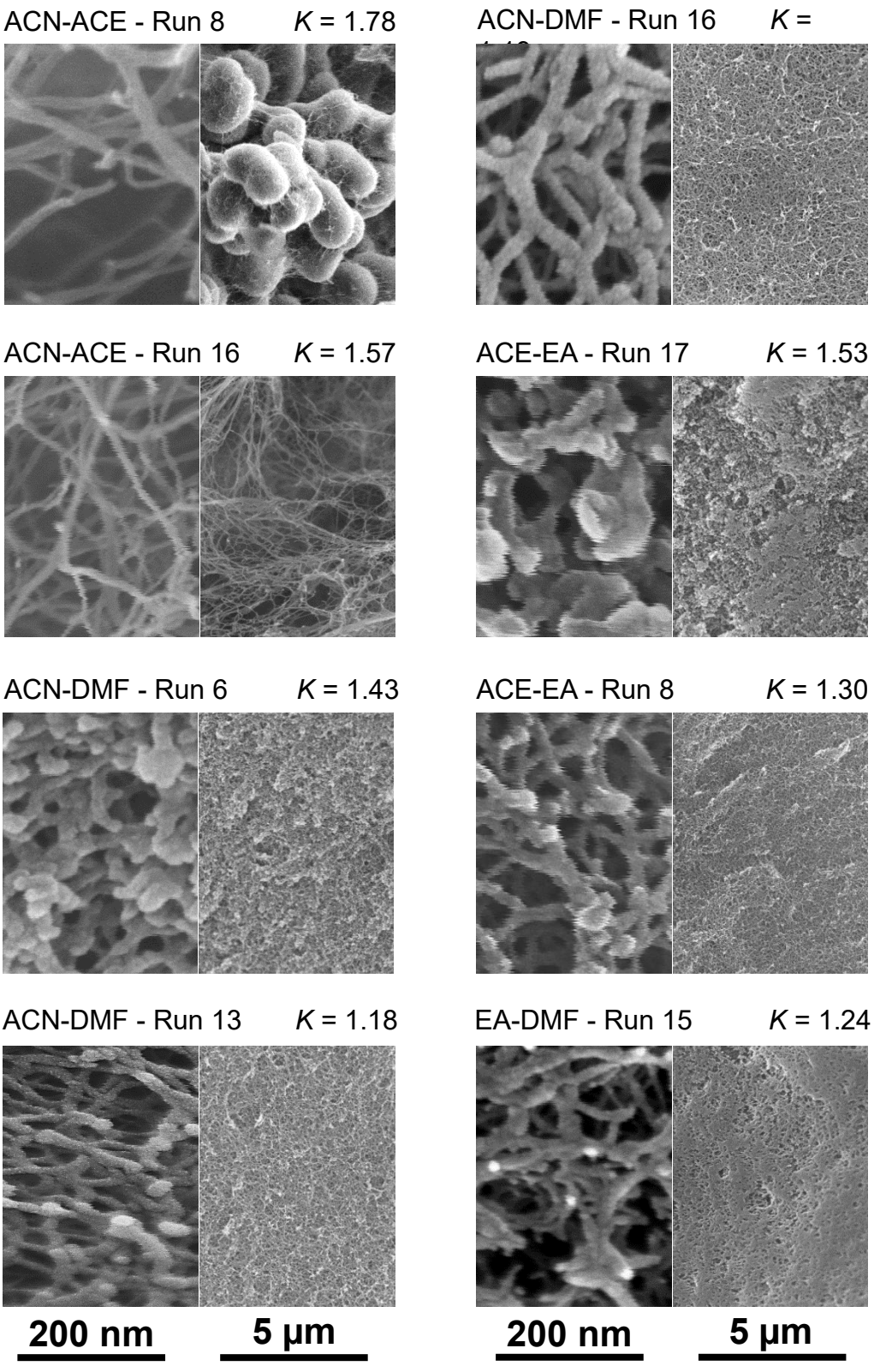

Figure S.VI.2. SEM Images of the 20 PUA Aerogels Prepared in Binary Solvents. (cont.)

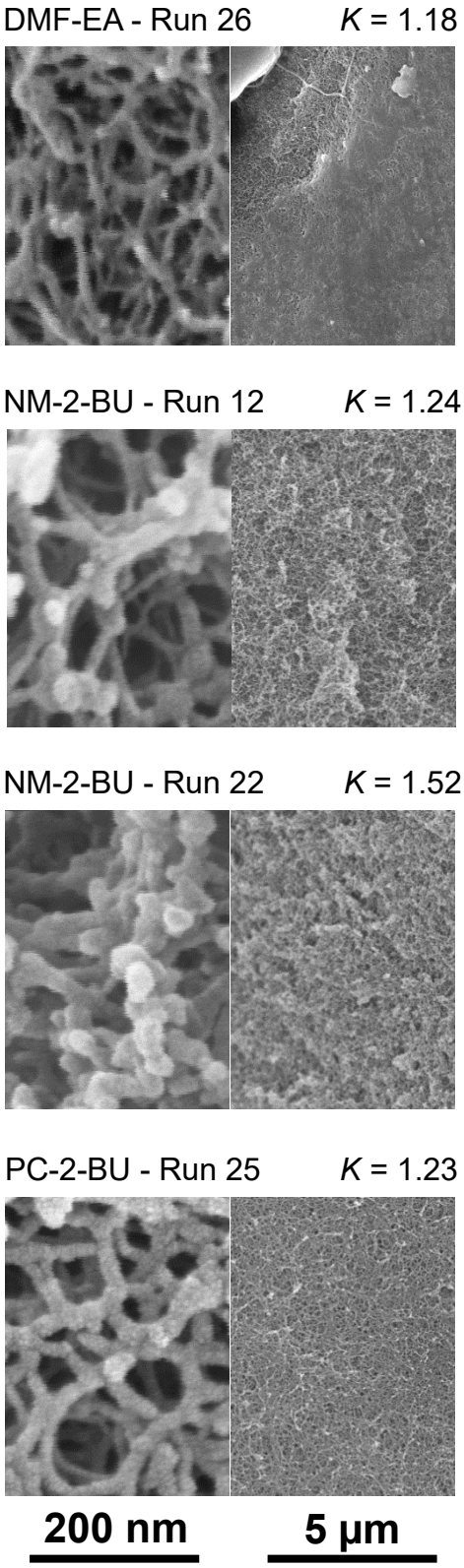

Figure S.VI.2. SEM Images of the 20 PUA Aerogels Prepared in Binary Solvents. (cont.)

APPENDIX VII. MATERIAL PROPERTIES WITH TECHNOLOGICAL SIGNIFICANCE

Table S.VII.1. Measured and Calculated Properties of PUA Aerogels Prepared in Individual Solvents, and Fitted to the Preparation Conditions (see Appendix X).

DoE run No.	*K*-index	contact angle (θ, deg.)	bulk density (ρ_b, g cm^{-3})	BET surface area (σ, m^2 g^{-1})	thermal conductivity (mW m^{-1} K^{-1}) [b]			mechanical properties		
					λ_{Total}	λ_g	λ_s	Young's modulus (E, MPa)	Ultimate Compressive Strength (UCS, MPa)	specific energy U_T (J g^{-1})
acetonitrile										
1	1.82 ± 0.03	125.2 ± 0.5	0.383 ± 0.001	20.4	-	-	-	-	-	-
2	1.80 ± 0.01	121.4 ± 0.6	0.387 ± 0.003	4.37	-	-	-	-	-	-
3	1.85 ± 0.06	133.3 ± 0.1	0.328 ± 0.029	9.32	-	-	-	-	-	-
4	1.82 ± 0.01	126.7 ± 0.9	0.327 ± 0.002	17.8	-	-	-	-	-	-
5	1.84 ± 0.02	132.4 ± 1.1	0.330 ± 0.004	17.2	64.8 ± 0.1	12.$_2$	52.$_6$	22 ± 1	206 ± 15	54 ± 2
6	1.85 ± 0.02	144.1 ± 0.1	0.259 ± 0.011	8.12	55.0 ± 0.1	17.$_2$	37.$_8$	12 ± 2	220 ± 4	59 ± 1
7	1.78 ± 0.01	137.8 ± 0.4	0.268 ± 0.002	8.53	56.9 ± 0.1	16.$_6$	40.$_3$	12.2 ± 0.1	236 ± 5	58 ± 1
8	1.79 ± 0.02	139.3 ± 1.4	0.265 ± 0.001	9.76	55.9 ± 0.1	16.$_4$	39.$_5$	13.7 ± 0.3	232 ± 11	57 ± 1
9	1.75 ± 0.01	137.1 ± 0.1	0.258 ± 0.001	23.1	54.5 ± 0.2	13.$_4$	41.$_1$	16.2 ± 0.2	236 ± 8	59 ± 1
10	1.73 ± 0.02	140.3 ± 1.1	0.234 ± 0.001	24.2	52.2 ± 0.1	14.$_3$	37.$_9$	38 ± 3	216 ± 1	54 ± 0
11	1.64 ± 0.02	134.6 ± 0.5	0.211 ± 0.003	113	47.1 ± 0.1	7.1	40.$_0$	27 ± 4	232 ± 8	69 ± 3
12	1.66 ± 0.02	142.5 ± 0.9	0.169 ± 0.006	16.9	42.3 ± 0.1	18.$_2$	24.$_1$	6.4 ± 0.1	241 ± 7	58 ± 2
13	1.66 ± 0.02	144.5 ± 0.4	0.151 ± 0.009	23.3	38.7 ± 0.1	17.$_9$	20.$_8$	6.3 ± 0.4	240 ± 12	65 ± 1
14	1.64 ± 0.01	145.6 ± 0.3	0.140 ± 0.002	32.8	35.7 ± 0.1	17.$_0$	18.$_7$	6.7 ± 0.2	129 ± 7	70 ± 3
15	1.62 ± 0.04	146.4 ± 1.6	0.122 ± 0.001	97.7	31.3 ± 0.1	12.$_2$	19.$_1$	10 ± 1	107 ± 11	83 ± 6
16	1.61 ± 0.04	152.3 ± 2.1	0.062 ± 0.001	60.2	31.0 ± 0.1	19.$_5$	11.$_5$	2.1 ± 0.1	235 ± 1	135 ± 1
17	1.92 ± 0.02	127.8 ± 1.1	0.396 ± 0.002	5.24	-	-	-	-	-	-
18	1.81 ± 0.03	128.5 ± 2.1	0.348 ± 0.002	4.85	-	-	-	-	-	-
19	1.83 ± 0.02	123.8 ± 1.4	0.381 ± 0.001	24.2	-	-	-	-	-	-
20	1.15 ± 0.01	90.00 ± 0.3	0.263 ± 0.009	110	45.2 ± 0.1	5.7	39.$_5$	108 ± 3	240 ± 10	73 ± 1
21	1.88 ± 0.01	128.7 ± 0.5	0.376 ± 0.003	8.12	-	-	-	-	-	-
22	1.84 ± 0.03	126.0 ± 1.2	0.372 ± 0.011	9.42	64.9 ± 0.1	13.$_7$	51.$_2$	28.1 ± 0.4	210 ± 19	55 ± 2
23	1.73 ± 0.04	132.8 ± 0.9	0.295 ± 0.005	18.0	57.6 ± 0.1	13.$_5$	44.$_1$	20 ± 2	249 ± 2	68 ± 1
24	1.25 ± 0.02	102.1 ± 1.6	0.216 ± 0.007	106	48.0 ± 0.1	7.2	40.$_8$	73 ± 2	220 ± 2	61 ± 2
25	1.61 ± 0.04	151.2 ± 1.8	0.071 ± 0.002	42.3	34.5 ± 0.1	20.$_2$	14.$_3$	2.3 ± 0.1	209 ± 4	118 ± 4
26	1.57 ± 0.02	152.3 ± 1.3	0.040 ± 0.001	202	30.5 ± 0.1	16.$_0$	14.5	2.2 ± 0.1	240 ± 3	191 ± 7

Table S.VII.1. Measured and Calculated Properties of PUA Aerogels Prepared in Individual Solvents, and Fitted to the Preparation Conditions (see Appendix X). (cont.)

DoE run No.	*K*-index	contact angle (θ, deg.)	bulk density (ρ_b, g cm^{-3})	BET surface area (σ, m^2 g^{-1})	thermal conductivity (mW m^{-1} K^{-1}) [b]			mechanical properties		
					λ_{Total}	λ_g	λ_s	Young's modulus (E, MPa)	Ultimate Compressive Strength (UCS, MPa)	specific energy U_T (J g^{-1})
nitromethane										
1	1.53 ± 0.09	52.2 ± 3	0.563 ± 0.035	29.1	-	-	-	-	-	-
2	1.45 ± 0.03	60.7 ± 1.3	0.467 ± 0.015	22.2	-	-	-	-	-	-
3	1.47 ± 0.03	62.6 ± 1.1	0.441 ± 0.012	22.1	53.3 ± 0.1	7.9	45.4	121 ± 28	319 ± 2	81 ± 4
4	1.45 ± 0.03	63.0 ± 1.2	0.440 ± 0.014	42.2	-	-	-	-	-	-
5	1.85 ± 0.01	64.0 ± 0.5	0.430 ± 0.005	38.8	51.9 ± 0.1	5.9	46.0	125 ± 2	293 ± 5	69 ± 2
6	1.77 ± 0.03	78.0 ± 1.1	0.260 ± 0.012	15.2	-	-	-	-	-	-
7	1.76 ± 0.03	79.9 ± 1.4	0.241 ± 0.015	23.2	-	-	-	-	-	-
8	1.76 ± 0.02	80.5 ± 1.0	0.229 ± 0.011	39.3	-	-	-	-	-	-
9	1.77 ± 0.02	80.0 ± 0.8	0.236 ± 0.009	44.5	-	-	-	-	-	-
10	1.72 ± 0.03	79.0 ± 0.3	0.248 ± 0.002	42.3	43.3 ± 0.1	10.8	32.5	34 ± 1	219 ± 14	50 ± 1
11	1.18 ± 0.05	80.2 ± 2.9	0.240 ± 0.035	95.2	-	-	-	-	-	-
12	1.67 ± 0.03	86.0 ± 1.4	0.167 ± 0.016	26.1	36.1 ± 0.1	16.6	19.5	21.3 ± 0.4	252 ± 5	61 ± 4
13	1.67 ± 0.01	87.5 ± 0.3	0.147 ± 0.002	17.4	33.4 ± 0.1	19.1	14.3	18.1 ± 0.3	247 ± 1	70 ± 3
14	1.65 ± 0.02	87.8 ± 0.9	0.146 ± 0.009	42.2	33.1 ± 0.1	15.4	17.7	16 ± 1	211 ± 11	71 ± 1
15	1.64 ± 0.02	88.9 ± 0.8	0.132 ± 0.003	119	31.9 ± 0.1	10.4	21.5	12 ± 1	179 ± 11	80 ± 1
16	1.60 ± 0.04	94.4 ± 2.3	0.068 ± 0.003	39.0	33.3 ± 0.2	20.7	12.6	2.4 ± 0.1	347 ± 7	180 ± 3
17	1.52 ± 0.05	56.8 ± 1.9	0.511 ± 0.023	9.36	-	-	-	-	-	-
18	1.50 ± 0.02	56.9 ± 0.7	0.509 ± 0.008	12.2	60.9 ± 0.1	8.5	52.4	155 ± 3	310 ± 3	84 ± 2
19	1.55 ± 0.04	53.0 ± 1.4	0.557 ± 0.016	45.1	-	-	-	-	-	-
20	1.35 ± 0.01	71.4 ± 0.5	0.337 ± 0.003	74.1	-	-	-	-	-	-
21	1.48 ± 0.01	60.4 ± 0.4	0.471 ± 0.005	15.1	58.0 ± 0.1	8.7	49.3	137 ± 10	316 ± 9	76 ± 1
22	1.49 ± 0.02	62.5 ± 0.7	0.444 ± 0.008	16.2	55.8 ± 0.1	9.1	46.7	126 ± 6	293 ± 3	67 ± 3
23	1.34 ± 0.01	65.3 ± 0.6	0.413 ± 0.007	45.3	56.9 ± 0.1	5.7	51.2	101 ± 4	279 ± 7	72 ± 4
24	1.33 ± 0.01	73.7 ± 0.6	0.313 ± 0.007	95.2	47.7 ± 0.1	5.0	42.7	72 ± 2	159 ± 19	18 ± 5
25	1.63 ± 0.02	93.0 ± 0.8	0.081 ± 0.001	32.9	31.6 ± 0.1	20.3	11.3	2.5 ± 0.1	261 ± 8	104 ± 7
26	1.56 ± 0.04	96.6 ± 2.7	0.041 ± 0.002	122	30.5 ± 0.1	18.6	11.9	2.3 ± 0.1	249 ± 1	176 ± 3

Table S.VII.1. Measured and Calculated Properties of PUA Aerogels Prepared in Individual Solvents, and Fitted to the Preparation Conditions (see Appendix X). (cont.)

DoE run No.	*K*-index	contact angle (θ, deg.)	bulk density (ρ_b, g cm^{-3})	BET surface area (σ, m^2 g^{-1})	thermal conductivity (mW m^{-1} K^{-1}) [b]			mechanical properties		
					λ_{Total}	λ_g	λ_s	Young's modulus (E, MPa)	Ultimate Compressive Strength (UCS, MPa)	specific energy U_T (J g^{-1})
propylene carbonate [a]										
1	1.53 ± 0.04	85.00 ± 0.8	0.529 ± 0.018	75.0	-	-	-	-	-	-
2	1.43 ± 0.05	80.40 ± 1.3	0.519 ± 0.020	81.5	-	-	-	-	-	-
3	1.43 ± 0.05	83.90 ± 1.1	0.504 ± 0.022	54.8	-	-	-	-	-	-
4	1.45 ± 0.04	91.20 ± 0.1	0.443 ± 0.019	73.5	-	-	-	-	-	-
5	1.43 ± 0.04	82.50 ± 0.8	0.500 ± 0.017	86.4	-	-	-	-	-	-
6	1.33 ± 0.03	95.00 ± 0.9	0.339 ± 0.015	82.4	-	-	-	-	-	-
7	1.34 ± 0.02	95.10 ± 0.5	0.350 ± 0.013	87.7	-	-	-	-	-	-
8	1.33 ± 0.03	95.30 ± 1.3	0.335 ± 0.012	78.3	-	-	-	-	-	-
9	1.32 ± 0.02	95.70 ± 0.9	0.328 ± 0.010	75.3	-	-	-	-	-	-
10	1.35 ± 0.03	96.20 ± 0.1	0.34 0± 0.017	69.1	-	-	-	-	-	-
11	1.65 ± 0.03	118.8 ± 1.2	0.337 ± 0.009	123	-	-	-	-	-	-
12	1.66 ± 0.01	145.0 ± 0.5	0.151 ± 0.006	67.6	-	-	-	-	-	-
13	1.65 ± 0.02	143.5 ± 1.3	0.156 ± 0.003	49.4	-	-	-	-	-	-
14	1.64 ± 0.05	140.4 ± 1.1	0.175 ± 0.005	46.3	-	-	-	-	-	-
15	1.63 ± 0.01	140.2 ± 0.9	0.171 ± 0.001	78.5	49.0 ± 0.1	$10._7$	$38._3$	5.6 ± 0.2	44 ± 6	21 ± 7
16	1.56 ± 0.04	147.4 ± 1.2	0.065 ± 0.001	60.9	21.8 ± 0.1	$19._2$	2.6	6 ± 1	8 ± 1	3.5 ± 0.2
17	1.53 ± 0.08	77.20 ± 0.5	0.596 ± 0.031	69.9	-	-	-	-	-	-
18	1.53 ± 0.08	78.50 ± 0.2	0.587 ± 0.034	47.3	-	-	-	-	-	-
19	1.44 ± 0.03	88.60 ± 0.4	0.461 ± 0.014	137	-	-	-	-	-	-
20	1.43 ± 0.08	88.40 ± 1.2	0.457 ± 0.041	237	79.2 ± 0.1	1.2	$78._0$	117 ± 8	205 ± 17	42 ± 13
21	1.44 ± 0.04	90.50 ± 0.1	0.444 ± 0.020	86.8	-	-	-	-	-	-
22	1.39 ± 0.03	90.50 ± 0.5	0.427 ± 0.018	73.4	-	-	-	-	-	-
23	1.44 ± 0.01	91.00 ± 0.1	0.442 ± 0.004	77.3	-	-	-	-	-	-
24	1.33 ± 0.09	88.40 ± 0.7	0.399 ± 0.054	227	78.4 ± 0.2	1.6	$76._8$	87 ± 8	171 ± 18	36 ± 12
25	1.57 ± 0.02	148.1 ± 1.4	0.066 ± 0.001	50.6	23.0 ± 0.1	$19._8$	3.2	5 ± 1	9 ± 1	6 ± 2
26	1.56 ± 0.02	146.0 ± 0.6	0.080 ± 0.001	198	26.4 ± 0.1	$11._2$	$15._2$	4 ± 1	3.6 ± 0.4	3.1 ± 0.4

Table S.VII.1. Measured and Calculated Properties of PUA Aerogels Prepared in Individual Solvents, and Fitted to the Preparation Conditions (see Appendix X). (cont.)

DoE run No.	*K*-index	contact angle (θ, deg.)	bulk density (ρ_b, g cm^{-3})	BET surface area (σ, m^2 g^{-1})	thermal conductivity (mW m^{-1} K^{-1}) [b]			mechanical properties		
					λ_{Total}	λ_g	λ_s	Young's modulus (E, MPa)	Ultimate Compressive Strength (UCS, MPa)	specific energy U_T (J g^{-1})
acetone										
1	1.50 ± 0.02	77.80 ± 0.9	0.584 ± 0.004	59.6	61.3 ± 0.1	2.4	58.9	302 ± 21	292 ± 18	69 ± 3
2	1.39 ± 0.02	81.90 ± 1.2	0.488 ± 0.005	60.1	56.6 ± 0.1	3.5	53.1	179 ± 16	298 ± 48	83 ± 2
3	1.44 ± 0.01	80.20 ± 0.4	0.531 ± 0.005	60.7	60.9 ± 0.1	2.9	58.0	187 ± 3	416 ± 2	88 ± 1
4	1.36 ± 0.01	95.40 ± 1.0	0.358 ± 0.001	105	43.7 ± 0.1	3.9	39.8	149 ± 1	267 ± 9	73 ± 3
5	1.36 ± 0.01	96.40 ± 0.4	0.349 ± 0.004	162	38.7 ± 0.1	2.8	35.9	155 ± 2	256 ± 12	72 ± 4
6	1.26 ± 0.00	97.10 ± 0.3	0.274 ± 0.001	133	41.1 ± 0.1	4.7	36.4	82.9 ± 0.1	194 ± 6	35 ± 3
7	1.27 ± 0.02	98.50 ± 1.4	0.270 ± 0.001	121	38.5 ± 0.1	5.1	33.4	85.8 ± 0.1	166 ± 4	54 ± 2
8	1.28 ± 0.00	98.50 ± 0.1	0.277 ± 0.002	151	36.5 ± 0.1	4.2	32.3	82 ± 3	157 ± 1	52 ± 1
9	1.28 ± 0.01	100.0 ± 0.3	0.266 ± 0.004	145	35.0 ± 0.1	4.6	30.4	83.4 ± 0.5	123 ± 1	45 ± 0
10	1.28 ± 0.01	99.50 ± 1.1	0.266 ± 0.003	178	33.4 ± 0.1	3.9	29.5	89 ± 3	145 ± 4	50 ± 1
11	1.29 ± 0.03	102.5 ± 2.0	0.244 ± 0.002	199	32.7 ± 0.1	4.0	28.7	84 ± 6	128 ± 9	46 ± 4
12	1.20 ± 0.01	104.3 ± 0.6	0.166 ± 0.002	178	31.2 ± 0.1	6.7	24.5	41.8 ± 0.1	81 ± 7	35 ± 9
13	1.22 ± 0.02	105.9 ± 1.8	0.162 ± 0.001	192	36.8 ± 0.1	6.4	30.4	38 ± 1	65 ± 9	24 ± 3
14	1.24 ± 0.01	107.1 ± 1.0	0.159 ± 0.001	175	34.3 ± 0.1	7.0	27.3	35.8 ± 0.1	62 ± 18	28 ± 9
15	1.22 ± 0.01	106.3 ± 0.7	0.150 ± 0.002	185	34.0 ± 0.1	7.1	26.9	36 ± 1	49 ± 4	23 ± 6
16	1.24 ± 0.03	115.3 ± 0.6	0.082 ± 0.001	220	35.9 ± 0.1	10.4	25.5	9.1 ± 0.3	12 ± 1	11 ± 2
17	1.50 ± 0.02	70.90 ± 0.3	0.625 ± 0.006	71.0	80.8 ± 0.1	1.6	79.2	384 ± 15	426 ± 8	81 ± 8
18	1.50 ± 0.04	71.90 ± 0.1	0.605 ± 0.006	65.4	68.6 ± 0.1	1.9	66.7	504 ± 3	442 ± 1	85 ± 1
19	1.43 ± 0.02	93.60 ± 0.5	0.416 ± 0.007	139	50.8 ± 0.1	2.4	48.4	192 ± 9	251 ± 1	81 ± 0
20	1.40 ± 0.01	102.3 ± 0.7	0.321 ± 0.003	175	37.6 ± 0.1	3.0	34.6	144 ± 1	210 ± 5	64 ± 2
21	1.43 ± 0.02	84.00 ± 1.1	0.492 ± 0.001	50.2	51.6 ± 0.1	4.0	47.6	148 ± 2	309 ± 7	73 ± 1
22	1.45 ± 0.00	86.90 ± 0.1	0.480 ± 0.001	53.5	53.9 ± 0.1	4.1	49.8	137 ± 5	262 ± 16	72 ± 4
23	1.32 ± 0.00	96.80 ± 0.1	0.321 ± 0.001	193	36.4 ± 0.1	2.8	33.6	128 ± 1	172 ± 6	66 ± 8
24	1.33 ± 0.01	97.30 ± 0.6	0.323 ± 0.002	205	36.3 ± 0.1	2.6	33.7	143 ± 7	144 ± 9	66 ± 5
25	1.20 ± 0.03	113.8 ± 0.2	0.064 ± 0.001	186	28.0 ± 0.1	13.3	14.7	7.6 ± 0.1	8 ± 1	10 ± 1
26	1.20 ± 0.03	112.6 ± 1.1	0.079 ± 0.001	242	34.8 ± 0.1	10.4	24.4	7 ± 1	7 ± 3	8 ± 3

Table S.VII.1. Measured and Calculated Properties of PUA Aerogels Prepared in Individual Solvents, and Fitted to the Preparation Conditions (see Appendix X). (cont.)

DoE run No.	*K*-index	contact angle (θ, deg.)	bulk density (ρ_b, g cm^{-3})	BET surface area (σ, m^2 g^{-1})	thermal conductivity (mW m^{-1} K^{-1}) [b]			mechanical properties		
					λ_{Total}	λ_g	λ_s	Young's modulus (E, MPa)	Ultimate Compressive Strength (UCS, MPa)	specific energy U_T (J g^{-1})
THF										
1	1.50 ± 0.10	66.70 ± 0.1	0.672 ± 0.037	73.1	65.6 ± 0.1	1.3	$64._3$	426 ± 4	337 ± 2	91 ± 4
2	1.53 ± 0.26	74.50 ± 0.6	0.604 ± 0.098	69.1	56.0 ± 0.2	1.8	$54._2$	357 ± 5	362 ± 14	86 ± 1
3	1.51 ± 0.05	70.90 ± 0.1	0.628 ± 0.018	109	59.0 ± 0.1	1.1	$57._9$	429 ± 26	376 ± 4	94 ± 2
4	1.53 ± 0.11	88.30 ± 0.7	0.507 ± 0.051	114	53.8 ± 0.1	1.9	$51._9$	266 ± 3	362 ± 22	89 ± 1
5	1.50 ± 0.02	89.10 ± 0.9	0.489 ± 0.009	157	48.9 ± 0.1	1.6	$47._3$	193 ± 14	286 ± 1	92 ± 1
6	1.45 ± 0.02	91.20 ± 0.1	0.437 ± 0.011	130	46.4 ± 0.1	2.2	$44._2$	261 ± 3	395 ± 2	80 ± 2
7	1.41 ± 0.03	91.50 ± 1.6	0.412 ± 0.008	152	43.7 ± 0.1	2.2	$41._5$	134 ± 1	318 ± 4	85 ± 1
8	1.30 ± 0.02	87.80 ± 0.1	0.384 ± 0.008	184	46.4 ± 0.1	2.1	$44._3$	127 ± 4	296 ± 3	79 ± 1
9	1.33 ± 0.02	90.20 ± 0.1	0.381 ± 0.009	181	42.3 ± 0.1	2.2	$40._1$	108 ± 3	292 ± 2	78 ± 1
10	1.33 ± 0.04	95.20 ± 1.3	0.341 ± 0.019	182	32.0 ± 0.1	2.6	$29._4$	116 ± 1	263 ± 2	80 ± 2
11	1.33 ± 0.01	92.80 ± 0.6	0.358 ± 0.007	208	32.3 ± 0.1	2.2	$30._1$	94 ± 1	271 ± 2	77 ± 4
12	1.20 ± 0.02	100.1 ± 0.5	0.201 ± 0.012	165	24.3 ± 0.1	5.8	$18._5$	37 ± 3	190 ± 5	65 ± 6
13	1.23 ± 0.02	97.80 ± 1.7	0.247 ± 0.001	199	27.7 ± 0.1	3.9	$23._8$	44 ± 2	172 ± 2	69 ± 1
14	1.22 ± 0.01	100.4 ± 0.4	0.211 ± 0.007	188	20.3 ± 0.1	4.9	$15._4$	41 ± 4	108 ± 3	61 ± 2
15	1.22 ± 0.02	101.4 ± 1.4	0.210 ± 0.005	231	23.1 ± 0.1	4.2	$18._9$	39 ± 2	92 ± 8	64 ± 6
16	1.20 ± 0.02	112.0 ± 1.4	0.079 ± 0.002	242	18.8 ± 0.1	$10._1$	8.7	13.3 ± 0.1	18 ± 1	17 ± 2
17	[c]	[c]	[c]	[c]	[c]	[c]	[c]	[c]	[c]	[c]
18	1.50 ± 0.04	69.60 ± 0.1	0.648 ± 0.01	81.9	64.8 ± 0.1	1.4	$63._4$	299 ± 4	325 ± 26	93 ± 2
19	1.52 ± 0.05	80.70 ± 1.1	0.560 ± 0.010	178	60.1 ± 0.1	1.0	$59._1$	222 ± 25	272 ± 14	92 ± 1
20	1.52 ± 0.03	100.8 ± 0.6	0.410 ± 0.014	219	49.0 ± 0.1	1.7	$47._3$	113 ± 3	250 ± 1	89 ± 1
21	1.54 ± 0.04	76.40 ± 0.1	0.608 ± 0.016	95.1	56.4 ± 0.1	1.4	$55._0$	311 ± 13	333 ± 6	83 ± 2
22	1.52 ± 0.04	67.20 ± 0.2	0.662 ± 0.007	71.2	56.5 ± 0.1	1.4	$55._1$	290 ± 7	327 ± 18	81 ± 3
23	1.48 ± 0.02	95.60 ± 0.1	0.431 ± 0.008	167	43.1 ± 0.1	1.9	$41._2$	168 ± 4	280 ± 4	80 ± 1
24	1.52 ± 0.08	115.1 ± 1.5	0.308 ± 0.036	242	36.8 ± 0.1	2.5	$34._3$	135 ± 6	186 ± 32	80 ± 1
25	1.22 ± 0.01	113.4 ± 0.1	0.082 ± 0.003	232	18.5 ± 0.1	$10._2$	8.3	13 ± 1	13 ± 1	26 ± 1
26	1.21 ± 0.01	113.8 ± 0.5	0.078 ± 0.002	242	18.8 ± 0.2	$10._2$	8.6	10 ± 1	11 ± 2	14 ± 1

Table S.VII.1. Measured and Calculated Properties of PUA Aerogels Prepared in Individual Solvents, and Fitted to the Preparation Conditions (see Appendix X). (cont.)

DoE run No.	*K*-index	contact angle (θ, deg.)	bulk density (ρ_b, g cm^{-3})	BET surface area (σ, m^2 g^{-1})	thermal conductivity (mW m^{-1} K^{-1}) [b]			mechanical properties		
					λ_{Total}	λ_g	λ_s	Young's modulus (E, MPa)	Ultimate Compressive Strength (UCS, MPa)	specific energy U_T (J g^{-1})
ethyl acetate										
1	1.38 ± 0.02	97.90 ± 0.1	0.347 ± 0.006	109	56.7 ± 0.1	3.9	52.8	160 ± 1	247 ± 7	61 ± 2
2	1.34 ± 0.01	91.40 ± 0.3	0.375 ± 0.003	63.7	48.0 ± 0.1	5.2	42.8	123 ± 3	239 ± 1	62 ± 1
3	1.33 ± 0.02	93.10 ± 1.4	0.358 ± 0.003	143	45.9 ± 0.1	3.0	42.9	119 ± 12	248 ± 1	69 ± 1
4	1.34 ± 0.02	96.50 ± 1.3	0.334 ± 0.001	136	45.2 ± 0.1	3.5	41.7	114 ± 8	221 ± 16	62 ± 4
5	1.32 ± 0.02	96.60 ± 1.5	0.323 ± 0.003	146	43.7 ± 0.1	3.5	40.2	111 ± 14	272 ± 3	75 ± 1
6	1.29 ± 0.02	98.50 ± 1.6	0.279 ± 0.001	106	38.1 ± 0.1	5.4	32.7	69 ± 4	265 ± 3	72 ± 2
7	1.27 ± 0.01	98.50 ± 0.1	0.279 ± 0.001	107	37.4 ± 0.1	5.5	31.9	69 ± 5	163 ± 3	53 ± 1
8	1.28 ± 0.00	98.70 ± 0.1	0.270 ± 0.003	156	35.2 ± 0.1	4.2	31.0	84 ± 1	257 ± 6	84 ± 7
9	1.27 ± 0.02	98.40 ± 1.6	0.270 ± 0.001	150	36.9 ± 0.1	4.4	32.5	72 ± 4	299 ± 21	73 ± 1
10	1.27 ± 0.01	98.60 ± 0.1	0.270 ± 0.004	148	37.6 ± 0.1	4.4	33.2	76 ± 4	213 ± 49	67 ± 2
11	1.26 ± 0.02	99.60 ± 0.2	0.254 ± 0.013	177	36.6 ± 0.1	4.2	32.4	76 ± 5	198 ± 1	58 ± 2
12	1.19 ± 0.02	102.5 ± 1.5	0.170 ± 0.001	145	30.5 ± 0.1	7.5	23.0	32 ± 2	165 ± 1	57 ± 1
13	1.24 ± 0.01	105.5 ± 0.1	0.177 ± 0.002	173	31.7 ± 0.1	6.3	25.4	32 ± 1	191 ± 3	36 ± 3
14	1.23 ± 0.01	106.2 ± 0.1	0.168 ± 0.004	200	30.5 ± 0.1	6.1	24.4	32 ± 1	190 ± 5	87 ± 1
15	1.22 ± 0.02	105.3 ± 1.4	0.167 ± 0.002	193	21.4 ± 0.1	6.2	15.2	35 ± 2	163 ± 4	72 ± 4
16	1.22 ± 0.02	114.2 ± 0.1	0.080 ± 0.003	206	25.4 ± 0.2	11	14.4	8 ± 1	23 ± 3	16 ± 2
17	1.43 ± 0.01	93.50 ± 0.1	0.405 ± 0.002	98.5	64.7 ± 0.1	3.3	61.4	147 ± 1	252 ± 5	66 ± 2
18	1.37 ± 0.01	90.10 ± 0.4	0.410 ± 0.004	124	60.0 ± 0.1	2.7	57.3	156 ± 2	231 ± 5	63 ± 1
19	1.36 ± 0.02	98.40 ± 0.9	0.327 ± 0.004	191	39.9 ± 0.1	2.7	37.2	134 ± 6	240 ± 34	77 ± 5
20	1.39 ± 0.02	101.8 ± 0.8	0.316 ± 0.008	188	51.7 ± 0.1	2.9	48.8	135 ± 3	238 ± 6	70 ± 4
21	1.35 ± 0.01	95.50 ± 0.6	0.346 ± 0.001	69.3	50.7 ± 0.2	5.5	45.2	99 ± 1	245 ± 19	65 ± 5
22	1.32 ± 0.01	93.20 ± 0.5	0.352 ± 0.002	139	51.5 ± 0.1	3.2	48.3	115 ± 4	239 ± 14	68 ± 5
23	1.30 ± 0.00	99.10 ± 0.1	0.285 ± 0.001	205	38.9 ± 0.1	3.1	35.8	96 ± 11	233 ± 1	69 ± 2
24	1.29 ± 0.01	99.40 ± 1.1	0.278 ± 0.001	210	37.6 ± 0.1	3.2	34.4	98 ± 1	212 ± 14	67 ± 6
25	1.23 ± 0.00	116.1 ± 0.1	0.071 ± 0.001	195	23.0 ± 0.1	12.1	10.9	10 ± 1	15 ± 1	25 ± 9
26	1.21 ± 0.01	114.1 ± 0.4	0.071 ± 0.003	214	23.8 ± 0.1	11.6	12.2	7.4 ± 0.2	12 ± 2	8 ± 1

Table S.VII.1. Measured and Calculated Properties of PUA Aerogels Prepared in Individual Solvents, and Fitted to the Preparation Conditions (see Appendix X). (cont.)

DoE run No.	*K*-index	contact angle (θ, deg.)	bulk density (ρ_b, g cm^{-3})	BET surface area (σ, m^2 g^{-1})	thermal conductivity (mW m^{-1} K^{-1}) [b]			mechanical properties		
					λ_{Total}	λ_g	λ_s	Young's modulus (E, MPa)	Ultimate Compressive Strength (UCS, MPa)	specific energy U_T (J g^{-1})
2-butanone										
1	1.50 ± 0.02	70.80 ± 0.6	0.624 ± 0.002	89.2	63.9 ± 0.1	1.3	$62._6$	356 ± 5	351 ± 6	84 ± 2
2	1.45 ± 0.03	79.70 ± 1.2	0.532 ± 0.011	78.5	52.6 ± 0.1	2.3	$50._3$	196 ± 9	324 ± 2	73 ± 1
3	1.45 ± 0.03	84.10 ± 0.1	0.496 ± 0.013	93.4	47.8 ± 0.1	2.3	$45._5$	188 ± 5	323 ± 2	78 ± 1
4	1.35 ± 0.02	96.70 ± 1.1	0.338 ± 0.009	174	36.3 ± 0.1	2.8	$33._5$	142 ± 3	248 ± 3	70 ± 2
5	1.35 ± 0.01	99.20 ± 0.1	0.318 ± 0.001	232	29.5 ± 0.1	2.4	$27._1$	134 ± 8	250 ± 7	73 ± 3
6	1.31 ± 0.02	96.80 ± 1.5	0.309 ± 0.002	107	34.7 ± 0.1	4.7	$30._0$	56 ± 9	254 ± 1	66 ± 2
7	1.30 ± 0.02	96.70 ± 1.1	0.310 ± 0.004	167	34.4 ± 0.1	3.3	$31._1$	73 ± 10	269 ± 1	66 ± 1
8	1.27 ± 0.02	99.30 ± 1.6	0.265 ± 0.004	170	29.1 ± 0.1	4.0	$25._1$	79 ± 6	242 ± 1	68 ± 4
9	1.26 ± 0.02	98.20 ± 1.4	0.266 ± 0.003	170	29.2 ± 0.1	4.0	$25._2$	76.9 ± 0.2	247 ± 2	62 ± 1
10	1.25 ± 0.02	98.60 ± 0.2	0.261 ± 0.001	172	30.2 ± 0.1	4.1	$26._1$	76.8 ± 0.3	242 ± 8	65 ± 2
11	1.26 ± 0.01	101.6 ± 0.7	0.230 ± 0.001	194	24.1 ± 0.1	4.3	$19._8$	64 ± 1	239 ± 1	73 ± 4
12	1.22 ± 0.03	106.5 ± 1.2	0.150 ± 0.001	191	26.4 ± 0.1	7.0	$19._4$	32 ± 2	240 ± 2	64 ± 2
13	1.25 ± 0.01	109.5 ± 0.1	0.147 ± 0.001	177	28.5 ± 0.1	7.5	$21._0$	28.5 ± 0.3	246 ± 1	63 ± 3
14	1.31 ± 0.02	113.9 ± 1.5	0.160 ± 0.002	197	25.6 ± 0.1	6.5	$19._1$	30 ± 4	243 ± 1	59 ± 6
15	1.29 ± 0.02	113.5 ± 0.1	0.149 ± 0.001	211	23.8 ± 0.1	6.6	$17._2$	30 ± 2	238 ± 1	64 ± 4
16	1.21 ± 0.04	114.7 ± 1.2	0.066 ± 0.002	216	23.1 ± 0.1	$12._1$	$11._0$	4.6 ± 0.2	247 ± 2	17 ± 2
17	1.50 ± 0.05	74.20 ± 1.4	0.610 ± 0.014	81.8	67.7 ± 0.1	1.6	$66._1$	288 ± 6	327 ± 4	81 ± 5
18	1.50 ± 0.01	72.50 ± 0.1	0.639 ± 0.004	85.9	66.3 ± 0.1	1.4	$64._9$	331 ± 5	332 ± 2	77 ± 1
19	1.36 ± 0.01	94.20 ± 0.1	0.365 ± 0.007	178	36.5 ± 0.1	2.4	$34._1$	156 ± 14	252 ± 4	82 ± 4
20	1.35 ± 0.00	96.80 ± 0.1	0.340 ± 0.002	199	37.7 ± 0.1	2.4	$35._3$	148 ± 3	244 ± 3	75 ± 3
21	1.45 ± 0.03	81.40 ± 0.9	0.519 ± 0.011	153	53.8 ± 0.1	1.3	$52._5$	220 ± 3	331 ± 2	76 ± 1
22	1.45 ± 0.01	90.70 ± 0.1	0.444 ± 0.006	164	47.7 ± 0.1	1.8	$45._9$	148 ± 6	285 ± 5	68 ± 5
23	1.31 ± 0.01	95.50 ± 0.6	0.319 ± 0.006	207	30.4 ± 0.1	2.6	$27._8$	147 ± 2	262 ± 7	77 ± 3
24	1.30 ± 0.02	98.10 ± 0.8	0.291 ± 0.008	227	36.2 ± 0.1	2.8	$33._4$	104 ± 2	241 ± 4	77 ± 6
25	1.17 ± 0.03	110.5 ± 0.6	0.069 ± 0.001	223	23.6 ± 0.1	$11._5$	$12._1$	6 ± 1	244 ± 1	21 ± 1
26	1.23 ± 0.03	117.6 ± 1.3	0.051 ± 0.001	242	19.6 ± 0.1	$13._2$	6.4	3.9 ± 0.2	262 ± 1	15 ± 1

Table S.VII.1. Measured and Calculated Properties of PUA Aerogels Prepared in Individual Solvents, and Fitted to the Preparation Conditions (see Appendix X). (cont.)

DoE run No.	*K*-index	contact angle (θ, deg.)	bulk density (ρ_b, g cm^{-3})	BET surface area (σ, m^2 g^{-1})	thermal conductivity (mW m^{-1} K^{-1}) [b]			mechanical properties		
					λ_{Total}	λ_g	λ_s	Young's modulus (E, MPa)	Ultimate Compressive Strength (UCS, MPa)	specific energy U_T (J g^{-1})
DMF [d]										
12	1.52 ± 0.01	111.4 ± 0.1	0.326 ± 0.002	133	41.8 ± 0.1	3.7	38.1	252 ± 3	262 ± 6	76 ± 2
13	1.45 ± 0.04	103.4 ± 0.1	0.350 ± 0.022	144	39.3 ± 0.1	3.2	36.1	226 ± 4	256 ± 5	80 ± 2
14	1.43 ± 0.02	106.3 ± 1.0	0.310 ± 0.004	128	42.7 ± 0.1	4.1	38.6	176 ± 2	281 ± 10	72 ± 3
15	1.45 ± 0.02	109.6 ± 0.1	0.298 ± 0.009	104	36.4 ± 0.1	5.1	31.3	156 ± 2	200 ± 2	71 ± 3
16	1.23 ± 0.01	113.3 ± 0.3	0.101 ± 0.003	228	25.3 ± 0.1	8.7	16.6	27 ± 2	29 ± 2	34 ± 2
25	1.22 ± 0.01	109.8 ± 0.8	0.121 ± 0.004	199	21.4 ± 0.1	8.2	13.2	33 ± 1	21 ± 1	32 ± 2
26	1.25 ± 0.01	116.0 ± 0.1	0.085 ± 0.003	230	25.4 ± 0.1	9.8	15.6	23 ± 1	19 ± 2	37 ± 1

[a] Samples for which numbers are not provided developed cracks during processing and were not suitable for the indicated tests.

[b] λ_{Total} was measured as described in the Experimental Section of the main article. The λ_{Total} values of selected runs was measured by two methods (laser flash and hot plate) and the results are compared in Table S.VII.3 below.

Data concerning the thermal conductivity through the solid framework, λ_s, were calculated *via* $\lambda_s = \lambda_{Total} - \lambda_g$. The gaseous thermal conductivity of each sample, λ_g, was measured *via* the Knudsen Equation (see references in the main article):

$$\lambda_g = \lambda_{g,0} \Pi [1 + 2\beta(l_g/\Phi)]$$

where $\lambda_{g,0}$ is the gaseous conductivity of the pore-filling gas (for air at 300 K and 1 bar pressure $\lambda_{g,0}$ = 0.02619 W m^{-1} K^{-1}, Π is the porosity of the samples (in decimal notation, from Tables S.II.1 and S.II.2 of Appendix II), β is a parameter that accounts for the energy transfer between the pore-filling gas and the aerogel walls (for air β = 2), l_g is the mean free path of the gas molecules (for air at 1 bar $l_g \approx$ 70 nm), and Φ is the average pore diameter from Tables S.II.1 and S.II.2 of Appendix II.

[c] That sample collapsed, the bulk density was >1.0 g cm^{-3} and the porosity was <30% v/v.

[d] All samples from Runs 1–11 and 17–24 collapsed, the bulk densities were >1.0 g cm^{-3} and the porosities were <30% v/v.

Table S.VII.2. Measured and Calculated Properties of PUA Aerogels Prepared in Binary Solvent Systems, and Fitted to the Preparation Conditions (see Appendix X). (cont.)

DoE run No.	*K*-index	contact angle (θ, deg.)	bulk density (ρ_b, g cm^{-3})	BET surface area (σ, m^2 g^{-1})	thermal conductivity (mW m^{-1} K^{-1}) [b]			mechanical properties		
					λ_{Total}	λ_g	λ_s	Young's modulus (E, MPa)	Ultimate Compressive Strength (UCS, MPa)	specific energy U_T (J g^{-1})
A: acetonitrile-nitromethane 1:1 v/v										
1	1.54 ± 0.05	83.80 ± 0.5	0.537 ± 0.020	23.2	65.5 ± 0.1	4.8	$60._7$	44 ± 5	244 ± 18	79 ± 3
24	1.28 ± 0.02	100.6 ± 1.0	0.257 ± 0.003	107	43.0 ± 0.1	5.9	$37._1$	72 ± 2	164 ± 12	51 ± 1
2	1.83 ± 0.02	128.1 ± 1.1	0.355 ± 0.005	17.5	63.7 ± 0.1	$11._2$	$52._5$	60 ± 3	250 ± 5	57 ± 2
B: acetonitrile-propylene carbonate 1:1 v/v										
1	1.54 ± 0.03	88.30 ± 0.1	0.508 ± 0.012	37.9	72.5 ± 0.1	4.5	$68._0$	175 ± 4	193 ± 3	86 ± 4
8	1.37 ± 0.02	109.2 ± 0.5	0.241 ± 0.008	63.7	54.1 ± 0.1	8.9	$45._2$	61 ± 5	65.3 ± 8	55 ± 2
16	1.57 ± 0.10	149.2 ± 1.5	0.059 ± 0.002	131	32.0 ± 0.1	$15._9$	$16._1$	6.6 ± 0.2	7.9 ± 0.1	13 ± 1
26	1.56 ± 0.19	149.8 ± 1.6	0.050 ± 0.004	222	30.8 ± 0.1	$13._9$	$16._9$	5 ± 1	4.49 ± 1	10 ± 1
C: acetonitrile-acetone 1:1 v/v										
17	1.52 ± 0.02	85.80 ± 0.3	0.511 ± 0.010	46.3	66.1 ± 0.1	4.2	$61._9$	306 ± 7	350 ± 20	92 ± 6
8	1.78 ± 0.03	138.6 ± 2.1	0.258 ± 0.004	58.9	41.2 ± 0.1	8.6	$32._6$	83 ± 4	260 ± 8	48 ± 3
16	1.54 ± 0.06	147.3 ± 2.3	0.054 ± 0.001	115	26.5 ± 0.1	$17._2$	$9._3$	8 ± 1	50.1 ± 3	12 ± 1
D: acetonitrile-DMF 1:1 v/v										
6	1.43 ± 0.02	93.60 ± 0.3	0.411 ± 0.007	67.7	49.6 ± 0.1	4.3	$45._3$	65 ± 3	194 ± 2	71 ± 1
13	1.18 ± 0.00	100.7 ± 0.1	0.175 ± 0.003	158	31.0 ± 0.1	6.9	$24._1$	28 ± 2	44.4 ± 4	43 ± 3
16	1.19 ± 0.02	110.8 ± 1.6	0.079 ± 0.002	204	23.8 ± 0.1	$11._0$	$12._8$	12 ± 1	12.9 ± 1	31 ± 3
E: acetone-ethyl acetate 1:1 v/v										
17	1.53 ± 0.01	78.80 ± 0.1	0.587 ± 0.004	57.9	63.0 ± 0.1	2.3	$60._7$	325 ± 3	320 ± 25	93 ± 2
8	1.30 ± 0.02	99.10 ± 1.2	0.274 ± 0.002	176	39.1 ± 0.1	3.7	$35._4$	75 ± 6	258 ± 7	55 ± 1
F: ethyl acetate-DMF 1:1 v/v										
15	1.24 ± 0.01	103.9 ± 1.0	0.191 ± 0.003	189	41.2 ± 0.1	5.5	$35._7$	37 ± 4	162 ± 6	64 ± 3
26	1.18 ± 0.03	110.3 ± 0.4	0.075 ± 0.003	263	24.2 ± 0.2	9.9	$14._3$	13 ± 3	18.3 ± 3	19 ± 2
G: nitromethane-2-butanone 1:1 v/v										
12	1.24 ± 0.01	107.8 ± 0.4	0.159 ± 0.002	105	35.7 ± 0.2	9.7	$26._0$	35 ± 1	256 ± 13	63 ± 4
22	1.52 ± 0.03	100.6 ± 1.6	0.405 ± 0.005	87.3	59.3 ± 0.1	3.7	$55._6$	153 ± 6	292 ± 16	72 ± 7
H: propylene carbonate-2-butanone 1:1 v/v										
25	1.23 ± 0.02	116.2 ± 1.5	0.065 ± 0.001	209	28.9 ± 0.1	$12._7$	$16._2$	4.6 ± 0.2	234 ± 18	16 ± 1

Table S.VII.3. Total Thermal Conductivity, λ_{Total}, of Selected Polyurea Aerogels *via* the Hot-plate and the Laser Flash Methods.

Sample ID	**Bulk density, ρ_b (g cm^{-3})**	**Heat capacity, c_P (J g^{-1} K^{-1})**	**Thermal diffusivity, R (mm^{2}s^{-1})**	**λ_{Total} (mW m^{-1} K^{-1}) *via* the laser-flash method [a]**	**λ_{Total} (mW m^{-1} K^{-1}) *via* the hot-plate method [b]**
acetonitrile - Run 12	0.169 ± 0.006	1.2$_2$ ± 0.10	0.205 ± 0.009	42.3 ± 0.1	39.7 ± 1.3
acetonitrile - Run 13	0.151 ± 0.009		0.210 ± 0.010	38.7 ± 0.1	33.9 ± 1.0
acetonitrile - Run 14	0.140 ± 0.002		0.209 ± 0.006	35.7 ± 0.1	32.7 ± 1.1
acetonitrile - Run 15	0.122 ± 0.001		0.210 ± 0.012	31.3 ± 0.1	32.0 ± 1.0
acetonitrile - Run 16	0.062 ± 0.001		0.410 ± 0.034	31.0 ± 0.1	29.0 ± 1.0
acetonitrile - Run 25	0.071 ± 0.002		0.398 ± 0.025	34.5 ± 0.1	31.5 ± 1.0
acetonitrile - Run 26	0.040 ± 0.001		0.625 ± 0.057	30.5 ± 0.1	29.4 ± 0.9
nitromethane - Run 16	0.068 ± 0.003		0.402 ± 0.061	33.3 ± 0.2	30.0 ± 1.0
nitromethane - Run 25	0.081 ± 0.001		0.320 ± 0.022	31.6 ± 0.1	30.1 ± 1.2
acetone - Run 7	0.270 ± 0.001		0.117 ± 0.010	38.5 ± 0.1	32.4 ± 1.0
acetone - Run 8	0.277 ± 0.002		0.108 ± 0.001	36.5 ± 0.1	31.6 ± 1.0
acetone - Run 10	0.266 ± 0.003		0.103 ± 0.003	33.4 ± 0.1	33.3 ± 1.0
acetone - Run 11	0.244 ± 0.002		0.110 ± 0.002	32.7 ± 0.1	29.2 ± 1.0
2-butanone - Run 10	0.261 ± 0.001		0.095 ± 0.003	30.2 ± 0.1	29.1 ± 1.0
2-butanone - Run 16	0.066 ± 0.002		0.287 ± 0.021	23.1 ± 0.1	23.0 ± 0.8
2-butanone - Run 25	0.069 ± 0.001		0.280 ± 0.006	23.6 ± 0.1	24.5 ± 0.9

[a] Average of 3 samples. Calculated *via* $\lambda_{Total} = \rho_b \times c_P \times R$.

[b] Single sample, average of 5 measurements of the heat flux. For construction of a calibration curve and analysis of standards, see Table S.8 in the Supporting Information of Reference S.R.6.

APPENDIX VIII. SEM OF ALL RUNS WITH *K*-INDEXES IN THE RANGE 1.45–1.64

2-BU - Run 2 ρ_b = 0.532 g cm^{-3} σ = 78.5 m^2 g^{-1} r = 33 nm

θ = 79.70°, Π = 55.1%, ***K*-index = 1.45**

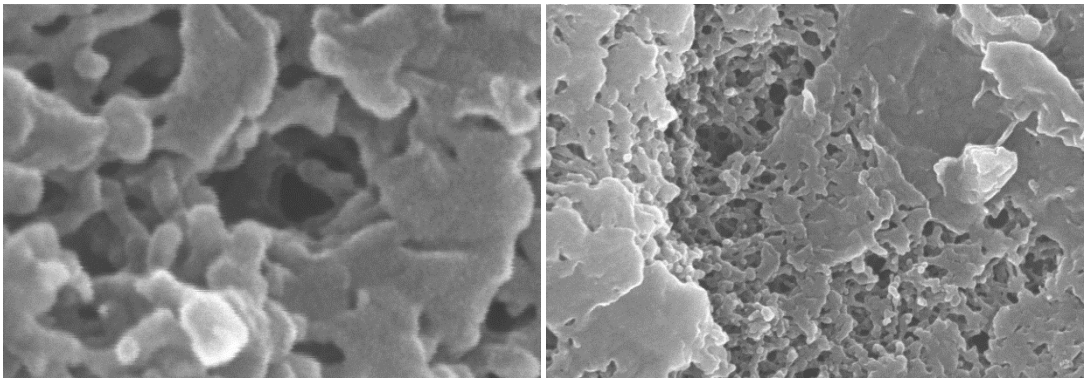

2-BU - Run 3 ρ_b = 0.496 g cm^{-3} σ = 93.4 m^2 g^{-1} r = 27 nm

θ = 84.10°, Π = 58.1%, ***K*-index = 1.45**

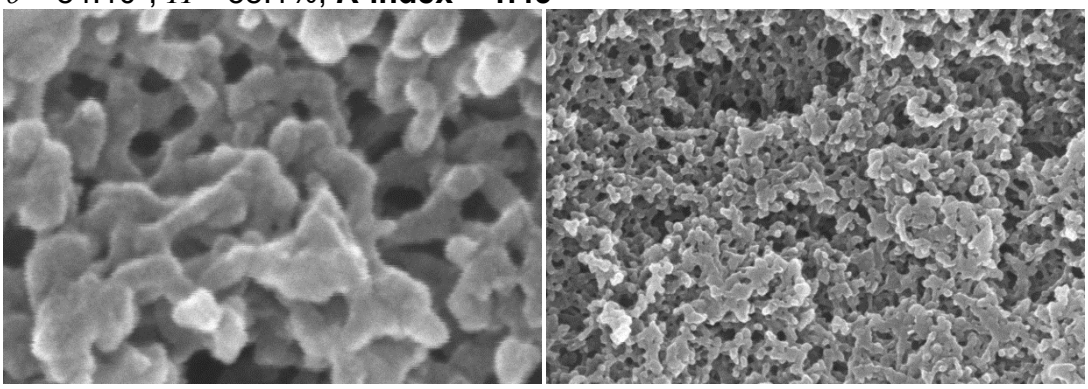

THF - Run 6 ρ_b = 0.437 g cm^{-3} σ = 130 m^2 g^{-1} r = 20 nm

θ = 91.20°, Π = 62.9%, ***K*-index = 1.45**

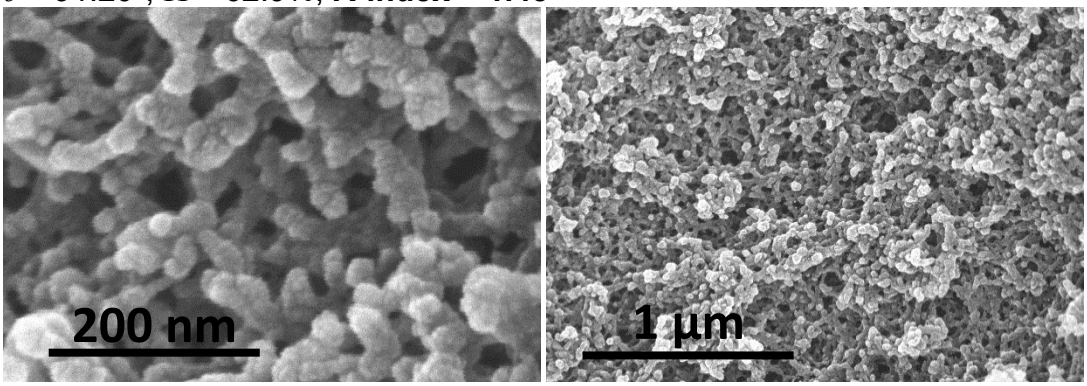

Figure S.IX.1. SEM images at two magnifications of all samples with *K*-index values in the range 1.45–1.64. Other pertinent information (solvent, run number, bulk density, BET surface area, water contact angle and porosity) are included with each pair of micrographs.

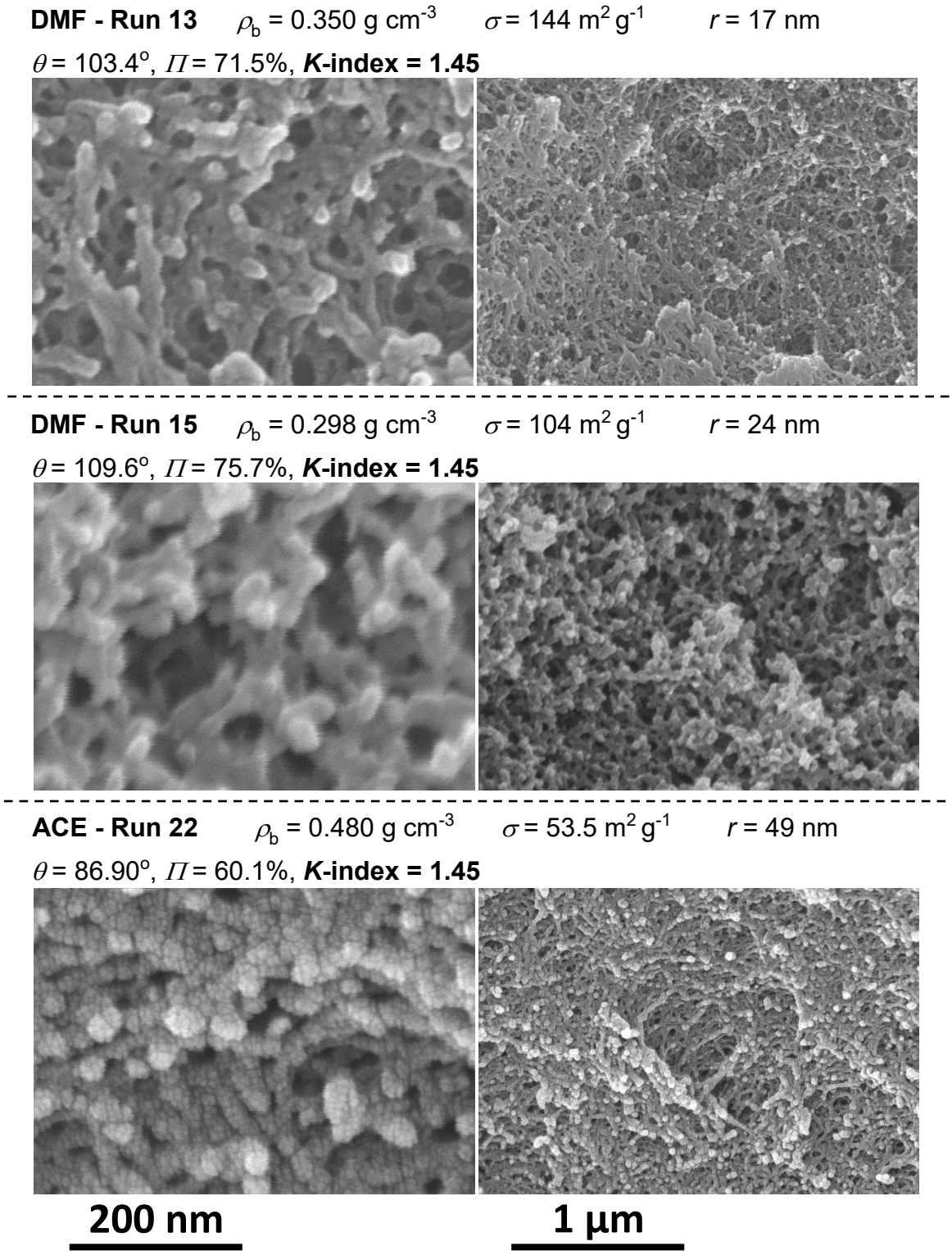

Figure S.IX.1. SEM images at two magnifications of all samples with *K*-index values in the range 1.45–1.64. Other pertinent information (solvent, run number, bulk density, BET surface area, water contact angle and porosity) are included. (cont.)

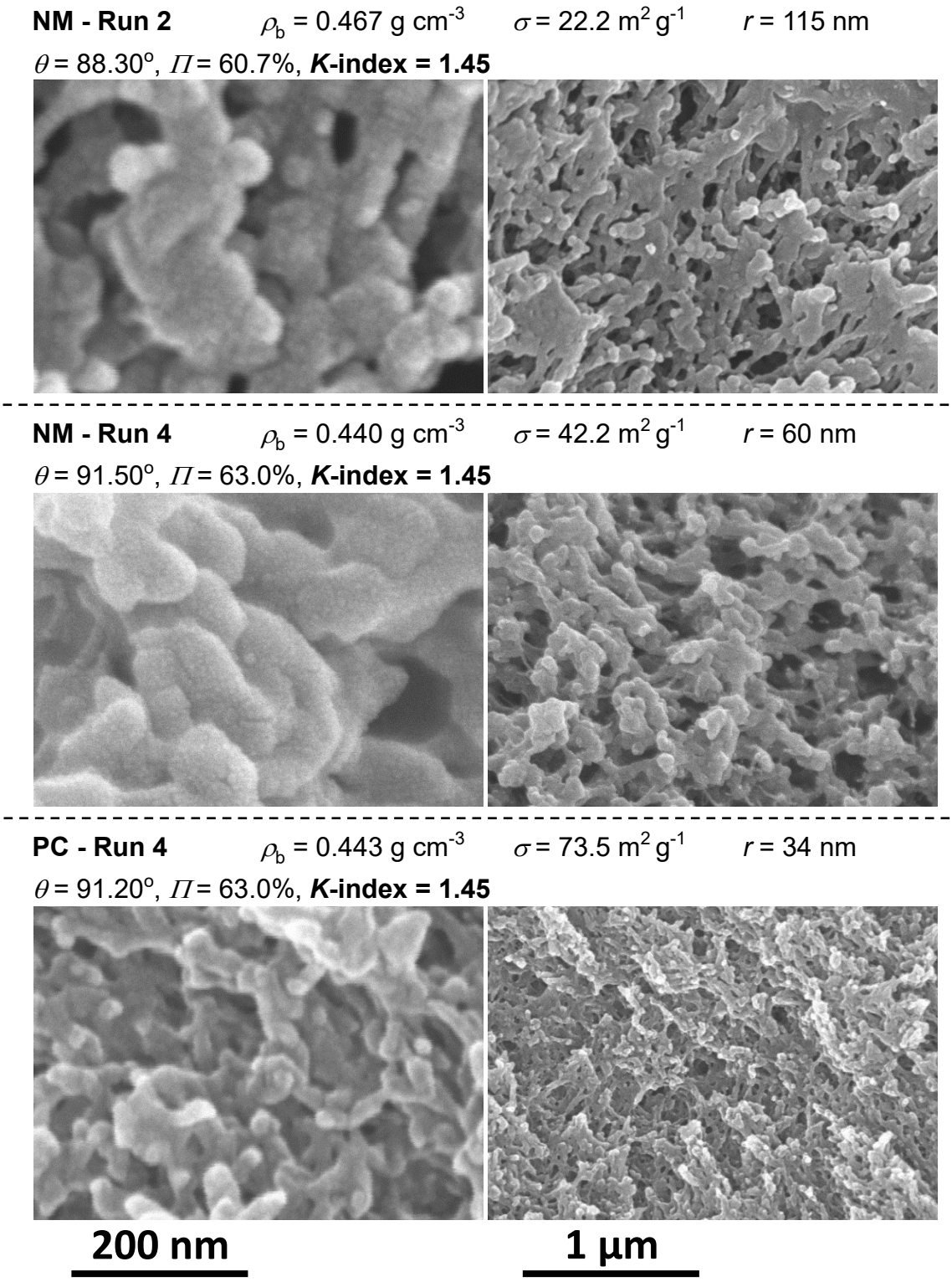

Figure S.IX.1. SEM images at two magnifications of all samples with *K*-index values in the range 1.45–1.64. Other pertinent information (solvent, run number, bulk density, BET surface area, water contact angle and porosity) are included. (cont.)

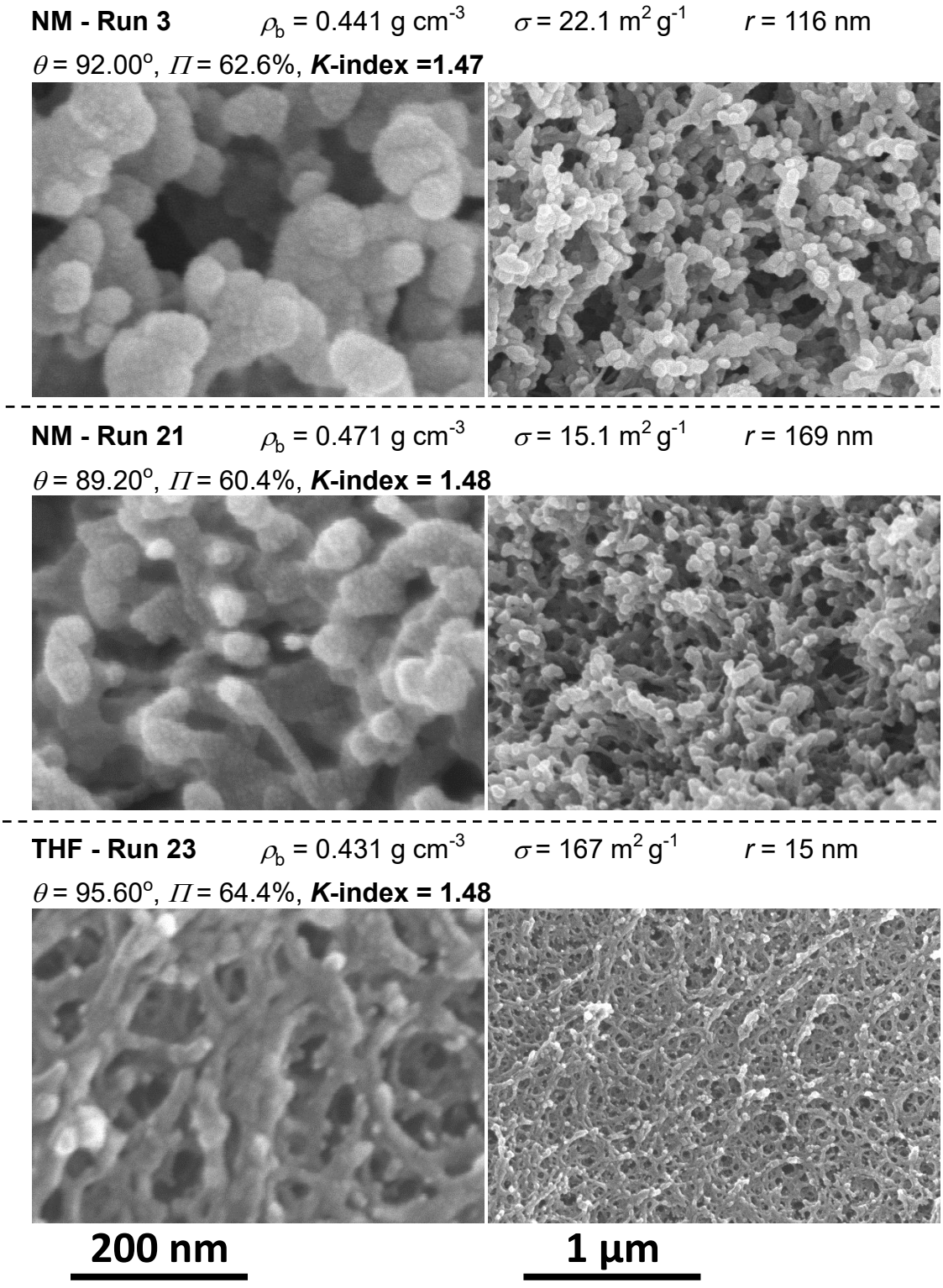

Figure S.IX.1. SEM images at two magnifications of all samples with *K*-index values in the range 1.45–1.64. Other pertinent information (solvent, run number, bulk density, BET surface area, water contact angle and porosity) are included. (cont.)

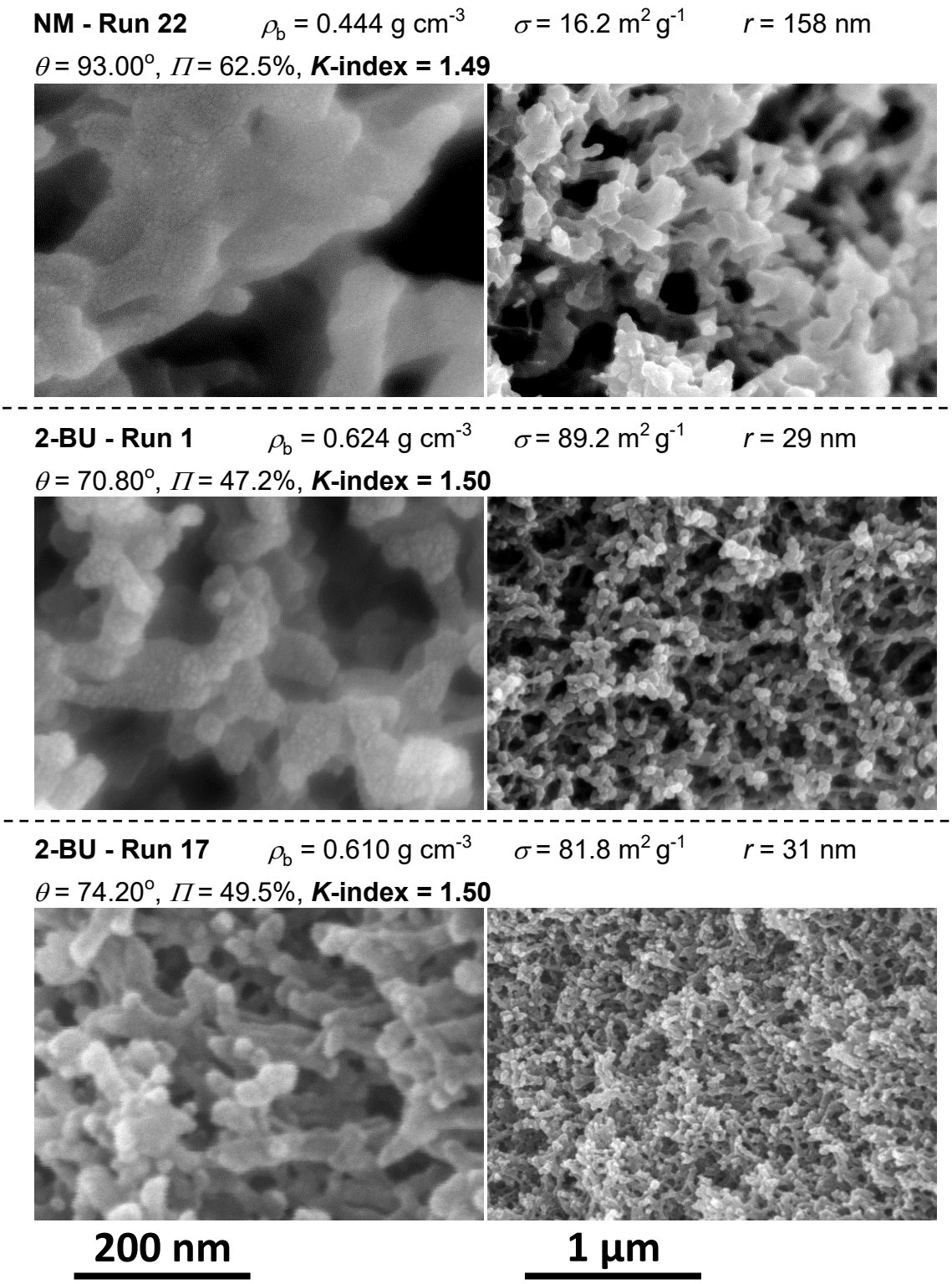

Figure S.IX.1. SEM images at two magnifications of all samples with *K*-index values in the range 1.45–1.64. Other pertinent information (solvent, run number, bulk density, BET surface area, water contact angle and porosity) are included. (cont.)

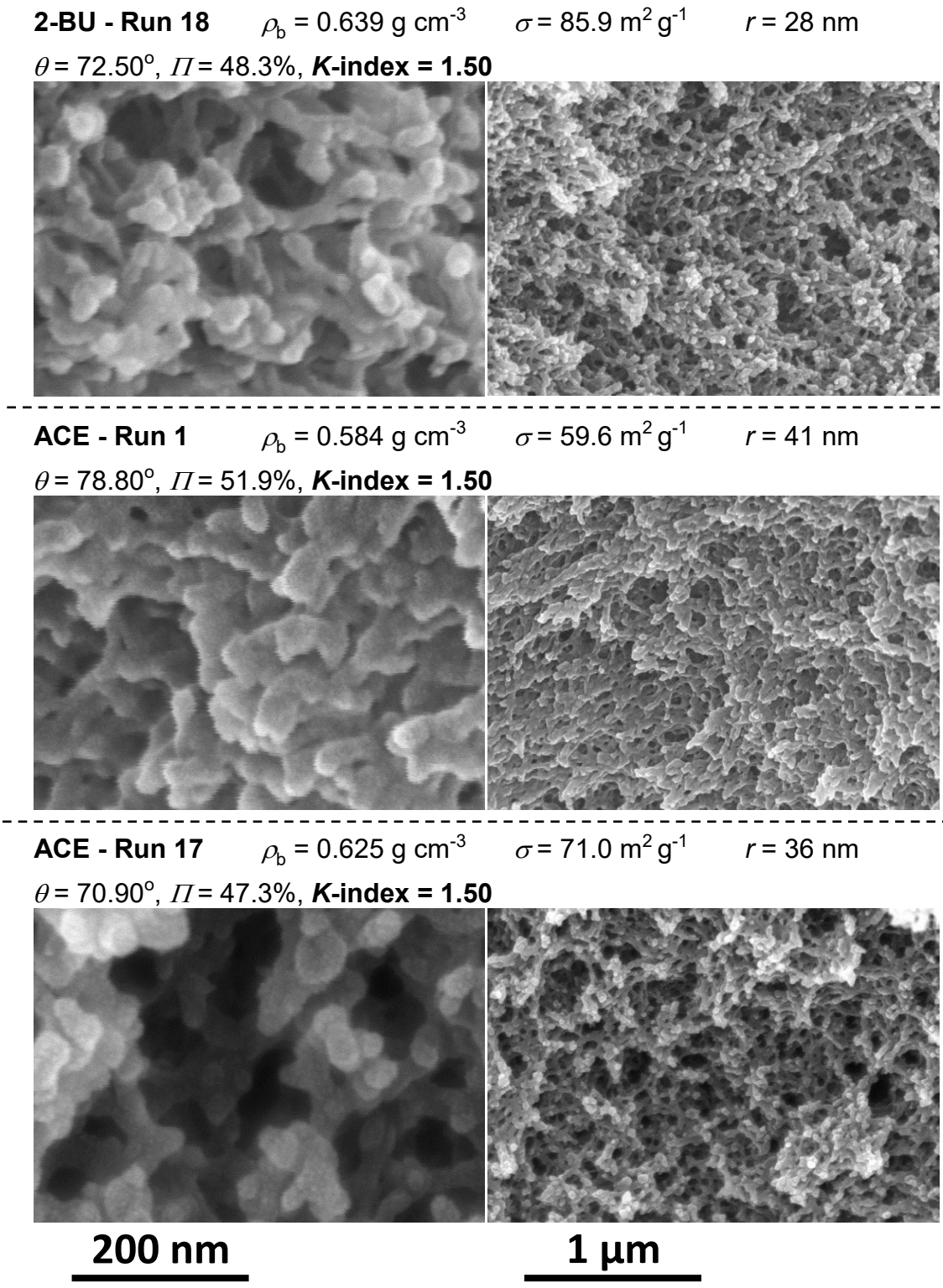

Figure S.IX.1. SEM images at two magnifications of all samples with *K*-index values in the range 1.45–1.64. Other pertinent information (solvent, run number, bulk density, BET surface area, water contact angle and porosity) are included. (cont.)

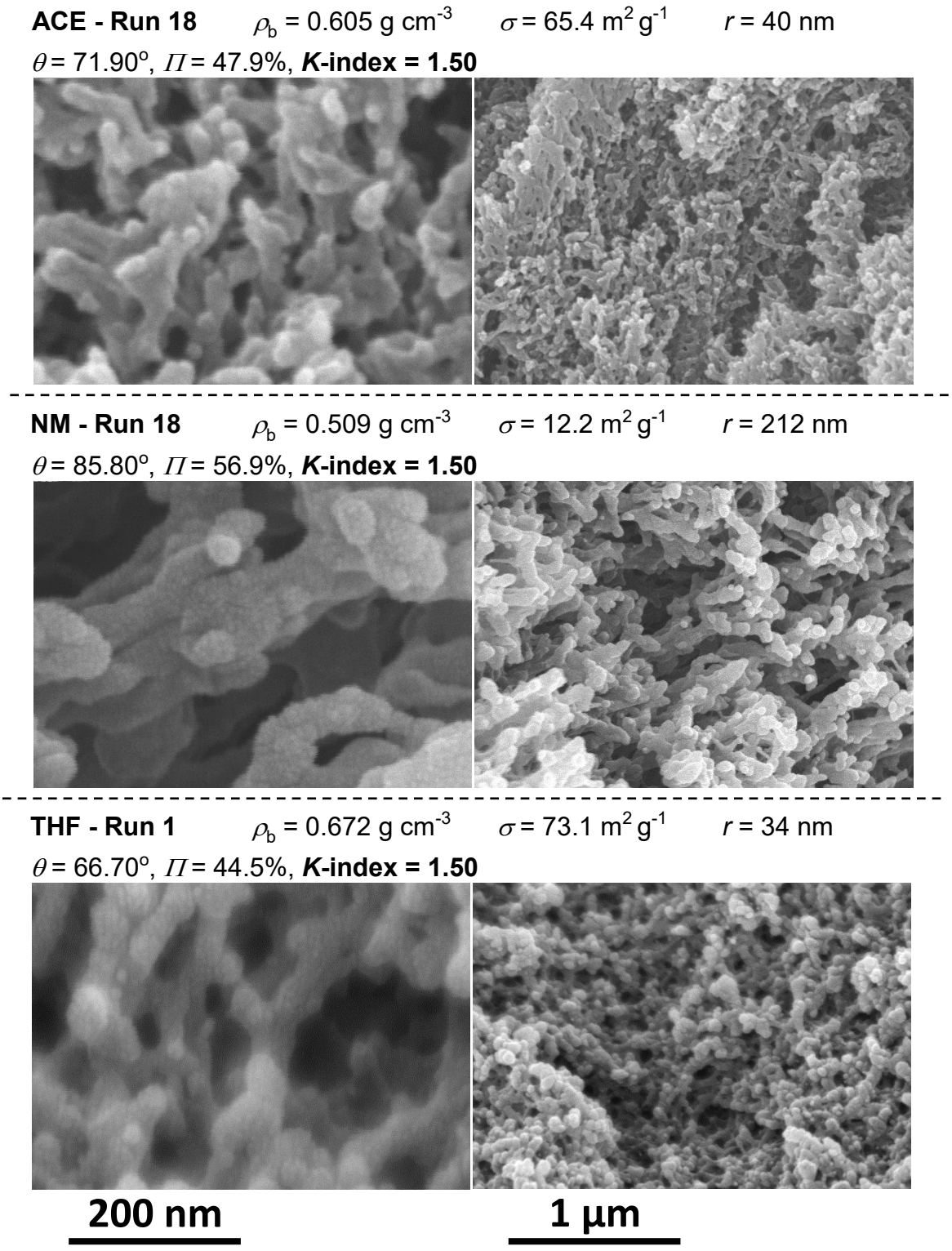

Figure S.IX.1. SEM images at two magnifications of all samples with *K*-index values in the range 1.45–1.64. Other pertinent information (solvent, run number, bulk density, BET surface area, water contact angle and porosity) are included. (cont.)

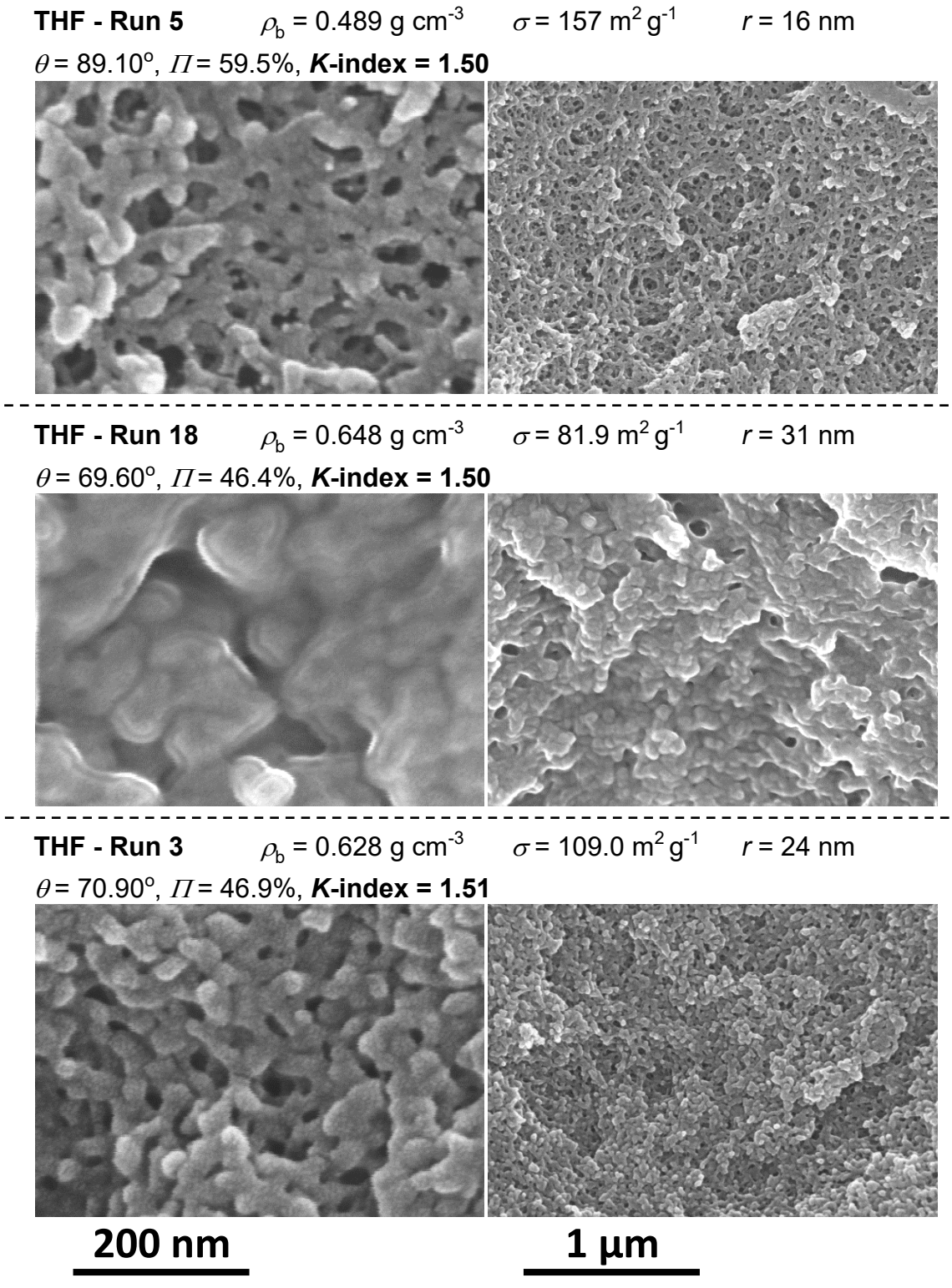

Figure S.IX.1. SEM images at two magnifications of all samples with *K*-index values in the range 1.45–1.64. Other pertinent information (solvent, run number, bulk density, BET surface area, water contact angle and porosity) are included. (cont.)

NM - Run 17 ρ_b = 0.511 g cm^{-3} σ = 9.36 m^2 g^{-1} r = 282 nm

θ = 86.50°, Π = 56.8%, ***K*-index = 1.52**

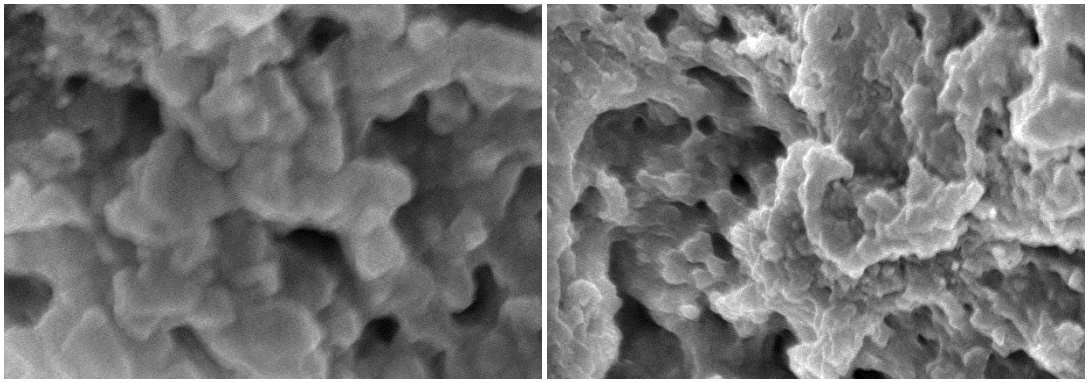

THF - Run 22 ρ_b = 0.662 g cm^{-3} σ = 71.2 m^2 g^{-1} r = 36 nm

θ = 67.20°, Π = 44.2%, ***K*-index = 1.52**

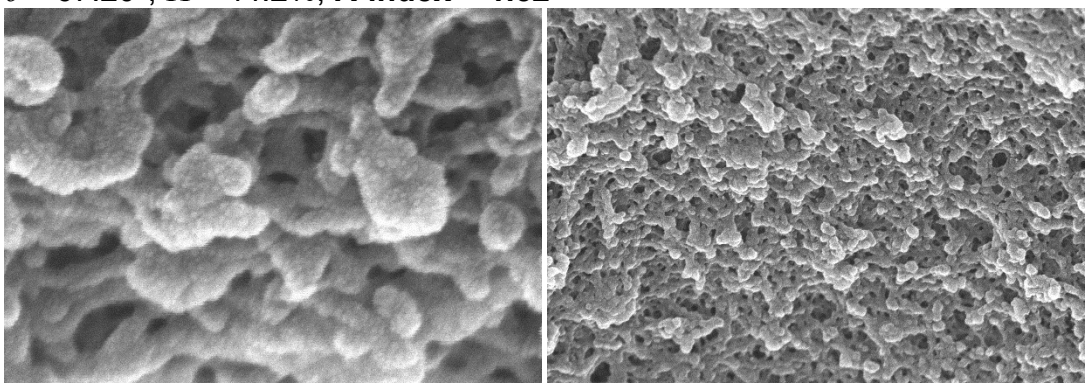

THF - Run 19 ρ_b = 0.560 g cm^{-3} σ = 178 m^2 g^{-1} r = 14 nm

θ = 80.70°, Π = 53.0%, ***K*-index = 1.52**

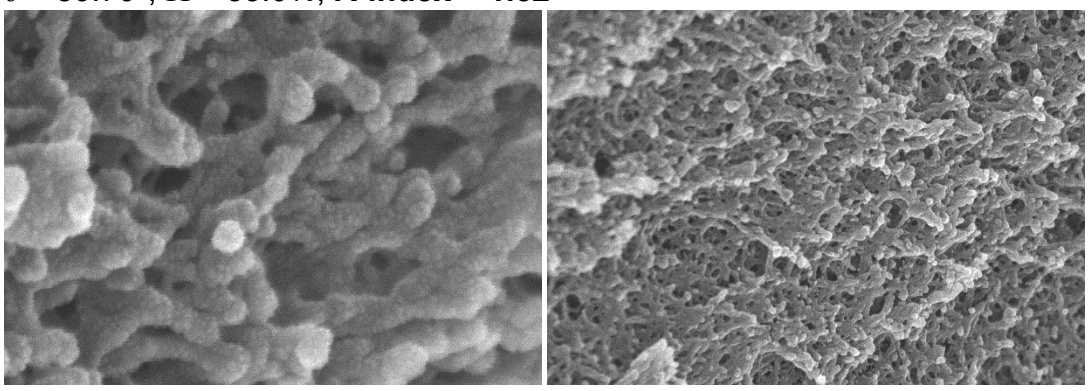

S.IX.1. SEM images at two magnifications of all samples with *K*-index values in the range 1.45–1.64. Other pertinent information (solvent, run number, bulk density, BET surface area, water contact angle and porosity) are included. (cont.)

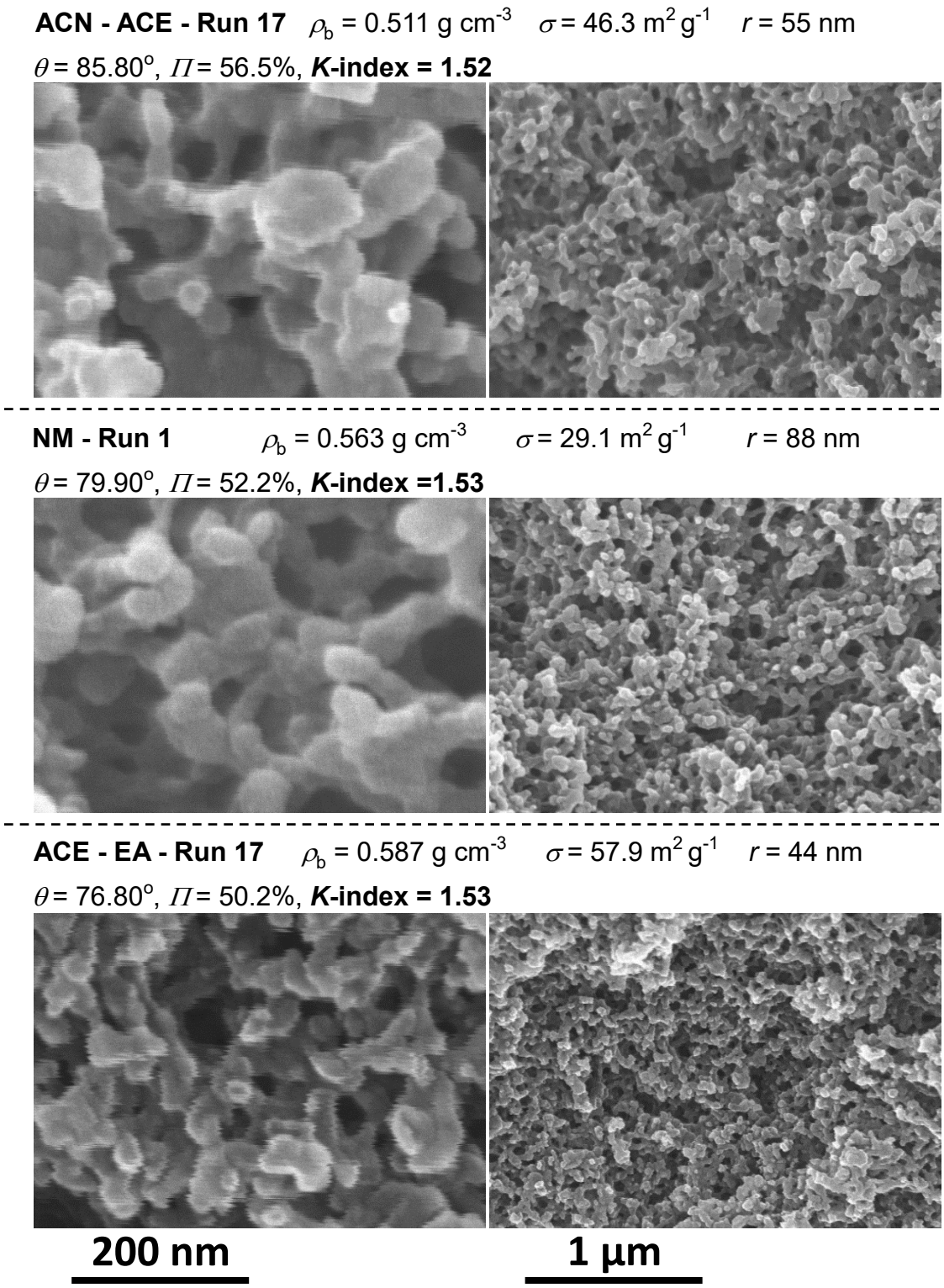

Figure S.IX.1. SEM images at two magnifications of all samples with *K*-index values in the range 1.45–1.64. Other pertinent information (solvent, run number, bulk density, BET surface area, water contact angle and porosity) are included. (cont.)

THF - Run 2 ρ_b = 0.604 g cm^{-3} σ = 69.1 m^2 g^{-1} r = 36 nm

θ = 74.50°, Π = 48.6%, ***K*-index = 1.53**

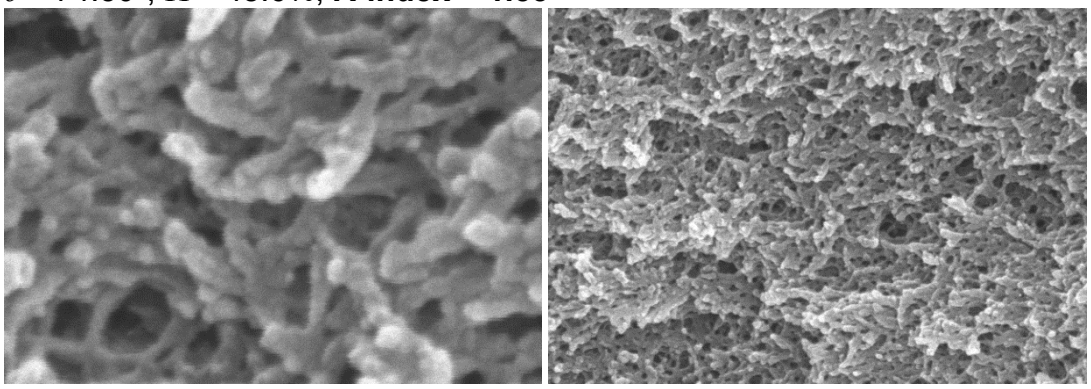

PC - Run 1 ρ_b = 0.529 g cm^{-3} σ = 75.0 m^2 g^{-1} r = 34 nm

θ = 85.00°, Π = 55.7%, ***K*-index = 1.53**

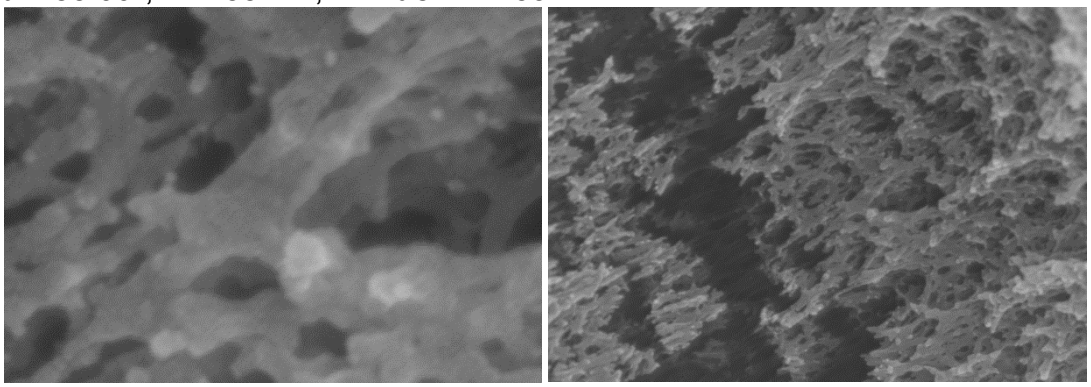

PC - Run 17 ρ_b = 0.596 g cm^{-3} σ = 69.9 m^2 g^{-1} r = 36 nm

θ = 77.20°, Π = 50.3%, ***K*-index = 1.53**

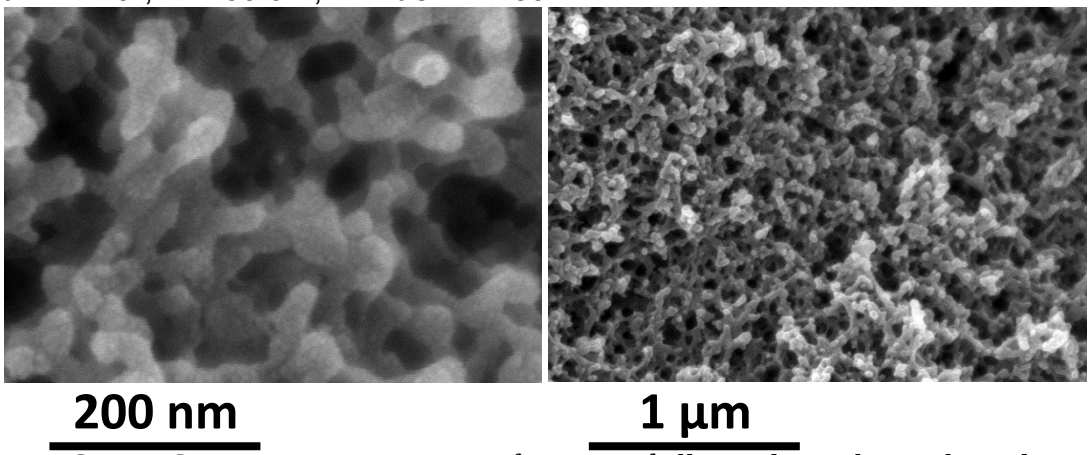

Figure S.IX.1. SEM images at two magnifications of all samples with *K*-index values in the range 1.45–1.64. Other pertinent information (solvent, run number, bulk density, BET surface area, water contact angle and porosity) are included. (cont.)

PC - Run 18 ρ_b = 0.587 g cm^{-3} σ = 47.3 m^2 g^{-1} r = 53 nm

θ = 78.5°, Π = 51.2%, ***K*-index = 1.53**

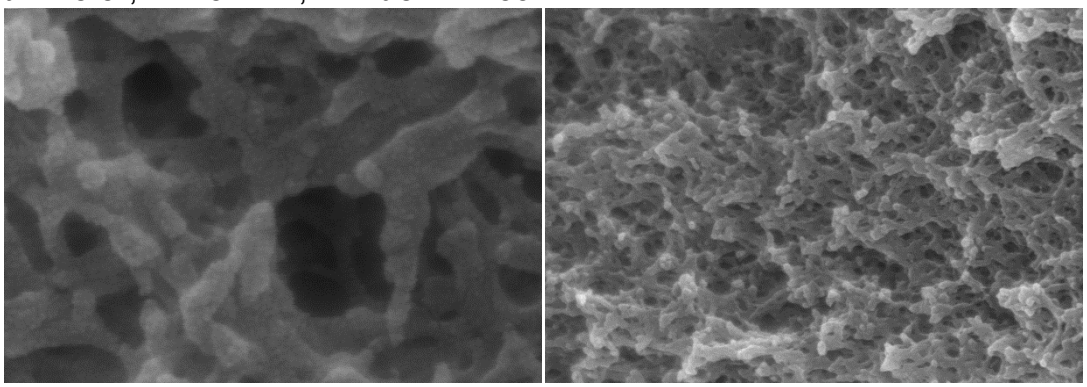

THF - Run 4 ρ_b = 0.507 g cm^{-3} σ = 114 m^2 g^{-1} r = 22 nm

θ = 88.30°, Π = 57.6%, ***K*-index = 1.53**

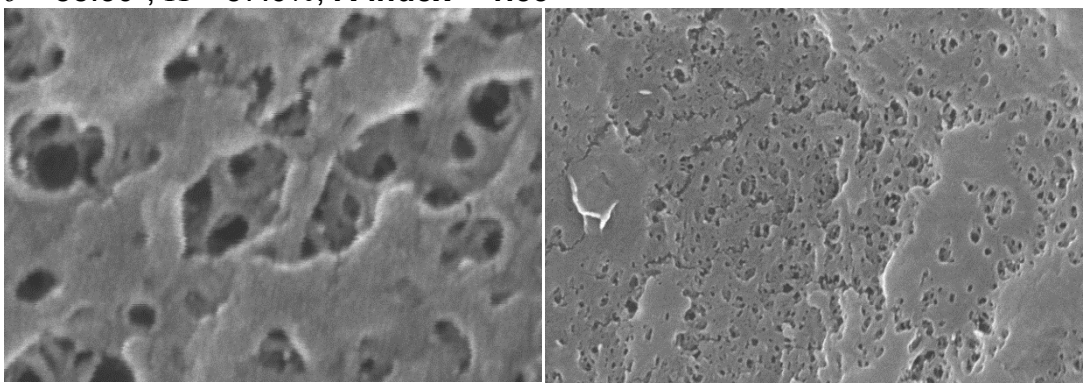

ACN - NM - Run 1 ρ_b = 0.537 g cm^{-3} σ = 23.2 m^2 g^{-1} r = 91 nm

θ = 83.80°, Π = 54.5%, ***K*-index = 1.54**

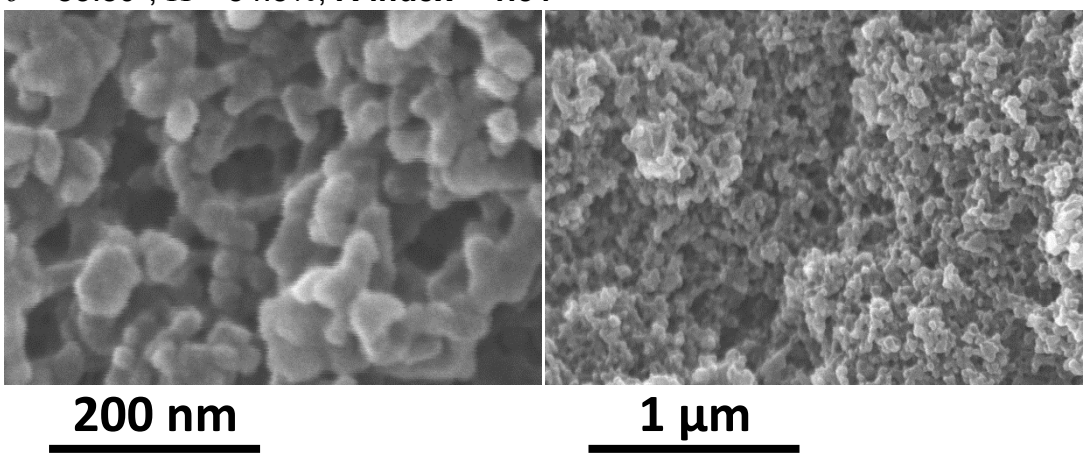

Figure S.IX.1. SEM images at two magnifications of all samples with *K*-index values in the range 1.45–1.64. Other pertinent information (solvent, run number, bulk density, BET surface area, water contact angle and porosity) are included. (cont.)

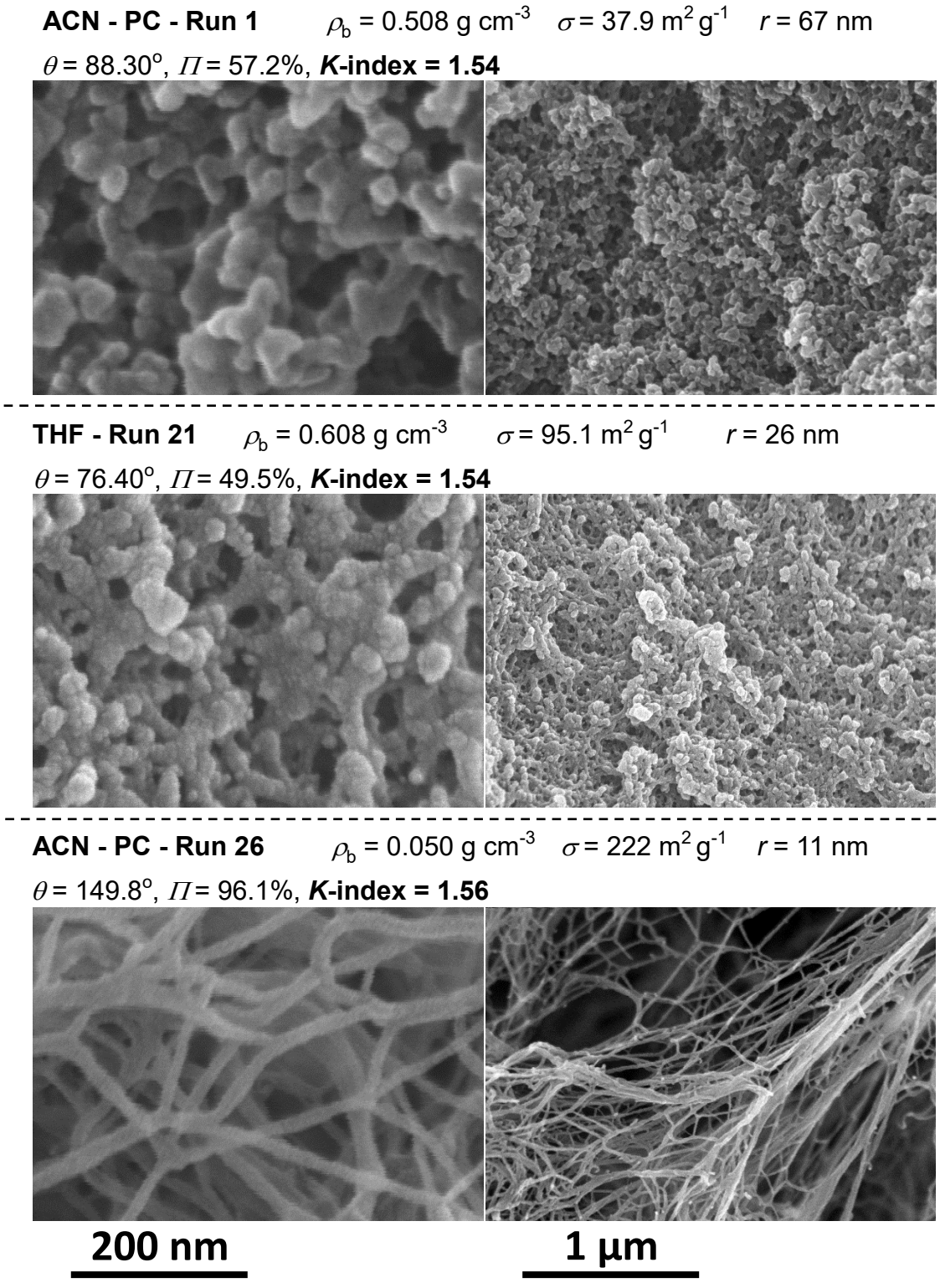

Figure S.IX.1. SEM images at two magnifications of all samples with *K*-index values in the range 1.45–1.64. Other pertinent information (solvent, run number, bulk density, BET surface area, water contact angle and porosity) are included. (cont.)

NM - Run 26 ρ_b = 0.041 g cm^{-3} σ = 122 m^2 g^{-1} r = 21 nm

θ = 150.7°, Π = 96.6%, ***K*-index = 1.56**

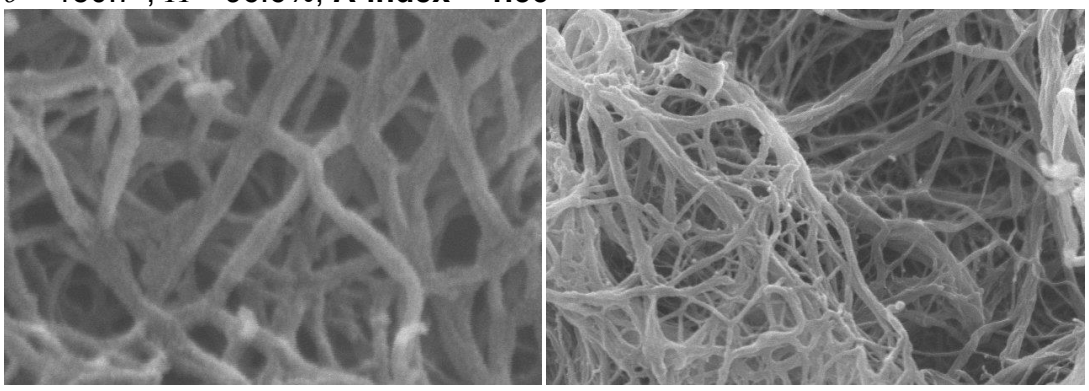

PC - Run 16 ρ_b = 0.065 g cm^{-3} σ = 60.9 m^2 g^{-1} r = 40 nm

θ = 147.4°, Π = 94.7%, ***K*-index = 1.56**

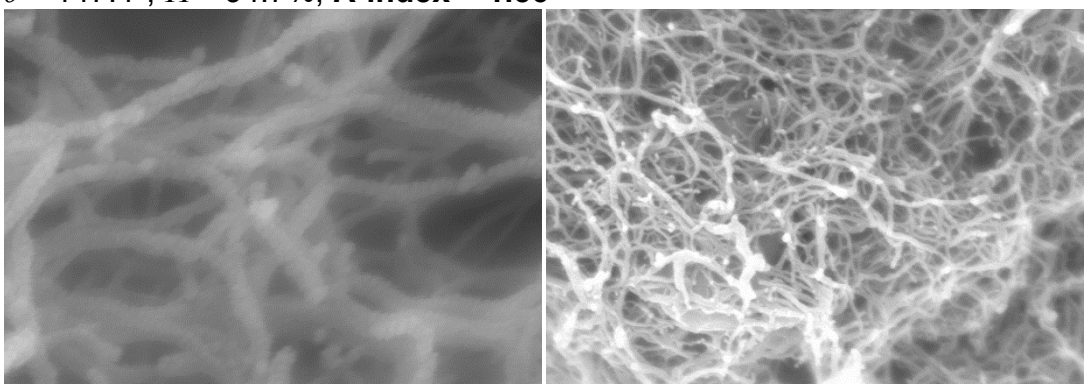

PC - Run 26 ρ_b = 0.080 g cm^{-3} σ = 198 m^2 g^{-1} r = 12 nm

θ = 146.0°, Π = 93.7%, ***K*-index = 1.56**

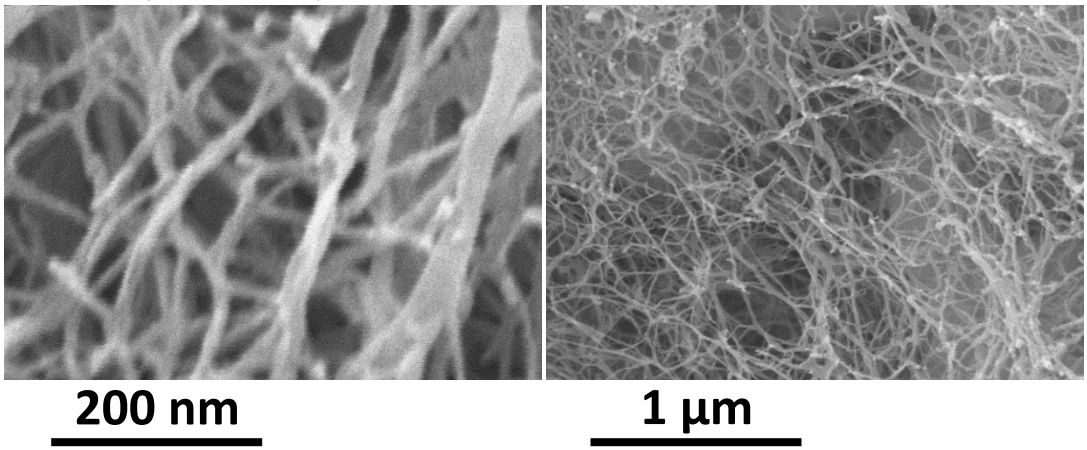

Figure S.IX.1. SEM images at two magnifications of all samples with *K*-index values in the range 1.45–1.64. Other pertinent information (solvent, run number, bulk density, BET surface area, water contact angle and porosity) are included. (cont.)

ACN - Run 26 ρ_b = 0.040 g cm^{-3} σ = 202 m^2 g^{-1} r = 12 nm

θ = 152.3°, Π = 96.8%, ***K*-index = 1.57**

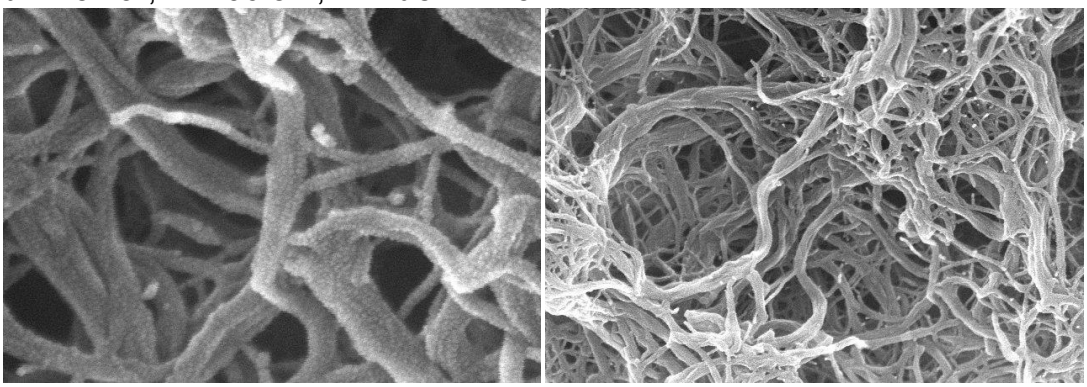

ACN - Run 16 ρ_b = 0.062 g cm^{-3} σ = 131.0 m^2 g^{-1} r = 18 nm

θ = 152.3°, Π = 95.3%, ***K*-index = 1.57**

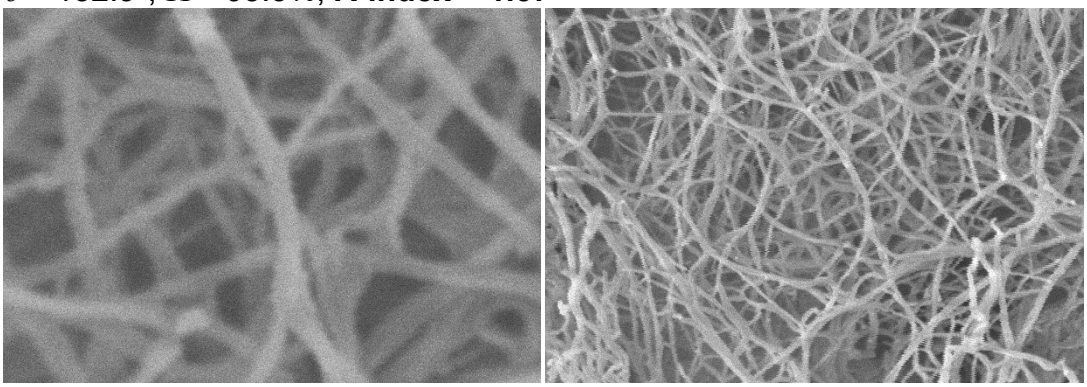

PC - Run 25 ρ_b = 0.066 g cm^{-3} σ = 50.6 m^2 g^{-1} r = 49 nm

θ = 148.1°, Π = 94.5%, ***K*-index = 1.57**

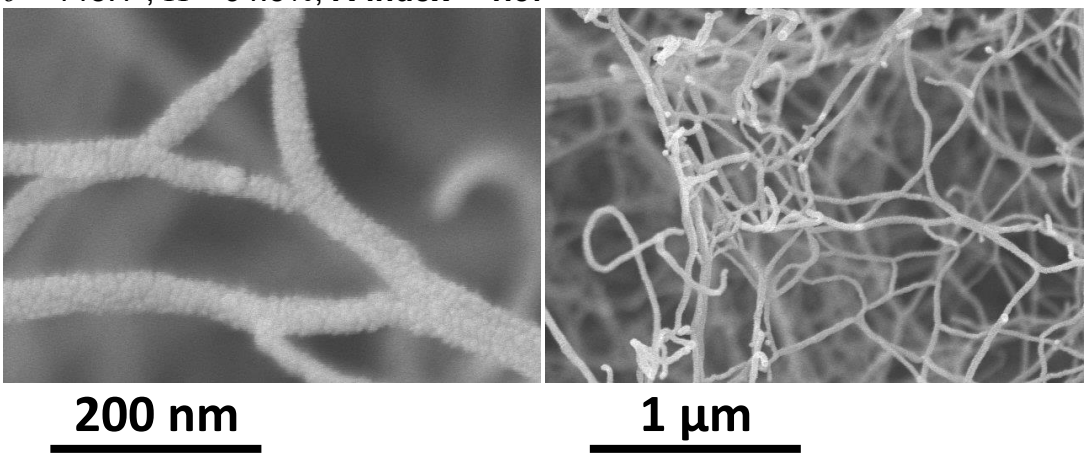

Figure S.IX.1. SEM images at two magnifications of all samples with *K*-index values in the range 1.45–1.64. Other pertinent information (solvent, run number, bulk density, BET surface area, water contact angle and porosity) are included. (cont.)

ACN - PC - Run 16 ρ_b = 0.059 g cm^{-3} σ = 131 m^2 g^{-1} r = 18 nm

θ = 149.2°, Π = 95.3%, ***K*-index = 1.57**

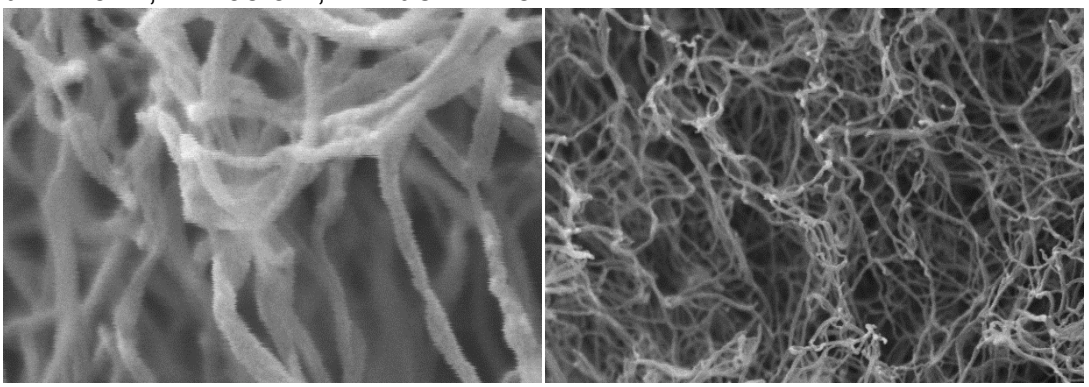

ACN - ACE - Run 16 ρ_b = 0.054 g cm^{-3} σ = 115 m^2 g^{-1} r = 22 nm

θ = 149.7°, Π = 95.5%, ***K*-index = 1.57**

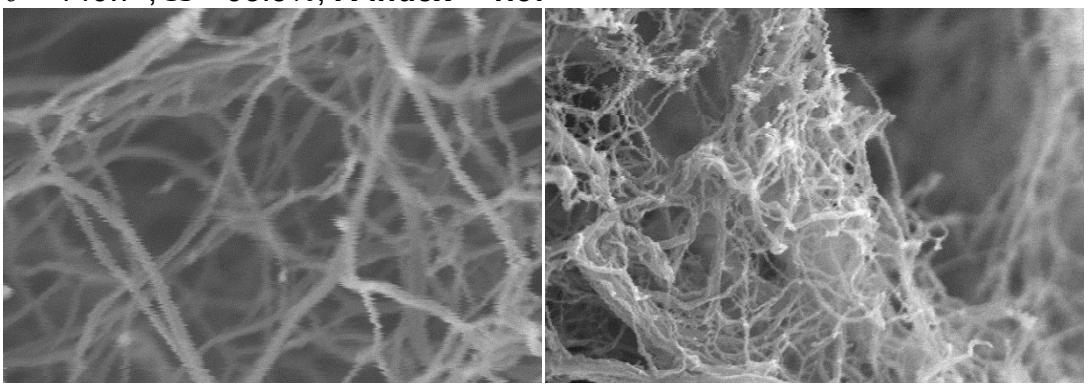

NM - Run 16 ρ_b = 0.068 g cm^{-3} σ = 39.0 m^2 g^{-1} r = 64 nm

θ = 151.4°, Π = 94.4%, ***K*-index = 1.60**

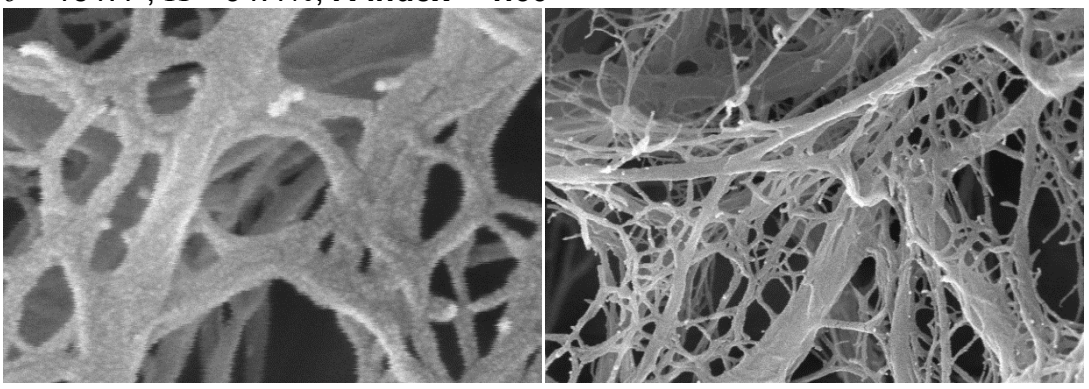

Figure S.IX.1. SEM images at two magnifications of all samples with *K*-index values in the range 1.45–1.64. Other pertinent information (solvent, run number, bulk density, BET surface area, water contact angle and porosity) are included. (cont.)

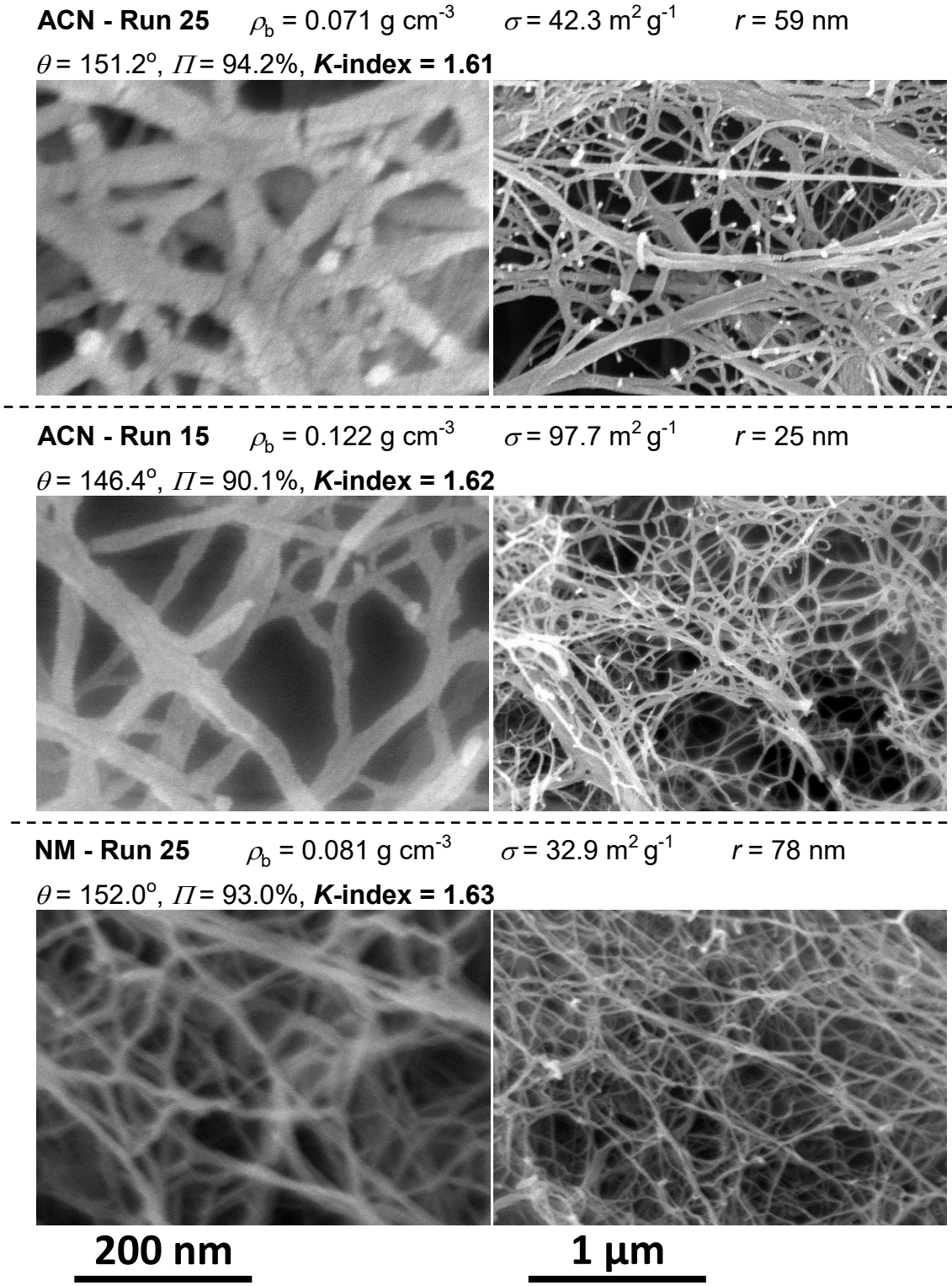

Figure S.IX.1. SEM images at two magnifications of all samples with *K*-index values in the range 1.45–1.64. Other pertinent information (solvent, run number, bulk density, BET surface area, water contact angle and porosity) are included. (cont.)

NM - Run 15 ρ_b = 0.132 g cm^{-3} σ = 119.0 m^2 g^{-1} r = 21 nm

θ = 145.5°, Π = 88.9%, ***K*-index = 1.64**

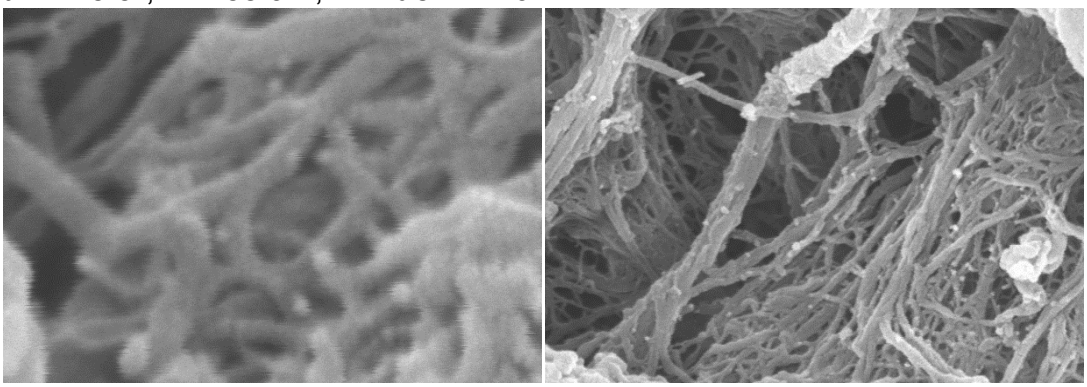

ACN - Run 11 ρ_b = 0.211 g cm^{-3} σ = 113 m^2 g^{-1} r = 23 nm

θ = 134.6°, Π = 82.0%, ***K*-index = 1.64**

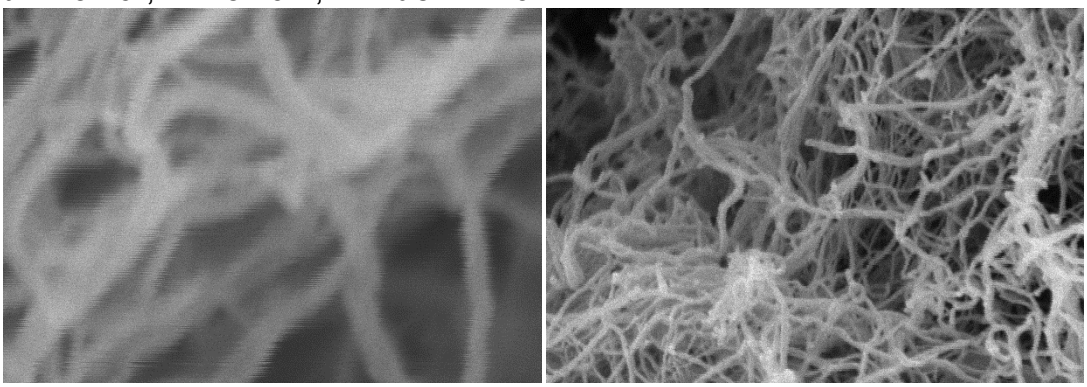

PC - Run 15 ρ_b = 0.171 g cm^{-3} σ = 78.5 m^2 g^{-1} r = 32 nm

θ = 140.2°, Π = 85.9%, ***K*-index = 1.63**

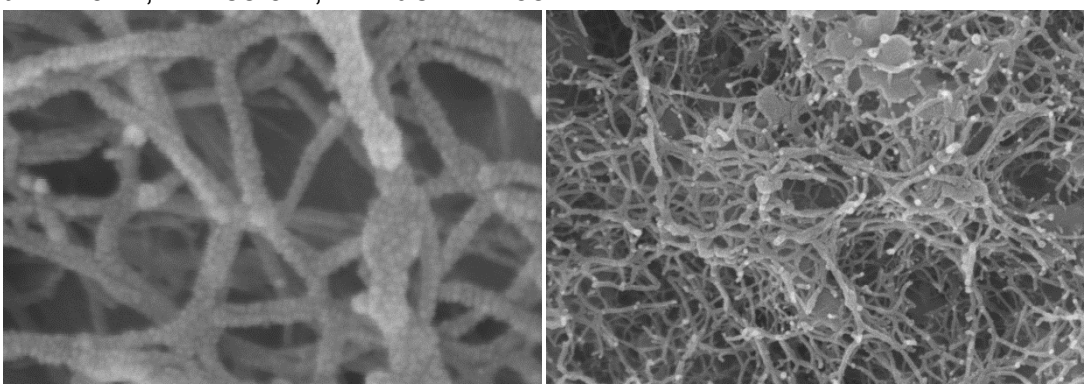

Figure S.IX.1. SEM images at two magnifications of all samples with *K*-index values in the range 1.45–1.64. Other pertinent information (solvent, run number, bulk density, BET surface area, water contact angle and porosity) are included. (cont.)

APPENDIX IX. LOCAL AND GLOBAL FITTING PROCEDURES AND RESULTING COEFFICIENTS

Several application-directed material properties, including the bulk density, surface area, thermal conductivity, the Young's modulus, Ultimate Compressive Strength, and specific energy absorption, the water contact angle and the *K*-index, of all polyurea aerogels prepared in all individual and binary solvents were measured or calculated as described in the Experimental Section (see mail article) and are tabulated in Tables S.VII.1 and S.VII.2. *K*-indexes and other material properties measured or calculated in individual solvents were fitted directly to the three independent variables: the mass of the triisocyanate monomer in 94 mL solvent, [ISO], the mol ratio of water to the trisocyanate monomer, [H_2O], and the catalyst concentration (% w/w of sol), [Et_3N]. This fitting is referred to Local Fitting. *K*-indexes and several other application-related material properties, as described above, were also fitted to six independent variables that take into consideration the properties of the solvent *via* the Hansen Solubility Parameters of the sol (δP_{sol}, δH_{sol} and δD_{sol}). The latter have been calculated and tabulated in the sample preparation section of Appendix I (Tables S.I.4 and S.I.12). That type of fitting of the *K*-index is referred to as Global Fitting and utilized simultaneously data from all 188 PUA aerogels prepared in individual solvents (and survived the drying process with no collapse: refer to the cases of THF and DMF in Tables S.II.1 and S.VII.1), plus the 20 samples in mixed solvents (Tables S.I.12, S.II.2, and S.VII.2) for a total of 208 samples. Fitting of mechanical properties and of the thermal conductivity unutilized a somewhat smaller set of runs, because as some samples were too brittle to machine cylinders from for mechanical testing, or crack-free discs for thermal conductivity. All global fitting procedures started by orthogonalizing all

six experimental explanatory variables ([ISO], [H_2O], [Et_3N], δP_{sol}, δH_{sol} and δD_{sol}) in the [–1,1] interval by using Eq 1, where x_i represents the orthogonalized value of a variable.[S.R.7]

$$x_i = \frac{(\text{exp}\,erimental\_value) - \frac{(highest\_value)+(lowest\_value)}{2}}{\frac{(highest\_value) - (lowest\_value)}{2}} \quad (1)$$

The actual expressions for the orthogonalized variables are cited in Table S.X.1. Using orthogonalized variables has the advantage that the fitting equations (see below) are completely general: the reader can copy-paste them and apply them in other situations between different upper/lower bounds of the independent variables. Eq 1 is the key for the translation of the orthogonalized values back to the actual values of the variables.

Table S.X.1. Based on Equation 1, Orthogonal Transforms (x_1–x_6) of the Actual (Experimental) Values of the Independent Variables Employed in this Study.

Orthogonal Transform:
$x_1 = ([ISO] - 24)/18.5$ [a]
$x_2 = ([H_2O] - 1.5)/0.841$ [b]
$x_3 = ([Et_3N] - 0.5)/0.420$ [c]
$x_4 = (\delta P_{sol} - 11.802)/6.419$ [d]
$x_5 = (\delta H_{sol} - 7.389)/3.597$ [d]
$x_6 = (\delta D_{sol} - 17.533)/2.243$ [d]

[a] [ISO] = grams of triisocyanate monomer in 94 mL solvent
[b] [H_2O] = molar ratio of water to the triisocyanate monomer
[c] [Et_3N] = percent weight of the catalyst (Et_3N) in the sol
[d] δP_{sol}, δH_{sol} and δD_{sol} of the sol composition including triisocyanate, water, catalyst and the solvent (values of δP, δH and δD are cited in Tables S.I.4 to S.I.12)

Fitting of every experimental property, *m*, was based on a fully quadratic model as described by Eq.

$$Property(m) = b_{m,0} + \sum_{i=1}^{n} b_{m,i}x_i + \sum_{i=1}^{n} b_{m,ii}x_i^2 + \sum_{i=1}^{n}\sum_{j<i} b_{m,ij}x_i x_j \quad \text{Eq.2}$$

In Local Fitting of the *K*-index and the water contact angle, θ, or of the Ln of the other material properties, Eq 2 included 16 terms, and x_1–x_3 represent the actual values of the variables: [ISO], [H_2O], [Et_3N]. In Global Fitting, only *K*-index was fitted directly to x_1–x_6. All other properties, including θ, were $\log_e$-transformed before fitting. In global fitting, Eq 2 included 28 terms, and x_1–x_6 represent orthogonalized values. Fitting determined the constant term $b_{m,0}$, and the coefficients $b_{m,i}$, $b_{m,ii}$ and $b_{m,ij}$.

Fitting of each *Property*(*m*) [or the Ln *Propetry*(*m*)] started with the full 16-term or 28-term form of Eq 2, as just described above. Terms with null-hypothesis *P* values > 0.1 were rejected and the fitting process was repeated until no terms with $P > 0.1$ remained. This procedure is referred to as a stepwise fitting technique. That protocol was used for fitting both *Property*(*m*) and the $\log_e$-transformed Ln [*Property*(*m*)]. Correlation coefficients, R^2, were in general higher from fitting the $\log_e$-transformed properties. For example, in global fitting of the bulk density $R^2 = 0.91$, but for Ln (bulk density) $R^2 = 0.96$ both with 18 surviving terms; for the BET surface area $R^2 = 0.89$ with 19 surviving terms, and for Ln (BET surface area) $R^2 = 0.90$ with 20 surviving terms; for thermal conductivity $R^2 = 0.89$ with 14 surviving terms, and for Ln (thermal conductivity) $R^2 = 0.89$, but with 16 surviving terms; for the Young's modulus $R^2 = 0.77$ with 16 terms, but for Ln (Young's modulus) $R^2 = 0.93$ albeit with 14 surviving terms; and, for the ultimate compressive strength $R^2 = 0.80$ with 15 terms, but for Ln (*UCS*) $R^2 = 0.85$ with 16 surviving terms.

In the case of the *K*-index, fitting the actual values, or the $\log_e$-transformed values did not make any difference in R^2, thus we proceeded with the actual values. However, the initial value of R^2 in global fitting of the *K*-index considering all 208 runs was relatively low (0.72). R^2 was improved by removing "outliers" using an iterative procedure whereas

runs were dropped out of the model by conducting a Weighted Least Square (WLS) fitting routine[S.R.8,S.R.9] of the predicted *versus* the experimental *K*-index values, and rejecting the runs whose residuals were more than ±2σ at first, and ±3σ later than the average residual value. After every iteration the remaining runs were fitted again to the full 28-term Eq 2, and terms were rejected again using the $P > 0.1$ criterion. The results after every iteration are cited in Table S.X.2.

Table S.X.2. Results from Iterative Global Fitting of the *K*-indexes (Global Fitting: Engaging all Runs in Both Individual and Mixed Solvents, Simultaneously).

Iteration	**Criterion for dropping runs: residual of WLS fitting > Ave residual ±**	**# of samples entered into current iteration**	**R^2 from Global Fitting**	**Fitted Line for Predicted *K* vs Actual *K* (WLS fit)**		
				R^2	**Slope**	**Y-intercept**
0		208	0.7160	0.6715	0.6698	0.4784
1	2σ	207	0.7330	0.7003	0.6957	0.4401
2	2σ	196	0.8215	0.8030	0.7983	0.2907
3	2σ	185	0.9006	0.8894	0.9077	0.1335
4	3σ	182	0.9159	0.9021	0.9198	0.1156
5	3σ	179	0.9288	0.9138	0.9346	0.0942
6	3σ	177	0.9470	0.9436	0.9433	0.0807

In the first iteration, one (1) point whose residual was > $\pm 2\sigma$ from the average residual of all the rest of the samples were dropped and R^2 improved marginally to 0.73. In the second iteration, 11 points had residuals > $\pm 2\sigma$ from the average residual value of all the rest of the samples. After dropping those runs, the R^2 value of the Global Fitting improved to 0.82. In the third iteration, 11 more runs with residuals > $\pm 2\sigma$ from the average residual were rejected and R^2 reached 0.90. After those three iterations, we started dropping runs with residuals > $\pm 3\sigma$ from the average residual. The number of runs rejected in the

fourth, fifth and sixth iterations were 3, 3 and 2, respectively. The plot of the residuals of the predicted *versus* the actual *K*-index values after the fifth iteration (179 runs) is shown in Figure S.X.1. After dropping the two runs having residuals >3σ, the slope of the regression line for predicted *K*-index *versus* the actual *K*-index values reached 0.94, with an intercept at 0.08 (Figure S.X.2). At that point (177 runs), the R^2 of from Global Fitting of the *K*-index was equal to 0.95 and Eq 2 included 19 surviving terms.

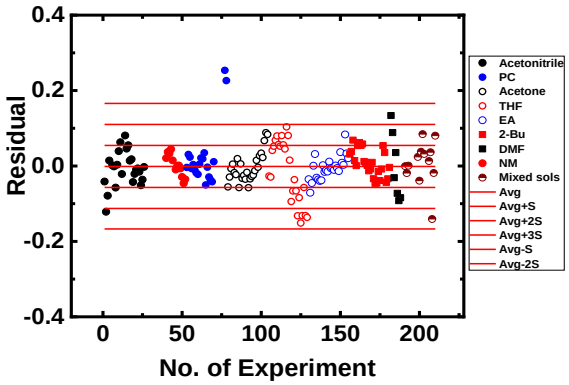

Figure S.X.1. Residuals from WLS fitting of predicted *versus* experimental *K*-index values after the fifth iteration (179 surviving runs).

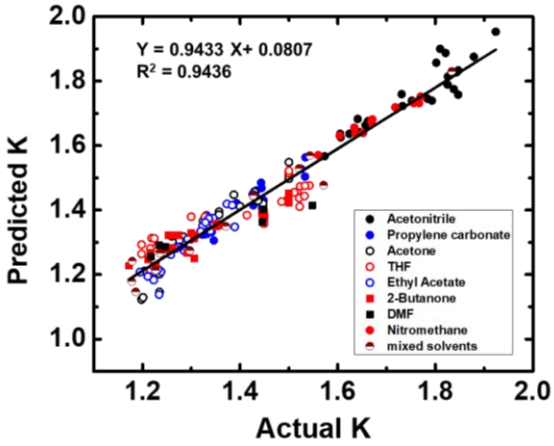

Figure S.X.2. Predicted *K*-index values (from WLS) *versus* actual *K*-index values after the last (sixth) iteration (177 surviving runs – refer to Table S.X.2).

The coefficients from Local Fitting of the *K*-index and other material properties to the three independent variables [ISO], [H_2O], and [Et_3N] in the "local" (*i.e.*, individual) solvents of this study are given in Tables S.X.3 to S.X.10.

The coefficients from Global Fitting of the *K*-index and all other properties to the six orthogonalized independent variables x_1–x_6 are given in Table S.X.11.

Table S.X.3. Coefficients from Local Fitting of the *K*-index *versus* the actual triisocyanate, water and catalyst concentrations (represented by x_1–x_3, respectively) in different solvents.

	ACN	**NM**	**PC**	**ACE**	**THF**	**EA**	**2-BU**
R^2	0.92	0.94	0.92	0.97	0.89	0.94	0.93
RMSE	0.06122	0.04527	0.03404	0.0210	0.0460	0.01546	0.02907
b_o	1.226	1.069	1.975	1.257	1.123	1.2	1.323
Coefficients for:							
x_1	0.0104	0.0228	0.03313	0.004978	0.01023	0.0007102	0.005585
x_2	0.6242	1.3460	0.6258	0.02905	-	0.01308	0.07545
x_3	0.05394	0.9846	1.093	-	-	-	-
x_1*x_1	-	0.0003475	0.0005412	0.0001881	-	0.0001077	0.0001172
x_1*x_2	-	-	0.008493	0.002124	-	-	0.004239
x_1*x_3	0.02235	-	0.01373	0.004978	-	-	-
x_2*x_2	0.08409	0.4138	0.1101	0.02905	-	-	-
x_2*x_3	0.3592	0.1385	0.5211	-	-	-	-
x_3*x_3	-	1.2600	-	0.0001881	-	-	-
No of runs [a]	24 (2)	20 (4)	21 (4)	26 (0)	25 (1)	26 (0)	26 (0)
Residual df [b]	23	19	20	25	24	25	25

[a] No of runs refers to the surviving runs after the number of iterations shown in (parentheses).

[b] Residual df: residual degrees of freedom (= number of surviving runs − 1)

Table S.X.4. Coefficients from Local Fitting of the Ln (bulk density), Ln ρ_b, *versus* the actual triisocyanate, water and catalyst concentrations (represented by x_1–x_3, respectively) in different solvents.

	ACN	**NM**	**PC**	**ACE**	**THF**	**EA**	**2-BU**
R^2	0.98	0.98	0.99	0.99	0.97	0.98	0.98
RMSE	0.09516	0.1206	0.07901	0.08410	0.1322	0.08627	0.1083
b_o	− 4.183	− 3.7	− 2.994	− 3.073	− 3.227	− 3.223	− 3.668
Coefficients for:							
x_1	0.1146	0.1011	0.1171	0.07264	0.1124	0.09778	0.09346
x_2	0.8251	0.2649	− 0.191	0.363	0.1237	0.3413	0.6072
x_3	0.5346	0.6538	0.03146	-	0.5564	-	0.1304
x_1*x_1	− 0.001439	− 0.001008	− 0.001592	− 0.000845	− 0.001564	- 0.001345	− 0.001102
x_1*x_2	-	-	0.007359	0.0116	0.006867	0.003946	0.008511
x_1*x_3	-	-	-	-	-	-	-
x_2*x_2	− 0.1885	-	-	− 0.1741	-	0.1213	− 0.2049
x_2*x_3	− 0.1957	− 0.2787	-	-	− 0.3007	-	-
x_3*x_3	-	-	-	-	-	-	-
No of runs	26	26	26	26	25	26	26
Residual df [a]	25	25	25	25	24	25	25

[a] Residual df: residual degrees of freedom (= number of surviving runs − 1).

Table S.X.5. Coefficients from Local Fitting of the Ln (BET surface area), Ln σ, *versus* the actual triisocyanate, water and catalyst concentrations (represented by x_1–x_3, respectively) in different solvents.

	ACN	**NM**	**PC**	**ACE**	**THF**	**EA**	**2-BU**
R^2	0.90	0.90	0.77	0.84	0.86	0.83	0.79
RMSE	0.3963	0.2392	0.2378	0.2186	0.1653	0.1578	0.1827
b_o	8.573	5.845	6.262	5.531	5.468	5.834	5.717
Coefficients for:							
x_1	− 0.1022	− 0.01488	0.008641	− 0.00101	0.00697	− 0.02545	0.001408
x_2	− 3.361	− 1.157	− 2.037	0.009823	0.1919	− 0.4037	0.04211
x_3	− 2.239	− 1.139	− 1.489	-	− 0.2865	0.3072	−1.373
x_1*x_1	0.00129	-	-	-	-	0.0005516	-
x_1*x_2	-	-	-	− 0.01638	− 0.01996	− 0.01063	− 0.01224
x_1*x_3	-	-	-	-	-	-	-
x_2*x_2	0.5989	-	0.4034	-	-	0.2094	-
x_2*x_3	0.9175	0.5139	0.8331	-	-	− 0.4076	-
x_3*x_3	-	-	-	-	-	-	1.267
No of runs	26	26	26	26	25	26	26
Residual df [a]	25	25	25	25	24	25	25

[a] Residual df: residual degrees of freedom (= number of surviving runs − 1).

Table S.X.6. Coefficients from Local Fitting of the Ln (total thermal conductivity), Ln λ_{Total}, *versus* the actual triisocyanate, water and catalyst concentrations (represented by x_1–x_3, respectively) in different solvents.

	ACN	**NM**	**PC**	**ACE**	**THF**	**EA**	**2-BU**
R^2	0.57	0.90	-	0.94	0.94	0.86	0.81
RMSE	0.1094	0.09049	-	0.07077	0.08165	0.08207	0.1085
b_o	2.809	2.948	-	3.384	2.881	3.221	3.238
Coefficients for:							
x_1	0.009695	0.01735	-	− 0.03669	− 0.02193	− 0.01523	− 0.01795
x_2	0.6508	0.07636	-	− 0.145	0.3163	− 0.09992	− 0.1168
x_3	-	-	-	0.2952	0.1132	-	-
x_1*x_1	-	-	-	0.0006311	0.0006	0.0003613	0.0003085
x_1*x_2	-	-	-	0.01098	0.009209	0.006631	0.009657
x_1*x_3	-	-	-	0.008123	-	-	-
x_2*x_2	0.1884	-	-	-	− 0.1346	-	-
x_2*x_3	-	-	-	-	-	-	-
x_3*x_3	-	-	-	− 0.4652	-	-	-
No of runs	18	15	-	26	25	26	26
Residual df [a]	17	14	-	25	24	25	25

[a] Residual df: residual degrees of freedom (= number of surviving runs − 1).

[b] Most samples prepared in this solvent had cracks and thermal diffusivity measurements were not reliable.

Table S.X.7. Coefficients from Local Fitting of the Ln (Young's modulus), Ln *E, versus* the actual triisocyanate, water and catalyst concentrations (represented by x_1–x_3, respectively) in different solvents.

	ACN	**NM**	**PC**	**ACE**	**THF**	**EA**	**2-BU**
R^2	0.95	0.97	-	0.95	0.98	0.97	0.96
RMSE	0.3102	0.2851	-	0.2683	0.1877	0.1655	0.2604
b_o	0.0135	2.948	-	1.680	1.283	1.420	− 0.2435
Coefficients for:							
x_1	0.2258	0.01735	-	0.1449	0.1626	0.1698	0.1898
x_2	− 0.4174	0.07636	-	− 0.1395	0.1403	-	1.419
x_3	1.058	-	-	-	1.229	-	-
x_1*x_1	– 0.002669	-	-	– 0.001598	– 0.002113	– 0.002085	– 0.001904
x_1*x_2	-	-	-	0.01141	0.009707	-	-
x_1*x_3	– 0.07861	-	-	-	0.02168	-	-
x_2*x_2	-	-	-	-	-	-	− 0.3976
x_2*x_3	-	-	-	-	-	-	-
x_3*x_3	-	-	-	-	− 1.617	-	-
No of runs	18	15	-	26	25	26	26
Residual df [a]	17	14	-	25	24	25	25

[a] Residual df: residual degrees of freedom (= number of surviving runs − 1).

[b] Only few samples prepared in this solvent could be machined for preparing specimens for mechanical testing, therefore fitting was not deemed reliable.

Table S.X.8. Coefficients from Local Fitting of the Ln (ultimate compressive strength), Ln *UCS*, *versus* the actual triisocyanate, water and catalyst concentrations (represented by x_1–x_3, respectively) in different solvents.

	ACN	**NM**	**PC**	**ACE**	**THF**	**EA**	**2-BU**
R^2	0.96	0.78	-	0.95	0.93	0.80	0.80
RMSE	0.2604	0.1381	-	0.2753	0.3196	0.4062	0.0633
b_o	0.2435	4.995	-	0.8269	1.01	2.104	5.655
Coefficients for:				0.2311	-	-	-
x_1	0.1898	− 0.07628	-	0.3012	0.2657	0.2325	− 0.01547
x_2	1.419	1.556	-	-	0.1914	-	− 0.07709
x_3	-	− 0.3142	-	-	1.9450	-	-
x_1*x_1	– 0.001904	0.00164	-	– 0.003037	– 0.004073	– 0.003722	0.0002444
x_1*x_2	-	-	-	-	-	-	0.006113
x_1*x_3	-	0.02164	-	-	-	-	-
x_2*x_2	− 0.3976	− 0.4620	-	-	-	-	-
x_2*x_3	-	-	-	-	-	-	-
x_3*x_3	-	-	-	-	–1.831	-	-
No of runs	18	15	-	26	25	26	26
Residual df [a]	17	14	-	25	24	25	25

[a] Residual df: residual degrees of freedom (= number of surviving runs − 1).

[b] Only few samples prepared in this solvent could be machined for preparing specimens for mechanical testing, therefore fitting was not deemed reliable.

Table S.X.9. Coefficients from Local Fitting of the Ln (specific energy absorption) *versus* the actual triisocyanate, water and catalyst concentrations (represented by x_1–x_3, respectively) in different solvents.

	ACN	**NM**	**PC**	**ACE**	**THF**	**EA**	**2-BU**
R^2	0.89	0.79	-	0.96	0.83	0.73	0.79
RMSE	0.1362	0.3192	-	0.1497	0.2208	0.3000	0.2253
b_o	5.764	4.836	-	1.248	2.505	1.806	2.576
Coefficients for:							
x_1	− 0.1223	− 0.2217	-	0.1277	0.1275	0.1467	0.1114
x_2	-	2.564	-	0.6692	-	-	-
x_3	− 0.6807	− 1.305	-	-	-	1.066	-
x_1*x_1	0.002051	0.004023	-	− 0.001537	− 0.001968	0.002144	0.001688
x_1*x_2	-		-	-	-	-	-
x_1*x_3	0.02829	0.06215	-	-	-	− 0.0296	-
x_2*x_2	-	− 0.7809	-	− 0.2049	-	-	-
x_2*x_3	-	-	-	-	-	-	-
x_3*x_3	-	-	-	-	-	-	-
No of runs	18	15	-	26	25	26	26
Residual df [a]	17	14	-	25	24	25	25

[a] Residual df: residual degrees of freedom (= number of surviving runs − 1).
[b] Only few samples prepared in this solvent could be machined for preparing specimens for mechanical testing, therefore fitting was not deemed reliable.

Table S.X.10. Coefficients from Local Fitting of the water contact angle, θ, *versus* the actual triisocyanate, water and catalyst concentrations (represented by x_1–x_3, respectively) in different solvents.

	ACN	**NM**	**PC**	**ACE**	**THF**	**EA**	**2-BU**
R^2	0.93	0.91	0.95	0.98	0.92	0.99	0.98
RMSE	4.591	9.456	5.835	1.950	4.486	0.8490	1.925
b_o	154.4	118.8	189.0	114.4	120.1	121.4	119.0
Coefficients for:							
x_1	− 1.806	− 1.889	− 3.682	0.2929	− 0.173	− 1.052	− 0.3703
x_2	6.838	105.2	− 27.59	− 8.003	0.3654	− 3.357	4.325
x_3	20.04	− 97.39		-	− 47.65	4.025	− 13.27
x_1*x_1	-	-	0.03913	− 0.01166	-	0.01676	-
x_1*x_2	0.3233	-		− 0.3603	− 0.4937	− 0.1604	− 0.4029
x_1*x_3	0.6622	-		-	-	-	0.3161
x_2*x_2	-	35.51	7.586	3.875	-	1.418	-
x_2*x_3	− 19.06	-		-	9.486	3.044	-
x_3*x_3	-	90.93		-	29.53	-	-
No of runs [a]	24 (2)	25 (1)	23 (3)	23 (3)	24 (1)	23 (3)	22 (4)
Residual df [b]	23	24	22	22	23	22	21

[a] No of runs refers to the surviving runs after the number of iterations shown in (parentheses).
[b] Residual df: residual degrees of freedom (= number of surviving runs − 1).

Table S.X.11. Coefficients from Global Fitting of the *K*-index and of Several Other $\log_e$-

transformed Properties *versus* the Orthogonalized Independent Variables x_1–x_6.

	***K*-index**	**Ln ρ_b (bulk density)**	**Ln σ (BET area)**	**Ln λ_{TOT} (thermal cond.)**	**Ln *UCS* (Ult. Comp. Strength)**	**Ln *E* (Young's modulus)**	**Ln U_T (specific energy)**	**Ln θ (contact angle)**
R^2	0.95	0.96	0.90	0.89	0.85	0.93	0.72	0.79
b_o	1.281	− 0.7226	4.985	3.711	2.173	6.353	− 3.674	− 4.700
Coefficients for:								
x_1	0.3137	0.9640	− 0.7141	0.7519	1.819	1.964	− 0.6690	0.1634
x_2	− 0.0003476	0.04069	− 0.2227	0.02455	0.002625	0.1444	− 0.08555	0.07012
x_3	0.01881	0.05288	− 0.1509	0.03004	0.07047	-	-	-
x_4	− 0.03576	0.1923	− 0.3001	0.1622	− 2.694	0.1921	0.7129	− 0.2012
x_5	0.2189	0.4519	− 0.5971	0.1734	− 0.4547	2.125	− 0.2722	− 0.1343
x_6	− 0.02228	0.5466	− 0.2126	− 0.2072	− 5.023	2.633	0.2646	− 0.4487
x_1*x_1	0.01833	− 0.4425	-	-	− 0.4917	− 0.6587	0.4177	-
x_1*x_2	-	0.04712	− 0.1942	0.06258	-	-	-	0.03305
x_1*x_3	0.01442	-	-	-	-	-	-	-
x_1*x_4	0.1039	-	− 0.4939	-	-	− 0.1545	0.4175	-
x_1*x_5	0.2370	-	− 0.6638	0.1917	2.521	-		-
x_1*x_6	0.03642	0.07542	0.2579	0.2951	-	0.6644	− 0.3852	-
x_2*x_2	-	− 0.05875	0.2153	− 0.04405	-	-	-	-
x_2*x_3	-	− 0.05285	0.104	-	-	-	-	-
x_2*x_4	-	-	− 0.3314	− 0.04309	-	-	-	− 0.03454
x_2*x_5	− 0.06521	-	-	− 0.1009	− 0.4199	-	-	-
x_2*x_6	-	− 0.1026	0.2594	-	-	-	-	0.06848
x_3*x_3	-	− 0.05349	-	-	− 0.269	-	-	-
x_3*x_4	0.01436	0.04009	− 0.09504	-	-	-	-	-
x_3*x_5	0.0289	-	-	-	-	-	-	-
x_3*x_6	-	-	-	-	-	-	-	-
x_4*x_4	0.1993	− 0.1952	− 0.7947	-	0.4023	− 1.114	− 0.4303	− 0.1703
x_4*x_5	-	− 0.3332	-	− 0.1577	-	− 1.279	-	− 0.1514
x_4*x_6	− 0.3934	-	0.9746	-	− 3.428	1.749	1.074	-
x_5*x_5	0.3517	-	− 0.6003	0.2386	6.379	− 1.028	− 0.9055	0.2598
x_5*x_6	-	0.5208	-	− 0.414	− 5.694	3.973	-	− 0.4934
x_6*x_6	0.1458	-	− 1.019	-	− 0.9094	-	-	− 0.358
No of runs [a]	177 [b] (6)	208 (0)	208 (0)	169 [c] (0)	169 [c] (0)	169 [c] (0)	169 [c] (0)	208 (0)
Residual df [d]	158	190	188	153	153	155	157	194

[a] In (parentheses): No. of iterations. [b] Refer to Table S.X.2. [c] Several samples could not be machined for compression testing, or discs had cracks and could not be used for measuring λ_{Total}. [d] Residual degrees of freedom (= number of surviving runs − 1).

The complete global fitting equations incorporating the values of the coefficients cited in Table S.X.11 are given below. The format is such that they can be cut-and-pasted directly to MATLAB.

Eq 3:

***K*-index** = 1.281 + 0.3137*x(1) - 0.0003476*x(2) + 0.01881*x(3) - 0.03576*x(4) + 0.2189*x(5) - 0.02228*x(6) + 0.01442*x(1)*x(3) + 0.1039*x(1)*x(4) + 0.237*x(1)*x(5) + 0.03642*x(1)*x(6) - 0.06521*x(2)*x(5) + 0.01436*x(3)*x(4) + 0.0289*x(3)*x(5) - 0.3934*x(4)*x(6) + 0.01833*x(1)^2 + 0.1993*x(4)^2 + 0.3517*x(5)^2 + 0.1458*x(6)^2

Eq 4:

Ln (bulk density) = - 0.7226 + 0.964*x(1) + 0.04069*x(2) + 0.05288*x(3) - 0.1923*x(4) + 0.4519*x(5) + 0.5466*x(6) + 0.04712*x(1)*x(2) - 0.05285*x(2)*x(3) + 0.07542*x(1)*x(6) + 0.04009*x(3)*x(4) - 0.1026*x(2)*x(6) - 0.3332*x(4)*x(5) + 0.5208*x(5)*x(6) - 0.4425*x(1)^2 - 0.05875*x(2)^2 - 0.05349*x(3)^2 - 0.1952*x(4)^2

Eq 5:

Ln (surface area) = 4.985 + 0.104*x(2)*x(3) - 0.2227*x(2) - 0.1509*x(3) – 0.3001*x(4) - 0.5971*x(5) - 0.2126*x(6) - 0.1942*x(1)*x(2) - 0.4939*x(1)*x(4) - 0.7141*x(1) - 0.6638*x(1)*x(5) - 0.3314*x(2)*x(4) + 0.2579*x(1)*x(6) - 0.09504*x(3)*x(4) + 0.2594*x(2)*x(6) + 0.9746*x(4)*x(6) + 0.2153*x(2)^2 - 0.7947*x(4)^2 - 0.6003*x(5)^2 - 1.019*x(6)^2

Eq 6:

Ln (total thermal conductivity) = 3.711 + 0.7519*x(1) + 0.02455*x(2) + 0.03004*x(3) + 0.1622*x(4) + 0.1734*x(5) - 0.2072*x(6) + 0.06258*x(1)*x(2) + 0.1917*x(1)*x(5) - 0.04309*x(2)*x(4) + 0.2951*x(1)*x(6) - 0.1009*x(2)*x(5) - 0.1577*x(4)*x(5) - 0.414*x(5)*x(6) - 0.04405*x(2)^2 + 0.2386*x(5)^2

Eq 7:

Ln (Ultimate Compressive Strength) = 2.173 + 1.819*x(1) + 0.002625*x(2) + 0.07047*x(3) - 2.694*x(4) - 0.4547*x(5) - 5.023*x(6) + 2.521*x(1)*x(5) - 0.4199*x(2)*x(5) - 3.428*x(4)*x(6) - 5.694*x(5)*x(6) - 0.4917*x(1)^2 - 0.269*x(3)^2 + 0.4023*x(4)^2 + 6.379*x(5)^2 - 0.9094*x(6)^2

Eq 8:

Ln (Young's modulus) = 6.353 + 1.964*x(1) + 0.1444*x(2) + 0.1921*x(4) + 2.125*x(5) + 2.633*x(6) - 0.1545*x(1)*x(4) + 0.6644*x(1)*x(6) - 1.279*x(4)*x(5) + 1.749*x(4)*x(6) + 3.973*x(5)*x(6) - 0.6587*x(1)^2 - 1.114*x(4)^2 - 1.028*x(5)^2

APPENDIX X. *K*-INDEX SURFACES FROM LOCAL FITTING OF EXPERIMENTAL DATA IN INDIVIDUAL SOLVENT VERSUS SURFACES PRODUCED FROM K-INDEXES BACK-CALCULATED VIA THE GLOBAL FITTING EQUATION

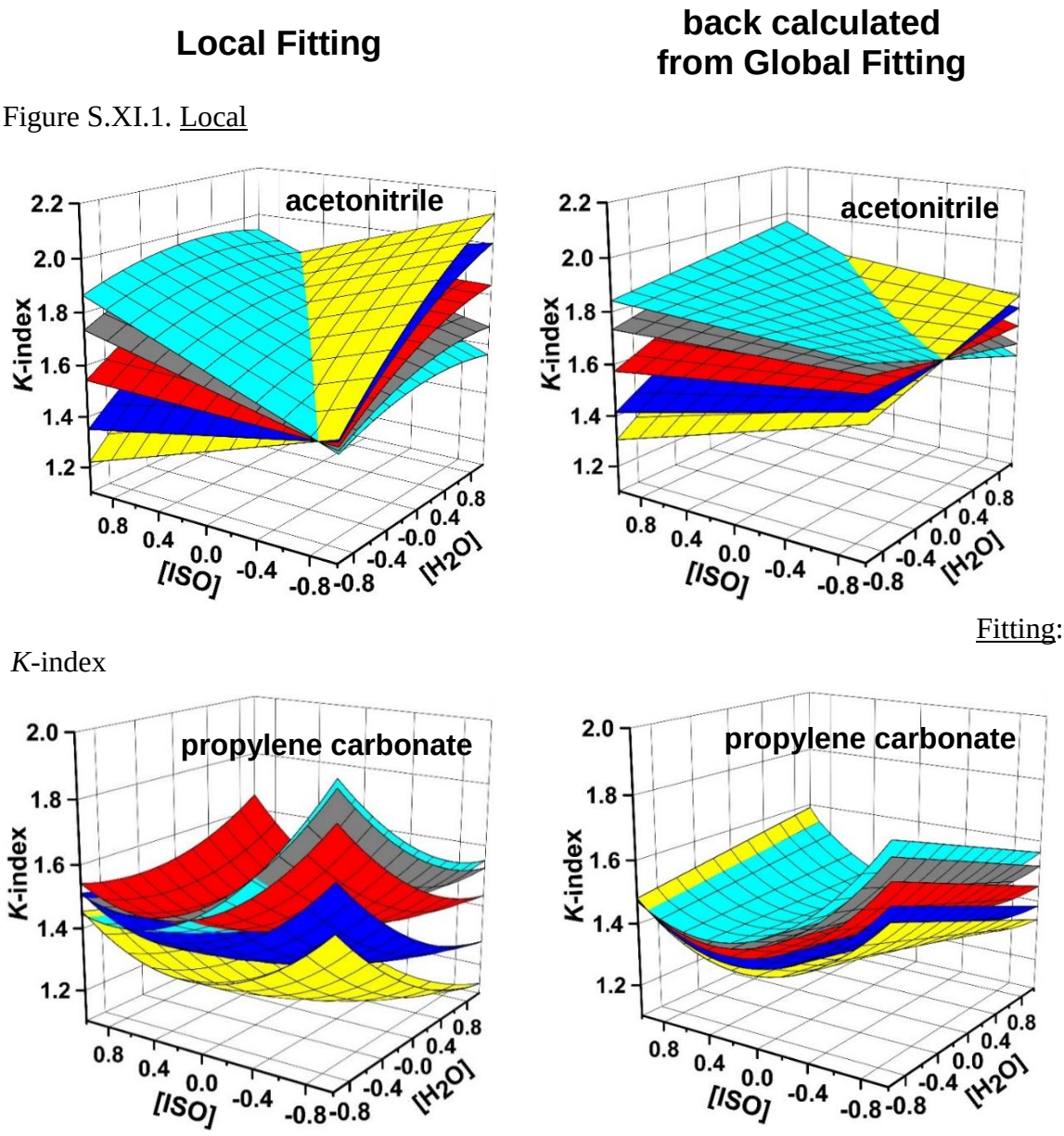

Figure S.XI.1. Local Fitting: *K*-index surfaces calculated directly from θ and Π data in individual solvents (data from Table S.X.3). Global Fitting: *K*-indexes back-calculated for individual solvents using Eq. 2 of Appendix X, and the coefficients of Table S.X.11. For the color-coding index for [Et_3N] see Figure S.XI.2.

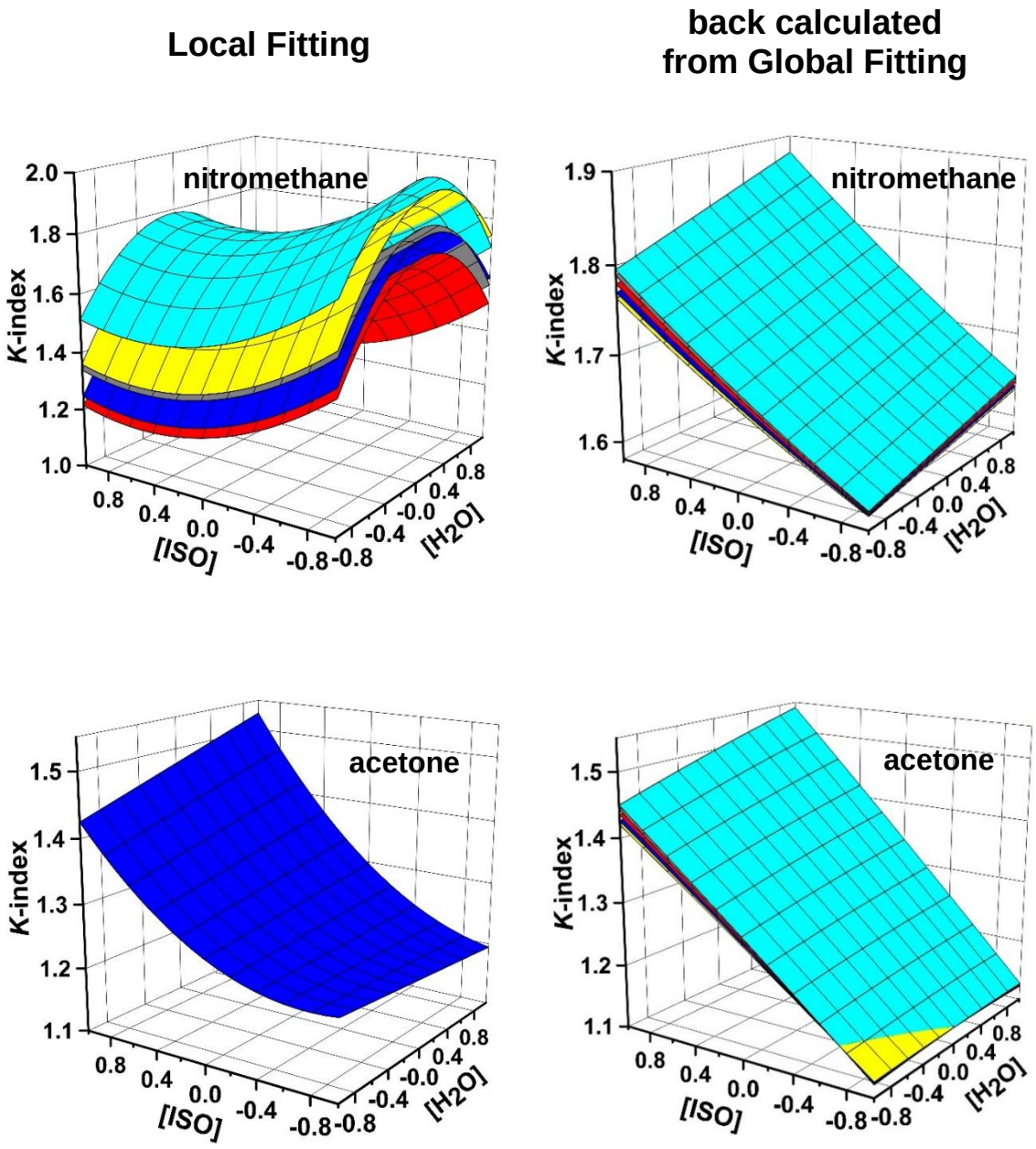

Figure S.XI.1. Local Fitting: *K*-index surfaces calculated directly from θ and Π data in individual solvents (data from Table S.X.3). Global Fitting: *K*-indexes back-calculated for individual solvents using Eq. 2 of Appendix X, and the coefficients of Table S.X.11. For the color-coding index for [Et_3N] see Figure S.XI.2. (cont.)

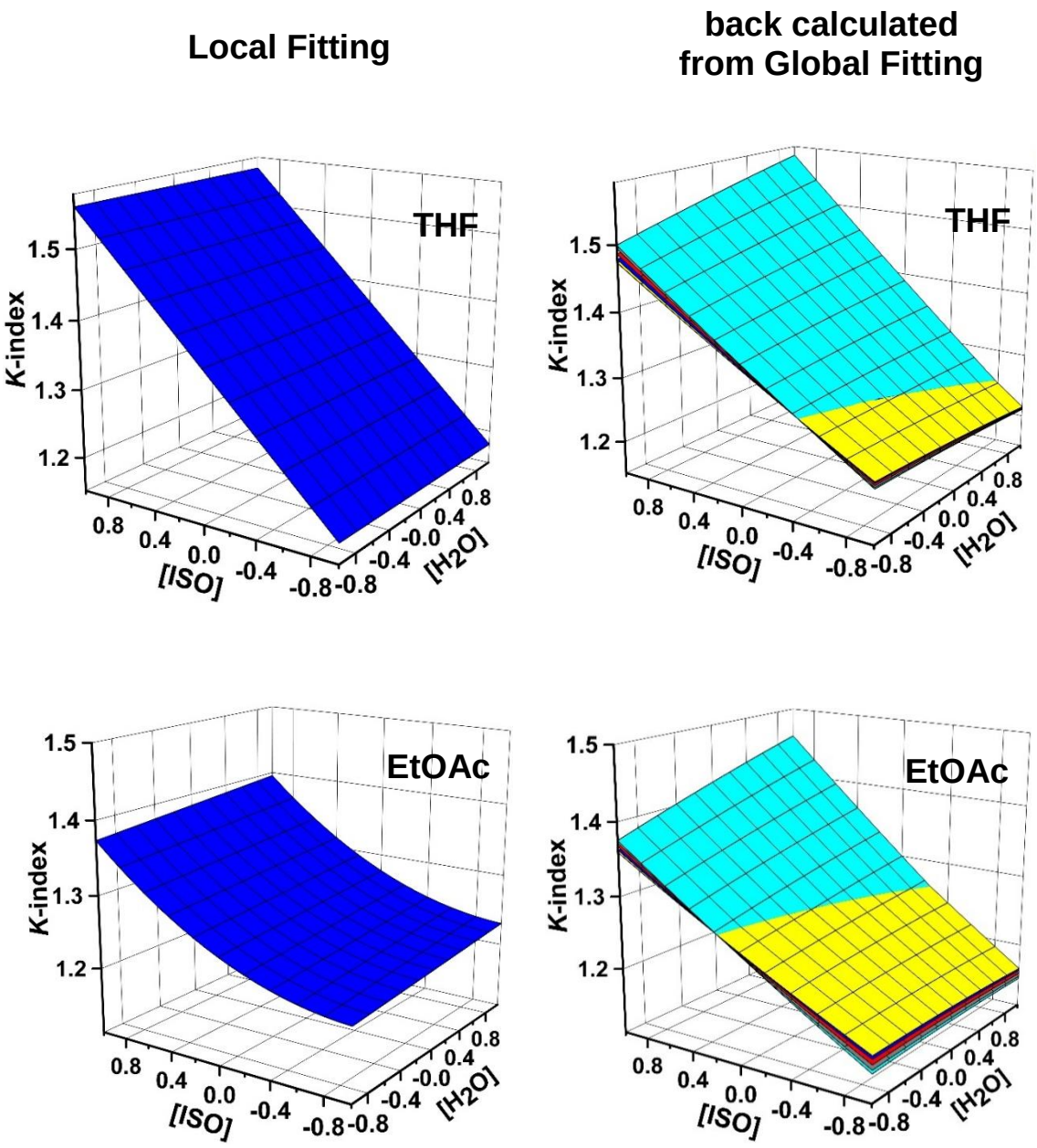

Figure S.XI.1. Local Fitting: *K*-index surfaces calculated directly from θ and Π data in individual solvents (data from Table S.X.3). Global Fitting: *K*-indexes back-calculated for individual solvents using Eq. 2 of Appendix X, and the coefficients of Table S.X.11. For the color-coding index for [Et_3N] see Figure S.XI.2. (cont.)

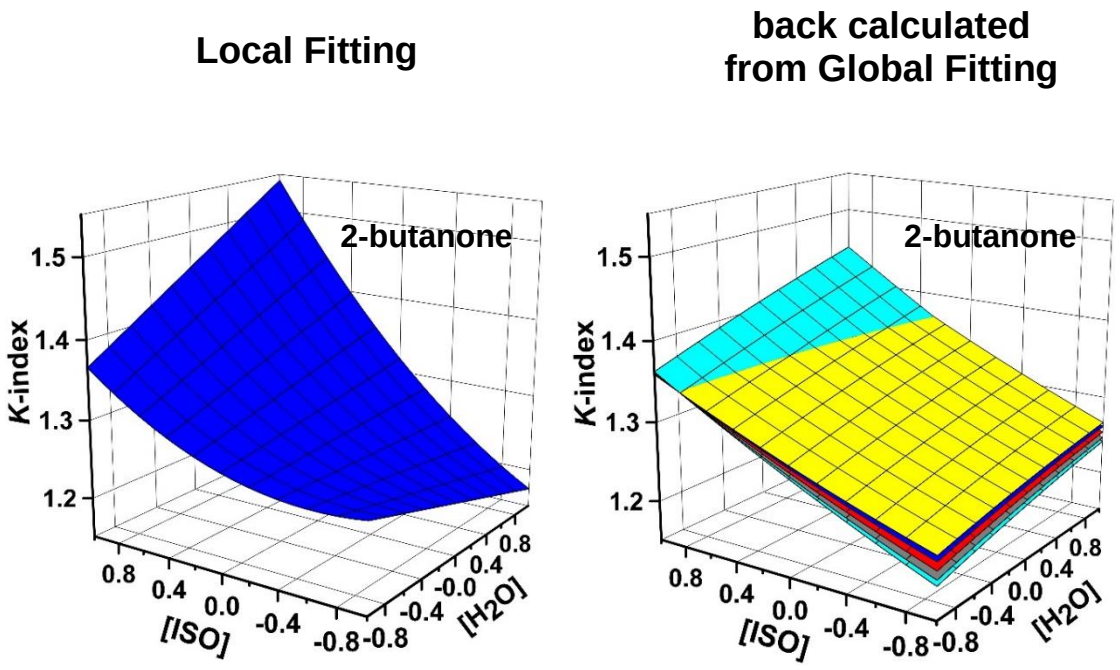

Figure S.XI.1. Local Fitting: *K*-index surfaces calculated directly from θ and Π data in individual solvents (data from Table S.X.3). Global Fitting: *K*-indexes back-calculated for individual solvents using Eq. 2 of Appendix X, and the coefficients of Table S.X.11. For the color-coding index for [Et_3N] see Figure S.XI.2. (cont.)

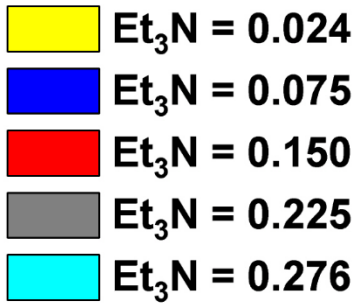

Figure S.XI.2. Index for color-coding of the five levels of the catalyst concentration (Et_3N) in Figure S.XI.1. Units of [Et_3N] in w/w in the sol. Whenever only one surface is visible in Figure S.XI.1 (shown in blue), it means that the five catalyst surfaces coincide, or that the *K*-index in that solvent was insensitive to [Et_3N].

APPENDIX XI. *K*-INDEX AS A TOOL FOR MATERIALS DESIGN: SYNTHESIS OF EIGHT TEST SAMPLES WITH SIX PREDETERMINED PROPERTIES

Scheme S.XII.1 shows the procedure that was followed for the preparation of 8 samples with pre-determined properties, including nanomorphology (*K*-index), the bulk density (ρ_b), the BET surface area (σ), the total thermal conductivity (λ_{Total}), the Ultimate Compressive Strength (*UCS*) and the Young's modulus (*E*).

Because the system is described with six independent variables including monomer, water and catalyst concentration and also Hansen solubility parameters ([ISO], [H_2O], [Et_3N], δP_{sol}, δH_{sol}, δD_{sol}), we pre-determined the values of six properties, including the *K*-index, the bulk density, the BET surface area, the total thermal conductivity, the ultimate compressive strength and the Young's modulus.

Solving the system of equations 3–8 of Appendix X we found the synthetic conditions and we prepared the samples. Their experimental material properties were compared with the pre-determined values (see next Appendix: Appendix XIII) and the match was considered satisfactory.

Scheme S.XII.1 outlines the protocol followed from sample synthesis to final property determination.

The translation of orthogonalized solutions to the actual experimental conditions was carried out *via* the formulas of Table S.X.1.

Scheme S.XII.1. Procedure for the Preparation of Polyurea Aerogels with Predetermined Properties.

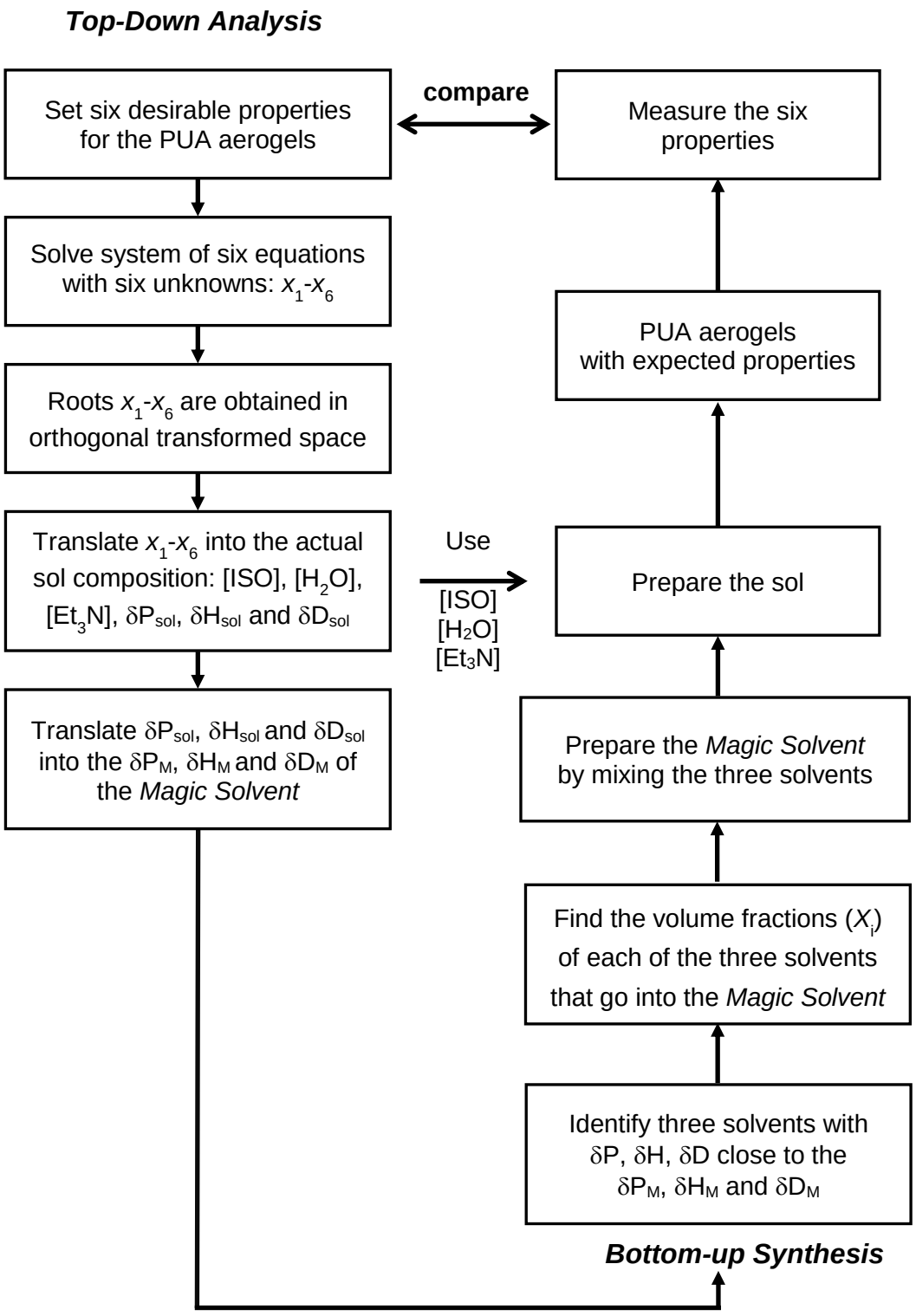

According to Scheme S.XII.1 the entire procedure consists of two well-defined branches: (a) top-down analysis and (b) bottom-up synthesis, in seven steps:

Top-down analysis:

Step 1. Choose six properties that need to be adjusted simultaneously and give them values. For example, let's assume that the six properties are the *K*-index, ρ_b (in g cm^{-3}), σ (in m^2 g^{-1}), λ (in mW m^{-1} K^{-1}), *E* (in MPa) and *UCS* (in MPa). Then take the natural logarithms of those values, except for *K*-index, which is used as is. Those values, together with Eq.s 3–8 of Appendix X define six equations with six unknows (x_1–x_6) that represent the preparation conditions; x_1: [concentration]; x_2: [water]; x_3: [catalyst] ; x_4: δP_{sol}; x_5: δH_{sol}; x_6: δD_{sol}.

Step 2. Solve the above system of the six equations for the six unknowns (preferred solver: MATLAB). The six chosen properties may have the six assigned values simultaneously only if the values of x_1-x_6 are real. (Note that solutions can be negative, in the range [–1.1].)

Step 3. Using either Eq. 1 of Appendix X in the most general application of this algorithm, or in the specific case of the values selected for this study the equations for the orthogonal transforms given in Table S.X.1, find the actual values for [ISO], [H_2O], [Et_3N], δP_{sol}, δH_{sol} and δD_{sol} that have to be used experimentally for making the PUA aerogels with the pre-determined properties set in Step 1. For example, let us assume that the value obtained in Step 2 for "x_1" by solving the system of the six equations above is "$x_{1\ (orthogonally\_\ transformed)}$." Then the value of [ISO] that has to be used experimentally, is calculated from: ([ISO] − 24)/18.5 = $x_{1\ (orthoganolly\_transformed)}$

Similarly, the actual experimental values for x_2–x_6 can be calculated using the equations for the orthogonal transforms from Table S.X.1.

Step 4. Translate δP_{sol}, δH_{sol} and δD_{sol} into the corresponding parameters of the *Magic Solvent* (δP_M, δH_M and δ_M) that will have to be used in order to make the sol with the prescribed δP_{sol}, δH_{sol} and δD_{sol} values. δP_M, δH_M and δ_M are calculated using the rules of mixing and the known δP, δH and δD values of ISO, H_2O and Et_3N. The procedure is demonstrated for each one of the 8 samples in Table S.XII.1 below.

Bottom-up synthesis:

Step 5. In the next step, first identify three solvents whose δP, δH and δD values bracket the δP_M, δH_M and δD_M of the *Magic Solvent*. Then, find the volume fractions (X_i) of those three solvents by fitting the following system of 3 equations:

$$X_1 * \delta P_{solvent\_\#\_1} + X_2 * \delta P_{solvent\_\#\_2} + X_3 * \delta P_{solvent\_\#\_3} = \delta P_M$$

$$X_1 * \delta H_{solvent\_\#\_1} + X_2 * \delta H_{solvent\_\#\_2} + X_3 * \delta H_{solvent\_\#\_3} = \delta H_M$$

$$X_1 * \delta D_{solvent\_\#\_1} + X_2 * \delta D_{solvent\_\#\_2} + X_3 * \delta D_{solvent\_\#\_3} = \delta D_M$$

with the additional constraint:

$$X_1 + X_2 + X_3 = 1$$

(When those three solvents are mixed at the X_i volume ratios they will produce the *Magic Solvent* with δP_M, δH_M and δD_M).

Step 6. Prepare the *Magic Solvent* by mixing the three identified solvents at the prescribed X_i volume ratios. Subsequently, make the sol by using the *Magic Solvent* together with the values of the [ISO], [H_2O] and [Et_3N] that were determined at Step 3 above.

Step 7. Dry the wet-gels from Step 6 and measure the six pre-determined properties. Compare the experimental values with the predicted ones. Table S.XII.1 lists the preparation conditions of eight samples with pre-determined properties.

Table S.XII.1. Preparation of Eight (8) Polyurea Aerogels with Six (6) Prescribed Properties.

a. Selecting properties for sample 1 of 8

K-index (caterpillar-like assembly of nanoparticles)	1.19
Bulk density, ρ_b (g cm^{-3})	0.181
BET surface area, σ (m^2 g^{-1})	179
Total thermal conductivity, λ_{Total} (mW m^{-1} K^{-1})	31.9
Ultimate Compressive Strength, *UCS* (MPa)	64.7
Young's modulus, *E* (MPa)	41.1

b. Solution of six property equations with six unknowns (x_1–x_6) from Step 2

independent variables	**Orthogonally transformed solutions**	**synthetic conditions (for the sol)**	***Magic Solvent***
x_1	− 0.5282	[ISO] = 14.2 [a]	-
x_2	0.1639	$[H_2O]$ = 1.638 [b]	-
x_3	0.2405	$[Et_3N]$ = 0.6 [c]	-
x_4	− 0.2972	δP_{sol} = 9.9 [d]	δP_M = 10.3
x_5	− 0.2185	δH_{sol} = 6.6 [d]	δH_M = 6.9
x_6	− 0.7418	δD_{sol} = 15.9 [d]	δD_M = 16.0

c. Preparing the *Magic Solvent* from three relevant solvents [e]

	acetone	**2-butanone**	**DMF**	**mixed solvent (@ X_i per solvent)**	**required for *Magic Solvent* from part 'b' above**
δP	10.4	9.0	13.7	10.3	10.3
δH	7.0	5.1	11.3	6.9	6.9
δD	15.5	16.0	17.4	16.0	16.0
X_i [f]	0.4375	0.4063	0.1562	$\sum X_i$=1	

[a] [ISO] = grams of triisocyanate in 94 mL of *Magic Solvent*
[b] $[H_2O]$ = molar ratio of water to ISO monomer
[c] $[Et_3N]$ = percent weight of the catalyst (Et_3N) in the sol
[d] δP_{sol}, δH_{sol} and δD_{sol} in MPa
[e] The three solvents are chosen so that their δP, δH and δD values bracket the values required for the *Magic Solvent* (see Step 5 above)
[f] Volume fraction of each solvent

Table S.XII.1. Preparation of Eight (8) Polyurea Aerogels with Six (6) Prescribed Properties. (cont.)

a. Selecting properties for sample 2 of 8

K-index (caterpillar-like assembly of nanoparticles)	1.16
Bulk density, ρ_b (g cm^{-3})	0.074
BET surface area, σ (m^2 g^{-1})	267
Total thermal conductivity, λ_{Total} (mW m^{-1} K^{-1})	19.9
Ultimate Compressive Strength, *UCS* (MPa)	24.0
Young's modulus, *E* (MPa)	8.4

b. Solution of six property equations with six unknowns (x_1–x_6) from Step 2

independent variables	**Orthogonally transformed solutions**	**synthetic conditions (for the sol)**	***Magic Solvent***
x_1	− 0.9690	[ISO] = 6.1 [a]	-
x_2	− 0.9411	[H_2O] = 0.709 [b]	-
x_3	− 0.9510	[Et_3N] = 0.100 [c]	-
x_4	− 0.8713	δP_{sol} = 6.2 [d]	δP_M = 6.1
x_5	− 0.1420	δH_{sol} = 6.9 [d]	δH_M = 7.1
x_6	− 0.5757	δD_{sol} = 16.2 [d]	δD_M = 16.2

c. Preparing the *Magic Solvent* from three relevant solvents [e]

	ethyl acetate	**2-butanone**	**THF**	**mixed solvent (@ X_i per solvent)**	**required for *Magic Solvent* from part 'b' above**
δP	5.3	9.0	5.7	6.1	6.1
δH	7.2	5.1	8.0	7.1	7.1
δD	15.8	16.0	7.2	16.2	16.2
X_i [f]	0.4763	0.3448	0.1789	$\sum X_i$=1	

[a] [ISO] = grams of triisocyanate in 94 mL of *Magic Solvent*
[b] [H_2O] = molar ratio of water to ISO monomer
[c] [Et_3N] = percent weight of the catalyst (Et_3N) in the sol
[d] δP_{sol}, δH_{sol} and δD_{sol} in MPa
[e] The three solvents are chosen so that their δP, δH and δD values bracket the values required for the *Magic Solvent* (see Step 5 above)
[f] Volume fraction of each solvent

Table S.XII.1. Preparation of Eight (8) Polyurea Aerogels with Six (6) Prescribed Properties. (cont.)

a. Selecting properties for sample 3 of 8

K-index (worm-like assembly of nanoparticles)	1.33
Bulk density, ρ_b (g cm^{-3})	0.292
BET surface area, σ (m^2 g^{-1})	102
Total thermal conductivity, λ_{Total} (mW m^{-1} K^{-1})	39.6
Ultimate Compressive Strength, *UCS* (MPa)	147
Young's modulus, *E* (MPa)	85.3

b. Solution of six property equations with six unknowns (x_1–x_6) from Step 2

independent variables	**Orthogonally transformed solutions**	**synthetic conditions (for the sol)**	***Magic Solvent***
x_1	− 0.0972	[ISO] = 22.2 [a]	-
x_2	0.4243	$[H_2O]$ = 1.857 [b]	-
x_3	0.2068	$[Et_3N]$ = 0.59 [c]	-
x_4	− 0.1282	δP_{sol} = 11.0 [d]	δP_M = 11.8
x_5	− 0.3707	δH_{sol} = 6.1 [d]	δH_M = 6.4
x_6	− 0.8451	δD_{sol} = 15.6 [d]	δD_M = 15.6

c. Preparing the *Magic Solvent* from three relevant solvents [e]

	acetone	**2-butanone**	**nitromethane**	**mixed solvent (@ X_i per solvent)**	**required for *Magic Solvent* from part 'b' above**
δP	10.4	9.0	18.8	11.8	11.8
δH	7.0	5.1	5.1	6.4	6.4
δD	15.5	16.0	15.8	15.6	15.6
X_i [f]	0.6842	0.1278	0.188	$\sum X_i$=1	

[a] [ISO] = grams of triisocyanate in 94 mL of *Magic Solvent*
[b] $[H_2O]$ = molar ratio of water to ISO monomer
[c] $[Et_3N]$ = percent weight of the catalyst (Et_3N) in the sol
[d] δP_{sol}, δH_{sol} and δD_{sol} in MPa
[e] The three solvents are chosen so that their δP, δH and δD values bracket the values required for the *Magic Solvent* (see Step 5 above)
[f] Volume fraction of each solvent

Table S.XII.1. Preparation of Eight (8) Polyurea Aerogels with Six (6) Prescribed Properties. (cont.)

a. Selecting properties for sample 4 of 8

K-index (nanoparticle aggregates)	1.42
Bulk density, ρ_b (g cm^{-3})	0.457
BET surface area, σ (m^2 g^{-1})	98.3
Total thermal conductivity, λ_{Total} (mW m^{-1} K^{-1})	48.0
Ultimate Compressive Strength, *UCS* (MPa)	360
Young's modulus, *E* (MPa)	172

b. Solution of six property equations with six unknowns (x_1–x_6) from Step 2

independent variables	**Orthogonally transformed solutions**	**synthetic conditions (for the sol)**	***Magic Solvent***
x_1	0.4679	[ISO] = 32.7 [a]	-
x_2	0.5645	[H_2O] = 1.975 [b]	-
x_3	0.2221	[Et_3N] = 0.59 [c]	-
x_4	− 0.1865	δP_{sol} = 10.6 [d]	δP_M = 11.6
x_5	− 0.6566	δH_{sol} = 5.0 [d]	δH_M = 5.0
x_6	− 0.6775	δD_{sol} = 16.0 [d]	δD_M = 16.2

c. Preparing the *Magic Solvent* from three relevant solvents [e]

	nitromethane	**2-butanone**	**propylene carbonate**	**mixed solvent (@ X_i per solvent)**	**required for *Magic Solvent* from part 'b' above**
δP	18.8	9.0	18.0	11.6	11.6
δH	5.1	5.1	4.1	5.0	5.0
δD	15.8	16.0	20.0	16.2	16.2
X_i [f]	0.2098	0.7298	0.0605	$\sum X_i$=1	

[a] [ISO] = grams of triisocyanate in 94 mL of *Magic Solvent*
[b] [H_2O] = molar ratio of water to ISO monomer
[c] [Et_3N] = percent weight of the catalyst (Et_3N) in the sol
[d] δP_{sol}, δH_{sol} and δD_{sol} in MPa
[e] The three solvents are chosen so that their δP, δH and δD values bracket the values required for the *Magic Solvent* (see Step 5 above)
[f] Volume fraction of each solvent

Table S.XII.1. Preparation of Eight (8) Polyurea Aerogels with Six (6) Prescribed Properties. (cont.)

a. Selecting properties for sample 5 of 8

K-index (thin hair-like entangled nanofibers)	1.58
Bulk density, ρ_b (g cm^{-3})	0.097
BET surface area, σ (m^2 g^{-1})	96.0
Total thermal conductivity, λ_{Total} (mW m^{-1} K^{-1})	35.5
Ultimate Compressive Strength, *UCS* (MPa)	121
Young's modulus, *E* (MPa)	7.0

b. Solution of six property equations with six unknowns (x_1–x_6) from Step 2

independent variables	**Orthogonally transformed solutions**	**synthetic conditions (for the sol)**	***Magic Solvent***
x_1	− 0.6625	[ISO] = 11.7 [a]	-
x_2	− 0.8244	$[H_2O]$ = 0.807 [b]	-
x_3	− 0.5102	$[Et_3N]$ = 0.29 [c]	-
x_4	0.8299	δP_{sol} = 17.1 [d]	δP_M = 18.2
x_5	− 0.5106	δH_{sol} = 5.6 [d]	δH_M = 5.9
x_6	− 0.8441	δD_{sol} = 15.6 [d]	δD_M = 15.6

c. Preparing the *Magic Solvent* from three relevant solvents [e]

	acetonitrile	**nitromethane**	**DMF**	**mixed solvent (@ X_i per solvent)**	**required for *Magic Solvent* from part 'b' above**
δP	18.0	18.8	13.7	18.2	18.2
δH	6.1	5.1	11.3	5.9	5.9
δD	15.3	15.8	17.4	15.6	15.6
X_i [f]	0.5362	0.4213	0.0426	$\sum X_i$=1	

[a] [ISO] = grams of triisocyanate in 94 mL of *Magic Solvent*
[b] $[H_2O]$ = molar ratio of water to ISO monomer
[c] $[Et_3N]$ = percent weight of the catalyst (Et_3N) in the sol
[d] δP_{sol}, δH_{sol} and δD_{sol} in MPa
[e] The three solvents are chosen so that their δP, δH and δD values bracket the values required for the *Magic Solvent* (see Step 5 above)
[f] Volume fraction of each solvent

Table S.XII.1. Preparation of Eight (8) Polyurea Aerogels with Six (6) Prescribed Properties. (cont.)

a. Selecting properties for sample 6 of 8

K-index (spheres embedded in fibers)	1.70
Bulk density, ρ_b (g cm^{-3})	0.380
BET surface area, σ (m^2 g^{-1})	23.6
Total thermal conductivity, λ_{Total} (mW m^{-1} K^{-1})	54.3
Ultimate Compressive Strength, *UCS* (MPa)	230
Young's modulus, *E* (MPa)	68.0

b. Solution of six property equations with six unknowns (x_1–x_6) from Step 2

independent variables	**Orthogonally transformed solutions**	**synthetic conditions (for the sol)**	***Magic Solvent***
x_1	0.3074	[ISO] = 29.7 [a]	-
x_2	0.5199	$[H_2O]$ = 1.937 [b]	-
x_3	0.0719	$[Et_3N]$ = 0.53 [c]	-
x_4	0.6259	δP_{sol} = 15.8 [d]	δP_M = 18.2
x_5	− 0.4876	δH_{sol} = 5.6 [d]	δH_M = 5.8
x_6	− 0.7587	δD_{sol} = 15.8 [d]	δD_M = 15.9

c. Preparing the *Magic Solvent* from three relevant solvents [e]

	acetonitrile	**nitromethane**	**DMF**	**mixed solvent (@ X_i per solvent)**	**required for *Magic Solvent* from part 'b' above**
δP	18.0	18.8	13.7	18.2	18.2
δH	6.1	5.1	11.3	5.8	5.8
δD	15.3	15.8	17.4	15.9	15.9
X_i [f]	0.1175	0.7833	0.0992	$\sum X_i$=1	

[a] [ISO] = grams of triisocyanate in 94 mL of *Magic Solvent*
[b] $[H_2O]$ = molar ratio of water to ISO monomer
[c] $[Et_3N]$ = percent weight of the catalyst (Et_3N) in the sol
[d] δP_{sol}, δH_{sol} and δD_{sol} in MPa
[e] The three solvents are chosen so that their δP, δH and δD values bracket the values required for the *Magic Solvent* (see Step 5 above)
[f] Volume fraction of each solvent

Table S.XII.1. Preparation of Eight (8) Polyurea Aerogels with Six (6) Prescribed Properties. (cont.)

a. Selecting properties for sample 7 of 8

K-index (microspheres with hair)	1.79
Bulk density, ρ_b (g cm^{-3})	0.451
BET surface area, σ (m^2 g^{-1})	15.6
Total thermal conductivity, λ_{Total} (mW m^{-1} K^{-1})	62.6
Ultimate Compressive Strength, *UCS* (MPa)	313
Young's modulus, *E* (MPa)	80.9

b. Solution of six property equations with six unknowns (x_1–x_6) from Step 2

independent variables	**Orthogonally transformed solutions**	**synthetic conditions (for the sol)**	***Magic Solvent***
x_1	0.7048	[ISO] = 37.0 [a]	-
x_2	0.4529	$[H_2O]$ = 1.884 [b]	-
x_3	0.088	$[Et_3N]$ = 0.54 [c]	-
x_4	0.528	δP_{sol} = 15.2 [d]	δP_M = 18.1
x_5	− 0.4691	δH_{sol} = 5.7 [d]	δH_M = 6.0
x_6	− 0.8836	δD_{sol} = 15.6 [d]	δD_M = 15.7

c. Preparing the *Magic Solvent* from three relevant solvents [e]

	acetonitrile	**nitromethane**	**DMF**	**mixed solvent (@ X_i per solvent)**	**required for *Magic Solvent* from part 'b' above**
δP	18.0	18.8	13.7	18.1	18.1
δH	6.1	5.1	11.3	6.0	6.0
δD	15.3	15.8	17.4	15.7	15.7
X_i [f]	0.4256	0.5039	0.0705	$\sum X_i$=1	

[a] [ISO] = grams of triisocyanate in 94 mL of *Magic Solvent*
[b] $[H_2O]$ = molar ratio of water to ISO monomer
[c] $[Et_3N]$ = percent weight of the catalyst (Et_3N) in the sol
[d] δP_{sol}, δH_{sol} and δD_{sol} in MPa
[e] The three solvents are chosen so that their δP, δH and δD values bracket the values required for the *Magic Solvent* (see Step 5 above)
[f] Volume fraction of each solvent

Table S.XII.1. Preparation of Eight (8) Polyurea Aerogels with Six (6) Prescribed Properties. (cont.)

a. Selecting properties for sample 8 of 8

K-index (bald microspheres)	1.87
Bulk density, ρ_b (g cm^{-3})	0.328
BET surface area, σ (m^2 g^{-1})	10.3
Total thermal conductivity, λ_{Total} (mW m^{-1} K^{-1})	60.7
Ultimate Compressive Strength, *UCS* (MPa)	210
Young's modulus, *E* (MPa)	26.5

b. Solution of six property equations with six unknowns (x_1–x_6) from Step 2

independent variables	**Orthogonally transformed solutions**	**synthetic conditions (for the sol)**	***acetonitrile*** [e]
x_1	0.3006	[ISO] = 29.6 [a]	-
x_2	0.4325	$[H_2O]$ = 1.864 [b]	-
x_3	0.3936	$[Et_3N]$ = 0.670 [c]	-
x_4	0.9358	δP_{sol} = 17.8 [d]	δP_M = 20.9
x_5	− 0.2550	δH_{sol} = 6.5 [d]	δH_M = 7.0
x_6	− 0.7310	δD_{sol} =15.9 [d]	δD_M = 16.1

[a] [ISO] = grams of triisocyanate in 94 mL of acetonitrile

[b] $[H_2O]$ = molar ratio of water to ISO monomer

[c] $[Et_3N]$ = percent weight of the catalyst (Et_3N) in the sol

[d] δP_{sol}, δH_{sol} and δD_{sol} in MPa

[e] Because one of the solvent parameters (δP) was extreme, preparation of a magic solvent from a mixture of solvents would require solvents outside the range of the δP, δH, δD of the eight solvents of the study and was not attempted. The single solvent of choice in this case was acetonitrile.

APPENDIX XII. MATERIAL PROPERTIES OF THE EIGHT RUNS OF APPENDIX XII.

Table S.XIII.1. General Material Properties of the Eight Polyurea Aerogel Samples Prepared by Solving the System of Six Equations with Six Unknowns of Appendix X with set property values assigned in Appendix XII.

sample ID	**linear shrinkage (%)** [a,b]	**bulk density (ρ_b, g cm^{-3})** [a]	**skeletal density (ρ_s, g cm^{-3})** [c]	**porosity (Π, % v/v)** [d]	**contact angle (θ, deg.)** [e]	**V_{Total} (cm^3 g^{-1})** [f]	**single point volume ads. (V_{max}, cm^3 g^{-1})** [g]	**average pore diameter (Φ, nm)** [i]	**particle radius (r, nm)** [j]
1	9.3 ± 0.3	0.176 ± 0.002	1.185 ± 0.002	85.1 ± 0.3	104.4 ± 0.3	4.84	1.951	95 [38]	25
2	10.8 ± 0.9	0.091 ± 0.003	1.178 ± 0.005	92.3 ± 0.6	111.7 ± 0.7	10.14	1.206	150 [18]	19
3	17.9 ± 0.6	0.325 ± 0.007	1.177 ± 0.001	72.4 ± 0.6	93.7 ± 0.1	2.23	0.104	125 [6]	71
4	22.4 ± 0.3	0.483 ± 0.004	1.182 ± 0.003	59.1 ± 0.4	84.5 ± 0.6	1.22	0.360	51 [15]	53
5	5.3 ± 0.2	0.132 ± 0.002	1.180 ± 0.002	88.8 ± 0.3	143.7 ± 0.2	6.73	0.198	214 [6]	40
6	10.6 ± 0.1	0.315 ± 0.003	1.182 ± 0.002	73.4 ± 0.3	126.4 ± 0.5	1.19	0.085	94 [7]	100
7	20.5 ± 0.2	0.490 ± 0.001	1.178 ± 0.001	58.4 ± 0.1	106.8 ± 1.2	2.33	0.007	1689 [5]	920
8	15.6 ± 0.1	0.291 ± 0.008	1.181 ± 0.001	73.4 ± 0.2	138.7 ± 0.7	2.20	0.033	967 [15]	287

[a] Average of 3 samples. [b] Linear shrinkage = 100 × (mold diameter – sample diameter)/ (mold diameter). [c] Single sample, average of 50 measurements. [d] Porosity (percent of empty space) $\Pi = 100 \times (\rho_s - \rho_b) / \rho_s$. [e] Data were collected using three separate discs for each sample, and ten measurements were taken for each disc and were averaged. [f] Calculated *via* $V_{Total} = (1/\rho_b) - (1/\rho_s)$. [g] The maximum volume of N_2 adsorbed along the isotherm as P/P_o approaches 1.0. [h] Cumulative volume of pores between 1.7 nm and 300 nm from N_2-sorption data and the BJH desorption method. [i] By the $4V/\sigma$ method (σ: BET surface area from Table S.XIII.2 below); for the first number, V was taken as equal to $V_{Total} = (1/\rho_b) - (1/\rho_s)$; for the number in [brackets], V was set equal to the maximum volume of N_2 adsorbed along the isotherm as P/P_o approaches 1.0. [j] Particle radius, $r = 3/(\rho_s \times \sigma)$.

Table S.XIII.2. Expected *versus* Actual (Experimental) Properties of the Eight Polyurea Aerogel Samples Prepared by Solving the System of Six Equations with Six Unknowns of Appendix X with set property values assigned in Appendix XII.

sample ID	***K*-index** [a]		**bulk density (ρ_b, g cm^{-3})**		**BET surface area (σ, m^2 g^{-1})**		**total thermal conductivity (λ_{Total}, mW m^{-1} K^{-1})**		**Ultimate Compressive Strength (*UCS*, MPa)**		**Young's modulus (*E*, MPa)**	
	Expected values	**Actual values**	**Expected values**	**Actual values**	**Expected values**	**Actual values**	**Expected values**	**Actual values**	**Expected values**	**Actual values**	**Expected values**	**Actual values**
1	1.19	1.23 ± 0.01	0.181	0.176 ± 0.002	179	203	31.9	31.8 ± 1.1	64.7	251 ± 11	41.1	32.1 ± 3.3
2	1.16	1.21 ± 0.01	0.074	0.091± 0.003	267	270	19.9	23.5 ± 0.9	24.0	277 ± 7	8.4	12.6 ± 2.2
3	1.33	1.29 ± 0.01	0.292	0.325 ± 0.007	102	71.4	39.6	37.4 ± 1.3	147	303 ± 15	85.3	56.1 ± 4.2
4	1.42	1.43 ± 0.01	0.457	0.483 ± 0.004	98.3	96.4	48.0	55.1 ± 2.2	360	345 ± 5	172	195 ± 9.6
5	1.58	1.62 ± 0.01	0.097	0.132 ± 0.002	96.0	126	35.5	34.2 ± 1.1	121	223 ± 3	7.0	20 ± 5
6	1.70	1.72 ± 0.01	0.380	0.315 ± 0.003	23.6	50.9	54.3	49.0 ± 1.6	230	241 ± 6	68.0	36.8 ± 5.3
7	1.79	1.83 ± 0.02	0.451	0.490 ± 0.001	15.6	5.51	62.6	57.9 ± 2.0	313	287 ± 4	80.9	66.4 ± 2.6
8	1.87	1.89 ± 0.01	0.328	0.291 ± 0.008	10.3	7.2	60.7	46.4 ± 1.3	210	245 ± 13	26.5	26.0 ± 1.3

[a] Calculated from the porosity and contact angle data cited in Table S.XIII.1 above.

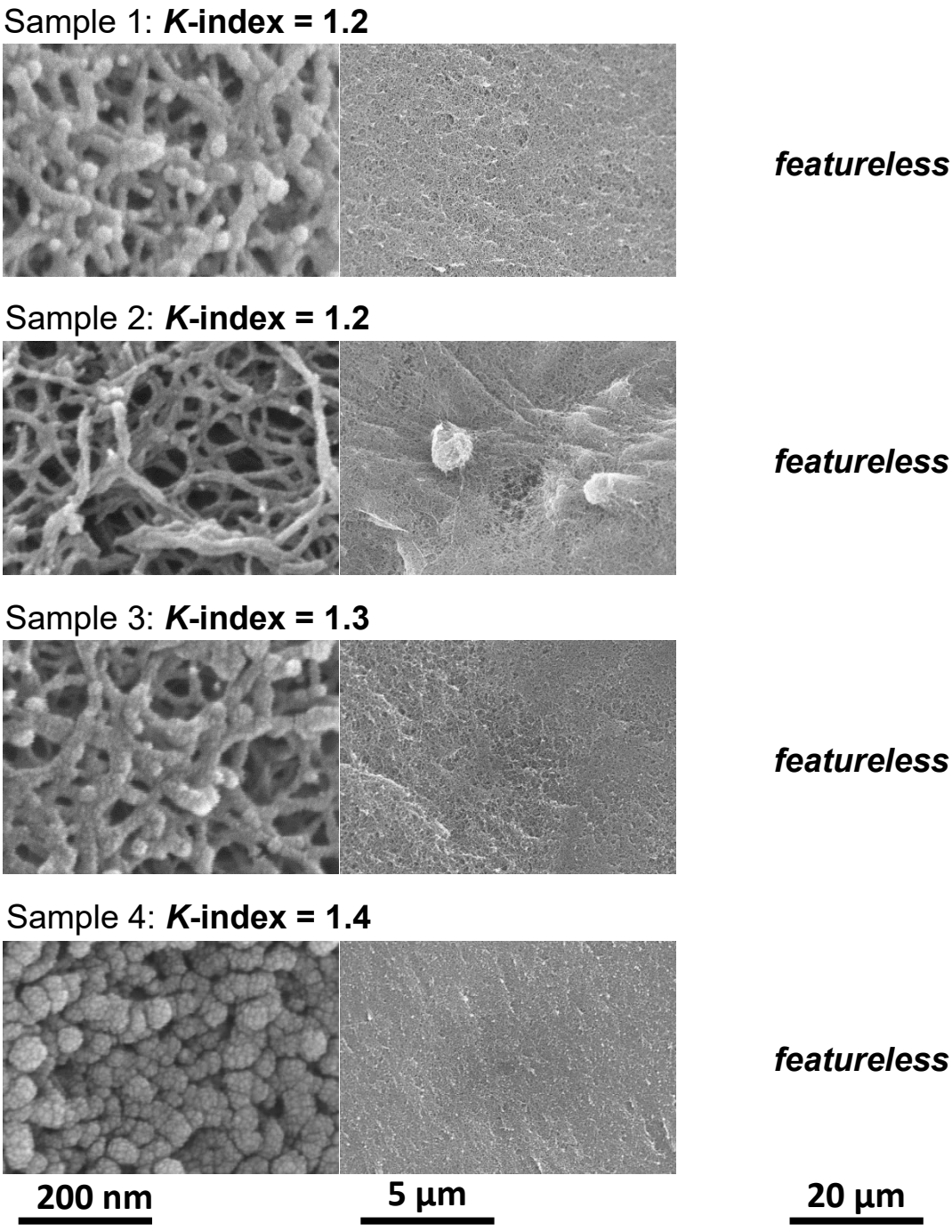

Figure S.XIII.1. SEM images at three different magnifications of the 8 predictive samples described in this and the previous Appendix. For other pertinent material properties refer to Tables S.XIII.1 and S.XIII.2 above.

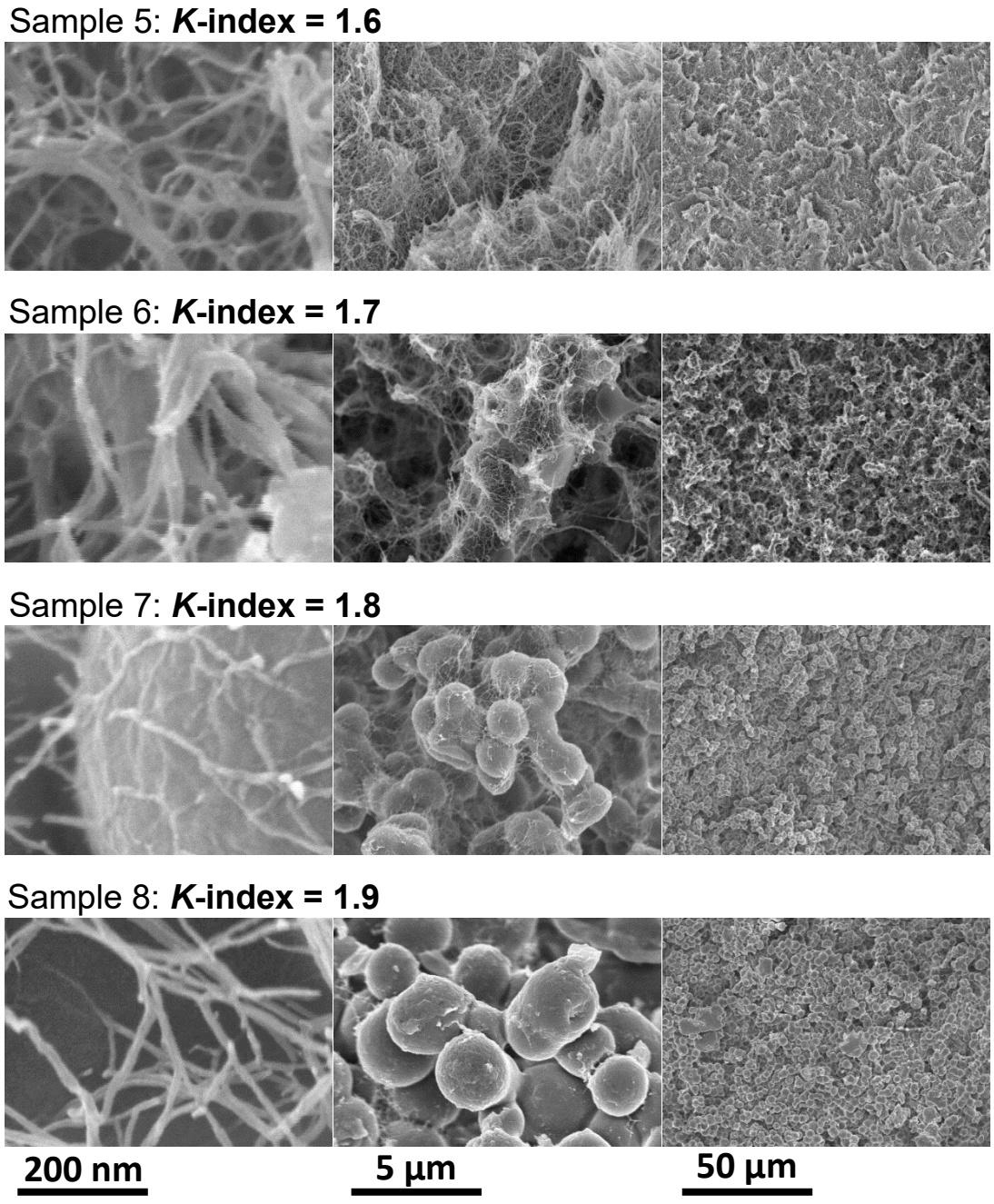

Figure S.XIII.1. SEM images at three different magnifications of the 8 predictive samples described in this and the previous Appendix. For other pertinent material properties refer to Tables S.XIII.1 and S.XIII.2 above. (cont.)

APPENDIX XIII. MORPHOLOGY AND *K*-INDEXES OF POLYURETHANR AEROGELS FROM PRIOR WORK

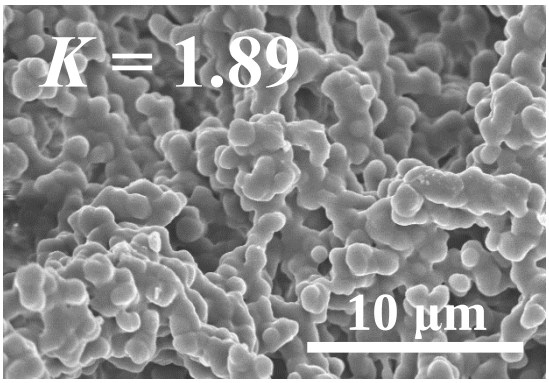

$\rho_b = 0.347 \pm 0.014$ g cm^{-3}

$\Pi = 71.5$ %

$\theta = 135.2$

$E = 0.066$ MPa

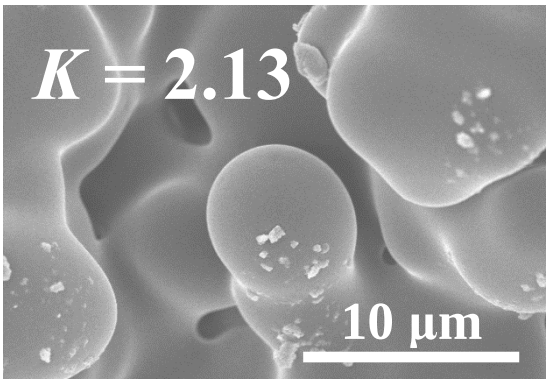

$\rho_b = 0.337 \pm 0.001$ g cm^{-3}

$\Pi = 72.2$ %

$\theta = 153.7$

$E = 0.048$ MPa

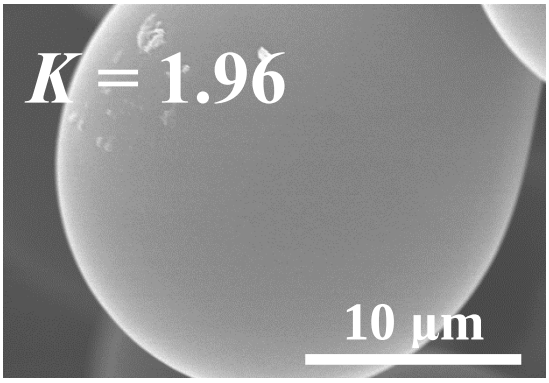

$\rho_b = 0.320 \pm 0.003$ g cm^{-3}

$\Pi = 74.0$ %

$\theta = 145.3$

$E = 0.031$ MPa

Figure S.XIV.1. SEM images and other relevant data of polyurethane aerogels prepared with the same isocyanate of this study (ISO: Desmodur N3300A) and tetraethylene glycol (TEG). The total monomer concentration was fixed at formulation TEG-4 of reference S.R.10. The gelation solvent was CH_3CN. Morphology was controlled with the amount of the catalyst.

APPENDIX XIV. SUPPLEMENTARY REFERENCES

S.R.1 Maleki, H.; Durães, L.; Portugal, A. Development of Mechanically Strong Ambient Pressure Dried Silica Aerogels with Optimized Properties. *J. Phys. Chem. C* **2015**, *119*, 7689−7703.

S.R.2 Montgomery, D. C. *Design and Analysis of Experiments*. John Wiley & Sons: New York, N.Y. 2006.

S.R.3 Goupy, J.; Creighton, L. *Introduction to Design of Experiments with JMP Examples*. SAS Institute Inc. Cary, New York, N.Y. 2007.

S.R.4 Hansen, C. M. *Hansen Solubility Parameters: A User's Handbook*. CRC Press, Boca Raton, FL 2007.

S.R.5 Leventis, N.; Sotiriou-Leventis, C.; Saeed, A. M.; Donthula, S.; Majedi Far, H.; Rewatkar, P. M.; Kaiser, H.; Robertson, J. D.; Lu, H.; Churu, G. Nanoporous Polyurea from a Triisocyanate and Boric Acid: A Paradigm of a General Reaction Pathway for Isocyanates and Mineral Acids. *Chem. Mater.* **2016**, *28*, 67–78.

S.R.6 Donthula, S.; Mandal, C.; Schisler, J.; Leventis, T.; Meador, M. A. B.; Sotiriou-Leventis, C.; Leventis, N. Nanostructure-Dependent Marcus-Type Correlation of the Shape Recovery Rate and the Young's Modulus in Shape Memory Polymer Aerogels. *ACS Appl. Mater. Interfaces* **2018**, *10*, 23321–23334.

S.R.7 Meador, M. A. B.; Capadona, L. A.; L. MacCorkle, L.; Papadopoulos, D. S.; Leventis, N. Structure-Property Relationships in Porous 3D Nanostructures as a Function of Preparation Conditions: Isocyanate Cross-Linked Silica Aerogels. *Chem. Mater.* **2007**, *19*, 2247–2260.

S.R.8 Pérez-Cruz, F.; Bousoño-Calzón, C.; Artés-Rodríguez, A. Convergence of the IRWLS Procedure to the Support Vector Machine Solution, *Neural Computation* **2005**, *17*, 7–18.

S.R.9 Sanchez-Fernández, M.; De-Prado-Cumplido, M.; Arenas-García, J.; Pérez-Cruz F. SVM Multiregression for Nonlinear Channel Estimation in Multiple-Input Multiple-Output Systems. *IEEE Trans Signal Processing* **2004**, *52*, 2298–2307.

S.R.10 Donthula, S.; Mandal C.; Leventis, T.; Schisler, J.; Saeed A. M.; Sotiriou-Leventis C.; Leventis, N. Shape Memory Superelastic Poly(isocyanurate-yrethane) Aerogels (PIR-PUR) for Deployable Panels and Biomimetic Applications. *Chem. Mater.* **2017**, *29*, 4461–4477.

II. MULTI-SCALE PROGRESSIVE FAILURE MECHANISM AND MECHANICAL PROPERTIES OF NANOFIBROUS POLYUREA AEROGELS[2]

Chenglin Wu *[a], Tahereh Taghvaee [b], Congjie Wei [a], Arman Ghasemi [c], Genda Chen [a], Nicholas Leventis [b] and Wei Gao [c]

[a]Department of Civil, Architectural, and Environmental Engineering, Missouri University of Science and Technology, Rolla, MO 65401, U.S.A. *Correspondence: wuch@mst.edu

[b]Department of Chemistry, Missouri University of Science and Technology, Rolla, MO 65401, USA

[c]Department of Mechanical Engineering, The University of Texas at San Antonio, San Antonio, TX 78249, USA

ABSTRACT

The nonlinear mechanical properties, deformation and failure mechanisms of polyurea aerogels (PUAs) were investigated using a multi-scale approach that combines nanoindentation, analytical and computational modeling. The atomistic structure of primary particles of PUAs and their mechanical interactions were investigated with molecular dynamics simulations. From nanoindentation we identified four deformation and failure modes: free ligament buckling, cell ligament bending, stable cell collapsing, and ligament crush induced strain hardening. The corresponding structural evolution during indentation and strain hardening were analyzed and modeled. The material scaling properties were found to be dependent on both the relative density and the secondary

---

[2] This paper was published in *Soft Matter 2018*, 14, 7801-7808.

particle size of PUAs. Using a porosity dependent material constitutive model, a linear relationship was found between the strain hardening index and secondary particle size instead the conventional power-law relationship. Finally, the structural efficiency of PUAs with respect to the capability for energy absorption is evaluated as a function of structural parameters and base polymeric material properties.

1. INTRODUCTION

Aliquam Aerogels are highly-porous (> 80%), low-density (typically < 0.5 g cm^{-3}) solids with an inorganic ceramic (oxide, carbide nitride) or a polymer framework.[1–3] They were first introduced in the 1930's as a means to study the framework of sol–gel derived wet-gels,[2] and prepared by converting the pore-filling solvent of wet gels into a supercritical fluid that was vented off like a gas. In the recent years, aerogels are emerging as strong lightweight materials for applications that range from thermal insulation,[4,5] to neural scaffolds,[6] to environmental remediation (oil-spill clean-up).[7–11] In most applications, high porosity is desirable, but it adversely affects the mechanical properties of the materials. A good trade-off between porosity and mechanical properties is reached when aerogels possess a bird-nest-like nanostructure of entangled fibers.[4] However, the constitutive law of such nanostructures is not well-understood or developed, rendering optimal aerogel design difficult.

With notable exceptions,[5] most microstructures of polyurea (PUA) aerogels are hierarchical assemblies of elementary primary and secondary particles.[30] The nanoscopic assembly of those elementary particles depends on kinetics (monomer concentration) and

solvent polarity during gelation.[7] Among various parameters of their nanostructures, the particle size, skeletal and bulk densities and their ratios can all be used to describe important features of the nanostructures. Although it does not affect the structural configurations of microstructures, they describe different perspectives of the mechanical properties of PUAs. How these parameters are related to the elastic and plastic behavior of PUAs is addressed in this article.

Characterization of the elastic and plastic behavior of porous materials has recently attracted significant amount of attention in research community. In macro-scale, the elastic modulus and Poisson's ratio of porous materials such as gas-injection-manufactured polymer foams with millimeter pores are usually determined from uniaxial compression experiments. However, the end frictions in this experiment often induces over-constrains. The resulting local stress variation makes the extraction of nano-scale properties of PUAs inaccurate, if not invalid.[12] To reduce the boundary effect of specimens and the requirements for surface preparation, nanoindentation has been widely used to characterize nanostructured solids.[13–15] In this case, the nonlinear tip effect must be accounted for. The elasticity, viscoelasticity, and porosity-dependent strain-hardening law must be known in order to characterize the mechanical behavior of nanoporous polymeric materials.

For example, the relaxation modulus extraction method[16] and the hardness interpretation approach[19] has been adopted to extract the effective elastic modulus, relaxation modulus, and the yield strength, respectively. In addition, determining the scaling properties failure mechanism of porous and cellular materials is also critical for current material system.[20–30] The scaling properties are referred to varying elastic modulus and yield strength as the relative density of the material changes. For macrocellular foams,

both open- and closed-cell scaling equations were proposed by Gibson and Ashby[20] based on the mechanics of deformation on a representative cell geometry. This cell geometry was ‘‘idealized’’ from the results of the mechanical experiments on foams with macro pores. These equations, however, cannot be directly applied to PUAs due to the absence of any representative cell geometry and size effect.[29,30] The effective shape coefficients need to be determined from the experimental data.

In this study, we discovered a progressive failure mechanism, which shows different responses at critical indentation depths. These critical indentation depths are associated with the varying failure mechanism. The scaling equation describing the change of effective elastic modulus with varying relative density was determined. The porosity-dependent strain hardening constitutive law was proposed and implemented to extract the hardening index. A contact mechanism was then found between secondary particles to explain the correlation between the hardening index and particle size.

2. PUA MATERILAS

PUA wet-gels were prepared at room temperature in dry acetone from an aliphatic triisocyanate (Desmodur N3300A, courtesy of Bayer Corporation) 3× the stoichiometric amount of water and triethylamine (catalyst) as described in eqn (1).[6] Pore-filling acetone was extracted with liquid CO_2 in an autoclave, and aerogels were obtained by taking CO_2 out as a supercritical fluid. Three different formulations were considered with 11.0 g, 16.5 g and 24.0 g of Desmodur N3300A in a fixed amount of solvent (94 mL). The corresponding aerogels are referred to as PUA-11, PUA-16 and PUA-24, respectively.

These three types of aerogels were selected since they provided different spatial structures, due to their different particle size and relative densities. These parameters will be linked to the mechanical properties providing the structure–property relationship for the Nanofibrous PUA materials.

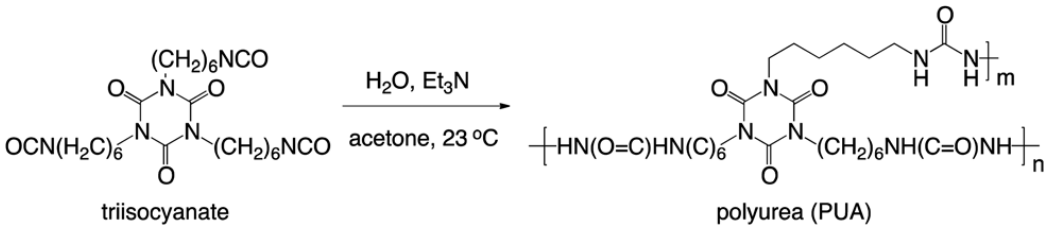

(1)

3. RESEARCH METHODS

3.1. NANOSTRUCTURE CHARACTERIZATION

The bulk density (ρ_b) of polyurea samples is determined by the geometric dimensions and weight of each cylindrical specimen. The skeletal density (ρ_s), which is the solid density of the ligament, was determined using helium pycnometer with a Micrometrics AccuPyc II 1340 instrument. Porosities, Π, was determined by $\Pi = 100 \times (\rho_s - \rho_b)/\rho_s$. The particle sizes were determined using ultra-small angle and small angle neutron diffraction (USANS/SANS). More detailed information about SANS can be found in the work by Leventis et al.[6] The scanning electron microscopy (SEM) was used to image the cellular structures of poluyrea samples. The atomic force microscopy (AFM) was used to image the deformation field after indentations.

3.2. MOLECULAR DYNAMIC (MD) MODELLING

Etiam All atoms optimized potential for liquid simulation (OPLS-AA is applied in our MD simulation since it was found in close agreement with the density functional theory.[32–34] For any atom type in the polyurea structure, force field parameters were chosen by matching the atom type with its corresponding atom defined in the OPLS parameter database. All MD simulations in this study are performed with LAMMPS in NVT ensemble at 300 K using the Nose–Hoover thermostat with an integration time step of 1 fs. More modelling details are listed in the ESI† (Note S1).

3.3. NANOINDENTATION EXPERIMENTS

Nanoindentation was conducted using the Hysitron TI 950 TriboIndentert equipped with a Berkovich diamond tip. Quasistatic indentations were performed on each sample under a triangular displacement over time profile with a loading/unloading rate of 1 nm s^{-1} at various depths. At least 20 indents were performed on a freshly cleaved surface of each specimen for each depth. During each test, loading and unloading cycles were performed with holding for approximately 1 s, and full unloading.

3.3.1. Elastic and Relaxation Modulus. Based on the polymeric nature of the PUA, the viscoelastic and plastic behavior were assumed. Following the approached proposed by Huang and Lu,[16] Lu et al.,[17] Du et al.[18] The elastic and relaxation modulus were extracted. More extraction details are presented in the Note S2, ESI.†

3.3.2. Hardness and Yield Strength. The hardness (H) of PUA is defined by the peak force (P) divided over the projected contact area (A_c). The yield strength (σ_y) can be linearly related to the hardness with a coefficient (C_P). For dense bulk material, C_P is

usually close to 2.5–3 due to the confinement effect from adjacent materials. For PUAs, the absence of confinement gives $C_P = 1$, which is similar as other highly porous materials such as nanoporous gold.[19]

3.4. FINITE ELEMENT MODELLING

Both of the extracted elastic and relaxation modulus was taken into account before PUA exceeds the yield strength. The strain hardening phenomenon observed from force–displacement responses were also considered the finite element modelling. By treating the PUA as continuum materials, a J2-flow based plasticity model was then implemented using ABAQUS with Subroutine UMAT. This model is based on the Desphande and Fleck's self-similar concept,[23] and has a modified shape of yield surface from the conventional von Mises criterion. More details of this model are shown in Note S3, ESI.†

A self-similar strain hardening relationship was assumed incorporating porosity changes.[23] In the uniaxial compression setting, the post-yielding stress–strain relationship is,

$$\frac{\bar{\sigma}}{\sigma_0} = 1 + \frac{\overline{\varepsilon_p}}{\overline{\varepsilon_D}} + \gamma \ln\left[\frac{1}{1-\left(\overline{\varepsilon_p}/\overline{\varepsilon_D}\right)^{\beta}}\right]. \quad (2)$$

where σ_0 is yield strength, $\overline{\varepsilon_p}$ is the uniaxial plastic strain. Assuming the porosity change comes from the volume reduction, the relationship between the current porosity strain ($\overline{\varepsilon_D}$) and plastic strain can be obtained, $\overline{\varepsilon_D} = \frac{f_0 - \overline{\varepsilon_p}}{1-\overline{\varepsilon_p}}$. Where γ and β are material constants, f_0 is the initial porosity of aerogels. As the stress rises, the plastic strain rises nonlinearly following an inverse power-law relationship. To extract the strain-hardening properties, the parameter β is assumed to be constant as it has small impact on the shape of the strain-

hardening law. The parameter γ, which contributes directly to the hardening behavior, is then obtained by fitting the experimental data.

4. RESULTS AND DISCUSSION

4.1. NANOSTRUCTURES

The SEM images of various PUAs are shown in Figure 1, the overall cellular structural features were observed. Based on the SANS data, the average diameters of the ligament are 24, 22, and 17, respectively. The particle size difference, through small, was found to contribute significantly to the strain hardening behavior as described later in this section (Table 1).

4.2. FORCE DISPLACEMENT AND DEPTH PROFILE

The representative load–displacement responses are presented in Figure 2. Significant plastic deformations were observed upon fully unloading. SEM images of the indentation site after different depths of indentation for PUA-11 are also shown in Figure 3a–d. The cellular nanostructure showed distinctive bending of ligaments after 500 nm of indentation. However, most of the pores were slightly deformed underneath the contact surface. As the indentation progresses, the pores start to collapse. We observed significant contacting and crushing of the ligaments as they were pressed against each other under compression. Therefore, it is suggested that prior to the 500 nm of indentation depth, most of the pores remained open with ligaments slightly bent under compression. When the indentation depth approaches to 1500 nm, the ligaments show clear contact which gives

rise to hardening behavior. These evidences indicate different stress bearing mechanisms at various indentation depths. The post-indentation AFM scanning was also conducted to characterize the deformation profiles which are used to calibrate the finite element modeming. More details of AFM scans are provided in the Note S4, ESI.†

4.3. PROGRESSIVE FAILURE MECHANISM AND INDENTATION DEPTH

The calculated elastic modulus (E_∞) and yield strengths (σ_y) at different indentation depths are presented in Figure 4a and b, respectively. The results showed four stages of depth (δ)-dependent behavior of these properties. In stages ①, where $0 < \delta < 200$ nm, both properties increase almost linearly proportional to δ. In stage ②, where $200 < \delta < 600$ nm, the properties showed drastic drop with respect to the increase of d. In stage ③, where $600 < \delta < 900$ nm, both the Elastic modulus and yield strength enters a short plateau at constant values. In stage ④, where $\delta > 900$ nm, the Elastic modulus show less increase for PUA-24 comparing to PUA-11 and 16. The yield strengths of all PUAs increased significantly, which are nonlinearly proportional to the increase of δ. These critical depths (200, 600, and 900 nm) are then determined to differentiate the corresponding stages as the nanostructure deforms progressively. The physics behind each stage can be explained as illustrated in Figure 5. In the first stage, there exist independent ligaments unconnected to cells. When pressing, the independent ligaments act as end-supported columns. The low elastic modulus and yield strength could result from the buckling of these columns. As the indentation depth enters the second stage, the connected ligaments (cell structure) started to bend under compression. The excessive bending caused configurational changes to the cell structure that leads to changed effective elastic modulus and yield strengths. After the

stress through ligaments exceeds the yield strengths of base materials, the cell shows stable collapsing stage ③. After the deformations exceed certain level, the ligament contact initiated causing the strain hardening behavior, which gives rise to increased effective elastic modulus and yield strengths in stage ④.

4.4. SCALING PROPERTIES

The average moduli of (20 indents for each sample) are 15.2,31, and 60 MPa for PUA-11, 16, and 24, respectively. Their corresponding standard deviations are 2.1, 1.8, and 2.3 MPa. The average yield strengths obtained at stage ③ are 2.35, 4.7, and 6.36 MPa for PUA-11, 16, and 24, respectively. Their corresponding standard deviations are 0.15, 0.15, and 0.2 MPa. These yield strength values are much higher than obtained from uniaxial compression test at larger scale (with a cylindrical specimen's size of 25 mm in diameter and 50 mm in height).[21]

For porous materials, the scaling rules refer to the relationship between the relative density ratio and material properties. The backbone of this rule is that the PUA shares the same base material and structural features, which was demonstrated from MD and SANS results. According to these scaling rules, the effective elastic modulus and yield strength of general cellular solids are proportional to the powers of their relative density (bulk/skeletal).[19–21]

As shown in the SEM images (Figure 1) of PUA with different densities, when density increases, the secondary particle size reduces leading to an increased slenderness ratio. Under compression, the bending deformation of the ligaments determines the

macroscopic strains.[19,23,24] The scaling equations for bending-dominant cellular materials have been proposed by previous studies,[19,20,25] and can be written as,

$$\frac{E_\infty}{E_s}, \frac{\sigma_y}{\sigma_{ys}} = \left(C_e, C_y\right)\left(\frac{\rho_b}{\rho_s}\right)^{\left(\alpha_e, \alpha_y\right)} \quad (3)$$

where E_∞, σ_y are effective elastic modulus and yield strength, ρ_b is the bulk density. E_s and σ_{ys} are base material's elastic modulus and yield strength, ρ_s is the skeleton density. The proposed equations can linearly fit the mean experimental data in the logarithm plot as shown in Figure 6. The fitting parameters are obtained as C_e = 0.87, C_y = 1.63, α_e = 1.9, α_y = 1.8 with the least square errors of 0.013 and 0.01. The properties of the base materials are then determined as Es = 1.6 GPa and σ_{ys} = 38 MPa. From the bending dominant deformation mechanics, α_e and α_y are 2 and 1.5[24, 30,35–39] respectively. These values are slightly lower than the ones obtained in this work. The difference comes from the random cell geometry. Table 2 summarizes the extracted properties and scaling parameters. These results showed significant reductions in effective elastic modulus (approximately 1/100 times of the base material modulus) and effective yield strengths (approximately 1/10 of the base material yield strength).

4.5. POROSITY-DEPENDENT STRAIN HARDENING

The strain-hardening properties exhibited in stage 4 can be extracted using the finite element modelling approach described in Section 3.4. More details of the finite element modeling can be found in the Note S5, ESI.†

The effective elastic and relaxation modulus obtained previously are used. The numerical load versus depth response are then compared with experimental data. By

iteratively varying the strain hardening power index γ, the numerical results converge to the experimental values as shown in Figure 2. It should be noted that the slight disagreement in depth range of 0–500 nm is due to the less prominent hardening effect. We also compared the AFM scanned displacement profiles of the post-indentation sites with the numerical results and found close agreement as shown in Figure 7a. The extracted γ values for PUA-11, 16, and 24 are 7, 5, and 3. β was set to be 6 for all PUA. The normalized stress versus plastic strain response in Figure 7b shows that PUA-11 has more rapid increase comparing to PUA-16 and 24, especially when plastic strain exceeds 0.3.

4.6. STRAIN HARDENING AND PARTICLE SIZE

To link the strain hardening behavior to the microstructure and deformation process. We analyzed the stress versus plastic strain response after yielding as shown in Figure 7b. The structure enters a short stress plateau (plastic strain from 0–0.3) followed by a sharp rising part. This plateau corresponds to the structural collapsing during compression. Beyond the plateau, the excessive bending of the ligaments causes compressive interactions among ligaments, which has been confirmed by SEM images taken after the tip retraction as shown in Figure 8a–d. In the highly densified region under indentation, secondary particles were deformed and then compressed into each other as shown in the insert of Figure 8e. During this process, the primary particles are pressed against each other causing densification.

As shown in Table 2, the strain hardening index g reduces as the secondary particle size reduces. We can explain these findings use the Herzian contact theory.[31] Given the same volume and applied uniaxial force at full compaction as illustrated in Figure 8e, we

know that the contact stress ($\sigma_c = (\frac{F}{A})$/(number of contacting points)) is proportional to the second order of the radius of secondary particle (R_2), *i.e.*, $\sigma_c \propto (R_2)^2$. From Herzian contact solution,[31] the contact stiffness (K) of the particle is proportional to the third order of the product of contact stress and the radius of secondary particle, i.e., $K \propto (\sigma_c R_2)^{1/3}$. Since the strain hardening index is linearly proportional to the contact stiffness K, we have $\gamma \propto K \propto R_2$, which means the strain hardening index reduces when particle size reduces. This linear relationship is demonstrated from our experiments as shown in Figure 8e. The standard deviation away from the average strain hardening ratio ($\frac{\gamma}{R} \approx 2.233$) is about 0.05. This deviation comes from the plastic contact and physical fusion explained earlier.

4.7. STRUCTURAL EFFICIENCY

Based on the scaling rules, we can identify the relationship between the increased density and increased impact resistance. The energy absorption is defined as the area underneath the equivalent plastic strength versus plastic strain curve. The energy absorbed during the uniaxial crushing process is then,

$$W = \sigma_0 \int_0^{\varepsilon_0} \frac{\bar{\sigma}}{\sigma_0} \mathrm{d}\left(\overline{\varepsilon_\mathrm{p}}/\overline{\varepsilon_\mathrm{D}}\right) = \sigma_0 \left(\varepsilon_0 + \frac{\varepsilon_0^2}{\bar{2}} + \gamma\left(R_\mathrm{p}\right) \int_0^{\varepsilon_0} \ln\left[\frac{1}{1-\left(\overline{\varepsilon_\mathrm{p}}/\overline{\varepsilon_\mathrm{D}}\right)^\beta}\right] \mathrm{d}\left(\overline{\varepsilon_\mathrm{p}}/\overline{\varepsilon_\mathrm{D}}\right) \right) \quad (4)$$

where ε_0 is the level of strain that the energy was accounted for, R_p is the secondary particle size. Based on this definition, we have two design approaches, one is to directly increase the yield strength of the base material. The second is to change the secondary particle size giving different γ. To evaluate the efficiency of both approaches, we define a structural efficiency index S_e. It is a ratio between the energy enhancements through the change of yield strength and the change of particle size, relative to PUA-11.

$$S_{\mathrm{e}} = \frac{W(\sigma_0)}{W(r_{\mathrm{p}})} = \frac{r_\sigma}{r_{\mathrm{P}} + \frac{\left(\varepsilon_0 + \frac{\varepsilon_0^2}{2}\right)(1 - r_{\mathrm{P}})}{\gamma_0 \int_0^{\varepsilon_0} \ln\left[\frac{1}{1-(\overline{\varepsilon_{\mathrm{p}}}/\overline{\varepsilon_{\mathrm{D}}})^{\beta}}\right] \mathrm{d}(\overline{\varepsilon_{\mathrm{p}}}/\overline{\varepsilon_{\mathrm{D}}}) + \left(\varepsilon_0 + \frac{\varepsilon_0^2}{2}\right)}} \quad (5)$$

where $r_\sigma = \frac{\sigma_0}{\sigma_{0,11}}$, $r_{\mathrm{p}} = \frac{R_{\mathrm{P}}}{R_{\mathrm{P},11}}$, $\sigma_{0,11}$, γ_0, $R_{\mathrm{P},11}$ are the yield strength, hardening index, and particle size of PUA-11. We plotted *S*e with practical range of r_σ and r_{p} with reference plane of $S_{\mathrm{e}} = 1$ in Figure 9. S_{e} can then be divided into the yielding favored zone (Se ≥ 1) and hardening favored zone (*S*e <1). In the yielding favored zone, the enhancement of yield strength of base materials gives higher energy absorption. In the latter, reducing hardening index (*i.e.*, reducing particle size), gives higher energy absorption. The Se surfaces with ε_0 = 0.25, and 0.75 are also compared in Figure 9. The two surfaces intersect at the plane of $r_{\mathrm{p}} = 1$. The results show, when $r_{\mathrm{p}} \geq 1$, the hardening-favored zone increases as ε_0 increases. This means it is more efficient to increase particle size to achieve higher energy absorption associated with large compressive strains. When $r_{\mathrm{p}} < 1$, as ε_0 increases, the yielding-favored zone increases. It means higher efficiency of increasing yield strength to achieve higher energy absorption with large strains.

5. CONCLUSIONS

Based on particle analyses, nanoindentation, and multi-scale modelling, the following conclusions can be drawn: (1) Primary particles were identified as the basic building elements of PUA structures that determined base material properties. A compound of approximately ten primary particles form the basis of a secondary particle. (2) Nanofibrous PUA can be characterized by an effective unit cell as widely used in cellular

structures. This feature allows a reliable prediction of crushing process of the PUA based on indentation experiments. (3) The nonlinear response of PUA samples resulted from various deformation mechanisms of nanocellular structures. This shows the nanostructures of PUA are highly stress sensitive, which makes PUA a potential candidate for the development of pressure sensing devices. (4) The smaller the particle size, the less significant the strain hardening effect through particle contact and the slender the ligament between particles. Smaller particles contribute to lower effective yield strength but higher PUA porosity as desired in some applications. Hence, controlling both particle size and ligament length independently is a future research direction to achieve the optimum properties of PUA in various applications. (5) Due to interrelation between the secondary particle size and the base material yield strength, high energy absorption can be achieved only by taking into account their coupling effect.

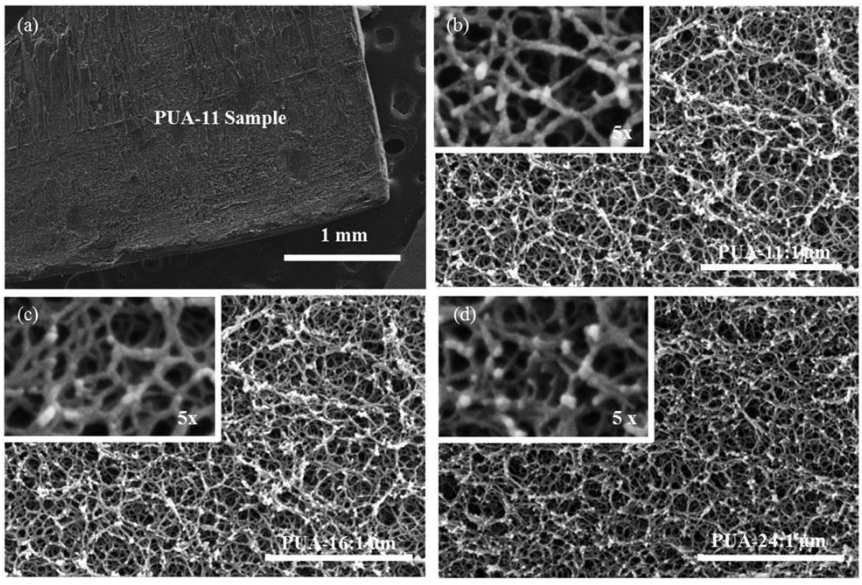

Figure 1. SEM images showing a) bulk PUA-11 and nanostructure of b) PUA-11, (c) PUA-16, (d) PUA-24. (Scale bar represents 1 mm, insets are 5-time zoomed.)

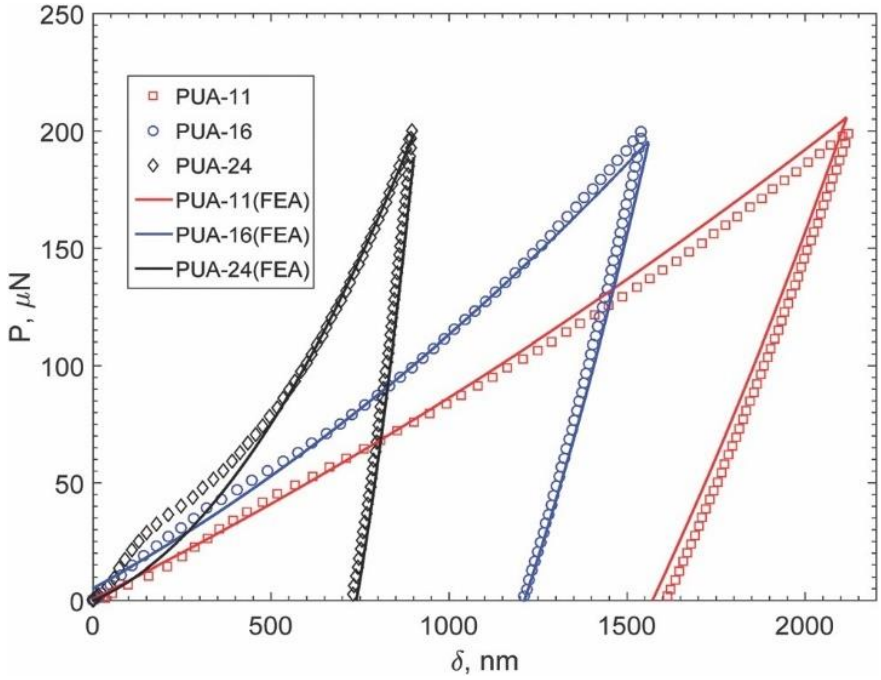

Figure 2. Typical force displacement response.

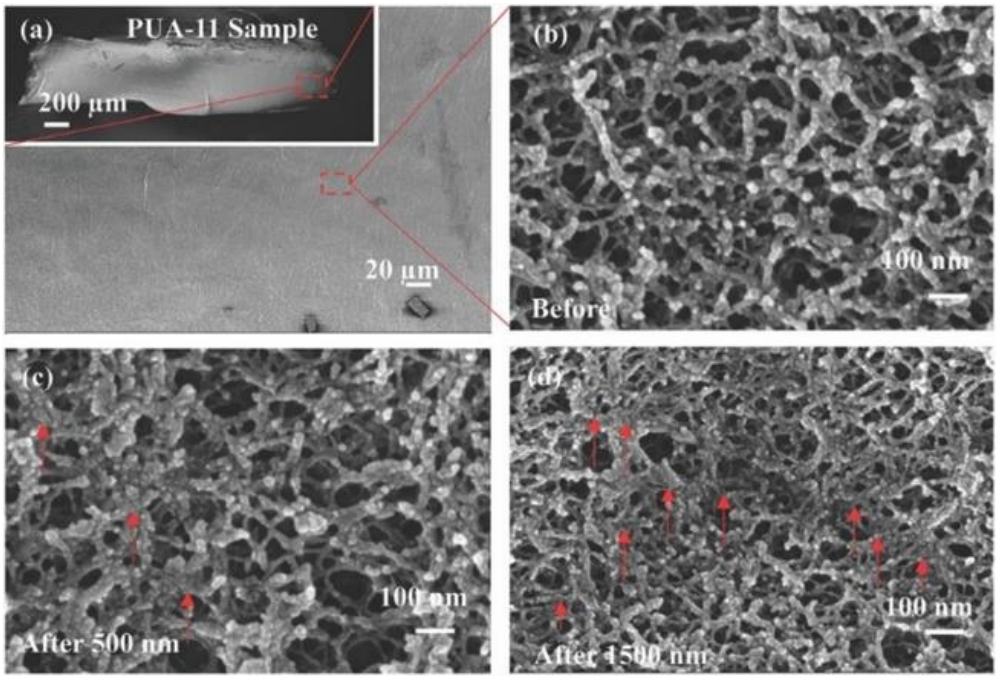

Figure 3. Deformation progression of PUA-11 at different depths: (a) indentation location, (b) prior-to indentation, (c) after 500 nm indent and full unloading, (d) after 1500 nm indent and full unloading.

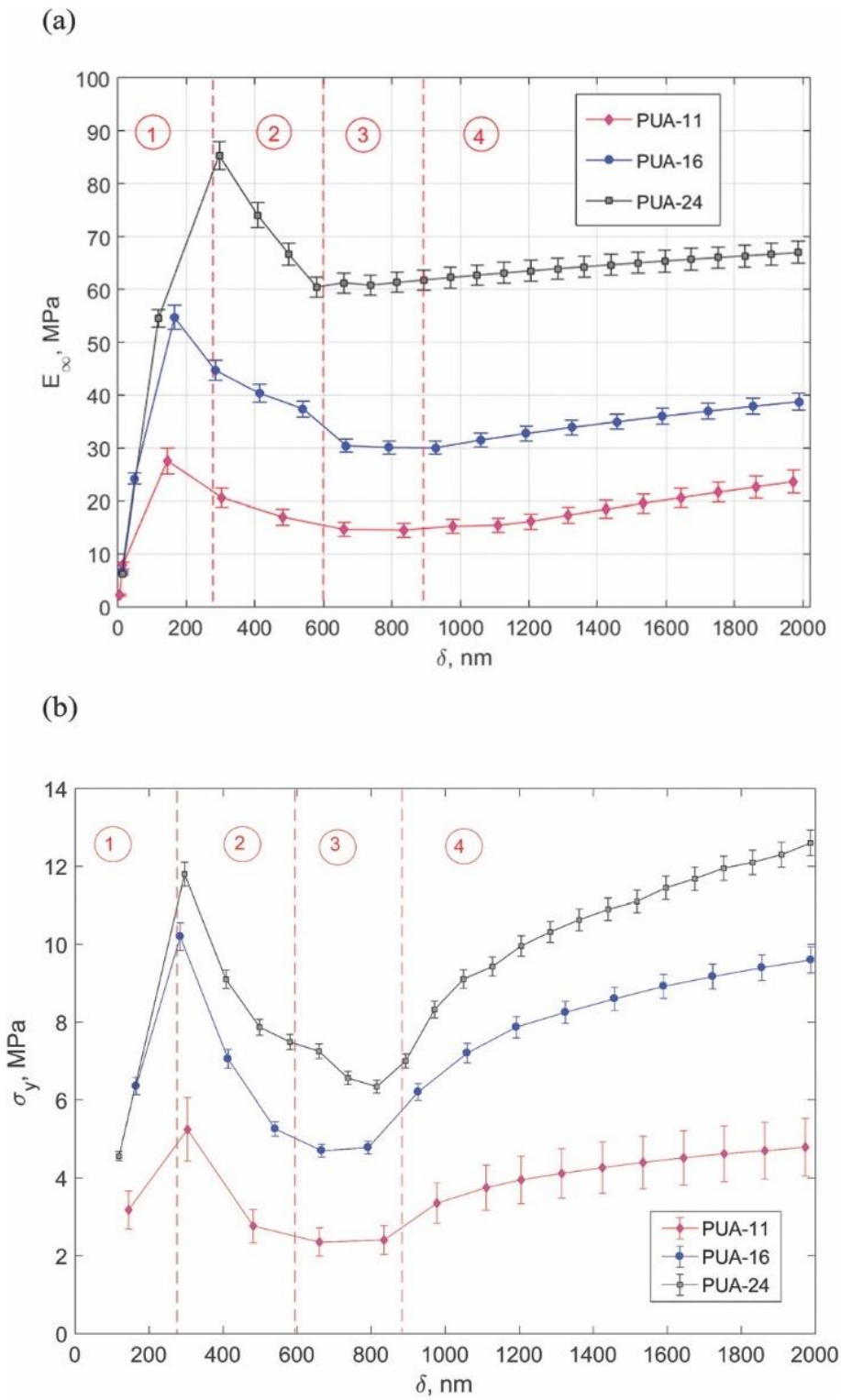

Figure 4. (a) Elastic modulus and (b) yield strength versus indentation depth.

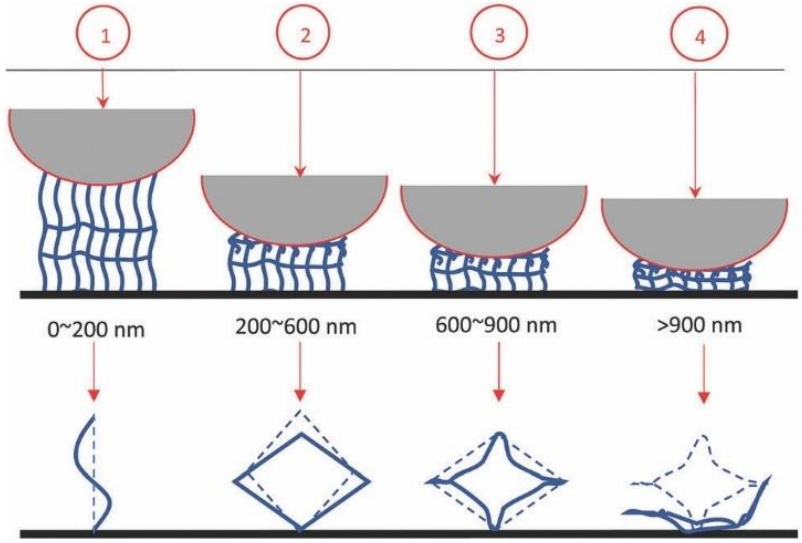

Figure 5. Illustration of deformation stages (dashed lines show previous configuration).

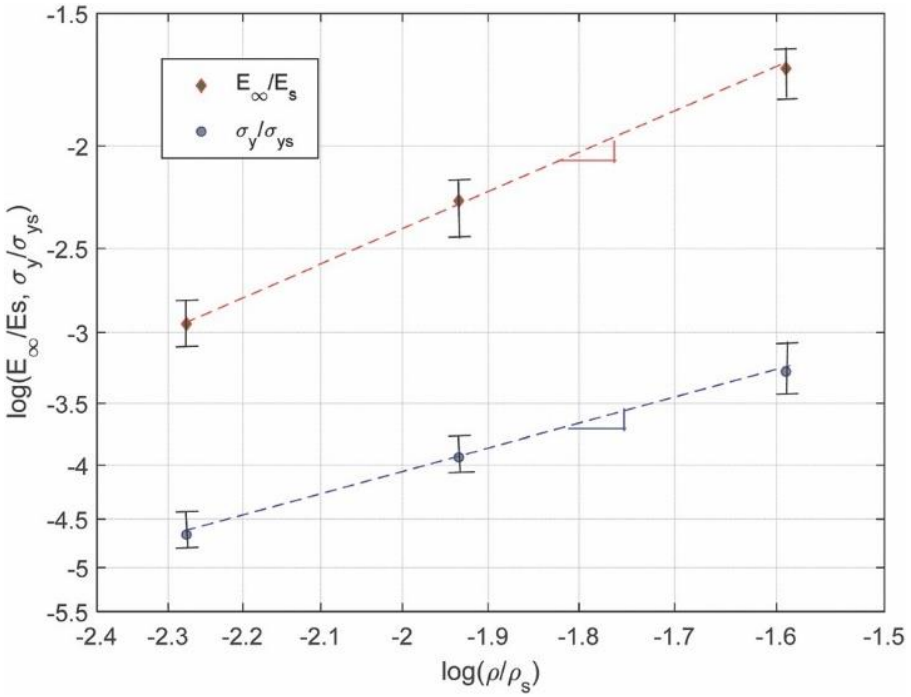

Figure 6. Scaling properties of PUA: log–log plot of relative elastic modulus, and yield strength versus relative density.

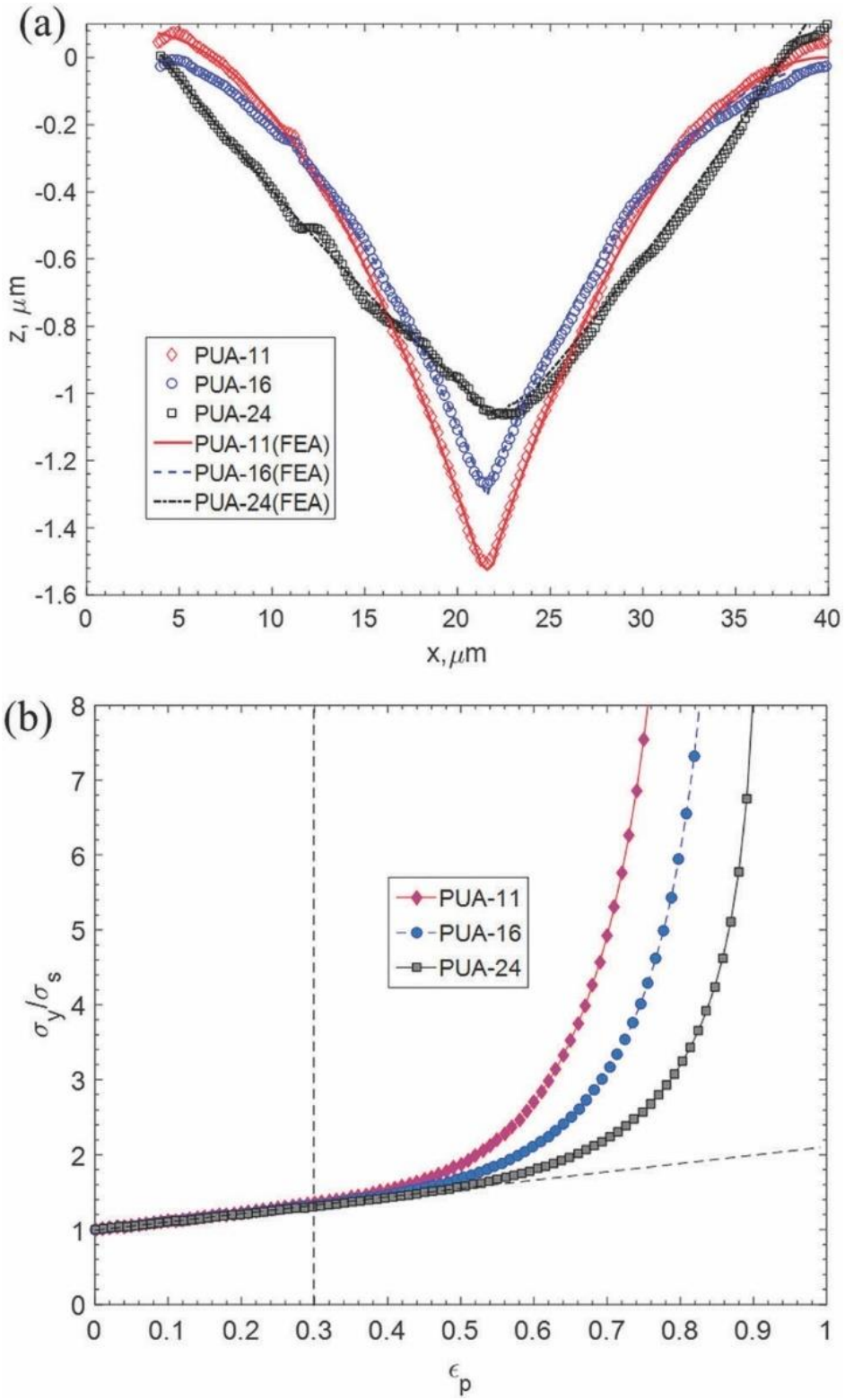

Figure 7. Finite element modelling results: (a) deformation profiles, (b) extracted hardening relations.

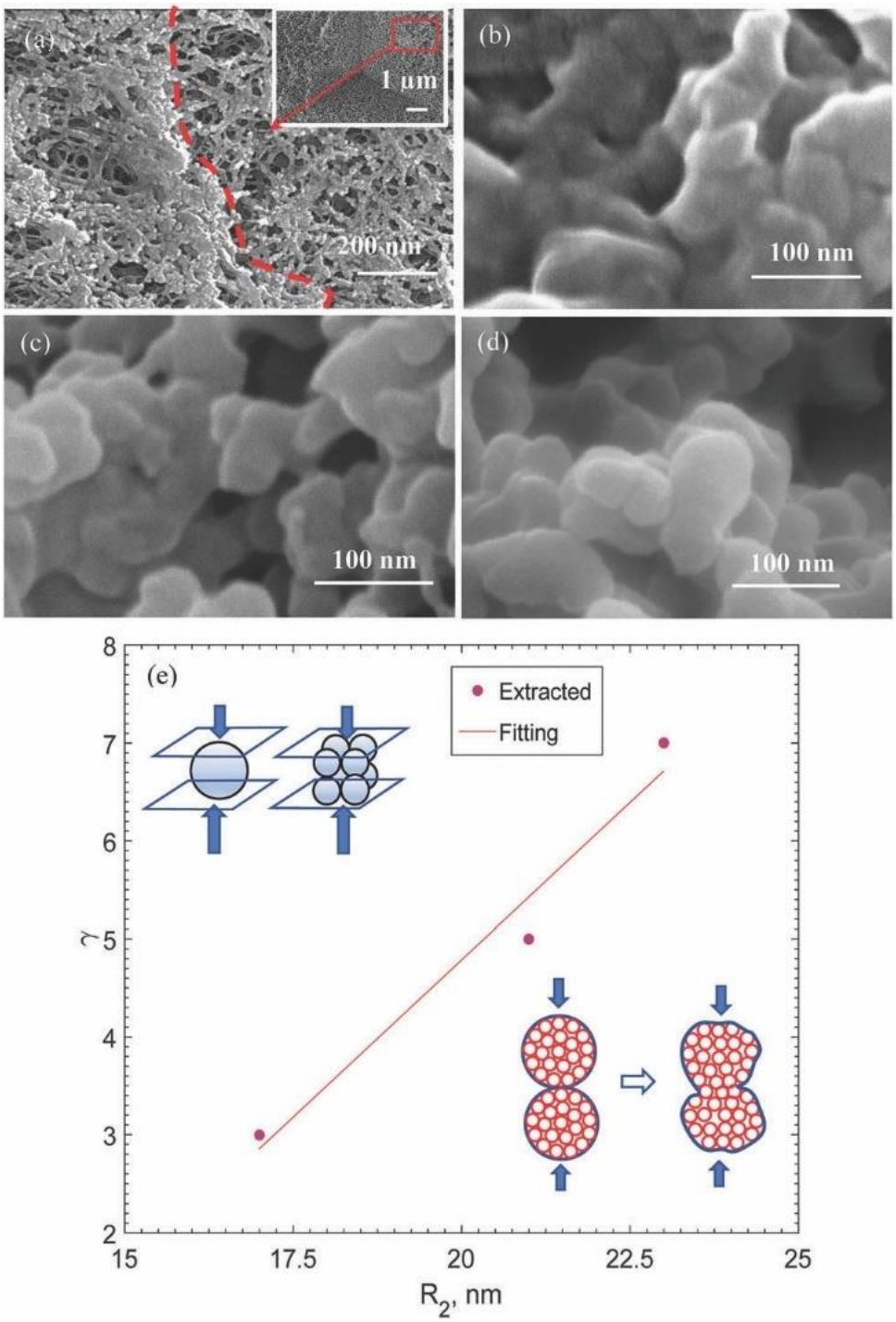

Figure 8. Strain hardening mechanism due to contact: (a) densified nanostructures after indentation, fused particles for (b) PUA-11, (c) PUA-16, (d) PUA-24, (e) strain hardening index versus secondary particle size.

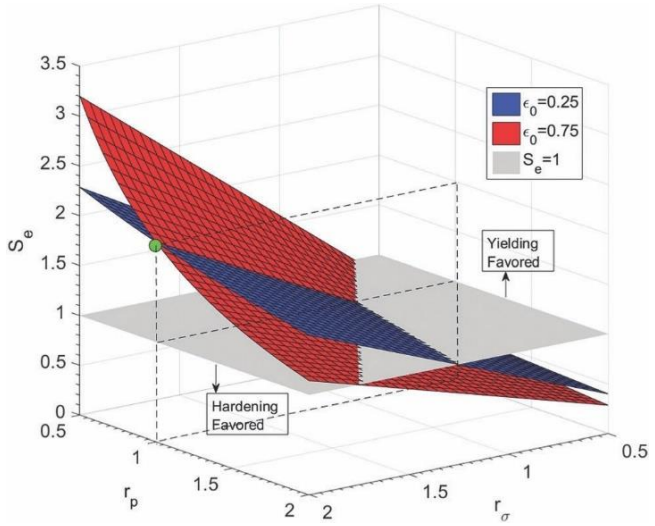

Figure 9. Material design of PUA: structure efficiency with varying yield strength and particle size ratios.

Table 1. SAXS data of polyurea aerogels.

Sample	ρ_b (g cm^{-3})	ρ_s (g cm^{-3})	Π (%)	R_1 [a] (nm)	R_2 [a] (nm)
PUA-11	0.123±0.004	1.197±0.007	89.7	7.03±0.48	23.7±0.83
PUA-16	0.173±0.002	1.199±0.002	85.5	8.09±0.47	21.9±0.1.34
PUA-24	0.244±0.016	1.200±0.002	79.7	6.8±0.30	17.0±3.92

[a] R_1, R_2: radii of primary and secondary particles, respectively; Calculated from the corresponding SAXS radii of gyration, RG, via R = RG/0.77.

Table 2. Scaling properties of polyurea aerogels.

Sample	***E* (MPa)**	**σ_y (MPa)**	**γ**	**β**	**E_s (MPa)**	**σ_s (MPa)**	**C_e**	**C_y**	**α_e**	**α_y**
PUA-11	15.2 ± 2.1	2.35 ± 0.15	7.1	6	1600	35	0.87	1.63	1.9	1.8
PUA-16	31.0 ± 1.8	4.70 ± 0.15	5.04	6						
PUA-24	60.0 ± 2.3	6.36 ± 0.13	3.02	6						

ACKNOWLEDGMENTS

Financial support for this study was provided by National Science Foundation under Award No. CMMI-1030399 and the ARO under Award No. W911NF-14-1-0369. We also thank Covestro LLC (formerly Bayer Corp. U.S.A.) for the generous supply of Desmodur N3300A. The authors would like to thank Professor Tengfei Jiang from Central Florida University and Professor Paul S. Ho from the University of Texas at Austin for their assistances during experiments and for their insightful discussion during the preparation of this paper.

REFERENCES

1. H. L.Tyan, C. Y. Wu and K. H. Wei, J. *Appl. Polym. Sci.*, **2001**, 81, 1742–1747.
2. S. S. Kistler, *Nature*, **1931**, 127, 741.
3. M. A. B. Meador, E. F. Fabrizio, F. Ilhan, A. Dass, G. Zhang, P. Vassilaras, J. C. Johnston and N. Leventis, *Chem. Mater*., **2015**, 17, 1085–1098.
4. G. Zhang, A. Dass, A.-M. M. Rawashdeh, J. Thomas, J. A. Counsil, C. Sotiriou-Leventis, E. F. Fabrizio, F. Ilhan, P. Vassilaras, D. A. Scheiman, L. McCorkle, A. Palczer, J. C. Johnston, M. A. B. Meador and N. Leventis, *J. Non-Cryst. Solids*, **2004**, 350, 152–164.
5. N. Leventis, C. Chidambareswarapattar, A. Bang and C. Sotiriou-Leventis, *ACS Appl. Mater. Interfaces*, **2014**, 6, 6872–6882.
6. N. Leventis, C. Sotirious-Leventis, N. Chandrasekaran, S. Mulik, Z. J. Larimore, H. Lu, C. Ghuru and J. T. Mang, *Chem. Mater*., **2010**, 22(24), 6692–6710.
7. G. Zhang, A.-M. M. Rawashdeh, C. Sotiriou-Leventis and N. Leventis, *Polym. Prepr*., **2003**, 44, 35–36.
8. F. Sabri, J. A. Cole, M. C. Scarbrough and N. Leventis, *PLoS One*, **2012**, 7, 125–132.

9. T. C. Bailey and A. C. Gatrell, *Interactive Spatial Data Analysis*, Addison Wesley Longman Limited, Essex, England, 1995.

10. H. L. Tyan, C. Y. Wu and K. H. Wei, *J. Appl. Polym. Sci*., **2001**, 81, 1742–1747.

11. A. Katti, N. Shimpi, S. Roy, H. Lu, E. F. Fabrizio, A. Dass, L. A. Capadona and N. Leventis, *Chem. Mater*., **2006**, 18, 285–296.

12. R. Haj-Ali, R. Eliasi, V. Fourman, C. Tzur, G. Bar, E. Grossman, R. Verker, R. Gvishi, I. Gouzman and N. Eliaz, *Microporous Mesoporous Mater*., **2016**, 226, 44–52.

13. T. Jiang, C. Wu, L. Spinella, J. Im, N. Tamura, M. Kunz, H. Y. Son, B. G. Kim, R. Huang and P. S. Ho, *Appl. Phys. Lett.*, **2013**, 103, 211906.

14. C. Wu, R. Huang and K. M. Liechti, *IEEE Trans. Device Mater. Reliab*., **2017**, 17(2), 1530–4388.

15. T. Jiang., C. Wu, J. Im, R. Huang and P. S. Ho, *J. Microelectron. Electron. Packag.*, **2015**, 12, 118–122.

16. G. Huang and H. Lu, *Mech. Time-Depend. Mater*., **2006**, 10, 229–243.

17. H. Lu, B. Wang, J. Ma, G. Huang and H. Viswanathan, *Time- Depend. Mater*., **2003**, 7, 189–207.

18. P. Du, I.-K. Lin, H. Lu and Z. Xin, *J. Micromech. Microeng.*, **2010**, 20, 095016.

19. A. M. Hodge, J. Biener, J. R. Hayes, P. M. Bythrow, C. A. Volkert and A. V. Hamza, *Acta Mater*., **2007**, 55, 1343–1349.

20. L. Gibson and M. Ashby, *Cellular Solids: Structure and Properties*, Cambridge University Press, Cambridge, 1997.

21. J. M. Loebs, Master thesis, *Missouri University of Science and Technology*, 2011.

22. R. Liu, S. Pathak, W. M. Mook, J. K. Baldwin, N. Mara and A. Antoniou, *Int. J. Plast.*, **2017**, 98, 139–155.

23. V. S. Deshpande and N. A. Fleck, *J. Mech. Phys. Solids*, **2000**, 48, 1253–1283.

24. L. Gibson and M. Ashby, *J. Proc. R. Soc. London*, **1982**, 382, 43–69.

25. A. N. Gent and A. G. Thomas, *J. Appl. Polym. Sci*., **1959**, 1, 107–113.

26. L. Gong, S. Kyriakides and W.-Y. Jang, *Int. J. Solids Struct*., **2005**, 42, 1355–1379.

27. L. Gong and S. Kyriakides, *Int. J. Solids Struct*., **2004**, 42, 1381–1399.

28. N. C. Hilyad and A. Cunningham, *Low Density Cellular Plastics: Physical Basis of Behavior*, Chapman and Hall, 1994, vol. 3, pp. 110–220.

29. T. P. Bigioni, X. Lin, T. T. Nguyen, E. I. Corwin and T. A. Witten, *Nat. Mater*., **2006**, 5, 265–270.

30. L. J. Gibson, *J. R. Soc., Interface*, **2012**, 9, 2749–2766.

31. H. Hertz, J. Reine Angew. *Math.*, **1881**, 92, 156–171.

32. K. Bertoldi, *Annu. Rev. Mater. Res*., **2017**, 47, 51–61.

33. L. R. Meza, S. Das and J. R. Greer, *Science*, **2014**, 345, 1322.

34. S. Pal, S. Maiti and G. Subhash, *Mech. Mater*., **2010**, 42, 118–133.

35. C. R. Tipton, E. Han and T. Mullin, *Soft Matter*, **2012**, 26, 6880–6883.

36. A. Minoia, L. Chen, D. Beljonne and R. Lazzaroni, *Polymer*, **2012**, 53(24), 5480–5490.

37. L. Gong and S. Kyriakides, *Int. J. Solids Struct*., **2005**, 42, 1381–1399.

38. L. Gong and S. Kyriakides, *Int. J. Solids Struct*., **2005**, 42, 1355–1379.

39. L. Gong and S. Kyriakides, *J. Appl. Mech*., **2006**, 73(5), 807–814.

SUPPORTING INFORMATION

Note 1. Molecular Dynamics Modelling

Note 2. Extraction of Elastic Relaxation Modulus

Note 3. Porosity Dependent Strain Hardening

Note 4. Characteristics of PUAs Nanostructures

Note 5. Finite Element Modeling Details

Note 1: Molecular Dynamics Modelling

N1.1 Force field. The individual components of the total force field energy are:

(S1)

$$V_{tot=} \sum_{ij}^{N_{bond}} \frac{K_{bij}}{2}(r_{ij} - r_{0ij})^2 + \sum_{ijk}^{N_{angle}} \frac{K_{aijk}}{2}(\theta_{ijk} - \theta_{0ijk})^2 + \sum_{ijkl}^{N_{tortion}} \sum_{n=1}^{4} \frac{K_{nijkl}}{2}[1 + (-1)^{n+} + \sum_{i=1}^{N-1} \sum_{j>1}^{N} \left\{ 4 \in_{ij} [(\frac{\sigma_{ij}}{r_{ij}})^{12} - (\frac{\sigma_{ij}}{r_{ij}})^{6}] \right\} + \frac{1}{4\pi\varepsilon_0} \frac{q_i q_j}{r_{ij}}$$

where N_{bond}, N_{angle}, $N_{torsion}$ and N are the numbers of bonds, angles, dihedrals and atoms, respectively; r_{ij} and K_{bij} are the distance and coefficient of bond between particles i and j, respectively; θ_{ijk} and K_{aijk} are the angle and coefficient of angle formed among particles i, j and k, respectively; ϕ_{ijkl} and K_{nijkl} are the dihedral angle and coefficient of dihedral among particles i, j, k and l, respectively. For the Lenard-Jones contribution, ϵ_{ij} is the depth of the potential and σ^{ij} is the finite distance at which the inter-particle potential is zero. They can be determined from geometric combination rules such as $\sigma_{ij} = (\sigma_{ii}\sigma_{jj})^{1/2}$ and $\epsilon_{ij} = (\epsilon_{ii}\epsilon_{jj}))^{1/2}$. For the Coulomb electrostatic interactions, q, is charge and ϵ is the dielectric constant. All atoms optimized potential for liquid simulation (OPLS-AA) contains functional forms for bond, angle, and dihedral deformations among bonded interactions. We use this force field for all our MD calculation since it was found in close agreement with the density functional theory [32-34]. For any atom type in the polyurea structure,

force field parameters were chosen by matching the atom type with its corresponding atom defined in the OPLS parameter database. The cut-off for all MD simulations was also considered as 10 Angstrom.

N1.2 Molecular structures and properties. PUAs result from the reaction of aliphatic triisocyanates (N3300A) and water [3,4], forming interconnected polymer chains with isocyanurate cores and urea linkage as illustrated in Figure S1a-b. By comparing the atomic structures simulated from molecular dynamics with x-ray diffraction results, about eight polymer chains were identified in a primary particle. The polymer chains of various primary particles were entangled together to form bonding, eventually giving rise to a secondary particle as illustrated in Figure 3d. The open polymer chains in the outer primary particles of each secondary particle were randomly connected to form a fibrous structure, as illustrated in Figure S1e. As the basic building block, the primary particle is the material genome for the mechanical properties, which will be the focus of the MD simulation.

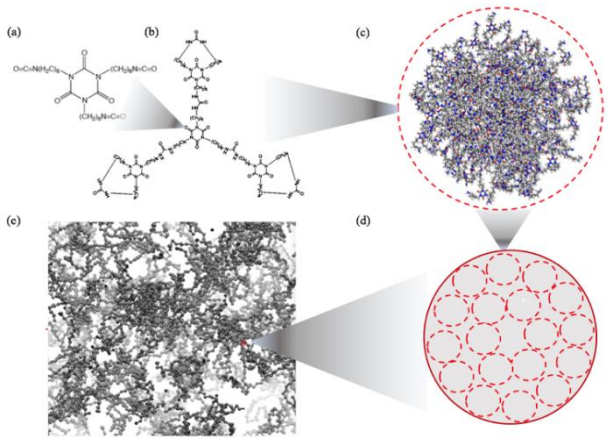

Figure S1. Hierarchical structures of PUAs: (a) chemical structure of isocyanurate core with urea linkages, (b) interconnected polymer chains, (c) primary particle formed with cluster of polymer chains, (d) secondary particle formed with cluster of primary particles, (e) network nanostructure of PUAs formed with linked secondary particles.

For the primary particle, our system of study consists of 8 layers of third generation aromatic polyurea chains (Figure S2a) and it has an initial configuration as it shown in Figure. S2b, in which, two stacks of layers are perpendicular together, where, each stack consists of four layers and the distance between the layers is equal to 4 Angstrom as illustrated in Figure S2b. As shown in Figure S2c-f, the polymer chains start to tangle at the beginning stages (30 ps and before), as time elapses, the tangled chains form a sphere, which has radius approximately 6.4 nm. This is quite close to the 7-nm estimation from experiment. To demonstrate the strong interactions between the primary particles, we conducted a tension simulation by fixing the box size and applying a uniaxial stretch of two primary particles

of with different overlapping distances as shown in Figure S1g. All of the force-distance responses show linear, nonlinear ascending stages followed by a peak strength and the slow force-decreasing force stage. The failure was found to initiate when the stable distance for LJ potentials between particles was exceeded in the contact zone between two particles. The residual strength mainly comes from the polymer chain entanglement. In addition, the tensile and residual strength increase with the increasing overlapping distance. This indicates that the polymer chain entanglement mainly contributes to the strength of the PUA nanostructures. However, the elastic stiffness, which is the slope of the linear ascending stage, does not vary significantly. This indicates that the elastic modulus of all PUA is constant due to the same internal structure of the primary particle. Therefore, we can assume a constant elastic's modulus for the base materials of all PUAs. However, without knowing the exact overlapping distance, the specific yield and residual strength remain undetermined from MD results. It also should be noted here that the viscoelasticity

was not modelled since the modelling time is relative short. However, this approximation will not reverse the claimed assumption that the base material properties should be same given the same primary particle structure.

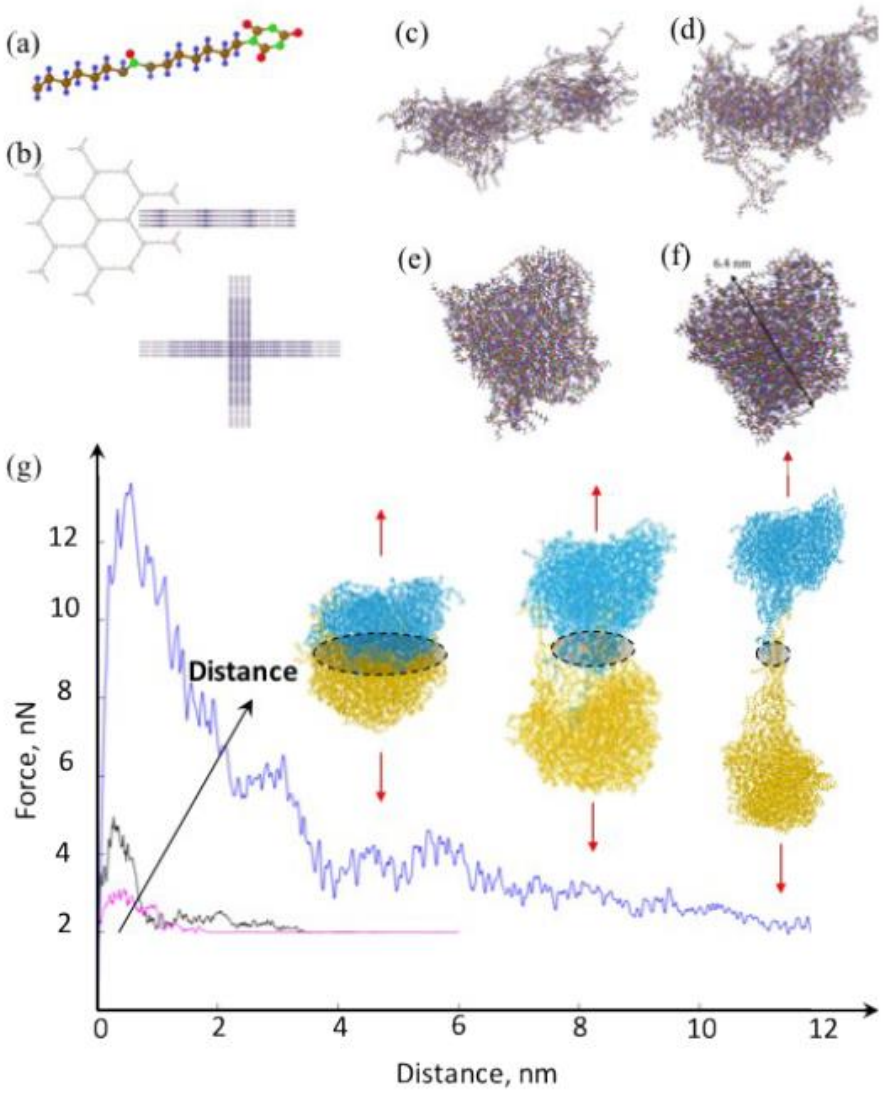

Figure S2. Determine primary structure of PUA: (a) aromatic chain monomer component and structure, the brown, red, green and blue colors indicate carbon, oxygen, nitrogen, and hydrogen atoms, respectively, (b) initial configuration of stacked chain structure for primary particle, (c) primary particle structure at t = 0 s prior to annealing, (d) t = 90 ps, (e) t = 200 ps, (f) t = 2ns after annealing. (g) Force-distance relationship of two primary particles with overlapping distances of: 2 nm (red), 4 nm (black), and 6.4 nm (blue), insert shows failure process and evolution of connecting radius during separation.

Note 2: Extraction of Elastic Relaxation Modulus.

From the proposed approach by Huang and Lu [16], the force (P) and displacement (δ) relation for a linearly ramped displacement loading, $\delta(t) = \delta_0 t$, can be expressed as,

$$P(t) = \frac{4\delta_0^2}{\pi(1-\nu^2)\tan\alpha}\int_0^t E(t-\xi)\xi d\xi \quad \text{(S1)}$$

where $\alpha \approx 70.5°$ for Berkovich tip, which can be re-written as,

$$E(t) = \frac{\pi(1-\nu^2)\tan\alpha d^2 P(t)}{4d\delta^2} \quad \text{(S2)}$$

Therefore, by selecting the form for the relaxation modulus, we have

$$E(t) = E_\infty + \sum_{i=1}^{N} E_i\, e^{-\lambda_i t} \quad \text{(S3)}$$

where E_∞ is the time independent elastic modulus, E_i and λ_i are the time dependent coefficients. By fitting the experimental data as illustrated in Figure S3, the extracted values for PUA-11, 16, and 24 are,

$$E(t)_{11} = E_{\infty,11}(1 + C_{11}\, e^{-0.1t} + D_{11}\, e^{-0.01t}) \quad \text{(S4a)}$$

$$E(t)_{16} = E_{\infty,16}(1 + C_{16}\, e^{-0.1t} + D_{16}\, e^{-0.01t}) \quad \text{(S4b)}$$

$$E(t)_{11} = E_{\infty,24}(1 + C_{24}\, e^{-0.1t} + D_{24}\, e^{-0.01t}) \quad \text{(S4c)}$$

After fitting all experimental data, it was found that E_∞ varies with indentation depths while C and D remains almost constant for each type of PUA. The extracted values for C and D are listed in Table S1. We also found that these coefficients change slightly for different type of PUAs.

Table S1. Time-dependent coefficients for PUAs.

	PUA-11	**PUA-16**	**PUA-24**
C	0.051 ± 0.005	0.045 ± 0.003	0.048 ± 0.006
D	0.110 ± 0.002	0.120 ± 0.007	0.110 ± 0.004

(a)

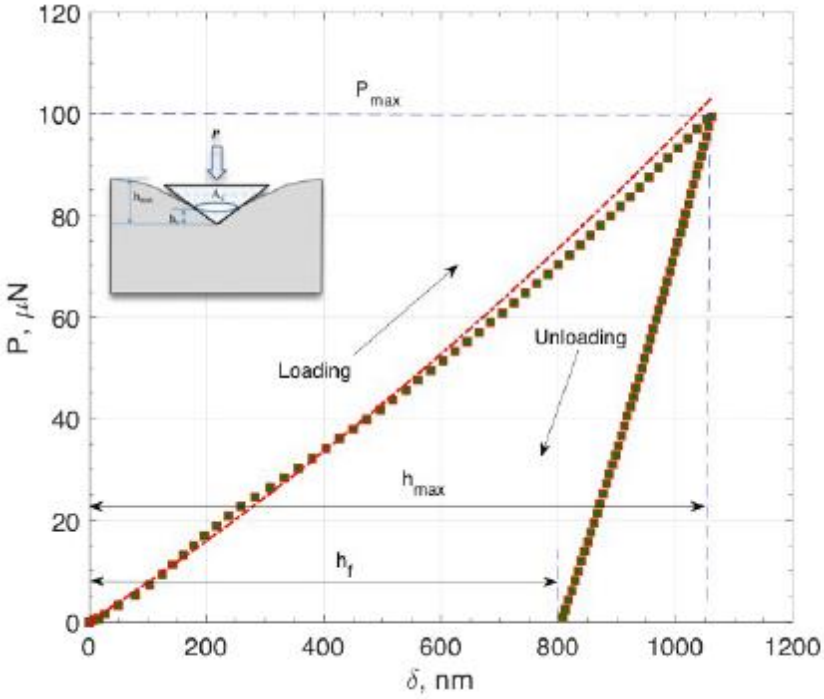

(b)

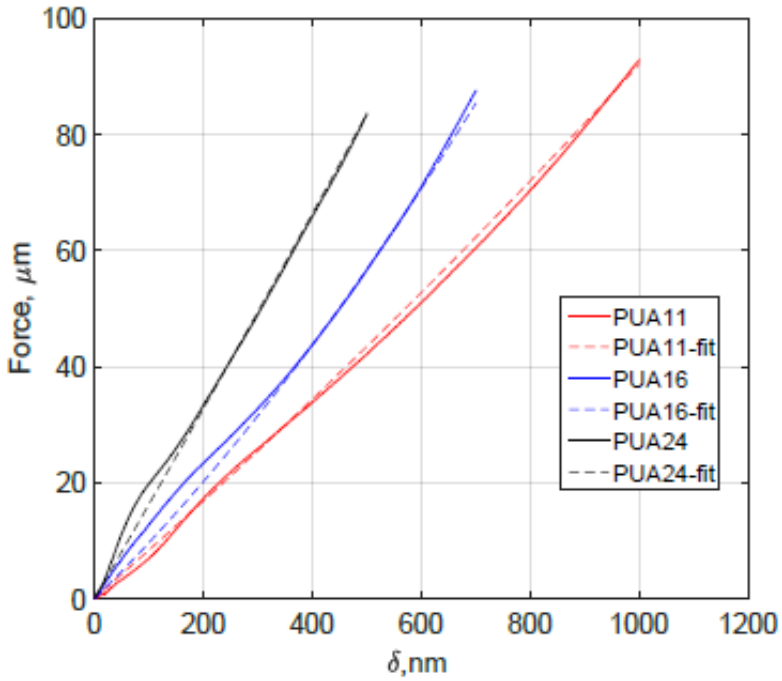

Figure S3. Extraction of elastic relaxation modulus (a) typical force-displacement response, (b) fitting between experiment and analytical values.

Note 3: Porosity Dependent Strain Hardening

The isotropic strain hardening is coupled with the porosity variation. In this model, the total elastic strain energy density of a material integration point w_{e} at the onset of yield for a hydrostatically pressurized condition is,

$$w_{\mathrm{e}} = \int_0^{\varepsilon_{\mathrm{ij}}} \sigma_{\mathrm{ij}} \mathrm{d}\,\varepsilon_{\mathrm{ij}} = \int_0^{\varepsilon_{\mathrm{ij}}} \left(s_{\mathrm{ij}} + p\delta_{\mathrm{ij}}\right)(\mathrm{d}\,e_{\mathrm{ij}} + \mathrm{d}\epsilon\delta_{\mathrm{ij}}), \tag{S5}$$

where σ_{ij} is the total stress tensor; $\varepsilon_{\mathrm{ij}}$ is the total elastic strain tensor, $p = \frac{1}{3}\sigma_{kk}$ is the hydrostatic pressure, δ_{ij} is Kronecker delta, e_{ij} is the deviatoric strain tensor; $\epsilon = \frac{1}{3}\varepsilon_{kk}$ is the hydrostatic strain. The dot product of the deviatoric tensor gives the strain energy density,

$$w_{\mathrm{e}} = \frac{1}{E}\left(\frac{1}{1+(\eta/3)^2}\right)(\sigma_{\mathrm{e}}^2 + \eta^2 p^2) \tag{S6}$$

where $\sigma_{\mathrm{e}} = \left(\frac{3}{2}S_{\mathrm{ij}}S_{\mathrm{ij}}\right)^{1/2}$ is von Mises stress, S_{ij} is the stress deviator, η defines the ellipcity of the yield surface, which is defined by an equation of plastic Poisson's ratio $\eta = \sqrt{\frac{9}{2}\frac{(1-2v_p)}{(1+v_p)}}$, the plastic Poisson's ratio $v_p \overset{\text{def}}{=\!=} -\frac{\mathrm{d}\varepsilon_{p11}}{\mathrm{d}\varepsilon_{p33}}$, with ε_{p11}, ε_{p33} are the transverse and loading directional component of the plastic strain tensor respectively under uniaxial compression. Note that when (which $vp \approx 0$ was found to be the case based the uniaxial compression experiment [19]), $\eta = \sqrt{4.5}$, which is significantly higher than the case of incompressible von Mises plasticity where $\eta = 0$. At uniaxially stressed state, the total elastic strain energy density is then $w_{\mathrm{e}} = \frac{\bar{\sigma}^2}{2E}$, where $\bar{\sigma}$ is the uniaxial stress. If we assume the critical value for the elastic strain energy density remains the same for different stress-states, then the uniaxial yield stress can be expressed as,

$$\bar{\sigma} = \sqrt{\left(\frac{1}{1+(\eta/3)^2}\right)(\sigma_e^2 + \eta^2 p^2)} \tag{S7}$$

This gives us the yield function for multi-axial loading in the form of

$$\Phi = \sqrt{\frac{1}{1+(\eta/3)^2}(\sigma_e^2 + \eta^2 p^2)} - \sigma_e = 0 \tag{S8}$$

Given this yield function, the plastic strain ε_{ij}^{p} is normal to the yield surface and is then defined under the flow-rule with the consistency requirement as,

$$d\varepsilon_{ij}^{p} = \frac{1}{H_p}\frac{\partial \Phi}{\partial S_{ij}}\frac{\partial \Phi}{\partial S_{kl}} dS_{kl}. \tag{S9}$$

where $H_p = \frac{d\bar{\sigma}}{d\bar{\varepsilon_p}}$ is tangent hardening modulus which can be obtained from uniaxial stress versus the plastic strain relationship.

Note 4: Characteristics of PUA Nanostructures

Table 1 summarizes material characterization data pertinent to this work. Bulk densities (ρ_b) increased from 0.123 g cm^{-3} to 0.244 g cm^{-4} for PUA-11 to PUA-24. Skeletal densities (ρ_s) remained constant, as expected from open porosity, Π, which, therefore, decreased in reverse order to ρ_b. The skeletal framework consists of interconnected fibers, which at higher magnification appear as strings of fused beads in all three types of samples. By SANS, all three skeletal frameworks consist of about same-size primary particles (7 nm in radius) with fuzzy interfaces (high-Q slope > 4.00 – Q: scattering vector). From the SANS results, the primary particles formed closely-packed secondary particles (within a low-Q slope of 3.0). The radius of the secondary particles ranged from 17 to 24 nm, which is in good agreement with the average size of the beads (about 40 nm in diameter) as observed from SEM. From these SEM images, all PUA share similar geometrical features in terms of randomness in cell shapes and size as shown in Figure 2. Each ligament of the

network structure has a slenderness ratio (length over radius) above 10. Together with the interconnected structures, a bending dominant deformation mechanism is expected under compression. The post-indentation sites as illustrated in Figure S4a were scanned using atomic force microscopy (AFM). No significant pile-ups were observed from both SEM and AFM images. The distinctive ridges following the shape of the Berkovich tip also indicate strong plastic behaviors as indicated from force-displacement responses. Figure S4a-c showed the typical deformed profiles after indentations of PUA-11, 16, and 24. The linearly fitted lines (dashed lines in Figure S4d) describe the anticipated indentation profiles following the Berkovich tip geometry. Comparing to the experimental results (symbols), the actual deformed profiles are deeper. This indicates an absence of the pile-up behavior usually caused by confinement of adjacent materials.

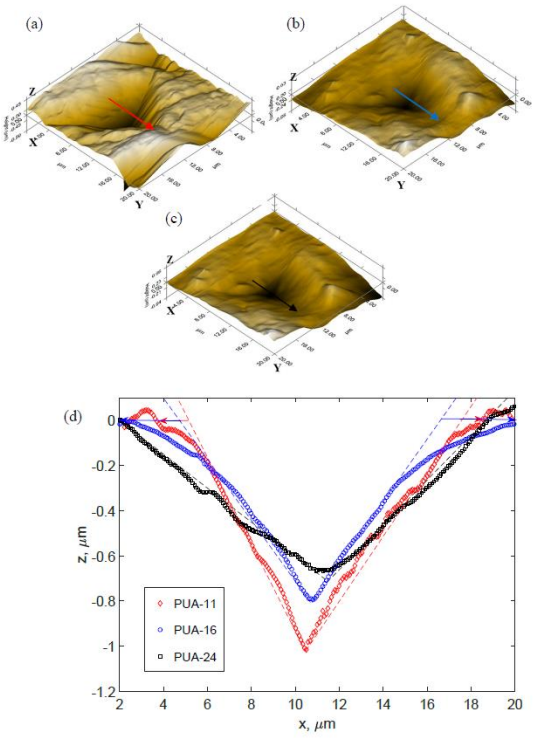

Figure S4. AFM scan of deformation profiles: (a) PUA-11, (b) 16, (c) 24, arrows show cross-section location, (e) cross-sectional profile along the arrows.

Note 5: Finite Element Modeling Details

A three-dimensional half-structure model of indentation was generated as shown in Figure S5a. A friction-free contact was assumed between the indenter and PUA. The radius of the tip is set at 100 nm. The element size is controlled at 25 nm at the contact area and gradually increased as moving away from the contact area as shown in Figure S5b-d.

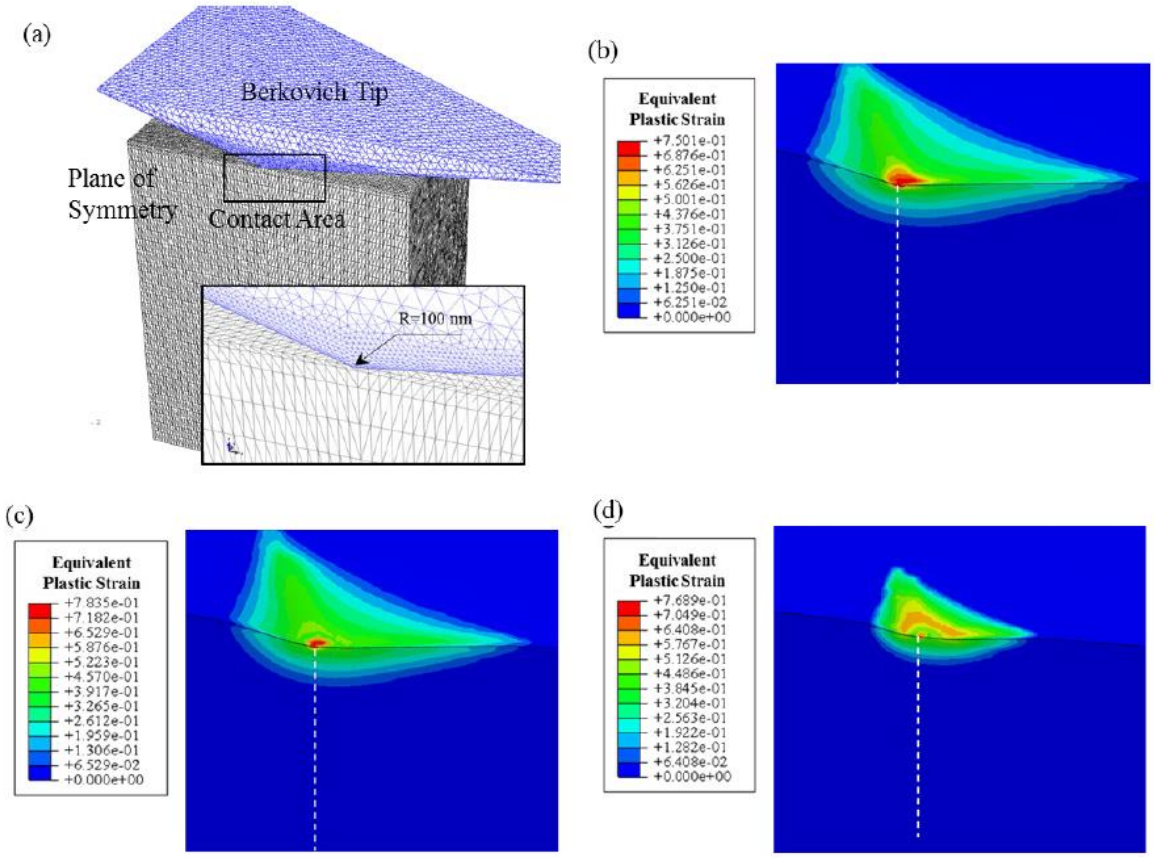

Figure S5. Finite element modelling: (a) half-structure model, (b-d) plastic strain contours near contact for PUA-11, 16, and 24.

SECTION

2. CONCLUSIONS

In paper I, sol-gel derived polyurea aerogels were chosen as a model system to study the factors that affect assembly of nanoparticles into different macroscopic geometries. The polyurea aerogels were well-suited for the purpose of this study as they comprise an archetypical example in which the microstructure can be varied easily from fibrous to particulate by controlling the synthetic parameters. Employing a statistical Design-of-Experiments model, the nanomorphology was studied as a function of various system parameters, which include the dispersion forces, the polarity and H-bonding ability of the gelation solvent as defined by the Hansen Solubility Parameters (HSP), as well as the factors that affect the gelation kinetics (i.e., concentration of monomer, water and catalyst). In total, 208 polyurea aerogel samples with diverse nanomorohologies ranging from caterpillar-like assemblies of nanoparticles, to thin nanofibers, to cocoon-like structures, to large bald microspheres were prepared in eight different solvents. Interestingly, the experimental analysis including CHN, XPS, carbon and nitrogen solid state NMR indicated that the chemical composition of all those samples are identical.

Other part of this work focused on correlating those morphology to the synthetic conditions. However, in order to correlate nanomorphology to synthetic factors, it seemed necessary to associate nano/micro-structure, which is intrinsically a qualitative entity with numbers. Upon reflecting on SEM images, it was realized that first impression about a nanostructure is related to its openness and texture which are quantified by porosity (Π),

and the contact angle (θ) of water droplets with the material, respectively. As a result, the θ/Π ratio referred to as the *K*-index was developed as a descriptor of the diverse nanomorphology of polyurea aerogels. It was noticed that all samples could be classified into eight *K*-index groups with separate nanomorphologies. The *K*-index was then validated by compressing samples to different strains: it was observed that as the porosity decreases, the water contact angle decreases proportionally, and the *K*-index remains constant. The predictive power of the *K*-index was shown with new polyurea aerogels prepared in eight new binary solvent systems. Subsequently, several material properties such as BET surface area, compressive strength and thermal conductivity were correlated to nanomorphology through the *K*-index and that, in turn, provided insight about the root cause of the diversity of the nanostructure in polyurea aerogels. Finally, using response surface methodology, *K*-indexes and other material properties of practical interest were correlated to synthetic conditions. Identification of three-way quantitative relationships among nanostructure, properties, and synthetic conditions is expected to be an essential point of departure for fundamental bottom-up simulations of nanostructure formation.

In paper II, it was concluded that although the polyurea aerogels with $1.2 \leq K \leq 1.5$ demonstrate vastly different macroscopic properties such as bulk density, mechanical strength and thermal conductivity but at nanoscopic level they all consist of the similar-size primary particles. The existence of uniform array of primary particles were proved through nanoindentation, SAXS, XRD, SEM and multi-scale modeling. Computationally, a mechanism for formation of primary particles through Molecular Dynamic (MD) simulations was proposed and it was concluded that a primary particle is not a single molecule and is the result of merging stacked-packed dendrimers.

BIBLIOGRAPHY

1. Aegerter, M. A.; Leventis, N.; Koebel, M. M., *Aerogels handbook*. Springer Science & Business Media: 2011.

2. McNaught, A. D.; McNaught, A. D., *Compendium of chemical terminology*. Blackwell Science Oxford: 1997; Vol. 1669.

3. Hüsing, N.; Schubert, U., Aerogels—airy materials: chemistry, structure, and properties. *Angewandte Chemie International Edition* **1998,** *37* (1-2), 22-45.

4. Leventis, N.; Sadekar, A.; Chandrasekaran, N.; Sotiriou-Leventis, C., Click synthesis of monolithic silicon carbide aerogels from polyacrylonitrile-coated 3D silica networks. *Chemistry of Materials* **2010,** *22* (9), 2790-2803.

5. Du, A.; Zhou, B.; Zhang, Z.; Shen, J., A special material or a new state of matter: a review and reconsideration of the aerogel. *Materials* **2013,** *6* (3), 941-968.

6. Kistler, S. S., Coherent expanded aerogels and jellies. *Nature* **1931,** *127* (3211), 741.

7. Kistler, S., Coherent expanded-aerogels. *The Journal of Physical Chemistry* **1932,** *36* (1), 52-64.

8. Carraher, C. E., General topics: silica aerogels—properties and uses. *Polymer News* **2005,** *30* (12), 386-388.

9. Schultz, J. M.; Jensen, K. I.; Kristiansen, F. H., Super insulating aerogel glazing. *Solar energy materials and solar cells* **2005,** *89* (2-3), 275-285.

10. da Cunha, J. P.; Neves, F.; Lopes, M., On the reconstruction of Cherenkov rings from aerogel radiators. *Nuclear Instruments and Methods in Physics Research Section A: Accelerators, Spectrometers, Detectors and Associated Equipment* **2000,** *452* (3), 401-421.

11. Wittwer, V., Development of aerogel windows. *Journal of Non-Crystalline Solids* **1992,** *145*, 233-236.

12. Gibiat, V.; Lefeuvre, O.; Woignier, T.; Pelous, J.; Phalippou, J., Acoustic properties and potential applications of silica aerogels. *Journal of Non-Crystalline Solids* **1995,** *186*, 244-255.

13. Jones, S. M., Aerogel: space exploration applications. *Journal of Sol-Gel Science and Technology* **2006,** *40* (2-3), 351-357.

14. Guise, M.; Hosticka, B.; Earp, B.; Norris, P., An experimental investigation of aerosol collection utilizing packed beds of silica aerogel microspheres. *Journal of non-crystalline solids* **2001,** *285* (1-3), 317-322.

15. Hrubesh, L. W., Aerogel applications. *Journal of Non-Crystalline Solids* **1998,** *225*, 335-342.

16. Schmidt, M.; Schwertfeger, F., Applications for silica aerogel products. *Journal of non-crystalline solids* **1998,** *225*, 364-368.

17. Rao, A. V.; Bhagat, S. D.; Hirashima, H.; Pajonk, G., Synthesis of flexible silica aerogels using methyltrimethoxysilane (MTMS) precursor. *Journal of colloid and interface science* **2006,** *300* (1), 279-285.

18. Lee, C.; Kim, G.; Hyun, S., Synthesis of silica aerogels from waterglass via new modified ambient drying. *Journal of materials science* **2002,** *37* (11), 2237-2241.

19. Rao, A. P.; Rao, A. V.; Gurav, J. L., Effect of protic solvents on the physical properties of the ambient pressure dried hydrophobic silica aerogels using sodium silicate precursor. *Journal of Porous Materials* **2008,** *15* (5), 507-512.

20. Karmakar, B.; De, G.; Ganguli, D., Dense silica microspheres from organic and inorganic acid hydrolysis of TEOS. *Journal of non-crystalline solids* **2000,** *272* (2-3), 119-126.

21. Durães, L.; Ochoa, M.; Portugal, A.; Duarte, N.; Dias, J. P.; Rocha, N.; Hernandez, J. In *Tailored silica based xerogels and aerogels for insulation in space environments*, Advances in Science and Technology, Trans Tech Publ: 2010; pp 41-46.

22. Brinker, C. J.; Scherer, G. W., *Sol-gel science: the physics and chemistry of sol-gel processing*. Academic press: 2013.

23. Loy, D. A.; Shea, K. J., Bridged polysilsesquioxanes. Highly porous hybrid organic-inorganic materials. *Chemical Reviews* **1995,** *95* (5), 1431-1442.

24. Haereid, S.; Dahle, M.; Lima, S.; Einarsrud, M.-A., Preparation and properties of monolithic silica xerogels from TEOS-based alcogels aged in silane solutions. *Journal of non-crystalline solids* **1995,** *186*, 96-103.

25. Maleki, H.; Durães, L.; Portugal, A., An overview on silica aerogels synthesis and different mechanical reinforcing strategies. *Journal of Non-Crystalline Solids* **2014,** *385*, 55-74.

26. Leventis, N.; Sotiriou-Leventis, C.; Zhang, G.; Rawashdeh, A.-M. M., Nanoengineering strong silica aerogels. *Nano letters* **2002,** *2* (9), 957-960.

27. Randall, J. P.; Meador, M. A. B.; Jana, S. C., Tailoring mechanical properties of aerogels for aerospace applications. *ACS applied materials & interfaces* **2011,** *3* (3), 613-626.

28. Einarsrud, M.-A.; Nilsen, E.; Rigacci, A.; Pajonk, G. M.; Buathier, S.; Valette, D.; Durant, M.; Chevalier, B.; Nitz, P.; Ehrburger-Dolle, F., Strengthening of silica gels and aerogels by washing and aging processes. *Journal of Non-Crystalline Solids* **2001,** *285* (1-3), 1-7.

29. Strøm, R.-A.; Masmoudi, Y.; Rigacci, A.; Petermann, G.; Gullberg, L.; Chevalier, B.; Einarsrud, M.-A., Strengthening and aging of wet silica gels for up-scaling of aerogel preparation. *Journal of sol-gel science and technology* **2007,** *41* (3), 291-298.

30. Bisson, A.; Rigacci, A.; Lecomte, D.; Rodier, E.; Achard, P., Drying of silica gels to obtain aerogels: phenomenology and basic techniques. *Drying Technology* **2003,** *21* (4), 593-628.

31. Vivod, S. L.; Meador, M. A. B.; Nguyen, B. N.; Quade, D.; Randall, J.; Perry, R., Di-isocyanate crosslinked aerogels with 1, 6-bis (trimethoxysilyl) hexane incorporated in silica backbone. **2008**.

32. Leventis, N., Three-dimensional core-shell superstructures: mechanically strong aerogels. *Accounts of Chemical Research* **2007,** *40* (9), 874-884.

33. Li, L.; Yalcin, B.; Nguyen, B. N.; Meador, M. A. B.; Cakmak, M., Flexible nanofiber-reinforced aerogel (xerogel) synthesis, manufacture, and characterization. *ACS applied materials & interfaces* **2009,** *1* (11), 2491-2501.

34. Zhang, Z.; Shen, J.; Ni, X.; Wu, G.; Zhou, B.; Yang, M.; Gu, X.; Qian, M.; Wu, Y., Hydrophobic silica aerogels strengthened with nonwoven fibers. *Journal of Macromolecular Science, Part A: Pure and Applied Chemistry* **2006,** *43* (11), 1663-1670.

35. Yuan, B.; Ding, S.; Wang, D.; Wang, G.; Li, H., Heat insulation properties of silica aerogel/glass fiber composites fabricated by press forming. *Materials Letters* **2012,** *75*, 204-206.

36. Lu, X.; Caps, R.; Fricke, J.; Alviso, C.; Pekala, R., Correlation between structure and thermal conductivity of organic aerogels. *Journal of Non-Crystalline Solids* **1995,** *188* (3), 226-234.

37. Pekala, R. W., Low density, resorcinol-formaldehyde aerogels. Google Patents: 1989.

38. Mulik, S.; Sotiriou-Leventis, C.; Leventis, N., Time-efficient acid-catalyzed synthesis of resorcinol− formaldehyde aerogels. *Chemistry of Materials* **2007,** *19* (25), 6138-6144.

39. Pekala, R.; Schaefer, D., Structure of organic aerogels. 1. Morphology and scaling. *Macromolecules* **1993,** *26* (20), 5487-5493.

40. Nakanishi, K.; Tanaka, N., Sol–gel with phase separation. Hierarchically porous materials optimized for high-performance liquid chromatography separations. *Accounts of Chemical Research* **2007,** *40* (9), 863-873.

41. Far, H. M.; Donthula, S.; Taghvaee, T.; Saeed, A. M.; Garr, Z.; Sotiriou-Leventis, C.; Leventis, N., Air-oxidation of phenolic resin aerogels: Backbone reorganization, formation of ring-fused pyrylium cations, and the effect on microporous carbons with enhanced surface areas. *RSC Advances* **2017,** *7* (81), 51104-51120.

42. Majedi Far, H.; Rewatkar, P. M.; Donthula, S.; Taghvaee, T.; Saeed, A. M.; Sotiriou-Leventis, C.; Leventis, N., Exceptionally high CO2 adsorption at 273 K by microporous carbons from phenolic aerogels: The role of heteroatoms in comparison with carbons from polybenzoxazine and other organic aerogels. *Macromolecular Chemistry and Physics* **2019,** *220* (1), 1800333.

43. Teichner, S. J.; Nicolaon, G. A., Method of preparing inorganic aerogels. Google Patents: 1972.

44. Taghvaee, T.; Donthula, S.; Rewatkar, P. M.; Majedi Far, H.; Sotiriou-Leventis, C.; Leventis, N., K-Index: A Descriptor, Predictor, and Correlator of Complex Nanomorphology to Other Material Properties. *ACS nano* **2019**.

45. Chidambareswarapattar, C.; Xu, L.; Sotiriou-Leventis, C.; Leventis, N., Robust monolithic multiscale nanoporous polyimides and conversion to isomorphic carbons. *RSC Advances* **2013,** *3* (48), 26459-26469.

46. Leventis, N.; Chidambareswarapattar, C.; Mohite, D. P.; Larimore, Z. J.; Lu, H.; Sotiriou-Leventis, C., Multifunctional porous aramids (aerogels) by efficient reaction of carboxylic acids and isocyanates. *Journal of Materials Chemistry* **2011,** *21* (32), 11981-11986.

47. Saeed, A. M.; Rewatkar, P. M.; Majedi Far, H.; Taghvaee, T.; Donthula, S.; Mandal, C.; Sotiriou-Leventis, C.; Leventis, N., Selective CO2 sequestration with monolithic bimodal micro/macroporous carbon aerogels derived from stepwise pyrolytic decomposition of polyamide-polyimide-polyurea random copolymers. *ACS applied materials & interfaces* **2017,** *9* (15), 13520-13536.

48. Donthula, S.; Mandal, C.; Leventis, T.; Schisler, J.; Saeed, A. M.; Sotiriou-Leventis, C.; Leventis, N., Shape memory superelastic poly (isocyanurate-urethane) aerogels (PIR-PUR) for deployable panels and biomimetic applications. *Chemistry of Materials* **2017,** *29* (10), 4461-4477.

49. Daniel, C.; Giudice, S.; Guerra, G., Syndiotatic Polystyrene Aerogels with β, γ, and ε Crystalline Phases. *Chemistry of Materials* **2009,** *21* (6), 1028-1034.

50. Mahadik-Khanolkar, S.; Donthula, S.; Sotiriou-Leventis, C.; Leventis, N., Polybenzoxazine aerogels. 1. High-yield room-temperature acid-catalyzed synthesis of robust monoliths, oxidative aromatization, and conversion to microporous carbons. *Chemistry of Materials* **2014,** *26* (3), 1303-1317.

51. Mohite, D. P.; Mahadik-Khanolkar, S.; Luo, H.; Lu, H.; Sotiriou-Leventis, C.; Leventis, N., Polydicyclopentadiene aerogels grafted with PMMA: I. Molecular and interparticle crosslinking. *Soft Matter* **2013,** *9* (5), 1516-1530.

52. Bang, A.; Buback, C.; Sotiriou-Leventis, C.; Leventis, N., Flexible aerogels from hyperbranched polyurethanes: probing the role of molecular rigidity with poly (urethane acrylates) versus poly (urethane norbornenes). *Chemistry of Materials* **2014,** *26* (24), 6979-6993.

53. Guo, H.; Meador, M. A. B.; McCorkle, L.; Quade, D. J.; Guo, J.; Hamilton, B.; Cakmak, M.; Sprowl, G., Polyimide aerogels cross-linked through amine functionalized polyoligomeric silsesquioxane. *ACS applied materials & interfaces* **2011,** *3* (2), 546-552.

54. Saunders, J.; Slocombe, R., The chemistry of the organic isocyanates. *Chemical reviews* **1948,** *43* (2), 203-218.

55. Davis, T. L.; Ebersole, F., Relative velocities of reaction of amines with phenyl isocyanate. *Journal of the American Chemical Society* **1934,** *56* (4), 885-886.

56. Leventis, N.; Sotiriou-Leventis, C.; Chandrasekaran, N.; Mulik, S.; Larimore, Z. J.; Lu, H.; Churu, G.; Mang, J. T., Multifunctional polyurea aerogels from isocyanates and water. A structure− property case study. *Chemistry of Materials* **2010,** *22* (24), 6692-6710.

57. De Vos, R.; Biesmans, G. L., Organic aerogels. Google Patents: 1996.

58. Lee, J. K.; Gould, G. L.; Rhine, W., Polyurea based aerogel for a high performance thermal insulation material. *Journal of sol-gel Science and Technology* **2009,** *49* (2), 209-220.

59. Jones, S. M., A method for producing gradient density aerogel. *Journal of Sol-Gel Science and Technology* **2007,** *44* (3), 255-258.

60. Leventis, N.; Chidambareswarapattar, C.; Bang, A.; Sotiriou-Leventis, C., Cocoon-in-web-like superhydrophobic aerogels from hydrophilic polyurea and use in environmental remediation. *ACS applied materials & interfaces* **2014,** *6* (9), 6872-6882.

61. Shinko, A.; Jana, S. C.; Meador, M. A., Crosslinked polyurea aerogels with controlled porosity. *RSC Advances* **2015,** *5* (127), 105329-105338.

62. Wu, C.; Taghvaee, T.; Wei, C.; Ghasemi, A.; Chen, G.; Leventis, N.; Gao, W., Multi-scale progressive failure mechanism and mechanical properties of nanofibrous polyurea aerogels. *Soft matter* **2018,** *14* (38), 7801-7808.

63. Moon, S.-Y.; Jeon, E.; Bae, J.-S.; Byeon, M.; Park, J.-W., Polyurea networks via organic sol–gel crosslinking polymerization of tetrafunctional amines and diisocyanates and their selective adsorption and filtration of carbon dioxide. *Polymer Chemistry* **2014,** *5* (4), 1124-1131.

64. Yang, Y.; Jiang, X.; Zhu, X.; Kong, X. Z., A facile pathway to polyurea nanofiber fabrication and polymer morphology control in copolymerization of oxydianiline and toluene diisocyanate in acetone. *Rsc Advances* **2015,** *5* (10), 7426-7432.

65. Chriti, D.; Raptopoulos, G.; Papastergiou, M.; Paraskevopoulou, P., Millimeter-Size Spherical Polyurea Aerogel Beads with Narrow Size Distribution. *Gels* **2018,** *4* (3), 66.

66. Li, Y.; Liao, W.; Taghvaee, T.; Wu, C.; Ma, H.; Leventis, N., Bioinspired strong nanocellular composite prepared with magnesium phosphate cement and polyurea aerogel. *Materials Letters* **2019,** *237*, 274-277.

67. Rewatkar, P. M.; Taghvaee, T.; Saeed, A. M.; Donthula, S.; Mandal, C.; Chandrasekaran, N.; Leventis, T.; Shruthi, T.; Sotiriou-Leventis, C.; Leventis, N., Sturdy, Monolithic SiC and Si3N4 Aerogels from Compressed Polymer-Cross-Linked Silica Xerogel Powders. *Chemistry of Materials* **2018,** *30* (5), 1635-1647.

68. Członka, S.; Bertino, M. F.; Kośny, J.; Shukla, N., Freeze-drying method as a new approach to the synthesis of polyurea aerogels from isocyanate and water. *Journal of Sol-Gel Science and Technology* **2018,** *87* (3), 685-695.

69. Lee, J. K., Organic aerogels reinforced with inorganic aerogel fillers. Google Patents: 2007.

70. Maleki, H.; Durães, L.; García-González, C. A.; del Gaudio, P.; Portugal, A.; Mahmoudi, M., Synthesis and biomedical applications of aerogels: Possibilities and challenges. *Advances in colloid and interface science* **2016,** *236*, 1-27.

71. Sabri, F.; Boughter Jr, J. D.; Gerth, D.; Skalli, O.; Phung, T.-C. N.; Tamula, G.-R. M.; Leventis, N., Histological evaluation of the biocompatibility of polyurea crosslinked silica aerogel implants in a rat model. *PloS one* **2012,** *7* (12), e50686.

72. Yin, W.; Venkitachalam, S. M.; Jarrett, E.; Staggs, S.; Leventis, N.; Lu, H.; Rubenstein, D. A., Biocompatibility of surfactant-templated polyurea–nanoencapsulated macroporous silica aerogels with plasma platelets and endothelial cells. *Journal of Biomedical Materials Research Part A: An Official Journal of The Society for Biomaterials, The Japanese Society for Biomaterials, and The Australian Society for Biomaterials and the Korean Society for Biomaterials* **2010,** *92* (4), 1431-1439.

73. Sabri, F.; Sebelik, M. E.; Meacham, R.; Boughter Jr, J. D.; Challis, M. J.; Leventis, N., In vivo ultrasonic detection of polyurea crosslinked silica aerogel implants. *PloS one* **2013,** *8* (6), e66348.

74. Hildebrand, J.; Scott, R., The solubility of nonelectrolytes, Reinhold Pub. *Co., New York* **1950,** *3*.

75. Launay, H.; Hansen, C. M.; Almdal, K., Hansen solubility parameters for a carbon fiber/epoxy composite. *Carbon* **2007,** *45* (15), 2859-2865.

76. Barton, A. F., *CRC handbook of solubility parameters and other cohesion parameters*. Routledge: 2017.

77. Zhu, Z.; Snellings, G. M.; Koebel, M. M.; Malfait, W. J., Superinsulating polyisocyanate based aerogels: a targeted search for the optimum solvent system. *ACS applied materials & interfaces* **2017,** *9* (21), 18222-18230.

VITA

Tahereh Taghvaee received her Bachelor of Science in 2008 in Pure Chemistry at Shahid Beheshti University in Tehran, Iran. From there, she went to University of Tabriz, where she earned a Master of Science in Inorganic Chemistry in 2011. In Fall 2013, she came to Missouri University of Science and Technology to pursue a doctorate degree in Chemistry under supervision of Prof. Nicholas Leventis. Her research work focused on syntheisis of polyurea aerogels and investigation of their properties for target-specific applications. During the course of her PhD, she coauthored seven (7) journal articles, and has contributed to seven (7) national and regional ACS meetings. She is also co-inventor of one U.S. patent which is filed in April 2018. She received the Chemistry Department's Outstanding Graduate Researcher Award in 2019. In July 2019, she received her PhD in Chemistry from Missouri University of Science & Technology.